High Temperature Ceramic Composites

by

Leonid C. Lev

Submitted to the Department of Mechanical Engineering
in partial fulfillment of the requirements for the degree of

Doctor of Philosophy

at the

MASSACHUSETTS INSTITUTE OF TECHNOLOGY

May 8, 1995

Author .....
Mechanical Engineering Department
May 8, 1995

Certified by .....
Quentin Berg Professor of Mechanical Engineering
Ali S. Argon
Thesis Supervisor

Accepted by .....
Professor Ain Ants Sonin
Chairman, Departmental Committee on Graduate Students
Mechanical Engineering Department

High Temperature Ceramic Composites

by
Leonid C. Lev

Submitted to the Department of Mechanical Engineering on May 8, 1995 in partial fulfillment of the requirements for the degree of Doctor of Philosophy in Mechanical Engineering

Abstract

The progress in a number of applications, including re-entry space vehicles, turbo-machinery and many others, is limited by an inadequate high temperature performance -- i.e., creep and oxidation resistance -- of existing materials, thereby restricting the specific power and effectiveness of the entire assembly. Such materials -- metals and intermetallic compounds -- have reached a limit in their potential. The goal of the present work has been the design, development and investigation of new materials for high temperature applications. As a result of these design efforts aluminum oxide fiber-aluminum oxide matrix composites have been proposed. New titanium and zirconium oxide fiber coatings have been developed for these composites. Experimental technique known as laser spallation method has been further expanded to allow for testing the adhesion strength of thin ceramic coatings and has been applied to newly developed coatings. A mathematical model of the laser spallation experiment has been proposed. Examination of the coatings has shown that the interfacial strength of titanium oxide coatings can be varied in a wide range, thus enabling formation of a weak layer, protecting the fiber of the composite under conditions of catastrophic failure. Inter-diffusion of the elements of the developed composite was found to be of a low level. Mechanical testing of composite has been conducted, showing very high creep resistance and limited deformation to failure in a wide temperature range.

Thesis Supervisor: Professor Ali S. Argon
Title: Quentin Berg Professor of Mechanical Engineering

Acknowledgments

I would like to express my sincere gratitude to all people at MIT and outside for making this work a memorable learning experience.

My deepest appreciation and gratitude goes to my scientific advisor, Prof. Ali S. Argon. During my entire years at MIT I relied on his friendly support. His tremendous intelligence and insightfulness guided me through all the obstacles in my research. His deep scientific knowledge and keen intuition were the precious assets as well as the source of continuous encouragement for me.

I would like to thank Prof. D. M. Parks for numerous fruitful discussions and his very warm and friendly encouragement during the course of my work.

I appreciate the deep professional knowledge of Prof. T. R. Akylas. I would like to thank him for his advice and for his participation in my Thesis Committee.

Prof. F. A. McClintock was a continuous source of wisdom as well as precise scientific knowledge for me throughout my work at MIT. His advice is gratefully acknowledged.

My special thanks go to my office-mates, who left MIT many years ago and who are still at MIT. Sarah Wineman cheered me with her friendship. Alex Staroselsky shared his preciseness in mathematics with me.

I would like to extend my gratitude to Dr. B. Chambers, for his moral support and encouragement.

My very special thanks go to A.-M. Seman, for her friendship and help.

My immense appreciation goes to my family, my parents Olga and Charles Lev, and my sister, Erna Sheyfer, who ultimately made it all possible.

This research has been supported by the ONR under contract ONR N00014 - 89 - J - 1609. For this and his keen interest in this work I am grateful to Dr. S. Fishman of that Agency.

I would like to acknowledge with thanks the support of Advanced Crystal Products, Inc. of Woburn, MA who donated single crystal fibers for this research. We are also grateful to Prof. W. D. Nix and Messrs. J. J. Vlassak and J. Barese of the Department of Material Science and Engineering of Stanford University for their kind help in the nano-indentation experiments and Dr. Richard Krutenat of Textron Specialty Materials for his help in spatter coating of films.

Table of content

List of Figures

Chapter 1

Introduction. Design of a High Temperature Composite Material

An increase in the performance of high temperature components and machinery relies on the development of new materials able to perform under the extreme operating conditions. For such high temperature applications components with continuous reinforcing fibers have many advantages. This work is devoted to the design, development and investigation of these composites.

There are four temperature ranges for which different design considerations are required for composite materials. These are:

1. Ambient and slightly elevated temperatures -- up to approximately 100^0 C. Organic polymer matrix composites reinforced with stiff graphite and ceramic fibers or

fillers offer the best specific mechanical characteristics (strength, elastic stiffness and fracture toughness per unit of weight)

2. In the range above the ambient temperature, up to approximately 400^0 C, composites with matrices of aluminum, magnesium and their alloys are the most suitable.

3. In the range between 400^0 C to 900^0 C, composites with intermetallic compound matrices such as NiAl and TiAl are the most promising.

4. In the range above 900^0 C and up to 1500^0 C (and, possibly, even higher), ceramic matrix composites with matching single-crystal reinforcing fibers appear as the only choices for these conditions.

The area of concentration of the present work is the design, processing and investigation of the properties of materials suited to perform under the conditions of the fourth category listed above, i.e. at temperatures of up to 1500^0 C. On the basis of analysis presented below, composites containing Al_2O_3 polycrystalline matrix reinforced with Al_2O_3 continuous single crystalline fibers was identified as the most promising system and is the focus of the present work.

1.1 Principles guiding the choice of composition

The development of new advanced structural materials for high temperature application remains an important technological goal. The progress in many areas of technology, such as gas turbines, space re-entry vehicle design and the like, is dependent on the development of new high temperature structural materials. The requirements for

these materials are stringent. They must bear high stresses at temperatures of up to 1500 ^{0}C; perform without changes in their properties for hundreds of hours (in some applications for years); withstand highly reactive and hostile environments and have adequate fracture resistance[1] and damage tolerance in the entire temperature range, from ambient temperature to service conditions.

Until recently, materials for high temperature structural applications have been largely restricted to advanced metallic alloys or intermetallic compounds. However, metallic materials and even intermetallic compounds have reached a limit in their potential for development [1.1]. Ceramics present themselves as materials which offer new avenues to a significant increase in service temperature [1.1 - 1.3].

One of the design limiting constraints for high temperature composites under normal operating conditions is creep, which causes a change in the shape and dimensions of the components made out of these composites, and ultimately leads to a time dependent fracture or more complex failure. By virtue of their strong chemical bonds, most ceramics considered as high temperature materials , i.e. oxides, borides, carbides, etc., are more creep resistant than metals, making them the natural choice for materials for high temperature applications. In these materials, up to quite high temperatures, the resolved shear stresses needed to produce dislocation motion on the known slip systems is often larger than what produces fracture in relatively flaw free sample [1.4], making inelastic response by dislocation motion impossible. To increase the resistance to diffusional flow (Nabarro-Herring , Coble creep) it is beneficial to use material with large grains. Another

[1] Normally fracture toughness is a desired response form. Successful fiber reinforced composites however do not exhibit distinct planar cracking that metals do, but fail in a more complex mode involving much delamination along fibers and axial splitting, etc.

consequence of the absence of easily activated dislocation plasticity is the intrinsic brittleness of these materials leading to catastrophic fracture, thus necessitating special means to prevent such behavior.

The successful composite material must utilize the best features of the performance of ceramic materials (i. e. high creep resistance) and to compensate for their disadvantages (low fracture toughness). The composite material with unidirectionally aligned single crystalline fibers is a natural choice to satisfy this requirement. Single crystal fibers will impart to the material high creep resistance. Also the single crystal fibers are usually stronger than the matrix[2] and, with the right choice of mechanical properties of a protective coating, the strong fibers will delaminate from the matrix during brittle fracture of the composite, thus providing the means for enhancing toughness of the composite by crack arrest.

Another design constraint is the chemical reactions that can occur under these conditions of high temperatures. There are two types of concern. One is reactions with the hostile environment - primarily oxidation. Another group is the chemical reactions and mutual solubility between the elements of the composite itself. Reactions of both of these types are very intense and rapidly lead to the deterioration of mechanical properties and eventual fracture. High rate kinetics at these temperatures makes the application of the protective coatings less than effective. Without reliable surface protection oxidation reactions drastically change the properties of the structure in short time, significantly decreasing all mechanical properties.

---

[2] The strength of ceramics (as with all brittle materials) is governed by a distribution of flaws. As single crystalline fibers do not have impurities and grain boundaries, they can be processed with lower levels of flaw populations then the matrix and thus made much stronger than the later.

Some material combinations, including those based on NiAl and MoSi compositions, generate a flux of oxide-forming element(s) from the interior toward the surface and form a continuously thickening oxide layer during the exposure to oxidizing environments at high temperature. This protects the structural components from further oxidation. However, the coefficient of thermal expansion (CTE) of these oxide films usually differs substantially from the CTE of the bulk. This causes generation of high levels of misfit stresses in the coatings during temperature changes, which cause oxide films to crack or spall off by blistering, leading to component failure in quick succession [1.5].

The solution to the oxidation problem demands using oxides. Composites, incorporating single crystal oxide fibers into polycrystalline *matching* oxide matrices of the same composition offer a number of advantages for use at high temperatures in oxidizing environments. This approach will alleviate, if not completely remove, issues of coefficient of thermal expansion (CTE) mismatch between the fibers and the matrix, chemical compatibility between the elements of the composite and atmospheric corrosion. Difference of CTEs between fibers and matrix in such materials is only as large as the difference in CTEs of the anisotropic crystal measured in different crystallographic directions.

The choice of oxides for this kind of composite is rather limited. Single crystalline fibers of only one composition are available commercially, namely, aluminum oxide fibers. While fibers of some other compositions are under development (YAG eutectic fibers, ZrO_2, mullite), excellent creep resistance of α-Al_2O_3 when loaded along the crystallographic *c* direction makes properly aligned aluminum oxide fibers one of the best

candidates for use as a reinforcement. Thus it becomes clear that for high temperature applications, a composite material consisting of unidirectionally aligned continuous single crystal α-Al_2O_3 fibers imbedded into a polycrystalline Al_2O_3 matrix is one of the most promising systems.

It is interesting to note that, not withstanding the common perception, the difference in CTEs of Al_2O_3 in different crystallographic directions is relatively small. Figure 1.1 shows the linear thermal expansion (integral of CTE) for Al_2O_3 over a broad temperature range [1.6]. The difference in the expansion of Al_2O_3 between two principal crystallographic directions during heating from room temperature to 1600 ^{0}C is no more than 0.2%. Moreover, the difference between the measured CTEs in principal directions and that of a polycrystalline matrix is only about half of this value. Thus, this level of thermal misfit could be accommodated by elastic deformation.

The mechanical properties of this Al_2O_3-Al_2O_3 composite, as well as other matching ceramic matrix/ceramic fibers composites, such as strength, fracture toughness and creep resistance are governed by the conditions of the fiber - matrix interfaces [1.7]. The desirable approach is to control the properties of these interfaces through the mechanical properties of the coating, deposited on fiber surfaces prior to incorporating the fibers into the matrix. A successful coating forms a durable chemically inert layer and performs the following functions:

(a) protects the fiber surface from possible mechanical damage during processing of the powder matrix around fibers;

(b) prevents sintering of the fiber to the matrix in the composite during operation, or grain growth of the fibers into the matrix;

(c) forms a mechanical fuse that protects the fiber during service by effective crack deflection.

Moreover, the fiber coating for this composite should be chemically stable in an oxidizing atmosphere, should not be soluble in or react with either matrix or fibers under the temperatures of interest for the desired service period and should be capable of transferring the shear stresses, from the matrix to fibers, associated with the regular service conditions.

To satisfy the above requirements it was proposed to apply a specially chosen metallic coating to the fiber surface prior to incorporating them into the composite. This coating would then later undergo in-situ oxidation during processing of the composite.

As coating material, metallic Zr and Ti were chosen which later oxidized into ZrO_2 and TiO_2 respectively. This choice was based on the phase diagram for TiO_2, Al_2O_3 and ZrO_2. Figure 1.2a shows the phase diagram for Al_2O_3- ZrO_2 As can be seen from the Figure 1.2a, there are no compounds formed between these two oxides in the temperature range up to (1710 +/- 10) ^{0}C. Moreover the solubility between these components was found to be negligible. Figure 1.2b shows the phase diagram for Al_2O_3-TiO_2 [1.8]. While the formation of Al_2TiO_5 phase is thermodynamically possible at a temperature above 1200 ^{0}C, it was hoped that the kinetic of this reaction might be slow at these temperatures due to very low solubility of TiO_2 in Al_2O_3 (about 0.30%) and absence of solubility of Al_2O_3 in TiO_2. As will be shown later, a few grains of Al_2TiO_5 were observed after exposure of TiO_2 coating on Al_2O_3 substrate to 1600 ^{0}C for 24 hrs. The ternary phase diagram of the system Al_2O_3-TiO_2-ZrO_2 is shown in Figure 1.2c and Figure 1.2d. Again, it was expected that while the formation of $ZrTiO_4$ is thermodynamically possible, the kinetics of this reaction might again be slow enough at the temperatures of the order of 1500 ^{0}C.

Thus, the composite of interest here consists of α-Al_2O_3 single crystalline fibers imbedded into a polycrystalline Al_2O_3 matrix. The α-Al_2O_3 fibers are to be coated prior to incorporating them into the matrix with a metal coating, such as Ti or Zr. During the processing of the matrix, which includes sintering in air, the metallic coatings will oxidize and form an oxide coatings with the compositions of TiO_2 or ZrO_2 respectively.

In this composite the creep resistance is supplied by the single crystal α-Al_2O_3 fibers. The creep resistance of single crystal α-Al_2O_3 is highly anisotropic. It is highest in the direction of the crystallographic c axis and is drastically lower in any direction perpendicular to the latter. Thus to utilize the high creep resistance of single crystal α-Al_2O_3, fibers were produced with their c-direction aligned with the fiber axis, and composites of such aligned fibers were studied. The single crystal α-Al_2O_3 fibers were also found to be much stronger than the matrix (almost by an order of magnitude) when loaded in c direction, and with the correct choice of the coating properties, they should also produce crack bridging in service.

This choice of composition answers the problems of creep, chemical compatibility, thermal stresses and thermal fatigue, chemical stability in most corrosive environments and, with the right selection of properties of fiber coating, substantially increases the fracture toughness of the composite. Some of the key properties of this composite will be addressed in what follows.

Chapter 2.

Processing of Al_2O_3 Fiber -- Al_2O_3 Matrix Composites.

2.1 Fiber Processing

The single crystal α-Al_2O_3 fibers used in the present study were grown from the melt using the Edge Defined Film Fed Growth (EFG) process [see 2.1.1 and numerous sources referenced therein]. Each fiber was grown from a hollow cylindrical die tip, to which the molten Al_2O_3 was continuously fed by capillary forces from a crucible. Metallic Mo was used as a crucible and die material, as it is wetted by molten Al_2O_3 and is compatible with it.

Each fiber was started by a seed, grown from a die surface by solidification. Continuous fibers are then grown from the molten film on the die surface by withdrawing the seed in a vertical direction at a speed consistent with the rate at which molten material can be supplied to maintain the continuous film of liquid Al_2O_3, and also extract the heat of solidification.

The fibers in the present study were grown at Advanced Crystal Products Co., (Woburn, MA) to our specifications. Fibers were continuously grown to a length of about 2m at a relatively slow speed of (1-2) m/hr, ensuring that the fiber was free of visible internal defects (voids) and the lateral surface of the fibers was of high quality. The diameter of the fibers was about 140 μm. The cross section of the fibers was not fully round, but had a slightly triangular shape, shown in Figure 2.3.4a. The misalignment of the fibers, i.e. the angle between the fiber axis and crystallographic c-direction, was less than 2.5^0 for all fibers.

2.2 Matrix Processing

2.2.1 Introduction

Forming and matrix processing is one of the critical steps in the design and development of a ceramic composite, as evidenced by the large body of literature devoted to this subject.

Essentially the underlying principle of all processing techniques is that a preform of fibers with required geometry is infiltrated with a matrix or a matrix precursor to form a "green" body with a density of about (65-70)% of theoretical, almost always with subsequent sintering and heat treatment, with the goal to densify the matrix (in most cases) as close to the theoretical density as possible. The infiltrating materials include:

a liquid metal to be oxidized later (the DIMOX® process);

a mixture of metallic and ceramic powder to produce an intermediate shape with sequential oxidizing and sintering and thus obtaining the ceramic body;

a powder slurry followed by Hot Isostatic Pressing (HIP);

liquid precursor infiltration and its variation, sol-gel fabrication;

chemical vapor deposition (CVD).

The obstacle to obtain a high-quality fully dense ceramic matrix is that during the sintering the green body undergoes a significant volumetric shrinkage. Presence of even a small amount of "rigid" reinforcement retards the densification significantly, in some cases

stopping the sintering process altogether [2.2.1, 2.2.2]. Hot isostatic pressure, even with a low level of applied stress, improves densification [2.2.3], but is prone to damage fibers with high anisotropy of strength properties (such as Al_2O_3). While there is some evidence that the densification of ceramic green bodies containing glass forming sintering aids is affected significantly less than those without such sintering aids [2.2.4], the formation of glassy intergranular layers in these materials is detrimental to the creep resistance of the overall composite.

It was proposed to coat the stiff elastic reinforcement with a fugitive coating made up of (a polymeric) material with a melting and evaporation temperature much lower than the temperature at which the ceramic green body starts sintering [2.2.5]. Evaporated polymer coating will leave gaps between the sintering matrix and the reinforcement to be closed during sintering and associated with it shrinkage, thus producing a defect-free composite by a so-called "shrink-fit" process. With the right choice of the polymer coating thickness the process should result in a homogeneously fully dense ceramic bodies.

The experimental verification of this proposition was conducted on a model composite, consisting of Al_2O_3 matrix reinforced with SiC fibers.

The experience of this investigation and results of others [2.2.6] show that for continuous fibers this method, while significantly improving the quality of the matrix, still does not produce the desired high quality ceramic body.

2.2.2 Experimental Methods

The material used in this study was 99.99% pure α- Al_2O_3 (AKP 30, Sumitomo Co. Ltd., Japan) with mean particle size of 0.3 μm. Two different kinds of fibers were used: Saphickon® single crystal Al_2O_3 fibers, of about 140 μm in diameter and 3M® SiC SCS-6 fibers, of 120 μm diameter. The slurry was prepared by suspension of Al_2O_3 powder in water (pH adjusted to 4 by addition of HNO_3) for 24 hours in a glass container with subsequent collection and use of only the middle part of the separated suspension. Different kinds of fugitive coatings on fibers were tried.

Fibers were installed into the mold made out of Teflon, shown in Fig. 2.1, forming a preform, into which the slurry was cast. The slurry was dried on a plaster of Paris board for 24 hours, to form a "green" body. The final stage of drying took place at (65 - 75) ^{0}C for 12-24 hours. Then the fugitive coating was burned away, leaving gaps to be filled during matrix sintering and the associated shrinkage. Specimens were sintered at pre-selected temperatures in the range between 1200 ^{0}C and 1500 ^{0}C for 2 to 4 hrs. in air.

After sintering the density of the processed composite was measured by Archimedes' buoyancy method. Specimens were then cut, ground and polished, using diamond polishing pastes up to a final one of 0.25 μm. Polished specimens were examined with a light microscopy and SEM.

2.2.3 Results and Discussion

The obtained specimens were found to attain 90 to 95% theoretical density after sintering at 1400 ^{0}C for 2 hrs. Further increase in sintering temperature or in time of

sintering did not improve the density. The cross section of a specimen is shown in Figure 2.2a and the embedded SiC fiber is shown in Figure 2.2b.

The specimen was found to contain a network of cracks, connecting fibers. Figures 2.3a and 2.3b show the skewed cross section of a SiC fiber. As can be seen in the figures, the cracks emanate from the fibers. The strength of these specimen was inadequate, with fracture taking place along these pre-existing cracks. Figure 2.4 shows the well-adhered interface between the SiC fiber and Al_2O_3 matrix.

It was found that these cracks were formed during sintering, after the matrix densified by closing up the gaps, left behind after the fugitive coating was removed. To avoid the formation of cracks the thickness of the fugitive coating was increased, which led to formation of wider gaps between the fiber and the matrix. These gaps were not filled in by a shrinking Al_2O_3 matrix and were found in the final sintered body, as is shown in Figure 2.5.

Although Hot Isostatic Pressing (HIP) is known to improve the densification processes [2.2.3], this route has not been taken, because the creep resistance of Al_2O_3 single crystal fibers is very anisotropic: these fibers have a very low deformation resistance in the direction along the basal plane (perpendicular to c-direction) and would have been damaged in the process of HIPing.

2.2.4 Reaction Bonded Aluminum Oxide

The specimens used in the present study of mechanical properties were obtained by oxidation of a green body containing 30% Al, 20% ZrO_2 and the rest -- Al_2O_3 [2.2.6].

Materials were processed in the Ceramics Laboratory of the Technical University of Hamburg-Harburg. This material represents a significant improvement in the development of Al_2O_3/ Al_2O_3 composite. The developed methods of simultaneous oxidation and sintering enables processing of almost defect free ceramic matrix composites. The resulting structure of the composite, although still not fully dense, was found of a higher quality than the structure of a composite, produced by conventional methods. This structure will be discussed in Chapter 5.

2.3 Fiber Coating

2.3.1 Introduction

As was mentioned in the Section 1.1, oxide-oxide composites require development of new kinds of oxide coatings, which in turn calls for the development of new processing ideas for a coating deposition.

One of the main requirements for the developed coatings is that it has to retain stable properties, i.e. strength, fracture energy, elastic moduli, after prolonged exposure to a high temperature environment. These mechanical properties depend directly on the coating structure, which is characterized by crystallinity (or absence thereof), flaw population parameters, pore size distribution and density, etc. Thus, the structure of the coating should be stable under the working conditions of the composite as a whole as they were stated in the Chapter 1, i.e. temperature in the range of up to 1600 ^{0}C, and exposure time in the range of hundreds of hours.

At the same time it should be pointed out that the existing standard methods of coating, such as sol-gel deposition, CVD and PVD, plasma spraying, etc., provide coatings, which are not fully dense, and/or not fully crystallized, i. e. that are not in equilibrium. Exposure to high temperatures triggers the processes, lowering free energy of the structure, such as crystallization and/or sintering. Also, it may cause the release of trapped gases, such as hydrogen from CVD SiC[2.3.1]. As a result, ceramic coatings tend

to shrink at high temperatures. If the coating is attached to a hard substrate, and, thus, constrained, high tensile stresses can develop in the coating, promoting pore enlargement and ultimately cracking [2.3.2, 2.3.3].

To illustrate the results of processes, mentioned above, an experiment with a SiC coating on an Al_2O_3 substrate was conducted. The coated specimen was heated up in the vacuum chamber, under a pressure of 10^{-6} torr. To prevent oxidation of SiC, the residual oxygen was bound by Ti chips.

Figure 2.3.1 shows the pattern of cracks in the CVD SiC coating after exposure to 1200 ^{0}C and associated with it sintering and shrinking. The coating in some spots is seen to delaminate completely, an indication of the residual stresses that are present in the coating and have not been relaxed completely by the cracking.

Figure 2.3.2 shows the crack pattern under higher magnification. It can be seen by the size of the formed cracks and crack opening displacements that the coating has undergone significant shrinkage, estimated to be about 6%. Deformation of this magnitude cannot be sustained elastically, thus leading to the cracking of the coating, which renders the coating useless. To overcome this difficulty and obtain a dense high quality coating a new method was suggested and tested on Ti and Zr.

2.3.2 Experimental procedure

As a coating material metallic Zr and Ti were chosen which later oxidized into ZrO_2 and TiO_2, respectively. Optically polished flat single crystal Al_2O_3 discs and single crystal Al_2O_3 [Advanced Crystal Products, Inc.] fibers were coated with Zr and Ti metal using either electron beam assisted vapor deposition or sputtering to thicknesses of 1μm, 2μm or

3μm and were later oxidized in air at 1100 ^{0}C or 1600 ^{0}C. Although the deposition rates produced by the electron beam assisted vapor deposition are small and typically in the range of microns per hour, this method of deposition was chosen for its versatility and ability to produce coatings of high integrity from most metals, as the studies were mostly exploratory and chemical composition of the coating was one of the unknowns to be determined. The coatings obtained with sputtering had a similar structure, showing that other methods of coating deposition can be employed successfully, should the need arise for higher deposition rates.

The substrate surfaces to be coated were carefully cleaned prior to the deposition processes. The surface preparation included chemical and mechanical cleaning in an ultrasonic bath of acetone and methanol, followed by etching in an oxygen plasma and finally heating up the specimens to a temperature of 1200 ^{0}C. After these surface preparation steps, ion beam assisted deposition was performed under a pressure of 10^{-6} torr with the substrates preheated to 300 ^{0}C, using standard Ti and Zr targets. The results of these processes were high quality, well-adhered metallic layers of Ti and Zr.

Sputtering was chosen for deposition of coatings on fibrous substrates and was made with dual opposed magnetrons operating at 1 kW power each. The three nominal thicknesses of Ti coating were 1μm, 2 μm and 3 μm. The SEM micrographs of the resulting metallic coating on a flat single crystal Al_2O_3 substrate is shown in Figure 2.3.3 and on a cross section of a single crystal Al_2O_3 fiber at four different levels of magnification is shown in Figs. 2.3.4a. Figure 2.3.4b shows the method of measurement of the thickness of the spattered Ti coating using scanning optical microscope.

The oxidation was performed as follows. The Al_2O_3 substrates bearing Ti and Zr coating were put into a controlled atmosphere furnace. The furnace was first evacuated to a pressure of 10^{-6} torr. Then the temperature was slowly raised to the controlled level between 900 and 1100 ^{0}C. At this point pressure was slowly raised and oxygen was allowed into the furnace and oxidation took place at these elevated temperatures above 900 ^{0}C(see Figure 2.3.5), to form continuous well-adhered coatings on the Al_2O_3 substrates. The reasons for this will be discussed in more detail in the following section.

2.3.3 Results and Discussion

The structures of the obtained TiO_2 and ZrO_2 coatings on flat substrates formed by electron beam assisted vapor deposition of metallic Ti and Zr, followed by oxidation at 1100 ^{0}C in air, are shown in Figures 2.3.6 and 2.3.7. The resulting TiO_2 coating on fibrous substrates is shown in Figures 2.3.8(a), and 2.3.8(b) at two different levels of magnification.

It should be pointed out here that metals during the process of oxidation undergo significant volumetric increases. The exact numerical values of these volumetric increases depend on the ratio of densities of the metal and its oxide and is about 28% for Al oxidized into Al_2O_3, 49% for Zr oxidized into ZrO_2 and 43% for Ti oxidized into TiO_2. The volumetric changes of this order cannot be accommodated by elastic deformations. High compressive stresses are generated in the coating during oxidation. These will cause the coating to buckle and delaminate from the substrate by blistering.

The process of buckling of a coating under the compressive residual stress in the case when coatings do not deform plastically is described in [2.3.4] and examples of application to buckled coatings are shown in [2.3.5].

Let us find a critical (elastic) residual deformation ε_{CR} in the coating, that causes the latter to blister, and compare its magnitude with the aforementioned magnitudes of deformations caused by the oxidation process.

Let us denote the magnitude of residual stresses in a continuous untracked coating by σ_0. Then, during the fracture along the coating-substrate interface and subsequent coating buckling, the elastic energy release rate per unit area ΔU is given by [2.3.4]:

$$\Delta U = \frac{h(1-\nu)^2}{2} \cdot \frac{(\sigma_0 - \sigma_1)^2}{E} \qquad (2.3.1)$$

where: h is the thickness of the coating;

ν and E are the Poisson's ratio and Young's modulus respectively of the coating;

σ_1 is the critical stress in the coating, resulting in the buckling of a free standing coating; σ_1 is given by the expression:

$$\sigma_1 = \frac{\pi^2 E}{12(1-\nu^2)}\left(\frac{h}{b}\right)^2 \qquad (2.3.2)$$

where b is a characteristic dimension of the coating [2.3.4].

In the present work, $h \approx 1\mu m$, while $b \approx 1mm$, thus providing an order of magnitude estimate for σ_1 as $\sigma_1 \approx E \cdot 10^{-6}$. As we are interested in a critical deformation ε_{CR} much larger than 10^{-6}, the stresses in the coating σ_0 are much larger than σ_1. Thus in equ. (2.3.1) σ_1 can be neglected compare to σ_0. The critical energy release rate ΔU_{CR} corresponding to the critical deformation ε_{CR} ,can be expressed as:

$$\Delta U_{CR} = \frac{h(1-\nu)^2}{2} \cdot \varepsilon_{CR}^2 E. \qquad (2.3.3)$$

The condition for the blistering of the coating then will be:

$$\Delta U = \Gamma_i(\theta) \qquad (2.3.4)$$

where: Γ_i is the average interfacial separation energy, that could depend on the mixture of modes K_I and K_{II} at the tip of a delaminating blister. The degree of mode-mixedness is designated by a phase angle θ.

The condition (2.3.4) provides the following expression for ε_{CR}:

$$\varepsilon_{CR} = \sqrt{\frac{2\Gamma_i(\theta)}{Eh(1-\nu^2)}}. \qquad (2.3.5)$$

Substituting typical values E = 100 GPa, h = 10^{-6} m, and Γ = 5 J/m^2, the latter being a typical value for a cleavage like separation between Si substrate and SiC coating [2.3.6], the typical value of ε_{CR} was found to be about 10^{-2}. This value is much lower than the

aforementioned strains developed during the oxidation. This deformation ε_{CR} will generate the stresses σ_{CR} in the coating $\sigma_{CR} = 10^{-2}E$.

In the physical experiments, stresses will quickly reach this point, and the coating will start buckling much earlier than the complete oxidation of the metallic film takes place, and this was observed in our prior experiments. To prevent this from happening, it was suggested to begin oxidizing the coatings at elevated temperatures, when the plastic resistance (flow stress) of pure metals Ti and Zr is lower than the σ_{CR}. During the oxidation of the metallic coatings in the temperature range where the creep resistance of metals is very low, the volumetric changes are accommodated inelasticaly by flow of the metallic part of the coating being oxidized.

The final structure of the oxide coatings was influenced by the flux of oxygen cations inside the coating and the flux of metal anions directed toward the surface of the coating being formed. It can be seen from the micrographs of the coatings (Figs. 2.3.6 and 2.3.7), that the Zr coating oxidizes to form a continuous fully dense ZrO_2 coating, while the Ti forms a TiO_2 coatings which had a two-layer structure, with a layer of voids, separating the two layers of the coating. The difference of behavior is a result of the difference in the ratios of diffusivities between oxygen and the metallic cations in ZrO_2 and TiO_2. If the rate of diffusion of metallic anions in the oxidizing layer is higher than the rate of diffusion of oxygen cations replacing them, this results in the formation of a layer of voids during oxidation as in the case of the TiO_2 coating. If, on the other hand, the rate of oxygen cation diffusion is higher than the rate of diffusion of metallic anions, as in the case of the ZrO_2 coatings, no voids are formed.

Thus, oxidation of Ti at elevated temperature produced a two-layer structure in the TiO_2 coating, the two layers being separated by a distinct layer of elongated voids. The formation of this void layer was attributed to the generation and coalescence of Kirkendahl-type voids in the Ti, caused by the diffusion of Ti cations toward the surface through the already-formed TiO_2 [2.3.8]. With increasing temperature, the rate of diffusion of Ti cations toward the surface of the coating in the process of oxidation increases, making void generation and coalescence more likely.

On the other hand the structure of the ZrO_2 coating appears to be fully dense. The coefficient of diffusion of oxygen anions in ZrO_2 is much higher, than in TiO_2 [2.3.9]. Therefore, the oxidation of Zr into ZrO_2 must have taken place on the boundary between the oxide layer and the substrate metal and was fed mostly by the transport of oxygen through the formed ZrO_2 layer rather than by the transport of Zr cations out toward the surface. Thus, the oxidation front between oxide and metal was assumed to be moving inward. This caused the structure of ZrO_2 coatings to be quite different [2.3.9, 2.3.10].

After oxidation at 1100 ^{0}C, coatings were exposed to temperatures of 1600 ^{0}C for periods of 4 to 24 hours in air. As a result of a prolonged exposure to 1600 ^{0}C, the structure of TiO_2 coating coarsened. The coating formed relatively large flat grains, of about 7 to 10 μm in diameter with less than a micron thickness (see Figure 2.3.11).

At this stage some preliminary observations can be made with regard to the adhesive strength between the coating and the substrate. As is shown in Figure 2.3.9, ZrO_2 forms a well-adhered coatings, where the toughness of the interface between the coating and the Al_2O_3 single crystal substrate is higher than the fracture toughness along of one of the cleavage planes of Al_2O_3. While the TiO_2 formed a well-adhered coating as well,

it easily fractured along the layer of voids, as evidenced by the Figure 2.3.10, thus providing a desirable low toughness interface around fibers.

It is important to note that exposure to 1600 ^{0}C for 24 hrs. coarsened the structure of TiO_2 coating and significantly decreased the strength of void layer, causing extensive fracture along it (Fig. 2.3.10). The fact that the structure and the strength of the void layer changes with temperature makes it possible to adjust this strength to a necessary level, depending on the properties of the matrix and fibers, by a heat treatment of the coating after oxidation, provided that the service temperatures will be sufficiently lower and will not cause further changes in the coating structure.

The structure of the ZrO_2 coating is shown in Figure 2.3.12. Zirconia does not wet alumina and, as a consequence, minimizes its free energy by forming menisci, as shown in the figure.

As mentioned above, thermodynamically it is more advantageous for TiO_2 to form $TiAl_2O_5$ at temperatures above 1200 ^{0}C. As the inter-solubility of TiO_2 and Al_2O_3 is negligible, the formation of $TiAl_2O_5$ is delayed. Although the process was found to be relatively slow, so the TiO_2 coating forms a clean layer on the surface of Al_2O_3 (Figure 2.3.13), the formation of an initial seed of $TiAl_2O_5$ leads to quick growth, as shown in Figure 2.3.14a, b and c. The TiO2 coating was found to fracture transgranually, as shown in Figure 2.3.15.

Chapter 3.

Laser spallation experiment

3.1. Introduction

The use of a spallation of a coating from a substrate, when the spallation is induced by a laser pulse generated pressure shock, is proving to be a very precise technique to determine the bond strength of a bimaterial interface formed by the substrate and the coating. With shock waves it is possible to apply a broad tensile pulse capable of causing simultaneous planar separation rather than nucleating and/or propagating cracks. Use of a laser beam to generate such shock waves and to produce spallation has been suggested by a number of investigators, and has been developed as a definitive method for measuring tensile strength in recent years [3.1 - 3.7].

A laser provides an efficient means of generating a well-defined pressure pulse of short duration and relatively high intensity. The pressure impulses generated with this method generally are of a duration that is approximately equal to the duration of a laser pulse, i.e., of order of 1 ns, which makes them particularly convenient for probing the adhesive strength of an interface between a substrate and a thin coating.

Development of fiber reinforced composite materials utilizing coated fibers has stimulated strong interest in the determination of interfacial adhesion between a thin film and a substrate. The mechanical properties of a fibrous composite material, such as their strength, overall work of fracture and creep resistance are governed by the conditions of the fiber - matrix interfaces [3.8, 3.9]. A sophisticated approach is to control the properties of these interfaces through tailoring the mechanical properties of the

coating(s), deposited on fiber surfaces prior to incorporating them into the matrix. In the present study the simulation of laser spallation experiment was conducted, and the laser spallation technique has been used to determine the tensile strength of the interfaces between (0.5 .. 2.0) μm thick special oxide ceramic coatings and the Al_2O_3 single crystal substrate. A new mathematical model of the processes involved in the technique has been developed based on a new strategy for the use of the laser spallation experiment. In the framework of the new mathematical model, the ranges of applicability of a prior simple one-dimensional model were determined. The experiments were conducted under the conditions of applicability of this one-dimensional model, and an accurate interpretation of the measurements was afforded through the use of the developed model. A particular set of experiments, conducted on newly developed oxide coatings of ZrO_2 and TiO_2, deposited on Al_2O_3 substrate, is reported in Chapter 4. The modified method was also applied to other pairs of coating and substrate materials.

3.2. Experimental Strategy

The experimental methodology used in the present series of laser spallation measurements represents a further development of the experimental arrangement reported previously [3.2, 3.11].

The experimental setup, as described previously, consists of a laser, condensing lens and the sandwiched specimen held in a special holder. A sketch of this holder containing the specimen is shown in Figure 3. 1.

The specimen consists of a flat substrate, covered with a thin coating forming the bimaterial interface to be investigated. The other side of the substrate is coated with an energy absorbing layer of appropriate thickness that converts the laser light pulse into a pressure pulse. In the experiments conducted in the present study the substrate consisted of optically polished single crystal Al_2O_3 wafers, while the coatings were thin TiO_2 and ZrO_2 layers, obtained by controlling oxidation of thin metallic coatings, and the energy absorbing layer was a metallic Sn coating. In addition, other energy absorbing layers of Al and Au were also tried. The energy absorbing layer in the typical experimental arrangement is sandwiched-in by an optical grade fused quartz plate, transparent to the wavelength of the laser beam that is used to generate the pressure pulse.

The set of experiments reported here was conducted using a Spectra-Physics DSR-3 Nd:YAG laser operating in the Q-switched mode with a temporal pulse width of about 2.5 ns**. The temporal profile of the beam of this laser was similar to the one shown in Figure 3. 2 [3.19]. The spatial energy distribution in the laser beam was nearly of a Gaussian shape. This laser was capable of generating light with a wavelength of 1064 nm, and the quartz plate is transparent to light of this wavelength. The energy of the

** As the previous studies [2, 11], the present experiments were also conducted in the George Harrison National Laser Laboratory at MIT.

laser beam and the illuminated area of the energy absorbing coating were varied in the experiments in order to produce different levels of laser irradiance.

Under typical experimental conditions, the pulsed laser beam with the nominal diameter of 12 mm was focused by the condenser lens to an average diameter of about 1.6 mm on the energy absorbing coating deposited on one of two float surfaces of the substrate. The nominal substrate thickness was 0.5 mm. As will be shown later, in laser spallation experiments conducted with this ratio of the beam diameter to the substrate thickness, the generated elastic wave can be considered to be propagating as a one-dimensional wave over the central portion of the spot exposed to the illumination. In the experiments reported in the present study, the energy of a single laser pulse was about 1J, and the duration was 2.5 to 3 ns.

As the pulsed laser beam strikes the specimen, the laser beam energy is partially reflected and partially absorbed by the energy absorbing metallic layer, which leads to the explosion-like expansion of the metallic layer. A typical resulting crater on the surface of an energy absorbing Au coating is shown in Figures 3. 3a and 3.3b. As can be seen from Figure 3. 3a, a significant part of the Au layer was evaporated by the laser beam and later condensed in the shape of spherical droplets. Also a pattern of shallow surface cracks on the surface of a polished single crystal Al_2O_3 wafer is readily observable in Figure 3. 3b. A more detailed description of a quite complicated set of processes taking place during the interaction of a laser beam with a metallic coating has been given by von Allmen [3.14], who also provides a rather extensive bibliography on this subject, including a number of mathematical simulations of these processes as well as experimental studies.

The rapid expansion of the confined energy absorbing layer, followed by its immediate collapse, generates a well defined, short duration elastic compression shock wave, propagating towards the coating under investigation. Upon reflection from the free

surface the compressive elastic shock wave reverses sign, becomes tensile and probes the interface between the coating and the substrate in tension.

In the present experiments the specific functional dependence between the laser beam energy and amplitude of a generated pressure pulse was established. A threshold laser fluence level that caused the coating to spall off was recorded, and the corresponding amplitude of the pressure pulse generated in the substrate was introduced into the computer simulation described below. The computer simulation then provided the stress-time history applied to the interface between substrate and coating that caused planar fracture along the interface.

3.3. Pressure Pulse Generation

In our preliminary experiments the shape and the amplitude of the laser-beam-generated pressure pulses were measured experimentally for Au, Al and Sn energy absorbing metallic coatings. On the basis of the analysis of the obtained pressure pulses, the Sn coating was selected, and all subsequent experiments were conducted using this coating. For a discussion and comparison of different materials for energy absorbing coatings see [3.13].

Experimental measurements of the resulting pressure pulses produced by the laser beam were conducted for different levels of laser irradiance. The measured dependence of the amplitude of the pressure pulse on the laser irradiance is shown in Figure 3. 4. An example of the recorded shape of the pressure pulse is shown in Figure 3. 19a.

The resulting stress history experienced by the energy absorbing interface was recorded by using a piezoelectric transducer in place of the specimen [3.5, 3.13], using the fixture similar to the design suggested by Gupta et al. [3.2]. The 2 mm thick wafer made out of piezoelectric X-cut quartz was installed into the specimen holder. One of flat surfaces of the quartz wafer was coated with the energy-absorbing Sn layer. The laser beam, concentrated by the condensing lens, was directed onto this surface. The stress applied to the piezo-electric crystal generates charge displacement, which was measured by a high speed digitizer. A detailed description of the present technique used in the measurement of parameters of the laser beam generated pressure pulses is given in Appendix 1.

Through the above mentioned set of experiments it was concluded that the shape of the pressure pulses was independent of the laser fluence. The amplitude of the pulse, on the other hand, showed the expected strong dependence on the laser fluence, which is in agreement with the results obtained by other investigators [3.20].

3.4. Elastic Wave Propagation. Problem Statement

In the laser spallation experiment, the energy of a laser beam is partially converted into the energy of a pressure pulse as a result of a series of complex processes at the energy absorbing coating and its interaction with the substrate, which are of no interest here. As should be intuitively clear, a short duration pressure pulse applied to the surface of a half space over a circular area will be projected forward into the medium and becomes gradually dispersed laterally from its borders, with increasing distance of penetration. While such lateral dispersion occurs, the pressure wave retains a simple planar character in the central region over a characteristic distance of penetration, which scales with the radius of the initial illuminated spot. Thus, to determine the limits in the specimen thickness inside which the propagating elastic wave may be considered one-dimensional, it was decided to carry out a special analysis of the problem. It is instructive to note here that numerical procedures that employ discretization of the space such as finite elements, etc. should be used with great caution, since they may result in spurious internal scattering of no physical significance, as we discuss further below in Section 3.7.

It is well known [3.34, 3.35] that a one-dimensional elastic wave generated by a pressure pulse with temporal profile, given by:

$$P = P_0 * f(t), \tag{1}$$

will propagate as:

$$\sigma(z,t) = -P_0 * f(t - \frac{z}{c}) \tag{2}$$

where P_0 is the amplitude of the pressure pulse imposed on the surface and $f(...)$ is a function of time (the same in (2) as in (1)). This function $f(...)$ usually is given as a boundary condition at the origin of wave propagation.

The important feature to note here is that *the shape of the stress pulse does not alter* as it propagates through a non-dispersive and non-dissipative (elastic) medium. This suggested the approach that was taken, i.e. to solve a three-dimensional wave propagation problem for a pressure pulse of a known simple shape propagating into an elastic half-space to find the conditions (penetration depth) under which the shape of the pulse in the central region remains unchanged. Clearly, within these bounds a one-dimensional approximation to the real wave propagation problem should be valid and can be used for distances of penetration less than the critical one.

Since the problem of elastic wave propagation is linear, to find the stresses generated in the substrate during the propagation of an arbitrary pressure pulse, it is sufficient to expand the temporal profile of the pulse into Fourier components and analyze in detail the propagation of only a single component.

In the Fourier expansion of the temporal shape of the pressure pulse a family of Walsh functions were used [3.30] as basic elements of analysis. As is known, the Walsh functions form a complete orthogonal set of functions for Hilbert space [3.30, 3.31] and can be used similar to the sinusoidal basis functions of the usual Fourier analysis. Propagation of one of the Walsh functions (namely $0.5(\mathrm{cal}(1, \phi) + 1.0)$, as it is called in mathematical literature) was monitored.

From geometrical considerations the distribution of the absorbed laser beam energy is taken as symmetric about the axis of the beam. In the present model the elastic half space was considered homogeneous, non-dispersive and isotropic with elastic properties given by the pair of Lame constants (λ, μ), and having a density ρ. Thus, the propagating elastic wave has an axial symmetry as well. Therefore, the elastic half-space was considered to be loaded by a compressive pressure pulse with amplitude $P = 1.0$, uniformly distributed over a circular area of radius A. Spatial distribution of the imposed load is shown in Figure 3. 5a, while the time dependence of the pressure pulse is shown

in Figure 3. 5b. This time dependence can be considered as either a difference between two Heaviside step functions H(0) - H(t_0) for $t_0 = 0.2(A/c)$, or as a Walsh function $0.5(\text{cal}(1, \phi) + 1.0)$.

Since the wave propagation problem is axisymmetric, we introduce cylindrical coordinates (r, z, θ) with the z-axis aligned parallel with the axis of the laser beam. We let u and w be the radial and axial components of displacements correspondingly, and let σ_{rr}, σ_{zz}, $\sigma_{\theta\theta}$ and σ_{rz} be the components of the associated stress tensor. Following [3.24] we introduce a non-dimensional space-time variable τ defined as:

$$\tau = \frac{t}{\left(\frac{A}{c}\right)} = \frac{tc}{A}, \tag{3}$$

where "c" is the velocity of P-waves in the solid given by:

$$c = \sqrt{\frac{\lambda + 2\mu}{\rho}}. \tag{4}$$

where: λ, μ are Lame constants and ρ is the density of the solid.

The only length scale in the problem is the radius A of the initially irradiated area, which is taken as the unit of length, and the corresponding time scale is given by the ratio (A/c), which is taken as the unit of time. *Thus in what follows, all the linear dimensions are expressed in terms of A and all the time intervals are measured in terms of (A/c).*

In the absence of body forces the two equations of motion are (written using just introduced convention):

$$\begin{cases} \dfrac{\partial \sigma_{rr}}{\partial r} + \dfrac{\partial \sigma_{rz}}{\partial z} + \dfrac{\sigma_{rr} - \sigma_{\theta\theta}}{r} = (\lambda + 2\mu)\dfrac{\partial^2 u}{\partial \tau^2} \\ \dfrac{\partial \sigma_{rz}}{\partial r} + \dfrac{\partial \sigma_{zz}}{\partial z} + \dfrac{\sigma_{rz}}{r} = (\lambda + 2\mu)\dfrac{\partial^2 w}{\partial \tau^2} \end{cases} \tag{5a, 5b}$$

The boundary conditions are given by a normal pressure pulse of a unit amplitude $P_0 = 1$, applied at the time $\tau = 0$ to the points on the surface of the elastic half-space lying inside the circle of radius A, and removed at the time $\tau_0 = 0.2$:

at $z=0$, $\sigma_{zz} = -p(r, \tau)$, $\sigma_{rz} = 0$, (6a)

where: $p = P_0$, for $r < A$ and $0 < \tau < \tau_0$; (6b)

$p = 0$, for $r > A$ for all times; (6c)

p=0 for r<A for $\tau > \tau_0$.

τ_0 here is the duration of the pulse, taken to be 0.2.

The stress-strain relations for a homogeneous isotropic elastic solid are:

$$\sigma_{rr} = (\lambda + 2\mu)\frac{\partial w}{\partial r} + \lambda\left(\frac{\partial w}{\partial z} + \frac{u}{r}\right); \tag{7a}$$

$$\sigma_{\theta\theta} = \lambda\left(\frac{\partial w}{\partial z} + \frac{u}{r}\right) + 2\mu\frac{u}{r}; \tag{7b}$$

$$\sigma_{zz} = \lambda\left(\frac{\partial w}{\partial z} + \frac{u}{r} + \frac{\partial w}{\partial r}\right) + 2\mu\frac{\partial w}{\partial z}; \tag{7c}$$

$$\sigma_{rz} = \mu\left(\frac{\partial u}{\partial z} + \frac{\partial w}{\partial r}\right). \tag{7d}$$

The basic equations (5a, b) of the problem were solved by Eason's method [3.24] using the Laplace-Hankel transform defined by:

$$\overline{f}(z,\xi,\zeta) = \int_0^\infty \int_0^\infty r f(r,z,\tau) J_k(\xi r) e^{-\zeta\tau} dr d\tau \tag{8}$$

where: $J_k(\xi r)$ is a Bessel function of the first kind of order k of an argument ξr;

ζ and ξ are independent dimensionless variables in the transformed space.

Bessel functions of zero and second order of the first kind were used to find transforms $\tilde{\sigma}_{rr}, \tilde{\sigma}_{zz}, \tilde{\sigma}_{\theta\theta}$ and $\tilde{w}$ of functions $\sigma_{rr}, \sigma_{zz}, \sigma_{\theta\theta}$ and w respectively; Bessel functions of first order were used to transform u and σ_{rz} to obtain $\widetilde{u}$ and $\tilde{\sigma}_{rz}$. After doing so and expressing all variables in terms of displacements u and w we obtain the differential equations for the transformed displacement components $\widetilde{u}$ and $\widetilde{w}$.

These equations were solved to yield the expressions for the transformed components of displacement:

$$\widetilde{u}=De^{-n_1 z}+\frac{n_2}{s}Be^{-n_2 z}, \tag{9a}$$

$$\widetilde{w}=\frac{n_1}{s}De^{-n_1 z}+Be^{-n_2 z}, \tag{9b}$$

where: $n_1=\sqrt{\xi^2+\zeta^2}$, and $n_2=\sqrt{\xi^2+\frac{\lambda+2\mu}{\mu}\zeta^2}$.

The transformed boundary conditions at z=0 were substituted:

$$\bar{\sigma}_{zz}=\frac{P_0}{\xi\zeta}J_1(\zeta)\left(1-e^{-0.2\zeta}\right), \tag{10}$$

and the inversion theorem for Laplace-Hankel transform was applied. After taking the integrals using the Cagniard technique [3.28], the following expressions for the displacements were found [3.24] :

$$\frac{w\mu}{P_0}=\frac{\mu}{2(\lambda+\mu)}I_1+\frac{K}{GH^2}I_2+I_3+I_4 \tag{11a}$$

$$\frac{u\mu}{P_0}=\frac{\mu}{2(\lambda+\mu)}I_5+\frac{1}{GH^2}I_6+I_7+I_8, \tag{11b}$$

where: H, K, G and L are constants involving combinations of the elastic constants of the medium. Their numerical values depend on the elastic properties of the medium and are given in Appendix 2.

The functions $I_1, I_2, I_3, I_4, I_5, I_6, I_7$ and I_8 of time and space include definite integrals with infinite limits, involving exponential, trigonometric and Bessel functions. Their expressions are given in Appendix 3.

The integrals involved in the functions $I_1, I_2, I_3, I_4, I_5, I_6, I_7$ and I_8 were expressed in terms of complete elliptic integrals of first, second and third kind, following Eason at al.[3.33]. The obtained expressions involving integrals of elliptic functions, were determined numerically [3.37] . The results depicting the stress distributions in the propagating elastic wave are shown in Figures. 3.6 to 3.17 for times ranging from $\tau = 0.2$ to $\tau = 2.8$.

3.5. Elastic Wave Propagation: Numerical Results

Figures 3.6 to 3.17 show the principal results of the simulation of the computed elastic wave propagating inside the half-space and display the evolution of the wave shape with time and depth of penetration. The dependent variable $\sigma_{zz}(r,z,\tau)$ normalized with respect to the initial pressure pulse P_0 is plotted as a function of two independent variables: radius r and depth z, at different times τ. The ratio of $\left(\frac{\sigma(r,z,\tau)}{P_0}\right)$ ranges between 0 and 1 and provides direct indication of how the amplitude of the stress component in the elastic wave becomes attenuated and the initial shape of the wave becomes distorted with time and penetration distance into the half-space. As the plots are three-dimensional, they are shown from two different perspectives separated by 60^0 for better visualization.

Figures 3.6a and 3.6b show the distribution of stresses at the time $\tau = 0.2$, when the external load was just removed from the boundary z=0 of the elastic half-space (cf. Figure 3. 5b). As can be seen in Figure 3. 6, at this moment the wave starts propagating as a plane wave. In 3-dimensional (r, z, θ) space, along each line of r = constant, the wave shape is given by:

$$\{\sigma_{zz}(r,\ z,\tau)\ \}_{r=const,\tau=0.2}$$

and it repeats the shape of the pressure pulse P, shown in Figure 3. 5b everywhere in the area r< 1.0, except at the periphery of the illuminated circle with coordinates r = 1.0, z = 0. The loading has a discontinuity along this edge and the stresses have a singularity. While the mathematical model can handle this discontinuity, the numerical tabulation of the model loses precision at these points. Although it is possible to improve the precision of the computations at such points, this was not considered to be necessary, since the discontinuity in the loading is caused by the artificial shape of the sharply defined

pressure pulse and would not be of a concern in the actual experiment where the edge displacements must smoothly, albeit steeply decline to zero.

The main feature to be pointed out here is that the wave propagates exactly as a one-dimensional longitudinal strain wave in the central region (in the sense that the resulting stress distribution is analogous to the one produced by a one-dimensional wave). As will be shown below, this continues to be the case (for the central part of the wave) for times τ less than 1.0, i. e. for a depth of penetration D about equal the radius A of initially illuminated circular region on the surface of the half-space.

The resulting stress distribution at time τ=0.3 is shown in Figures. 3.7a and 3.7b. As can be seen from a comparison with Figure 3. 6, the wave has now propagated exactly a distance z = 0.1 inside the medium, consistent with the speed of propagation *c*. Although the wave starts losing its shape near the edge at r = 1.0, the central region of the wave retains its shape and amplitude.

The stress distribution at time τ=0.4 is shown in Figures. 3.8a and 3.8b when the wave has propagated a distance z = 0.2 into the medium. The early stage of the formation of a Raleigh surface wave can be noticed at the surface along the circular periphery at $r = 1.0$, $z = 0$.

Further alteration of the stress distribution at time τ=0.6 is shown in Figures. 3.9a and 3.9b, where the wave has now propagated a distance of 0.4 into the medium. The Raleigh wave, initiated earlier can be noticed now propagating along the front surface at z=0. Although the peripheral parts of the wave have been distorted from the initial shape, the central part remains of a constant shape and amplitude.

The progressive alterations of the stress distributions with increasing time τ, increasing in steps of 0.2 are shown in Figures 3.6 to 3.17, (a) and (b). The figures show clearly how the stress distribution propagates by 'fraying' at the periphery into the radial

direction and how this fraying progressively propagates toward the center with increasing depth of penetration. The propagation of the Rayleigh wave along the surface at z = 0 is also shown clearly.

It is important to note that even at time $\tau = 2.8$, i. e. when the wave has reached a depth of z = 2.8, the central part of the wave is still not distorted, and the amplitude of the central part remains unaffected and equal to the amplitude of the initial pressure pulse, i. e. the ratio $\left(\frac{\sigma(r,z,\tau)}{P_0}\right)$ remains equal to unity.

The central part of the axially symmetrical wave is of particular interest in the modeling of elastic wave propagation, as it is the location where the magnitude is the highest and where spallation occurs in experiments. Present simulation shows that in the central region there is no geometrical attenuation. This condition is maintained over a penetrating depth of more than two radii A of the initially illuminated circle. In the current spallation experiments where the adhesive strength between coatings and substrates was measured and for which the present simulation has been carried out to validate an earlier one-dimensional simulation of Gupta at al [3.2], the ratio of substrate thickness Z to the illuminated spot radius A ranged typically between 0.5 and 0.65, i. e.:

$$0.5 \leq \frac{Z}{A} \leq 0.65.$$

The present simulation also demonstrates that the experimental results reported earlier by Gupta at al [3.2], where the $\frac{Z}{A}$ ratios ranged between 0.12 to 2.0 were all unaffected by geometrical attenuation in the central region from which the information was collected.

The bounds of applicability of a one-dimensional wave propagation model based on the information provided here is mostly a question of computational error tolerance.

If the ratio of the thickness of the substrate Z to the illuminated spot radius A, $\left(\frac{Z}{A}\right)$, is conservatively chosen to be less than unity, a one-dimensional character for the penetration of the central part will be assured over a radius of r = 0.5, as is clear from Figure 3.11. This range is optimum and was adopted in the present experimental program. Under these conditions, the interpretation of the experimental results suffers from no ambiguity. In particular, the processes of transmission and reflection of the elastic wave from the bimaterial interface formed by a coating and a substrate, and the reflection from a free surface may be mathematically described as a series of reflections of one-dimensional waves, as will be discussed in Section 6 below.

3.6. Stress-Time History On Interfaces Between Coatings And Substrates.

As stated in the introduction the interest in the present simulation was for the purpose of developing a reliable tool for measuring adhesive strength between thin coatings and substrates in non-dissipative media. Thus, the stress-time history across the bimaterial interface between substrate and coating is of primary interest.

As the propagating elastic wave reaches the substrate-coating interface, it will be partially reflected and partially transmitted into the coating. Then the wave reaches the free surface, reflects from it and undergoes multiple reflections inside the coating, while the stress across the interface rises and then progressively becomes attenuated as more of the energy is transmitted into the substrate. For cases of dissimilar elastic constants of the substrate and the coating with no inelastic dissipation, the contributions from multiple reflections form a geometric series. A superposition of these contributions determines time rate of evolution of the net stress acting across the interface between the substrate and the coating.

Thus, the stress history across the interface is produced by a superposition of an infinite number of incident and reflected waves [3.36]. To accomplish this superposition, a process of reflection and attenuation of an infinite harmonic elastic wave $\sigma_i\left(\vec{\mathbf{R}}, \tau\right)$ incident onto the bimaterial interface is considered. On the basis of the simulation discussed in Section 5, and recommendations made there, regarding geometric ratios of the substrate thickness to the radius of illuminated area (i. e., $\left(\frac{Z}{A}\right) < 1.0$), for the purpose of modeling of transmission and reflection the elastic waves can be considered as one-dimensional, propagating normal to the interface. Introducing a new coordinate system with its origin coinciding with the bimaterial interface and its positive direction OX, perpendicular to the interface, the incident elastic wave $\sigma_i(x,t)$ will be given by:

$$\sigma_i(x,t) = \Lambda \exp\left[-i\left(-\frac{x}{c_1}+\tau\right)k_1 c_1\right], \qquad (13)$$

where: c_1 is the speed of a P-wave in medium 1 (substrate), and k_1 is the wave number.

Figure 3.18 gives a graphical illustration of this process of reflection and attenuation of the elastic waves and shows the initial infinite harmonic elastic wave $\sigma_i(x,t)$ incident onto the bimaterial interface in this planar model.

The time-varying character of the signal is represented by the usual complex notation. The axis OX is taken parallel to the direction of the incoming wave propagating perpendicular to the bimaterial interface. The wave number k_1 is defined by:

$$k_1 = \frac{\omega}{c_1}, \qquad (14)$$

where the ω is the radial frequency of the wave.

The bimaterial interface in Figure 3. 18 separates the two elastic media, representing the substrate and the coating. Properties of the substrate and the coating are characterized by their Lame constants and densities, where λ_1, μ_1, ρ_1 are the appropriate values of Lame constants and density for the substrate, while λ_2, μ_2, ρ_2 are those for the coating, which is taken to be of thickness l.

The coefficient of transmission of elastic waves through the substrate-coating interface is ξ_T:

$$\xi_T = \frac{2\rho_2 c_{L,2}}{\rho_2 c_{L,2} + \rho_1 c_{L,1}}. \qquad (15)$$

We introduce two coefficients of reflection of elastic waves: ξ_{R1} and ξ_{R2}, defined as:

$$\xi_{R1} = \frac{\rho_1 c_{L,1} - \rho_2 c_{L,2}}{\rho_2 c_{L,2} + \rho_1 c_{L,1}}; \quad \xi_{R2} = -1, \qquad (16a, b)$$

These coefficients characterize the reflection from the substrate-coating interface and the free surface respectively (see Figure 3. 18). As interface 2 is a free boundary, $\xi_{R2} = -1$. $c_{L,1}$ and $c_{L,2}$ are longitudinal wave speeds in the substrate and the coating given by:

$$c_{L,i}^2 = \frac{\lambda_i + 2\mu_i}{\rho_i}. \qquad (17)$$

It should be noted, that if the elastic constants of the substrate and the coating are numerically close, almost all elastic wave energy is transmitted back through this interface (the amplitude of the reflected wave σ_2 is very small, see Figure 3. 18), and the elastic reflections of higher orders can be neglected, as was done in [3.13].

Thus, the incident wave σ_i is partially transmitted into the coating through the interface 1 with the coefficient of transmission ξ_T, and partially reflected (Figure 3. 18). The transmitted part σ_0 is given by:

$$\sigma_0 = \xi_T P_0 e^{-i\left(-\frac{x}{c_2}+t\right)k_2 c_2} \qquad (18)$$

where P_0 is the amplitude of the incoming one-dimensional pressure wave, and $k_2 = \frac{\omega}{c_2}$.

The elastic wave σ_0 propagates forward inside the coating and is reflected from the free surface (interface 2) with the coefficient of reflection of ξ_{R2}, forming the wave σ_1:

$$\sigma_1 = \xi_{R2}\xi_T P_0 e^{2ik_2 l} e^{-i\left(\frac{x}{c_2}+t\right)k_2 c_2} \qquad (19)$$

If the absolute value of ξ_{R2} is less than 1, a part of the energy is transmitted through the interface 2. Wave σ_1 is propagating in the direction ($-x$), opposite to the direction of propagation of the initial wave σ_i and σ_0, and its phase is delayed by ($2l/c_2$). When this wave, σ_1, reaches the interface 1 between the coating and the substrate, it is transmitted

partially into the substrate and is partially reflected back into the coating with a coefficient of reflection ξ_{R1}, forming the wave σ_2:

$$\sigma_2 = \xi_{R1}\xi_{R2}\xi_T P_0 e^{2ik_2 l} e^{-i\left(-\frac{x}{c_2}+t\right)k_2 c_2} \qquad (20)$$

The wave σ_2 propagates in the same direction as the wave σ_0. It reflects from the interface 2, forming the wave σ_3:

$$\sigma_3 = \xi_{R1}\xi_{R2}^2\xi_T P_0 e^{4ik_2 l} e^{-i\left(\frac{x}{c_2}+t\right)k_2 c_2} \quad , \qquad (21)$$

propagating in the direction, opposite to that of the initial wave σ_i , and its phase is delayed further by the $(2l/c_2)$ compared to the wave σ_2. As should be clear, the processes of multiple reflection and loss of energy through the reflection of waves back into medium 1 will continue, and leads to a generic recursion relation of:

$$\sigma_{n+2}=\sigma_n \xi_{R1}\xi_{R2}\, e^{2ik_2 l} . \qquad (22)$$

The net stress σ_{net}, acting across the boundary is obtained by superposition of all the elastic waves σ_n, thus giving:

$$\sigma_{net} = \sum_{n=0}^{\infty} \sigma_n \quad . \qquad (23)$$

While the number of the terms in the sum is infinite, when grouped in pairs the sum forms a geometric progression with the first term σ_0 and geometric ratio B:

$$B = \xi_{R1}\xi_{R2} e^{2ik_2 l} . \qquad (24)$$

Thus the ratio of the stresses generated inside the coating, to the stress in the incident wave is:

$$\frac{\sigma_{net}}{\sigma_i} = \xi_T \frac{1+\xi_{R2} e^{2i(l-x)k_2}}{1-\xi_{R1}\xi_{R2} e^{2ilk_2}} \qquad (25)$$

This ratio is a function of the position (coordinate x) and the ratio of the elastic constants of the coating and the substrate.

Finally the net stress acting across the substrate-coating interface (x = 0), in units of the stress amplitude of the incoming wave becomes:

$$\frac{\sigma_{net}}{\sigma_i} = \xi_T \frac{1 - e^{2ilk_2}}{1 + \xi_{R1}\, e^{2ilk_2}}$$

This expression gives the "transformation ratio" between the incident stresses and the stresses on the substrate-coating bilateral interface as a function of the wave numbers k_2 or radial frequencies ω of the incident waves and transmission and reflection coefficients.

The typical initial temporal profile of a laser generated pressure pulse, which was measured by a piezo-electric transducer as described in the Section 3, is shown in Figure 3. 19a. Considering the findings stated in Section 4, we conducted experiments in the present study on specimens with typical substrate thickness to laser beam radius ratio of $Z/A = 0.63$(Z = 0.5 mm and A = 0.8 mm). Thus, the elastic wave is transmitted through the specimen without distortion in its shape in the central region of interest. Assuming that there was no inelastic dissipation or dispersion we conclude that the temporal profile of the incident wave just before the bimaterial boundary is reached is identical to the temporal profile of the initially generated pressure pulse. This initial temporal profile was taken as that of the incident elastic wave, and was expanded using the Fast Fourier Transform (FFT) method. The obtained spectrum is shown on Figure 3. 19b in the frequency domain. The spectrum is symmetric because of aliasing. The resulting stress history on the bimaterial interface, obtained by applying the above transformation ratio and taking the inverse FFT was found to be dependent on the coating thickness and on the elastic constants of the coating and substrate, as could be expected. Figure 3.20a shows the results for the case when the coating and substrate have identical elastic

properties. Figures 3.20b and 3.20c show in turn the results for TiO_2 and ZrO_2 coatings on Al_2O_3 substrate respectively. Figures 3.21a and 3.21b show a resulting stress amplitude on an interface between a C coating and a Si substrate as a function of the coating thickness for two different ranges of coating thicknesses. It is noteworthy that while the stresses on the interface grow almost linearly in the range of small coating thicknesses (Figure 3. 21a), they reach an asymptotic value, corresponding to the coating thickness sufficient to contain the whole pressure pulse.

3.7. Conclusions

The combination of theoretical analysis and experimental measurements with a laser spallation experiment provides a reliable functional dependence between the energy of a laser pulse and stresses generated across bimaterial interfaces, provided the media of interest has negligible inelastic dissipation and other forms of dispersion. During the subsequent measurements of the adhesion between a coating and a substrate the energy of a laser beam is varied in controlled manner up to a point when the stresses acting across the bimaterial interface produce a spallation of the coating, thus determining the level of tensile strength of the substrate-coating interfaces.

Laser spallation experiments, making use of the results of the present work, were conducted on new coating and substrate materials mentioned above and described in detail elsewhere [3.13, 3.38]. In these experiments specimens were probed using laser beams of an increasing energy. In each experiment the threshold laser beam energy level causing the coating to spall was recorded. These energy levels were converted into corresponding stresses using the results of the newly developed simulation. These stresses determined the strength of the bond on bimaterial interface.

APPENDIX 1. Experiments With X-Cut Piezo-Electric Quartz Crystals

A laser beam, impinging on a thin energy absorbing metallic film deposited on an elastic media, triggers a complex set of processes resulting in a partial conversion of a laser beam energy into the elastic energy of a pressure pulse. The shape and the amplitude of the pressure pulse generated by these processes were measured using special piezo-electric quartz transducer.

This piezo-electric transducer, with its top and side views shown on Figures 3.A1a and 3.A1b, consisted of a flat wafer, made out of x-cut quartz crystal, with its two opposite surfaces optically polished. One of the surfaces, which will be referred to as a front surface, was coated with 1.0 μm thick tin coating, used later in experiments as an energy absorbing coating. As tin is a conductor, this tin coating also formed one of two electrodes, attached to piezo-electric quartz crystal and used for an electric signal pick up. The opposite surface of the x-cut quartz wafer, which will be referred to as a back surface, was coated with a 0.1 μm thick gold coating, thus forming the second electrode. It should be noted that the gold coating was used here exclusively for an electric signal pick up and not for pressure pulse generation. Furthermore, the influence of the gold coating on the processes of elastic wave propagation and reflection on the back surface of the x-cut quartz wafer was considered to be negligible because of small thickness of the gold coating and was neglected.

The tin coating was deposited by rf sputtering and the gold coating was deposited by electron beam evaporation. During the gold deposition the crystal was masked so that only the center 2.0 cm of the disk surface was coated.

These two coatings --tin on a front surface and gold on the back surface -- formed two electrodes, designed to pick up electric current generated during the deformation of the x-cut quartz wafer. Electric conductive wire was glued to the gold coating with a silver-containing conductive epoxy (Tracon‰ Tra-duct 2922), connecting a back surface

electrode to a BNC connector and further to a measuring device. In earlier designs, used for the experiments, reported in [3.2], connection to the gold electrode was made by a mechanical contact and was subsequently found to be a source of electrical noise in the measurements.

The electrical connection between the laser absorbing film and the grounded case of the fixture was enhanced using a silver containing paint to produce a line between the edge of the x-cut quartz crystal and the fixture case across the optical quartz. The access port arranged for this purpose is shown in the Figure 3. A1, (b).

A Lecroy 1.2 GHz digitizer with a 50 ohm internal impedance was used to measure the transient voltage induced by the pressure wave. It was connected to the BNC outlet of the electrode assembly and, together with the back surface gold electrode and conductive wire, completed the electric circuit.

Graham et al. [3.A3.1] have shown that if the time variant stresses are applied to two opposite surfaces of an x-cut quartz crystal coated with a conductive metal and, thus, transformed into electrodes, and if these electrodes are electrically connected by a short circuit, than the instantaneous value of the electric current will be proportional to the instantaneous stress intensity:

$$\sigma_o = \frac{l}{fAU_s} i \qquad (A.1)$$

where l is the thickness of the crystal, A is the area of impact, U_S is the wave propagation velocity, and f is the piezo-electric polarization coefficient. U_S and f are 5720 m/s and 2.15×10^{-12} C/m^2/Pa, respectively for x-cut quartz [3.A3.1].

The pressure wave measurement was made by focusing the laser to a nominal diameter of 1.6 mm at the tin coating on a front surface. The beam intensity was separately measured for a number of different levels on the unfocused beam with the laser operating in a 10 Hz continuous pulse mode. Then for each level of the beam intensity the laser was switched to the single pulse mode and the power meter was

removed from the beam path. A single laser pulse was fired onto the tin coating, while the digitizer was simultaneously trigged by the laser. The digitizer recorded the transient voltage signal. This information was stored, the digitizer's memory was reset, and the procedure was repeated for the next level of beam intensity.

The voltage peak intensity was used to calculate the peak stress using equation A.1.

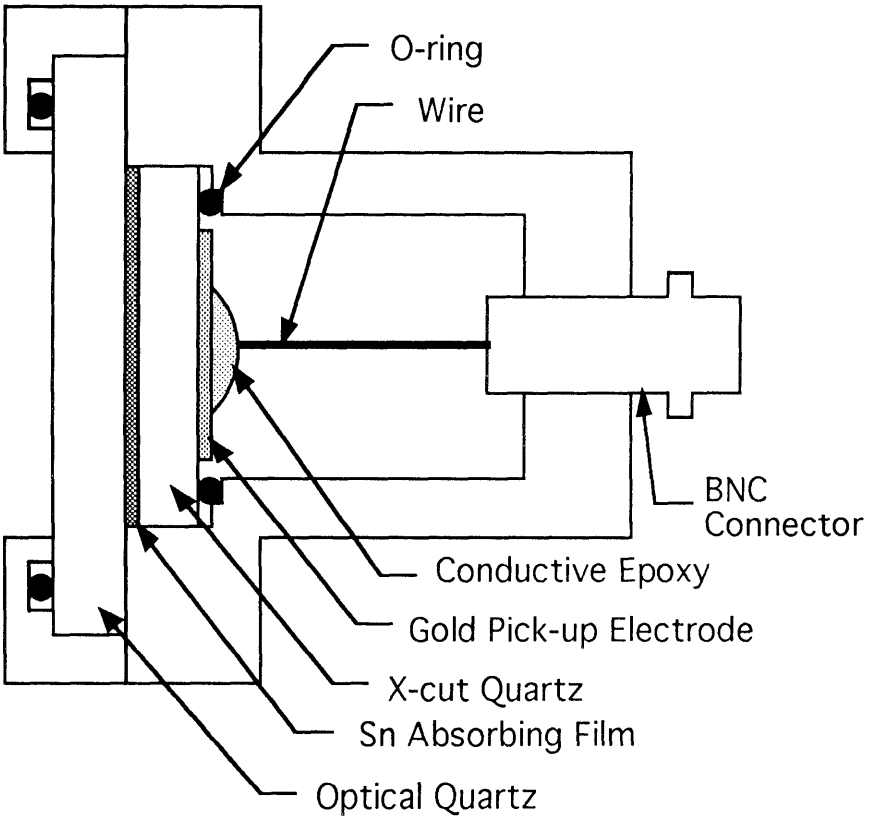
O-ring
Wire
BNC
Connector
Conductive Epoxy
Gold Pick-up Electrode
X-cut Quartz
Sn Absorbing Film
Optical Quartz

(a) Side View

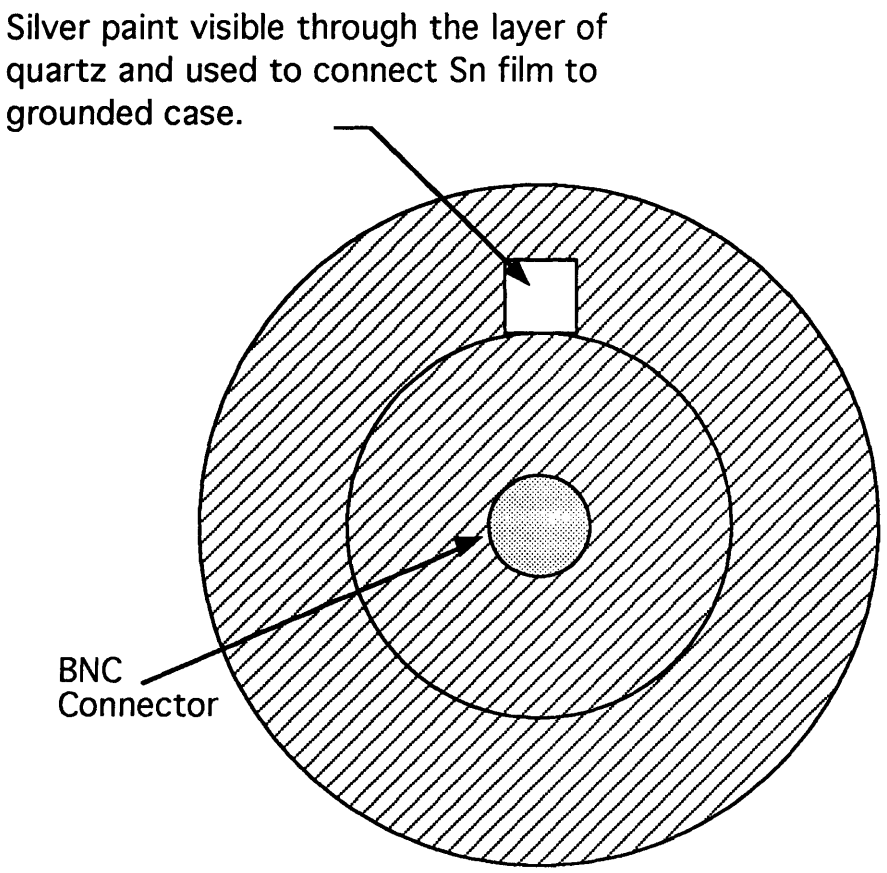

(b) Top View

Figure 3.A1, (a) and (b). Schematic of electrode containing piezo-electric x-cut quartz

Appendix 2. Expressions For The Constants H, K, G And L In Terms Of Elastic Constants Of The Elastic Medium.

For a material with Poisson ratio $\nu = 0.25$:

$$H = \frac{\sqrt{2(3 - \sqrt{3})}}{3};$$

$$K = \sqrt{1 - H^2};$$

$$G = 2(\frac{\lambda+2\mu}{\mu})(1 - 0.5(\frac{\lambda+2\mu}{\mu})H^2) - \frac{L}{K} - (\frac{\lambda+2\mu}{\mu})\frac{K}{L};$$

$$L = \sqrt{1 - (\frac{\lambda+2\mu}{\mu})^2 H^2};$$

Appendix 3. Expressions For The Integrals I_1, I_2, I_3, I_4, I_5, I_6, I_7 And I_8.

$$I_1 = \int_0^{\infty} \frac{\frac{\lambda+2\mu}{\mu} + hz(\frac{\lambda+2\mu}{\mu} - 1)}{h} J_0(hr)J_1(hA)e^{-hz}\, dh$$

$$I_2 = \int_0^{\infty} \mathrm{dh}[\frac{(1 - 0.5\frac{\lambda+2\mu}{\mu}H^2)e^{-Khz} - e^{-Lhz}}{h}] *$$

$$[J_0(hr)\, J_1(hA)\cos(\sqrt{\mathrm{H}}\mathrm{h}\tau)]\ ;$$

$$I_3 = \frac{1}{2\pi}\int_1^{\infty} dy \int_0^{\infty} dh\{\frac{\sqrt{y^2 - 1}}{y((1 - 0.5(\frac{\lambda+2\mu}{\mu})y^2)^2 + \sqrt{y^2 - 1}\sqrt{\frac{\lambda+2\mu}{\mu}y^2 - 1}}\} *$$

$$\{J_0(hr)\, J_1(hA)[(1 - 0.5\frac{\lambda+2\mu}{\mu}y^2\frac{\cos[(y\tau + z\sqrt{y^2 - 1})h]}{h} +$$

$$(1 - 0.5(\frac{\lambda+2\mu}{\mu})y^2)\cos[(y\tau - z\sqrt{y^2 - 1})h] -$$

$$\cos[(y\tau + z\sqrt{\frac{\lambda+2\mu}{\mu}y^2 - 1})h] - \cos[(y\tau - z\sqrt{\frac{\lambda+2\mu}{\mu}y^2 - 1})h]\ \}\ ;$$

$$I_4 = \frac{1}{2\pi}\int_{\sqrt{\frac{\mu}{\lambda+2\mu}}}^{1} dy \int_0^{\infty} dh\ \{\frac{\sqrt{1 - y^2}}{y((1 - y^2)(\frac{\lambda+2\mu}{\mu}y^2 - 1) + (1 - 0.5\frac{\lambda+2\mu}{\mu}y^2)^4)}\} *$$

$$\{\frac{J_0(hr)J_1(hA)}{h}[2(1 - 0.5\frac{\lambda+2\mu}{\mu}y^2)\sqrt{1 - y^2}\sqrt{\frac{\lambda+2\mu}{\mu}y^2 - 1}\, e^{-hz\sqrt{y^2 - 1}}\cos(hy\tau) +$$

$$2(1 - 0.5\frac{\lambda+2\mu}{\mu}y^2)^2 \sin(hz\sqrt{\frac{\lambda+2\mu}{\mu}y^2 - 1})\cos(hy\tau) -$$

$$2\sqrt{1 - y^2}\sqrt{\frac{\lambda+2\mu}{\mu}y^2 - 1}\cos(hy\tau)\cos\left(hz\sqrt{\frac{\lambda+2\mu}{\mu}y^2 - 1}\right);$$

$$I_5 = \int_0^\infty dp \frac{J_1(hr)J_1(hA)}{h} e^{-hz}\left(1 - hz\frac{\lambda + \mu}{\mu}\right);$$

$$I_6 = \int_0^\infty dp \frac{J_1(hr)J_1(hA)}{h}\cos(Hp\tau)\left[\left(1 - 0.5H^2\frac{\lambda+2\mu}{\mu}\right)e^{-Kpz} - KLe^{-Lpz}\right];$$

$$I_7 = \frac{1}{2\pi}\int_1^\infty dy \int_0^\infty dp\left\{\frac{1}{y\left[\left(1 - 0.5\frac{\lambda+2\mu}{\mu}y^2\right)^2 + \sqrt{y^2 - 1}\sqrt{\frac{\lambda+2\mu}{\mu}y^2 - 1}\right]}\right\} *$$

$$\left\{\frac{J_1(hr)J_1(hA)}{h}\left[\left(2 - \frac{\lambda+2\mu}{\mu}y^2\right)\cos(py\tau)\sin\left(z\sqrt{y^2 - 1}\right) +\right.\right.$$

$$\left.\left.2\sqrt{y^2 - 1}\sqrt{\frac{\lambda+2\mu}{\mu}y^2 - 1}\cos(py\tau)\sin\left(z\sqrt{\frac{\lambda+2\mu}{\mu}y^2 - 1}\right)\right];\right.$$

$$I_8 = \frac{1}{2\pi}\int_{\sqrt{\frac{\mu}{\lambda+2\mu}}}^1 dy \int_0^\infty dh\left\{\frac{\sqrt{\frac{\lambda+2\mu}{\mu}y^2 - 1}\sqrt{1 - y^2}}{\left[\left(1 - 0.5\frac{\lambda+2\mu}{\mu}y^2\right)^4 + (1 - y^2)\left(\frac{\lambda+2\mu}{\mu}y^2 - 1\right)\right]}\right\} *$$

$$\left\{\frac{J_1(hr)J_1(hA)}{h}\left[2\left(1 - 0.5\frac{\lambda+2\mu}{\mu}y^2\right)e^{pz\sqrt{-1 - y^2}}\cos(py\tau) -\right.\right.$$

$$\left.2\left(1 - 0.5\frac{\lambda+2\mu}{\mu}y^2\right)^2\cos(py\tau)\cos\left(pz\sqrt{\frac{\lambda+2\mu}{\mu}y^2 - 1}\right) +\right.$$

$$\left.\left.2\sqrt{1 - y^2}\sqrt{\frac{\lambda+2\mu}{\mu}y^2 - 1}\cos(pz\tau)\sin\left(z\sqrt{\frac{\lambda+2\mu}{\mu}y^2 - 1}\right)\right].\right.$$

In these expressions $J_k(\xi)$ is a Bessel function of the first kind of order k of argument ξ.

Chapter 4.

Ambient Temperature Properties Of Al_2O_3-Al_2O_3 Composite

4.1 Statistics of Fiber Tensile Strength

As the mechanical properties of the Al_2O_3/Al_2O_3 composite are determined to a large degree by both strength of the reinforcing fibers and variability of their strength, the strength distribution of the Al_2O_3 single crystal fibers was determined experimentally. To this end Al_2O_3 single crystal fibers of various gauge lengths were tested in tension.

Strength distribution of Al_2O_3 single crystal ceramic fibers, as in all brittle solids, is expected to be governed by a distribution of critical flaws, which are usually assumed to be distributed quasi-uniformly.

As the fibers used for specimen preparation were made under the same manufacturing conditions and order in which the specimens were cut from the (longer) fibers was randomized, the assumption of quasi-uniform distribution of flaws should be satisfied.

When the distribution of fiber tensile strength is represented by a classical Weibull model in which the probability of fracture $F(\sigma)$ in a fiber of length l at or below a stress σ in a large population of similar fibers is given by the Weibull weakest link hypothesis as:

$$F(\sigma) = 1 - \exp[- (\sigma/\sigma_0)^m (l/l_0)]. \qquad (6)$$

In this formula the exponent m is the so called Weibull modulus and σ_0 is the average population strength for fibers of length l_0, where the strength is based on a probability of fracture of 0.63. As is pointed out in [4.1-1], this model results in a rather severe length effect on fiber strength. For the purpose of describing the length effect better the experimentally obtained fiber strength distributions are fitted by the introduction of a new parameter α to give a new expression for the probability of fracture at σ or less as:

$$F(\sigma) = 1 - \exp[- (\sigma/\sigma_0)^m (l/l_0)^{\alpha}], \qquad (7)$$

where α is a parameter between 0 and 1[4.1-2, 4.1-3]. Experimentally determined numerical values of α were shown to be in this range, starting from near 0 for ultra high-strength polyethylene fibers, 0.6 for Kevlar-49 fibers, 0.9 for carbon fibers and near 1 for Hercules IM-6 carbon fibers [4.1-2, 4.1-4].

Taking the log transformation of the last equation and plotting on log-log coordinate, one obtains:

$$\ln (-\ln [1- F(\sigma)]) = m \ln (\sigma) - m \ln (\sigma_0) + \alpha \ln (l/l_0). \qquad (8)$$

Based on this representation a Weibull modulus m, scale factor σ_0 for a fiber length l_0, and a parameter α can be calculated using linear regression.

The testing of Al_2O_3 single crystal fibers in the present study was performed on fibers of three widely different gauge lengths: $l_1 = 4$ mm, $l_2 = 20$ mm and $l_3 = 100$ mm, to investigate the influence of the sample length on the strength. The experimental results are plotted in Fig. 4.1 on Weibull coordinates. This figure shows the probability of fracture of fibers as a function of an applied tensile stress on a log-log scale for each of the three specimen gauge lengths. From this data the Weibull modulus m, the fiber length exponent α and the scale factor σ_0 can be determined by a standard regression technique. The results are presented in Table I.

As was expected, the fibers are very strong and the strength of some small specimens is almost 4 GPa. As the Young's modulus of Al_2O_3 is about 400 GPa, this strength approaches the ideal strength of Al_2O_3. At the same time the average Weibull modulus of fibers is rather small, of the order of 3, which signals a fairly substantial variability in the flaw sizes. Moreover, the length effect exponent α was also found to be significantly less than unity.

Examination of fracture surfaces of failed fibers showed that the flaws were not on the lateral surfaces of the fibers but more in the volume and had the nature of entrapped low angle boundaries. The example of fracture surface is shown in Figure 4.2.

The fact that the fiber strength distributions for different fiber lengths of 4 mm, 20 mm and 100 mm have the same Weibull modulus m , most probably suggests, that the

fracture stresses were governed by the same population of volumetric inhomogeneities over the whole range of lengths [4.1-5].

4.2 Properties (Strength of adhesion and structure) of TiO_2 and ZrO_2 ceramic coatings

4.2.1 Strength of adhesion measurements and results

As stated in Chapter 1 of the present work, one of the main functions of a fiber coating in a ceramic matrix composite is to provide a weakly bonded interface for fiber delamination during the catastrophic fracture of the composite. The coating on the fibers in the composite is supposed to protect the fibers from the crack, propagating in the plane perpendicular to the fiber axis. Since TiO_2 and ZrO_2 are considered as candidate materials for coatings on Al_2O_3 fibers for Al_2O_3 /Al2O3 composite, the strength of adhesion of these coatings to the Al2O3 fibers is of foremost importance. To this end this interfacial strength of adhesion was measured using laser spallation technique, as described in details in Chapter 3 of the present study.

The strength of adhesion between the TiO_2 and ZrO_2 ceramic coatings and Al_2O_3 substrate was measured across a plane bimaterial interface. Specimens in the shape of thin discs were prepared for this set of experiments, and coatings were deposited onto flat surfaces of these discs. The single crystal Al_2O_3 fibers used in the Al_2O_3 / Al_2O_3 composite are drawn in c-orientation, i.e. the c-axis of the crystal is parallel to the lateral surface of the fiber to optimize their creep resistance (see Chapter 1 and Chapter 5 for further discussion on the orientation and creep resistance of Al_2O_3). To simulate this geometrical arrangement, flat single crystal Al_2O_3 discs with the c-axis laying in disc plane were cut out

of single crystal Al_2O_3. The diameter of the Al_2O_3 discs was 25.4 mm (1") and the thickness of the discs was 0.5 mm (see Figure 4.3). The flat surfaces of the discs were polished to an optical quality, and the discs were transparent. TiO_2 and ZrO_2 coatings were formed on one of the two flat surfaces of this single crystal Al_2O_3 substrate using methods described in Chapter 2. This surface of the specimen, which forms the bi-material interface of interest, will be referred to as a back surface of the specimen. During the deposition of metallic Ti and Zr coatings, part of the specimen was masked, and the thickness of the coatings was monitored with precision of +/- 10 nm by measuring the height of the formed step (Figure 4.4). The specimens with coating thicknesses of 1, 2 and 3 μm were processed. After the subsequent oxidation the thickness of the coating would grow and would be in the range of 1.6 to 4μm.

Opposite (front) plane surfaces of the crystals were coated with an energy absorbing metallic layer of Sn, with thickness of 0.5 to 1μm as described in Chapter 3.

Obtained specimens were installed into the specimen holder and enclosed by a transparent quartz cover. The laser was used in the pulsing mode of operation. The pulsing laser beam was condensed by a lens and directed onto the front surface of the specimen, where it initiated a series of pressure pulses. After each pulse the specimen was rotated, so each pulse would strike a fresh location. An example of the locations of the illuminated by a laser beam areas is shown in Figure 4.5, which represents a mask of a blackened paper, used to measure and control the size of the illuminated spots. As can be seen from Figure 4.5, the radius of the spots (which was denoted as A in simulations of Chapter 3) is about 1.1 mm. Comparing this to the thickness of the Al_2O_3 substrate (0.5 mm), we can conclude that the wave propagation in these specimens can be assumed planar

in the center part of the illuminated area, which assumption was made in the analysis of the results of the experiment.

The energy of a single laser pulse was being changed continuously in a controlled manner. After each laser pulse the ceramic coating on the back surface of a specimen was evaluated, and finally the level of the laser pulse energy was reached which caused the ceramic coating to spall. With the aid of the previously measured dependency of amplitude of pressure pulse on laser beam energy (Figure 3.4), the critical pressure pulse amplitude in each case was detected, from which the stresses acting across bi-material interface were deduced.

Since the resulting stress response to a laser generated pressure pulse during the laser spallation experiment depends on the elastic properties of the substrate and coating and on the coating thickness, the resulting stress-time history for the TiO_2 coating on a Al_2O_3 substrate, for a coating thickness of 1.6 μm, was found using the methodology, described in Chapter 3. The resulting stress history across the interface between the substrate and the coating is shown in Fig. 3.21,(b).

The results for the adhesive strength between the TiO_2 and ZrO_2 coatings and single crystal Al_2O_3 substrate obtained by the outlined procedure are shown in Figs 4.6, (a) and (b) respectively. The strength is plotted for two sets of processing parameters, i.e. different temperatures of oxidation.

As was expected, the fracture of the TiO_2 /Al_2O_3 interface took place along the layer of voids inside the TiO_2 coating. The resulting spalled surface is shown in Fig.4.7. It can be noted that the resulting strength of the bi-material interface was found to depend

on processing parameters (temperature of oxidation), which suggests the possibility to adjust the strength of the adhesion as desired.

4.2.2 Nano-indentation of coatings

The obtained structures of TiO_2 and ZrO_2 coatings were probed by nano-indentation experiments which have measured both the mechanical properties of the coating and their state of adhesion to the substrate. The load-displacement results of these experiments are presented in Figs. 4-8, (a) and (b). The load-displacement curve for the formed ZrO_2 coating (Fig. 4-8, (a)) has the appearance of a normal indentation curve of a fully dense material. It has a linear unloading region from which the indentation modulus $(\frac{E}{1 - \nu^2})$ was determined to be $(151 \pm 29)\ GPa$.

The indentation curve for the formed TiO_2 coating of Fig. 4-8 , (b) is typical for porous material. Discontinuities in the curve were caused by the spalling of the coating beneath the indentor.

4.2.3 Investigation of diffusional stability of TiO_2 and ZrO_2 coatings

Al_2O_3/Al_2O_3 composite is being designed for a prolonged load bearing at elevated temperatures. The chemical composition and mechanical properties of all the components of the composite are to be stable during the entire life-span. Thus the inter-diffusion of elements of the composite becomes important.

To examine the diffusional stability of TiO_2 and ZrO_2 coatings, they were exposed to temperatures of up to 1600 ^{0}C for periods of 4 to 24 hours. The diffusion of Ti and Zr ions inside the Al_2O_3 substrate and Al ions outside of the coating surface was investigated using Scanning Electron Microscopy (SEM) and Secondary Ion Mass Spectrometry (SIMS).

The specimens used for this study were prepared as described in Section 4.2.1, and had the shape of Al_2O_3 wafers coated with 1 to 3 μm thick ceramic film of TiO_2 or ZrO_2 coatings. To prevent surface charging and to enable the observation under SEM, all specimens were coated with about 20 nm thick layer of gold.

SEM study was performed in the regime of micro-probe. Some results of the investigation are shown in the Figures 4.9 and 4.10 for ZrO_2 and TiO_2 coatings on Al_2O_3 substrate. Each figure includes micro-image, showing the spot which was investigated, and the spectrum of detected X-ray radiation, on which the wavelengths, characteristic for the atomic species, are marked for identification.

Figure 4.9a shows the results of the investigation of diffusion of Al ions through the ZrO_2 coating. As can be seen on the figure, the intensity of the Al peak is much smaller than that of Zr peak, which means, that the surface layer consists mostly of ZrO_2. As the thickness of the ZrO_2 coating in this study was of the order of 2 μm, it is likely that some electrons were able to pass the coating and some signal was generated by the layer of Al_2O_3 under the coating*** .

Figure 4.9b shows the results of the investigation of the diffusion of Zr ions inside of Al_2O_3 . As can be seen in the figure, the studied area was centered about 5 μm deep inside of the specimen. The locus on the X-ray energy axis, where the characteristic Zr signal is to be expected, is marked. The figure shows that there is no signal corresponding to Zr atoms. Hence, under the conditions of the experiment, there is no detectable diffusion of Zr inside of Al_2O_3.

Figure 4.10a shows the results of the investigation of diffusion of Al ions through TiO_2 coating. As can be seen from the fig., the intensity of the peak, corresponding to radiation characteristic for Al atoms, is present and somewhat weighty, which signifies presence of some of diffusion of Al through the TiO_2 coating.

Figure 4.10b shows the results of the investigation of diffusion of Ti ions inside the Al_2O_3. As indicated by the peak, corresponding to the Ti atoms, there is some solubility of Ti inside of Al_2O_3. The largest level of solubility (under the equilibrium conditions) of Ti in Al_2O_3 is reported to be 0.30% [1.8], and this gives indirect indication of the sensitivity of the testing method.

*** The peak corresponding to the gold (marked Au in the figure) is a result of gold coating the specimen to insure the surface conductivity.

Figure 4.10c shows the results of the investigation of a large grain of $TiAl_2O_5$, formed on the surface of the TiO_2 coating. As is seen in the figure, the results show that both Ti and Al atomic species are present.

As spatial resolution of the SEM was not considered sufficient for a definitive answer in case of the TiO_2 coatings, additional study involving SIMS was conducted. SIMS was performed in the ion probe mode of operation. Flux of primary ions (oxygen O_2^+)was directed at the Al_2O_3 surface coated with TiO_2 to obtain high yield of secondary ions to erode the surface. Changes of elemental composition with depth were monitored to obtain a depth profile[4.2-1].

Because the TiO_2 coating and Al_2O_3 substrate are non-conductive, the surface of the specimen was flooded with low energy electrons to neutralize the charge build up. A portion of the particles released from the surface was ionized and was analyzed. The diameter of the bombarded area was 500 μm, over the initial coating thickness of about 1 μm.

The waviness and scatter of the depth profile for the TiO_2 oxidized at 1100 °C was attributed to non-uniform sputtering due to small grain size of the coating (average grains smaller than 1μm, see Figure 4.12). It is known that crystallites do not amorphize under ion bombardment and the different crystal orientations sputter at different rates [4.2-2], which leads to a roughening of the sputtered surface, to a decrease in the depth resolution, and to scatter of the signal similar to that observed in the present study.

The results of SIMS of a metallic Ti coating on an Al_2O_3 substrate are shown in Fig. 4.11.

As can be seen in the figure, around the 10th minute of ion bombardment, when the eroded depth reaches 1 μm, (i.e. the boundary between the coating and the substrate), the intensity of Al-27 ions rises sharply (by more than 4 orders of magnitude), and the intensity of Ti-48 ions begins to drop sharply by 1.5 orders of magnitude. This behavior corresponds to a very sharp interface, with little Al penetrating into the Ti coating but some Ti penetrating into the Al_2O_3 substrate.

Figure 4.12 shows the results of SIMS of the TiO_2 coating after oxidation at 1100 °C. The interface is still quite well defined but showing a limited amount of diffusion of Ti atoms into the Al_2O_3 substrate and Al into the coating.

Finally Fig. 4.13 shows the results of SIMS generated elemental depth profile for TiO_2 coating on Al_2O_3 substrate after exposure to 1600 °C for 12 hours. As can be seen from the figure, the width of the boundary between TiO_2 and Al_2O_3 has now increased to about 0.5 μm and the interface has diffused somewhat. This can also be seen in the Figure 2.18, which represents an SEM image of the boundary between TiO_2 coating and Al_2O_3 substrate after exposure to the same conditions.

4.2.4 AFM Studies of TiO_2 coating

The quality of the TiO_2 coating was studied using high resolution of atomic force microscope. Also, crystallographic structure and orientation of crystallites was investigated using this method. The materials and processing details of the specimen are given in the Chapter 2.

The results of the investigation are shown in Figure 4.14 . As can be seen from the figure, the TiO_2 coating forms well-formed rutile grains (hexagonal) with the base plane parallel to the substrate.

Chapter 5

High Temperature Mechanical Properties Of The Oxide-Oxide Composite

5.1 Introduction

The material under investigation was an oxide-oxide composite material, formed by incorporating single crystal c-oriented Al_2O_3 fibers into ceramic oxide matrix, consisting of a mixture of aluminum oxide Al_2O_3 and zirconium oxide ZrO_2, the latter partially stabilized by yttrium oxide Y_2O_3 (Y-PSZ). This composite was obtained by a process of oxidation and sequential sintering of a green body, as described in Chapter 2 of the present work. The initial green body consisted of metallic aluminum, aluminum oxide powder and zirconium oxide powder, with the exact composition presented in the Table 5.1 [5.1]. After oxidation and sintering, this green body forms a ceramic polycrystalline conglomerate, which will be referred to as a reaction bonded aluminum oxide (RBAO).

Two aspects of the mechanical behavior were investigated in the present study: elastic properties of the RBAO and time-dependent creep deformation. Two sets of material parameters -- elastic constants and power law creep constants --were determined correspondingly.

Table 5.1 Composition of RBAO

Material	Composition of the RBAO Powder, %	Theoretical Density, g/cm^3
Al (Alcan 105)	40	3.95 (fully oxidized)
Al_2O_3 (Ceralox MPA - 4)	40	3.95
ZrO_2 (Tosoh TZ - 2Y)	20	5.963[1]
Fully dense matrix	-	4.353

The density of the matrix was measured independently and was found to be (3.99 +/- 0.002) g/cm^3, which amounts to 91.67% of theoretical density (TD). The Young's modulus of RBAO and power law creep parameters were investigated in 4-point bending.

[1] Estimated from data in [1].

5.2 Theoretical Estimate of High Temperature Elastic Constants Of Oxide-Oxide Composites

As the elastic constants of single crystal Al_2O_3 fibers are well known and have been measured in a wide temperature interval (see, e.g. [5.7]), to predict elastic constants of the Al_2O_3/ Al_2O_3 composite, elastic constants of the matrix with specific porosity and composition must be known.

To this end elastic properties of a RBAO were measured experimentally in the temperature interval between ambient temperature to 1250 ^{0}C. At the same time the elastic constants of constituents composing RBAO (Al_2O_3 and ZrO_2), are known, so that the elastic constants of RBAO can be estimated by finding Voigt and Reuss bounds theoretically. We computed these bounds and compared experimental results with them.

The theoretical bounds on the elastic modulus of porous RBAO, containing aluminum oxide Al_2O_3 and zirconium oxide ZrO_2 (yttria-partially stabilized zirconia, Y-PSZ) in proportions given in the Table 5.1, were established first, finding the elastic constants of a fully dense Al_2O_3/Y-PSZ composite and then adjusting for the level of porosity of the material at hand. The former task was accomplished by computing elastic constants of polycrystalline body of Y-PSZ and Al_2O_3 separately. Elastic constants of Y-PSZ were calculated under the assumption that the material has a cubic structure under an ambient temperature and that the results can be extrapolated for 2%mol of Y_2O_3 content.

Thus, the computations were done in the following steps:

1. Dependence of elastic constants of single crystal Y-PSZ on Y_2O_3 content was found and the results were extrapolated to give the properties of the Y-PSZ with 2% Y_2O_3.

2. Bounds on the elastic constants of a fully dense polycrystalline body, consisting of ZrO_2/2mol% Y_2O_3 were determined as a function of temperature in the range from ambient temperatures to 1250 ^{0}C from the elastic constants of single crystals of cubic ZrO_2.

3. Bounds on the elastic constants of a fully dense polycrystalline Al_2O_3 body were determined as a function of temperature in the range from ambient temperature to 1250 ^{0}C from the elastic constants of single crystal Al_2O_3.

4. Bounds on the elastic constants of the fully dense RBAO in the temperature range from 20 ^{0}C to 1250^0 C were found.

5. Elastic constants of porous RBAO were found in the temperature range from ambient temperatures to 1250 ^{0}C.

5.2.1 Estimates Of The Elastic Constants Of Y-PSZ

Elastic constants of ZrO_2 have been measured and reported for single crystals at various compositions and temperatures [see 5.2, 5.3, 5.4 and references therein]. The magnitude of measured elastic constants, as well as symmetry of the crystals and, thus, the number of constants necessary to characterize it, was shown to depend on the crystallographic forms of ZrO_2.

There are some discrepancies in the literature regarding the phase diagram of partially stabilized Zirconia and the temperature/composition boundaries of each crystallographic form. Under ambient conditions ZrO_2 forms a monoclinic mineral known as baddeleyite [5.3]. At $\approx$1170 ^{0}C ZrO_2 undergoes a crystallographic transformation from monoclinic to tetragonal [5.4] (other authors give a somewhat wider range of between 1000 ^{0}C and 1200 ^{0}C, [5.3]). In the range of $\approx$2600 ^{0}C to 2640 ^{0}C tetragonal ZrO_2 undergoes transformation to the cubic fluorite structure.

The fluorite cubic structure can be stabilized to ambient temperatures by the introduction of greater than 10 - 20% impurities such as Y_2O_3, CaO and/or MgO [5.3].

Extensive studies, involving X-ray diffraction, TEM, dilatometry and Raman spectroscopy showed that under ambient temperatures ZrO_2 with 12 to 8.5 mol. % (20 to 15 wt%) of Y_2O_3 were fully cubic ZrO_2 [5.4, 5.5]. As the Y_2O_3 content was decreased from 7 to 2.5 mol%, increasing amounts of second-phase tetragonal ZrO_2 were observed. Compositions with less than 2.5 mol% Y_2O_3 had increasing content of monoclinic ZrO_2 with decreasing content of cubic and tetragonal phases. Pure ZrO_2 was found to be completely monoclinic.

Our material contained ZrO_2 with 2 mol% of Y_2O_3 and the measurements were conducted in the range of up to 1250 ^{0}C. Particles of ZrO_2 of about 0.3μm in size were distributed in the continuous Al_2O_3 matrix. On the basis of the referenced sources, it was assumed that the particles of Zirconia were in the three-phase cubic plus tetragonal plus monoclinic forms.

The results of the calculations of elastic constants of ZrO_2 with different Y_2O_3 content are shown in Figure 5.1. Despite the mentioned variability of crystallographic forms for ZrO_2, the bounds of the effective elastic moduli for polycrystalline ZrO_2 aggregate having two or three phases (cubic plus tetragonal plus monoclinic) vary monotonicaly for the entire range of Y_2O_3 content, as was shown in [5.2] and is seen in Fig. 5.1. No sudden jumps in the value of the elastic constants, associated with changes in crystallographic structure, were detected. This gives the grounds to assume that the bounds of the elastic constants of polycrystalline ZrO_2 agglomerate can be found as if the crystal structure were cubic, although with decreased amount of Y_2O_3 content.

This also agrees with the results of [5.6], where monoclinic ZrO_2 crystals were studied. Results of [5.6] when used to compute the average Young's modulus of polycrystalline aggregate at room temperature and are compared with the results of the computation for the cubic ZrO_2 in Figure 5.1a.

These results, although giving rather wide estimates, point out on the possibility that Young's modulus of a monoclinic Zirconia is slightly higher than the extrapolation of the results of computation of elastic constants of fully Yttria-stabilized cubic Zirconia to the zero Yttria content would otherwise suggest. Also a strong upward trend of all averages (Hasin-Shtrikman, Reuss, Voigt) for Young's modulus for Zirconia with Yttria content of less than 3% can be seen from the Figure 5.1b, showing the linearized dependence of ZrO_2 on Y_2O_3 content. Additional studies are needed to clarify this question.

Thus, the high temperature elastic constants of the polycrystalline ZrO_2 aggregate were found as if ZrO_2 were cubic in the entire range of Y_2O_3 content. It was assumed that the dependence of the elastic constants on the Y_2O_3 content at elevated temperatures is the same as is at room temperature.

Under these assumptions we can use the cubic constants measured in [5.4] for the temperature range 20 ^{0}C to 700 ^{0}C and extrapolate them for the temperature interval of the present study, i.e. 20 ^{0}C to 1250 ^{0}C.

The results of extrapolation of data from [5.4] are shown in Figure 5.2. From these results we obtained the estimates of elastic constants of ZrO_2 with 2 mol% Y_2O_3 in temperature range of up to 1200 ^{0}C (Figure 5.3)

5.2.2 High Temperature Elastic Constants Of Al_2O_3

The elastic constants for Al_2O_3 were found by extrapolation of results from [5.7] and verifying them by comparison with the results in [5.8]. The results are plotted in Figure 5.4.

5.2.3 Elastic Constants Of A Fully Dense $Al_2O_3/ZrO_2/Y_2O_3$ Composite As A Function Of Temperature

Elastic constants of a fully dense $Al_2O_3/ZrO_2/Y_2O_3$ composite were found as a function of temperature first and then the correction for the porosity of the RBAO was introduced. In these computations we assumed that Zirconia inclusions are uniform spheres, randomly and isotropically distributed in the alumina continuous matrix. Although the monoclinic/tetragonal/cubic transformation in Zirconia may be induced by the inelastic deformation or applied stress and thus the material may develop a texture, this effect was neglected.

Considering Al_2O_3 as a continuous phase in which there are 20% of ZrO_2 inclusions, using the method described in [5.9], the following expression for the shear modulus μ of the alumina/Zirconia composite is obtained:

$$\mu = \mu_{Al_2O_3}\left(1 - \frac{(\mu_{Al_2O_3} - \mu_{ZrO_2})f}{\mu_{Al_2O_3} + 2(\mu_{Al_2O_3} - \mu_{ZrO_2})(f-1)S_{1212}}\right), \qquad (5.1)$$

where: $\mu_{Al_2O_3}$ and μ_{ZrO_2} are the shear moduli of Al_2O_3 and ZrO_2 correspondingly;

f is the volume fraction of ZrO_2 in Al_2O_3, $f = 0.2$;

S_{1212} is a component of an Eshelby tensor.

Assuming that the Zirconia inclusions are spherical, the explicit expression for S_{1212} is given in [5.9]:

$$S_{1212} = \frac{4 - 5\nu_{Al_2O_3}}{15(1 - \nu_{Al_2O_3})}. \qquad (5.2)$$

The effective bulk modulus κ is obtained by considering a uniform applied strain field [5.9]. Then under assumption of the sphericity of inclusions:

$$\kappa = \kappa_{Al_2O_3} + f\frac{\kappa_{ZrO_2} - \kappa_{Al_2O_3}}{\kappa_{Al_2O_3}K}, \qquad (5.3)$$

where K is:

$$K = 1 + (\kappa_{ZrO_2} / \kappa_{Al_2O_3} - 1)(1 - f)\frac{(1 + \nu_{Al_2O_3})}{3(1 - \nu_{Al_2O_3})}. \quad (5.4)$$

In the calculation of the effective elastic constants of the composite the average elastic constants of the constituents were used. Averaging was done over all previously obtained bounds: Reuss, Voigt and two Hashin-Shtrickman bounds.

The computed averaged effective elastic constants of the $Al_2O_3/ZrO_2/Y_2O_3$ are plotted in Figure 5.5.

5.2.4 Elastic Constants of RBAO

As the composite has the density of (about) 91.6% of the theoretical, the correction for the porosity of the composite was introduced on this stage. Again, assuming the voids in the ceramic body to be spherical, the effective elastic moduli of the porous material are found as a moduli of a composite with one of the phases being voids. Thus, the bulk modulus of the porous material is given [5.9] by:

$$\kappa_{91.6\%} = \kappa_{comp}(1 - f_{voids}/P), \quad (5.5)$$

where: $\kappa_{91.6\%}$ - bulk modulus of 91.6% dense composite;

$$P = \frac{1 - (1 - f_{voids})(1 + \nu_{comp})}{3(1 - \nu_{comp})}; \quad (5.6)$$

ν_{comp}, and κ_{comp} are constants of the $Al_2O_3/ZrO_2/Y_2O_3$ composite found previously;

f_{voids} is a volume share of voids.

The shear modulus of the porous material is given by the following expression [5.9]:

$$\mu_{91.6\%} = \mu_{comp}(1 - f_{voids}\frac{1}{1 - 4(1 - f_{voids})S_{1212}}) \quad (5.7)$$

where: μ_{comp} - the shear modulus of an the $Al_2O_3/ZrO_2/Y_2O_3$ composite found previously;

$\mu_{91.6\%}$ - the effective elastic modulus of 91.6% dense material;

S_{1212} - previously defined component of the Eshelby tensor.

The resulting bounds on Young's modulus of the 91.6% dense material are plotted in Figure 5.6, together with the results of experiment. The computed value of elastic modulus will be compared with results of experiment (see section 5.4).

5.3 Creep Resistance Of The Oxide-Oxide Composite.

It has been widely recognized that creep and creep-related time-dependent failure is the major cause of failure in high temperature materials under normal conditions of loading [5.10, 5.11]. To mathematically describe and predict the response of the composite to the specific creep conditions it is necessary to know the creep properties of each component : fibers, matrix and fiber coating on fiber-matrix interfaces. We will address creep properties of the matrix of Al_2O_3- Al_2O_3 composite and the composite itself below.

Reinforcement in this composite consists of sapphire (single crystal α–Al_2O_3) fibers, oriented such that the basal (0001) plane is perpendicular to the fiber axis, so that crystallographic "c" axes is aligned with the fiber axis. These fibers will be referred to as 0^0 or *c*-oriented fibers.

Creep properties of sapphire have been widely investigated. Sapphire is rhombohedral in structure with oxygen atoms forming an hcp lattice and aluminum ions filling 2/3 of the available octahedral sites [5.12]. The creep in Al_2O_3 single crystals is usually found to be the result of dislocation glide on primary or secondary slip systems [5.13]. Three slip systems have been macroscopically identified in sapphire. They are basal (0001) <11$\underline{2}$0>, prismatic {1120} <01$\underline{1}$0>, and pyramidal {1011} <01$\underline{1}$1> slip

systems [Bretheau et al., 1979, 5.14]. Some discussion continuous regarding the anisotropy of deformation when pyramidal planes operate as slip planes.

Among these three slip systems, pyramidal slip is of primary interest here. It is the most difficult slip system to activate and sapphire fibers used in the present study utilized this property. Application of stresses parallel to the c-axes of single crystalline Al_2O_3 produces a zero resolved shear stress on the basal planes (they are perpendicular to the "c" axes) and the prismatic planes (they are parallel to c axes). It has been found [Gooch, 1973, [5.15]; Haggerty, 1991 [5.16]], that fibers with small amount of misorientation, i.e. having angles of up to 3.0^0 between the fiber axis and crystallographic c axis, are quite similar in their creep behavior to perfectly aligned single crystals, loaded exactly along the c-direction. In particular, they do not exhibit basal deformation. In the studies cited above the creep was accomplished by dislocation glide along $\{10\underline{1}x\}$ family of planes. Also, no creep strain was detectable under the temperatures below 1600 ^{0}C. The specimens were found to always fractured before any creep was detected, despite the 50-hour exposure to elevated temperatures.

According to the measurements conducted at Advanced Crystal Products Co., the misalignment of the fibers used in the present study (the angle between the crystallographic "c" axes and the geometric axes of the fiber) did not exceed 3.0^0. The fibers were embedded into the matrix as shown on the Figure 5.7. As fibers were situated near the surface of the specimen and the fiber diameter (about 100 μm) was much smaller than the height of the specimen (3 mm), it was assumed, that the fibers were loaded exclusively in tension, neglecting small shear stresses along the basal planes acting on them. It was presumed that the composite will be used in such a way that the fibers will be loaded along the c-direction, and this choice of the specimen would model the real loading.

Our creep experiments were conducted under the temperature of 1200 ^{0}C. Thus, from the above, we can conclude that under the conditions of our experiment, reinforcing sapphire fibers should not develop any creep deformation. Thus the long term deformation of the Al_2O_3- Al_2O_3 composite under the temperatures of below 1600 ^{0}C will develop in such a way, that at the very beginning, immediately after the load application, the stress will be distributed approximately uniformly between the fibers and the matrix of the composite (neglecting the slight difference in elastic moduli of the fibers and the matrix). As the time progresses, though, the stresses in the matrix will be relaxed by the creep deformation, and the load-bearing function will be completely shifted to fibers. Since the fracture of a critical fiber cluster will almost unavoidably lead to the fracture of the composite, the long term strength of the composite will be determined by the strength of the fibers, while the creep deformation will be near zero (total deformation should not exceed the maximum elastic deformation of the fibers).

At temperatures above 1600 ^{0}C sapphire fibers start to exhibit some creep as well. But the creep of the Al_2O_3 matrix is so much more intensive [5.13], that to the first approximation the same processes will take place: the load-bearing function will be shifted to the fibers, and integral strength of the fibers will determine the strength of the composite as a whole.

At the same time, the matrix is an important load bearing component in oxide-oxide composite. Among the reasons for this are the small volume fraction of the fibers caused by limitations of processing technique and the nature of the loading.

During the processing it does not seem possible to incorporate a significant volume fraction of fibers into the matrix because of processing difficulties. Our experiments were conducted on a specimens containing a limited number (3 to 5) of hand-laid fibers. It is not expected that the volume fraction of fibers can be increased to more than 30%. With the

uniform fiber distribution in hexagonal array and fiber diameter of about 100 μm, the distances between the adjacent fibers become too small, of order of 1μm. Gaps of this size in the fibrous preform are difficult if not impossible to infiltrate successfully with the material which forms matrix.

Also, the loading on the composite in most applications varies extensively with time. For example, in the airplane turbine applications, the turbine power peaks for 30 - 45 seconds, during the plane take-off and landing [5.31]. This gives the estimate of the time during which the highest forces will have to be born by the composite and the highest temperatures of the working environment will be developed. Since the response of the composite to a short time creep loading is determined to a large degree by a matrix, its creep resistance becomes of importance. The creep of the matrix was investigated in a set of separate experiments.

As structure evolution and damage accumulation mechanism is associated with the creep process [5.17], the resulting microstructure is changing continuously throughout the creep process, leading to non-uniform stress distribution, possible fiber damage and ultimately to a time-dependent failure (creep rupture). The structure of the composite and its evolution was investigated using SEM.

5.3.1 Flexural Creep Analysis.

As mentioned above, the creep testing was done in four-point bending. Traditionally the flexural analysis of creeping bodies in four point bending has been done under the assumption, that the behavior of the material under compressive and tensile loading is identical [e.g., 5.18]. Under this assumption the neutral plane (plane in which both compressive and tensile stresses are zero) is a midplane of the specimen. Mechanical behavior of a number of materials was investigated using this assumption [5.19].

On the other hand, an ample body of evidence exists proving that the creeping behavior of most materials, including Al_2O_3, is quite far from being symmetric [e.g., 5.20, 5.21 and numerous references cited therein]. The difference in the behavior is attributed to the microstructure evolution during the creep and associated with it cavitation [5.17]

Recently the method was suggested for analysis of creep of materials having different behavior in tension and compression [5.22]. Unfortunately, the method requires an approximate solution to the equations and suffers from insufficient accuracy, as was pointed out in [5.23].

In the present work an attempt was made to overcome these shortcomings and to design the method of analysis of a creeping solid in bending. The method hereby presented enables the investigator to determine the specific parameters of the creep behavior in tension and compression from a flexure experiments. The experiments in 4-point bending are generally easier to implement, particularly for the fibrous composite specimens. It becomes a particularly important issue for a composite materials with unidirectionally aligned strong fibers, where separate testing in both compression and tension along the fiber axis is

complicated. The developed method was applied to Al_2O_3/ ZrO_2 and to Al_2O_3/ ZrO_2 / Al_2O_3 composite specimens.

Traditionally, three stages of the creep are observed and are distinguished: primary creep, secondary creep and tertiary creep. During secondary creep, which constitutes the largest and the best studied part of the overall creep life, the strain rate $\dot{\varepsilon} = \frac{\partial \varepsilon}{\partial t}$ is constant and is usually described by a power-law function of an absolute value of stresses [5.24]:

$$\dot{\varepsilon} = Const \frac{DGb}{kT}\left[\frac{b}{d}\right]^p \left[\frac{\sigma}{G}\right]^n, \qquad (5.8)$$

where: $D = D_0 e^{-\frac{Q}{RT}}$ is the diffusion coefficient with Q as the diffusion activation energy;

G - shear modulus at absolute temperature T;

b - Burgers vector;

d - grain size;

σ - applied stress.

Usually the first two multipliers are combined into one constant, to arrive at the formula:

$$\dot{\varepsilon} = A_i \sigma^{n_i} \qquad (5.9)$$

where: A_i and n_i are material-specific creep parameters, which are constant during the secondary creep and are to be determined experimentally. Their values are different for the compressive and tensile deformation and index i takes the values C for compression and T for tension. In Eq. (5.9) the stress is always assumed positive, independently of whether the loading is in tension or in compression.

In four-point bending test (Figure 5.7) two pairs of forces $F/2$ are applied to the specimen and create a state of a pure bending inside a minor span with a constant bending moment M:

$$M = \frac{F(L_2 - L_1)}{4} \tag{5.10}$$

where L_1 and L_2 are the geometric dimensions of an inner and outer span respectively, given in Fig. 5.7 . The existence of a region in which the bending moment is constant and stresses are well characterized is an advantage of a four-point bending test.

Symmetry considerations are employed to arrive at the usual planar cross section hypotheses: for each cross section inside of the inner span the conditions on the right are exactly the same as on the left, so there is no reason for the cross section which was planar before the deformation to change its shape and become non-planar. Under the assumption that this hypotheses holds true, the creep strain ε in the specimen is proportional to the distance from the neutral plane *Y*:

$$\varepsilon = KY, \tag{5.11}$$

where K is the (local) curvature of a neutral axis. If the material is homogeneous and isotropic, the surfaces that were plane before the deformation, will become a part of a circle under the action of a constant moment.

By expressing stresses along the cross section of the specimen in terms of ε using the equ. (5.9) and substituting equ. (5.11) into it, the following expression is obtained, giving stresses $\sigma_i(A_i, n_i)$ as a function of material constants for a given value of a curvature rate $\dot{K}$:

$$\sigma_i(A_i, n_i) = \left(\frac{\dot{K}Y}{A_i}\right)^{1/n_i} \tag{5.12}$$

In this equation, *i* is either T for tensile part of the specimen or C for compressive part. Compressive force F_C, acting along the rectangular cross section of the specimen, will be:

$$F_C = B\int_0^{H_c} \sigma_C(A_C, n_C)\cdot dy, \qquad (5.13)$$

where H_C is the height of the part of the specimen which is in compression, and B is the width of the specimen. Also a tensile force F_T acting on the cross section of the specimen will be:

$$F_T = B\int_0^{H_c} \sigma_T(A_T, n_T)\cdot dy, \qquad (5.14)$$

where H_T is the height of the part of the specimen which is in tension; obviously,

$H_C + H_T = H,$ (5.15)

where H is the height of the whole specimen.

During a quasi-static deformation these forces F_C and F_T are equal, so their difference, e, is zero:

$$e = F_T - F_C = 0. \qquad (5.16)$$

Bending moments M_T and M_C, acting in the cross section, produce the applied moment, given by (5.10):

$$M_T = B\int_o^{H_C} \sigma_T(A_T, n_T)\cdot y\cdot dy \qquad (5.17)$$

$$M_C = B\int_o^{H_C} \sigma_C(A_C, n_C)\cdot y\cdot dy \qquad (5.18)$$

$$M = M_T + M_C. \qquad (5.19)$$

It is proposed to conduct the experiment (at least) twice for each material, using two levels of forces. For each level of forces the strain rate is measured. Thus, for each

material two groups of measurements for two different levels of forces F_1 and F_2, and correspondingly for two different bending moment M_1 and M_2 are obtained, which generates a system of four equations:

$$\begin{cases} e_1 = 0 \\ e_2 = 0 \\ M_1 = M_{T1} + M_{C1} \\ M_2 = M_{T2} + M_{C2} \end{cases} \qquad (5.20a, b, c, d)$$

Moments and forces in this system are functions of material parameters A_i and n_i. Their explicit expressions in terms of four constants A_T, A_C, n_T and n_C are given in the Appendix A5.2. After the dimensions H_T and H_C are estimated for each group from independent measurements, this system is sufficient for determination of four material parameters A_T, A_C, n_T, n_C.

Dimensions H_T and H_C were estimated from the measurements of changes of length of surface as described in section 5.4.

5.4 Experimental Procedure

The specimen preparation procedure is described in Chapter 2 of the present work. After oxidation and sintering, the specimens for the test were machined to dimensions close to the ones suggested in standard ASTM C 1161 (1990). The dimensions of the specimen are hight*width*length, in mm: 3*4*36, and are given in the Figure 5.7 . The machining was performed at Chand Kare Technical Ceramics Co., using diamond abrasive grinding and cutting wheels. Final finish on the surface included mechanical polishing with 0.3 μm diamond polishing paste. The sharp edges of the specimens were chamfered. The final non-flatness of the specimen was controlled on profilometer and was found not more than 2.5 μm.

The tensile creep machine used in the present study is described elsewhere [5.28]. The high temperature mechanical behavior was investigated in four-point bending, by using a special bending fixture, made out of high quality high density graphite (UNOCAL POCO Graphite Co.). The photo of the vacuum chamber with the bending fixture inside is shown in Figure 5.8, and the technical sketch of the bending fixture is shown in Figure 5.9. The creep machine chamber was evacuated to a pressure of $5*10^{-6}$ Torr. The temperature was maintained by a controller (RESEARCH, Inc.) and was measured by a tungsten-rhenium thermocouple, introduced inside of the bending fixture as shown in Figure 5.9 .

During the measurement of Young's modulus the specimen was installed into the bending fixture in the creep machine. The assembly was heated to a desired temperature and kept at the same temperature level for at least 30 min. After this the specimen was loaded by a known force. Each loading was repeated for at least 3 times. The (elastic)

displacement of the points at which the specimen was supported was measured by four linear variable differential transformers (LVDT), and the result was averaged over four measurements.

The compliance of the fixture was measured first and was found to be much lower than the compliance of the specimen.

The specimen was modeled as an elastic beam. On the basis of elastic analysis provided in Appendix 5.1, the following expression, relating the Young's modulus E, applied force P, the displacement of one support relative to another $\delta\omega$ and the dimensions of the inner and outer span of the specimen ℓ_1 and ℓ_2 was obtained:

$$E = \frac{P l_1^2 \left(l_2 + \frac{l_1}{3} \right)}{I \cdot \delta\omega} \qquad (5.21)$$

The results of the found elastic modulus E from known load P and geometric parameters of the beam are compared with computed Voigt and Reuss bounds in Figure 5.6.

The creep behavior of Al_2O_3/ZrO_2 composite which is used as a matrix when reinforced with single crystal Al_2O_3 fibers, as well as the creep behavior of the composite itself was investigated experimentally at 1200 ^{0}C. The process of the specimen preparation was analogous to that of the specimens used for the investigation of high temperature elastic constants.

A pair of markings was inscribed with either the diamond pencil or diamond wheel on the tensile surface of the specimen inside of the inner span, and another pair of markings was produced on the compressive surface of the specimen, as shown in the Figure 5.7 . The distance between the markings on each side was measured before the creep experiment was started using either microscope or a profilometer. The same measurements were repeated after the test, providing the information about the strains in the uppermost and

lowermost layers of the specimen, which was necessary to estimate the location of a neutral plane. From equation (5.11) the largest compressive strain ε_{Cmax} and the largest tensile strain ε_{Tmax} will be:

$$\varepsilon_{C\max} = KH_C, \qquad (5.22)$$

and:

$$\varepsilon_{T\max} = KH_T, \qquad (5.23)$$

so that

$$\frac{H_C}{H_T} = \frac{\varepsilon_{C\max}}{\varepsilon_{T\max}}. \qquad (5.24)$$

ε_{Cmax} and ε_{Tmax} were determined from the length measurements and two Equations 5.15 and 5.24 give the information to determine both H_C and H_T.

The creep displacements were measured by LVDTs continuously during the experiment. The final displacements and associated curvature were verified by finding a profile of the deformed surface using profilometer-profilograph. During these measurements the profile of the initially flat ground surface was recorded. Since it was expected that after the deformation by the bending moment the flat surface inside the inner span should become a part of a circle, the circle was approximately fitted to the obtained curve and the average radius of the curvature was found (by a least square procedure). The example of obtained curves and fitted radii of curvature are shown in Figure 5.10a, which shows the final curvature for RBAO specimen, and 5.11b, which shows the final curvature for Al_2O_3/ Al_2O_3 composite. The example of measured displacement curve is shown in Figure 5.12. The results of measurements obtained with LVDTs and with profilometer coincided, with correspondence between the two better than 5%. The strains in the specimen were found on the basis of the hypothesis of plane cross sections. After the

experiment both RBAO and composite specimens were investigated using the scanning electron microscope (SEM).

The dimensions H_C and H_T were estimated, using the changes in the dimensions between the markings, as described above, to obtain estimates for H_C and H_T. These values were substituted into the system of equations (5.20).

5.5 Results and discussion

The system of equations (5.20) was solved numerically, using the software package Mathematica® [Wolfram Research, Inc.]. The listing of the solution is given in Appendix 5.2.

The resulting stress-strain rate dependencies are shown in the Figure 5.10, where they are compared with creep rates of pure Al_2O_3 and ZrO_2 [5.26, 5.29]. It may be noticed that the creep resistance of the Al_2O_3/ ZrO_2 composite is somewhat higher than the creep resistance of a pure Al_2O_3 of the same level of porosity and same grain size. The explanation of this is suggested below based on the specific features of microstructure of Al_2O_3/ Al_2O_3 composite and on the mechanism of creep deformation and failure.

Structure of Al_2O_3/ Al_2O_3 composite was investigated using SEM. SEM representation, showing elemental contrast in secondary electrons is presented in Figure 5.13a and under higher magnification in Figure 5.13b. Since atomic weight of Zr (91.22) is much higher than Al (26.98), in these figures lighter fields correspond to ZrO_2, and darker fields correspond to Al_2O_3. As can be seen on these Figures, the structure of RBAO is characterized by a relatively small grain size of Al_2O_3 (about 1 μm) with even smaller ZrO_2 grains (about 0.3 μm) situated along the boundaries of Al_2O_3. This results in ZrO_2 grains "pinning" Al_2O_3 grains, thus making the grain growth and grain sliding difficult.

With regards to the influence of ZrO_2 particles on the creep behavior of Al_2O_3 it should be said, that there is some disagreement among published data on the creep behavior of polycrystalline ZrO_2. Ingel (1982) noted that bend specimens of Yttria-partially stabilized Zirconia (Y-PSZ) with about 6wt% of Yttria, exhibit very little plasticity at temperatures below 1500 ^{0}C [5.25]. Evans in 1970 studied creep of Yttria-PSZ and

Scandia-PSZ and observed two regimes for stress dependence during the creep of Y-PSZ, one with the exponent n=1 and another with exponent n=6 [5.26]. He argued that the former regime corresponds to a case when the strain rate controlling mechanism is cation diffusion and the later one corresponds to formation, coalescence of voids and propagation of cracks. The study of Dimos and Kohlstedt [5.27] also concluded that the rate-controlling mechanism was a cation lattice diffusion and the stress exponent n was found to be 1.2. It can be expected *a priori*, that the deformation is accomplished through some diffusional processes, considering the structure of partially stabilized Zirconia, consisting of a mixture of monoclinic, tetragonal and cubic crystallographic form. It does not seem probable that the deformation accomplished by the dislocation motion would have been possible in the this material.

Figure 5.12 also shows the strain rate-stress dependence for creep of polycrystalline Y-PSZ, computed on the basis of the above cited references [5.25, 5.26 and 5.27], extrapolated to the average grain size of 0.3 μm. Although, as can be seen from the Figure 5.12, the strain rate of Y-PSZ is higher than that of Al_2O_3, the Y-PSZ particles still have the higher creep resistance than the grain boundary layer of Al_2O_3 and decrease the creep strain rate.

It has been found that pure Al_2O_3 during the creep conditions deforms by grain boundary sliding (GBS) [5.29 and therein]. The same mode of creep deformation characterizes RBAO as well, as evidenced by intergranular voids (Figures 5.14a, b, c and d), showing the presence of intergranular sliding. Figures 5.15a and 5.15b show grain facets opened as a result of GBS. Also, the creep exponent of 2 computed for RBAO is compatible with GBS.

Thus, it is suggested that two factors contributed to an increase in creep resistance of RBAO compared with pure Al_2O_3. They are:

1. Presence of reinforcing ZrO_2 pinning particles along the Al_2O_3 grain boundaries.

2. As ZrO_2 does not dissolve in Al_2O_3, nor does it form a new low-melting temperature form [see fig. 2.2], no glassy phase formed along the grain boundaries, which makes otherwise GBS much easier in Al_2O_3 sintered with the help of sintering aids.

Other consequences of the pinning action of ZrO_2 particles are rapid accumulation of creep damage with deformation, and, thus, smaller strains to failure, and absence of creep induced grain growth, characteristic for pure Al_2O_3 [5.29].

It should be pointed out that the pure Al_2O_3 can undergo a large creep deformations before it fractures, with strains in the range of 20% to 30% reported [5.17]. The residual deformation left in the crept RBAO specimen, as inferred from resulting curvature shown in Fig. 5.10a, reaches about 0.48% in the outermost layers of the specimen. Thus, pinning action of ZrO_2 particles results not only in the increase in creep resistance but also in the decrease of the deformation to fracture.

With regards to the morphology evolution during the creep in RBAO, the material possessed some porosity, so the void nucleation stage during the creep was not detectable. However, since the tendency for porosity retention during processing has as its driving force the same mechanism as localization of the porosity during creep induced void nucleation [5.30], the resulting porosity in crept and pressureless sintered material is similar, if not identical. Sequential cavity growth mechanism took place by the GBS, leading to cavity coalescence and to crack growth, with the rate controlled by sliding. Figures 5.16a and 5.16b present the SEM image of the fracture surface, showing the results of grain boundary crack propagation, and Figures 5.17a, b and c present magnified part of fracture surface, showing four-grain corner cavity. Figure 5.18a and b show the part of the surface of the specimen, which has undergone tensile deformation during creep. Cracks are seen propagating along the boundaries of Al_2O_3 and ZrO_2.

The creep of Al_2O_3/ Al_2O_3 composite was investigated in four-point bending in the same bending fixture. The residual deformation, inferred from the final curvature, Fig. 5.10a, is about 0.157% in the outermost layers of the specimen. This deformation is of the order of the maximum elastic deformation of the Al_2O_3 fibers, thus suggesting that, while in the beginning of the test the load was distributed (almost) uniformly along the cross section of the specimen and was born by the fibers and the matrix, the stresses in the matrix were relaxed by creep in due time, leading to transfer of larger and larger shear of the load to the fibers. Fibers finally broke and the RBAO matrix fractured catastrophically.

Examination of the composite specimens after the test revealed that they had cracks in them, emanating from the fibers, as shown in Figures 5.19a to 5.19f and in Figures 5.20a to 5.20e. It is apparent (particularly under higher magnification), that the cracks developed on a stage when the matrix contained enough unoxidized Al to undergo some local plastic deformation. At the same time, as can be seen in Figure 5.21a to 5.21f, there is a gap present between the fiber and the matrix. The most probable explanation is that the cracks were formed in the matrix before Al started oxidizing into Al_2O_3, but the matrix was shrinking. The reason for the shrinkage of the matrix on this stage could have been the sintering of Al_2O_3, or the sintering of Al particles into one metallic body. The oxidation of Al into Al_2O_3 could have been delayed because of slow diffusion of oxygen through the matrix. The gaps between the fibers and the matrix could have opened later, when Al started oxidizing into Al_2O_3, since such oxidation is accompanied by a volumetric expansion. This scenario is consistent with the results of dilatometric studies, reported elsewhere [2.2.6]. Further work is needed to improve the properties of the matrix.

Appendix 5.1 Displacement Analysis of 4-point bending

Only the half of the beam was considered and this half was considered consisting of two parts, part 1 and part 2. As the beam and the loading are symmetric around the middle plane, this plane remains undeformed. In the area 1:

$$M = P(l_2+l_1-x),$$

where: M is the moment acting in cross section;

Thus the deflection, ω_1 will be found as a solution to the differential equation:

$$\omega_{1,xx}=M(EI)^{-1}= P(l_2+l_1-x)\ (EI)^{-1},$$

which lead to the expression for the deflection:

$$\omega_1= P(l_2+l_1-x)^3(6EI)^{-1} + C_1x+C_2,$$

where C_1 and C_2 are the constants of integration. They will be found later from the conditions that the deflection is smooth at $x=l_2$.

In the part 2 of the specimen the moment M is:

$$M=Pl_1,$$

thus:

$$\omega_{2,xx}= Pl_1(EI)^{-1},$$

so:

$$\omega_2= Pl_1x^2(2EI)^{-1}+C_3x+C_4.$$

As the left end of the beam is considered as fixed, at $x=0$, $\omega=0$, thus $C_3= C_4=0$, and:

$$\omega_2= Pl_1x^2(2EI)^{-1}.$$

At $x=l_2$ $\omega_1= \omega_2$ and $\omega_1'= \omega_2'$, where prime denotes differentiation with respect to x. From these two conditions find C_1 and C_2, and ω_1:

$$\omega_1 = P(l_2+l_1-x)^3(6EI)^{-1} + Pl_2x(2l_2+l_1)(2EI)^{-1} - Pl_1(l_2^2+l_1^2/3+l_1l_2)(2EI)^{-1}.$$

Difference in the displacements at $x=l_2$ and $x=l_1+l_2$ is:

$$\delta\omega = Pl_1^2(l_2+l_1/3)(EI)^{-1}.$$

References

Chapter 1.

1.1 A. G. Evans, "Prospective on the Development of High Toughness Ceramics", J. Amer. Cer. Soc., 73 (1990), 187.

1.2 "Ceramic Matrix Composites", R. Warren, editor. Black, London, GB, 1992.

1.3 "Engineering Composite Materials", B. Harris, The Institute of Metals, London, GB, 1986.

1.4 W. D. Kingery, H. K. Bowen and D. R. Uhlman. "*Introduction To Ceramics*", (Wiley & Sons: New York). (1976)

1.5 E. P. Busso, "Cyclic Deformation of Monocrystal Nickel Aluminide and High Temperature Coatings". Ph. D. Dissertation. MIT, 1990

1.6 Y.S. Touloukian, R. K. Kirby, R. E. Taylor and T. Y. R. Lee, Editors Thermophysical Properties Of Matter, Volume 13. (Plenum Press, New York), 1977.

1.7 A.S. Argon and V. Gupta, in "*Damage and Oxidation Protection in High Temperature Composites* ", vol. 25-2, (ASME, New York)(1991).

1.8 R. S. Roth, J. R. Dennis and H. F. McMurdie, General Editors. "Phase Diagrams For Ceramists", Volume VI, (Amer. Ceram. Soc., Columbus, Ohio). 1965 and 1975 Supplement.

Chapter 2.

2.1.1 W. B. Perry "Improved Methods For Producing Small Diameter Single Crystal Fibers Of Alumina and Yttria-Alumina Compounds Using Edge Defined Film Fed Growth". NASA Contractor Report. Contract NAS3-26811, 1994.

2.2.1 W. J. Tseng And P. D. Funkenbusch. "Microstructure and Densification of Pressureless-Sintered Al_2O_3/Si_3N_4-Whisker Composites" , J. Am. Ceram. Soc., **75**, 1171-75, (1992)

2.2.2 O. Sudre, G. Bao, F. F. Lange and A. G. Evans "Effect of Inclusions on Densification" , J. Am. Ceram. Soc., **75**, 525-31 (1992)

2.2.3 R. K. Bordia and R. Raj, "Hot Isostatic Pressing of Ceramic/Ceramic Composites at Pressures < 10 MPa", Adv. Ceram. Mater., **3**, 122-26 (1988)

2.2.4 T. N. Tiegs and D. M. Dillard, "Effect of Aspect Ratio and Liquid-Phase Content on Densification Of Alumina-Silicon Carbide Whiskers Composites", J. Am. Ceram. Soc., **73**, 1440-42, (1990)

2.2.5 S. J. Barclay, J. R. Fox and H. K. Bowen, "Processing of Pressureless Sintered SiC-Whisker Reinforced Al_2O_3 Composites". J. Mater. Sci., 22, 4403-406, (1987)

2.2.6 N. Claussen and S. Wu, "Processing and Properties of Reaction-Bonded Al_2O_3 (RBAO) And Mullite Ceramics, Ceramic Transactions, Aug. 1991

2.3.1 B. V. Chambers, "The Synthesis and Characterization of Model Interface Couples for Inorganic Matrix Composite Applications", Ph.D. Dissertation, MIT, 1994

2.3.2 R. K. Bordia and R. Raj, "Sintering Behavior of Ceramic Films Constrained by a Rigid Substrate", J. Amer. Ceram. Soc., **68**, 287-92 (1985)

2.3.3 T. J. Garino and H. K. Bowen, "Kinetics of Constrained Film Sintering", J. Amer. Ceram. Soc., **73**, 251-57 (1990)

2.3.4 J. W. Hutchinson and Z. Suo, "Mixed Mode Cracking in Layered Materials", in: "Advances In Applied Mechanics", Editors: J. W. Hutchinson and T. Y. Wu, (Academic Press, New York) V. 29, 63-191, (1992)

2.3.5 M. D. Thouless, "Combined Buckling and Cracking of Films", J. Amer. Ceram. Soc., 76, 2936-38, (1993)

2. 3. 6 V. Gupta, "Problems In Interfacial Fracture", Ph.D Dissertation, MIT, 1989

2.3.7 M. F. Ashby and D. R. H. Jones. Engineering Materials, V.1. (Pergamon Press, Oxford). (1980)

2.3.8 G. R. Wallwork and A. E. Jenkins, *J. Electrochem.. S.*, **106,** 10, (1959).

2.3.9 K. Osthagen and P. Kofstad, *J. Electrochem.. S.*, **109**, 204, (1962).

2.3.10 P. J. Pemsler,*J. Electrochem. S.*, **111**, 381, (1964).

Chapter 3.

3.1. Vossen, J. L., in " Adhesion Measurement of Thin Films, Thick Films and Bulk Coatings", K. L. Mittal, editor, STP-640, ASTM: Philadelphia, pp. 122 -133.

3.2. Gupta, V., Argon, A. S., Cornie, J. A. and Parks, D. M. Measurement of interface strength by a laser spallation technique. *J. Mech. Phys. Solids*, **40**, 141-180, 1992.

3.3. Cornie, J. A., Argon, A. S. and Gupta, V. Designing interfaces in inorganic matrix composites. *MRS Bulletin*, XVI(4):32-38, 1991.

3.4. Gupta, V. An evaluation of the interface tensile strength-toughness relationship. *MRS Bulletin*, XVI(4):39-45, 1991.

3.5. Gupta, V., Argon, A. S., Cornie, J. A and Parks, D. M.. Measurement of interface strength by laser-pulse-induced spallation. *Mater. Sci. & Eng.*, **A126**, 105-117, 1990.

3.6. Yuan, J. and Gupta, V. Measurement and Control of Interface Strength. In: Proceedings of International Conference on Lasers (San Diego, CA, 1991).

3.7. Eliezer, S., Gilath, I. and Bar-Noy, T. Laser-induced spall in metals: experiment and simulation. *J. Appl. Phys.*, 67(2):715-724, 1990.

3.8. He, M.-Y., and Hutchinson, J. W., Crack deflection at an Interface between dissimilar elastic materials. *Int. J. Solids Struct.*, **25**, 1053-67 (1988).

3.9. Gupta, V., Argon, A. S., and Suo, Z. Crack deflection at an interface between two orthotropic media. *J. Appl. Mech.*, **59**, 579-587, 1992.

3.10. Evans, A. G. The mechanical performance of fiber reinforced ceramic composites, Mater. Sci. Eng., **A107**, 227-39 (1989).

3.11. Lev, L. C., Argon, A. S. Development of oxide coating for matching oxide fiber-oxide matrix composite. To appear in: Proceedings of 18th annual Cocoa Beach meeting of ACS, (1994)

3.12. American Institute of Physics Handbook, 3D Ed. D. E. Gray, editor. McGraw-Hill, 1972.

3.13. Chambers, B. V. The Synthesis and Characterization of Model Interface Couples for Inorganic Matrix Composite Applications. PhD thesis. Massachusetts Institute of Technology, Cambridge, MA, 1994.

3.14. Martin von Allmen, (1987). Laser-Beam Interactions with Materials. Physical Principles and Applications. Spring-Verlag, Berlin, New York, London.

3.15 Oppenheim, A. V. and Schafer, R. W. Digital Signal Processing. Prentice-Hall, N.J., 1975

3.16. Yuan, J. and Gupta, V. Measurement of Interface strength by the modified laser spallation technique. J. Appl. Phys., January 1993.

3.17. Yuan, J., Gupta, V. and Pronin, A. Measurement of Interface strength by the modified laser spallation technique. J. Appl. Phys., January 1993.

3.18. Pronin, A., Gupta, V. Interferometry on Diffuse surfaces in high-velocity measurements. Rev. Sci. Ins., January 1993.

3.19. Laser QSR 3. Company materials.

3.20. Pronin, A., Gupta, V., Yuan, J., Chawla, K. K., Vaidya, R. U. Tensile strength of interface between SnO2 coating and Alumina substrate. Scripta Metallurgica et Materialia, Vol. 28, pp1371-1376, 1993.

3.21. Lamb, H. On the propagation of tremors on the surface of an elastic solids. Philos. Trans. Royal Soc., London, Ser. **A 203**, 1-42, (1904).

3.22. Sobolev, S. and Smirnov, V. I. On a new method in the problem of elastic vibrations. Akad. Nauk, SSSR Seism. Institute. Trudy 20, 1932.

3.23. Eason, G., Fulton, J. and Sneddon, I. N. The generation of waves in an infinite elastic solid by variable body forces. Phil Trans. Royal Soc., No. 955, Vol. 248, p. 575-607, 1956.

3.24. Eason, G. The displacement Produced in an elastic halfspace by a suddenly applied surface force. J. Inst. Maths Applics. 2, 299-326, 1966.

3.25. Gakenheimer, D. C. and Miklowitz, J. Transient exatation of an elastic half space by a point traveling on the surface. J. Appl. Mech., 36, 505-515, 1969.

3.26. El-Raheb, M. and Wagner, P. Transient waves in a thick disk. J. of Acou. Soc. Amer., 1993.

3.27. Guan, F. and Novak, M. Transient response of an elastic homogeneous half space to suddenly applied rectangular loading. J. Apple. Mech., 1993.

3.28. Cagniard, L. Reflection and Refraction of Progressive Seismic Waves. McGraw - Hill, N. Y., 1962.

3.29. Al-Rushid, unpublished.

3.30. Walsh, J. L. A closed set of orthogonal functions. Amer. J. of Mathematics, 45, 5-24, 1923.

3.31. Harmuth, H. F. Transmission of information by Orthogonal Functions, Springer-Verlag, Berlin, 1970.

3.32. Pichler, F. Walsh functions, signals and systems. In: Applications of Walsh functions and sequence theory, edited by H. Schreiber and G. Ferrel Sandy, New York, 1974.

3.33. Eason, G., Noble, B., and Sneddon, I. J. On certain integrals of Lischitz-Hankel type involving products of Bessel functions. Phil. Trans. of the Royal Soc., Vol. 247, A. 935, 1954.

3.34. Achenbach, J. D. Wave propagation in elastic solids. North-Holland Publ. Co., (1973).

3.35. Graff, K. F. Wave motion in elastic solids. Ohio State Sniv. Press, 1975.

3.36. Lee, S. S. and Williams, J. H. Stress wave attenuation in thin structures by Ultrasonic through-Transmission. NASA

3.37. Carlson, B. C. Numerische Mathematik, v. 33, p. 1- 16, 1979.

3.38. Lev, L. C. and Argon, A. S. Oxide Fiber - Oxide Matrix Composites. To appear in Journal of Materials Science and Engineering

Chapter 4.

4.1-1 S. L. Phoenix, P. Schwartz and H. H. Robinson. *Composites Sci and Techn* **32**, 1 (1988)

4.1-2. A. S. Watson and R. L. Smith. *J. Material Science*, **20**, 3260, (1985)

4.1-3. J. Gutans and V. Tamuzs. *Textile Research J.*, **20**, 1107, (1984)

4.1-4. P. Schwartz, A. Netravali and S. Sembach. *Textile Research J*, **56**, 502, (1986)

4.1-5. A. M. Freudenthal. Statistical Approach to Brittle Fracture. In: Fracture, An Advanced Treatise. Edited by H. Liebowitz. Volume 2, p. 591. Academic Press, 1968.

4.2-1.). D. Briggs, A. Brown and J. C. Vickerman, editors. Handbook of static secondary ion mass spectrometry (SIMS) John Wiley & Sons, New York, 1989.

4.2-2. R. G. Wilson, F. A. Stevie and C. W. Magee. Secondary Ion Mass Spectrometry. John Wiley & Sons, New York, 1989

Chapter 5.

5.1 N. Claussen And S. Wu, "Processing And Properties Of Reaction-Bonded Al_2O_3 (RBAO) And Mullite Ceramics, Ceramic Transactions, Aug. 1991

5.2 R. P. Ingel and D. Lewis III. Elastic Anisotropy in Zirconia Single Crystals. J. Am. Ceram. Soc., 71 [4] 265 - 71 (1988)

5.3 R. E. Cohen, M. J. Mehl and L. L. Boyer. Phase transformations and elasticity in Zirconia. Physica B, 150 (1988) 1 -9

5.4 H. M. Kandil, J. D. Greiner and J. F. Smith. Single-Crystal Elastic Constants of Yttria-Stabilized Zirconia in the Range 20 ^{0}C to 700 ^{0}C. J. Am. Ceram. Soc., 67 [5] 340-346 (1984)

5.5 R. P. Ingel, D. Lewis, B. A. Bender and R. W. Rice. Physical, Microstructural and Thermomechanical Properties of ZrO_2 Single Crystals, in : Advances in Ceramics, Vol.12, Science and Technology of Zirconia. Edited by N. Claussen, M. Ruhle and A. H. Heuer. American Ceramic Society, Columbus, OH, 1984.

5.6 M. V. Nevitt, S.-K. Chan, J. Z. Liu, M. H. Grimsditch and Y. Fang. The Elastic properties of monoclinic ZrO_2. Physica B 150 (1988), 230 - 233.

5.7 W. E. Tefft. Elastic constants of Synthetic Single Crystal Corundum. J. Res. Nat. Bur. Stand. 70A, 277 (1966)

5.8 E. S. Zouboulis and M. Grimsditch. Refractive index and elastic properties of single-crystal corundum up to 2100 ^{0}K. J. Appl. Phys., Vol. 70, 2, 772-776 (1991).

5.9 T. S. Chow. Effect Of Particle Shape At Finite Concentration On The Elastic Moduli Of Filled Polymers. J. Polymer Sc., Pol. Phys., Vol. 16, 959-965 (1978).

5.10 H. J. Frost and M. F. Ashby. "Deformation-Mechanism Maps. The plasticity and Creep of Metals and Ceramics". Pergamon Press, Oxford, Toronto. (1982)

5.11 F. A. McClintock And A. S. Argon, "Mechanical Behavior of Materials", Addison-Wesley, (1966).

5.12 M. L. Kronberg, "Plastic Deformation Of Single Crystals Of Sapphire: Basal Slip And Twinning". Acta Met.,5 (9),507 - 524 (1957).

5.13 L. E. Jones And R. E. Tressler, "The High Temperature Creep Behavior Of Oxides And Oxide Fibers", NASA Contractor Report 187060, (1991)

5.14 T. Bretheau, J. Castaing, J. Rabier And P. Veyssiere, "Movement Des Dislocations A Haute Temperature Des Oxydes Binaires Et Ternaires." Adv. Phys., 28 [6], 835-1014

5.15 D. J. Gooch, G. W. Groves (1973)."The Creep Of Sapphire Filament With Orientation Close To The *C*-Axis". Journal Of Material Science, 8, 1238-1246.

5.16 J. S. Haggarty And K. C. Wills (1991). "Growth And Properties Of Single Crystal Fibers". Ceram. Eng. Sci. Proc., 12, 1785-1801

5.17 A. Xu And A. A. Solomon, "Diffusional Creep And Cavitational Strains In High Purity Alumina Under Tension And Subsequent Hydrostatic Compression", J. Am Ceram. Soc., **75**, [4], 985 - 95 (1992)

5.18 G. W. Hollenberg, G. R. Terwillinger and R.S. Gordon (1971). "Calculation of Stresses and Strains in Four-Point Bending Creep Test", J. Am. Ceram. Soc., 54, 196-99

5.19 G. D. Quinn and R. Morrell (1991). "Design Data for Engineering Ceramics: a review of the flexure test". J. Am. Ceram. Soc., 74, 2037-65

5.20 M. K. Ferber, M. G. Jenkins And V. J. Tennery (1990). "Comparison Of Tension, Compression And Flexure Creep For Alumina And Silicon Nitride Ceramics", Ceram. Eng. Sci. Proc., 11, 1028-45

5.21 T. Fett (1992). "Measurements Of Non-symmetric Creep In Al_2O_3 With A Glass Phase", J. Am. Ceram. Soc., 75, 1691-93

5.22 T. J. Chuang (1986). "Estimation Of Power-Law Creep Parameters From Bend Test Data", J. Mater. Sci., 21, 165-75

5.23 R. F. Krause (1992). "Observed And Theoretical Creep Rates For An Alumina Ceramic And Silicon Nitride Ceramic In Flexure", J. Am. Ceram. Soc., 75, 1307-310

5.24 A. G. Evans And T. G. Langdon, "Structural Ceramics", Prog. Mater. Sci., **21**, 350, (1976)

5.25 R. P. Ingel, D. Lewis, B.A. Bender, R. W. Rice (1982) "Temperature Dependence Of Strength And Fracture Toughness Of ZrO_2 Single Crystals", Comm. Amer. Ceram. Soc., C-150 - C-152

5.26 P. E. Evans, "Creep In Yttria- And Scandia-Stabilized Zirconia." J. Amer. Ceram. Soc., 53 [7], 365-369

5.27 D. Dimosand D. L. Kohlstead, "Diffusional Creep And Kinetic Demixing In Yttria-Stabilized Zirconia", J. Amer. Ceram. Soc., 70 [8], 531 - 536.

5.28 I-Wei Chen, "Creep cavitation in 304 stainless steel", Ph.D Dissertation, MIT, 1980

5.29 H. T. Lin And P. F. Becher, "Creep Behavior Of A SiC-Whisker-Reinforced Alumina", J. Am. Ceram. Soc., 73 [5], 1378 - 81 (1990)

5.30 A. G. Evans, "The High Temperature Failure Of Ceramics", In "Recent Advances In Creep And Fracture Of Engineering Materials And Structures", Edited By B. Wilshire And D. R. Owen.

5.31 J. C. Williams, "Material Challenges For The Aircraft Engine Industry", MIT DMSE Lecture, MIT, Cambridge, 1995.

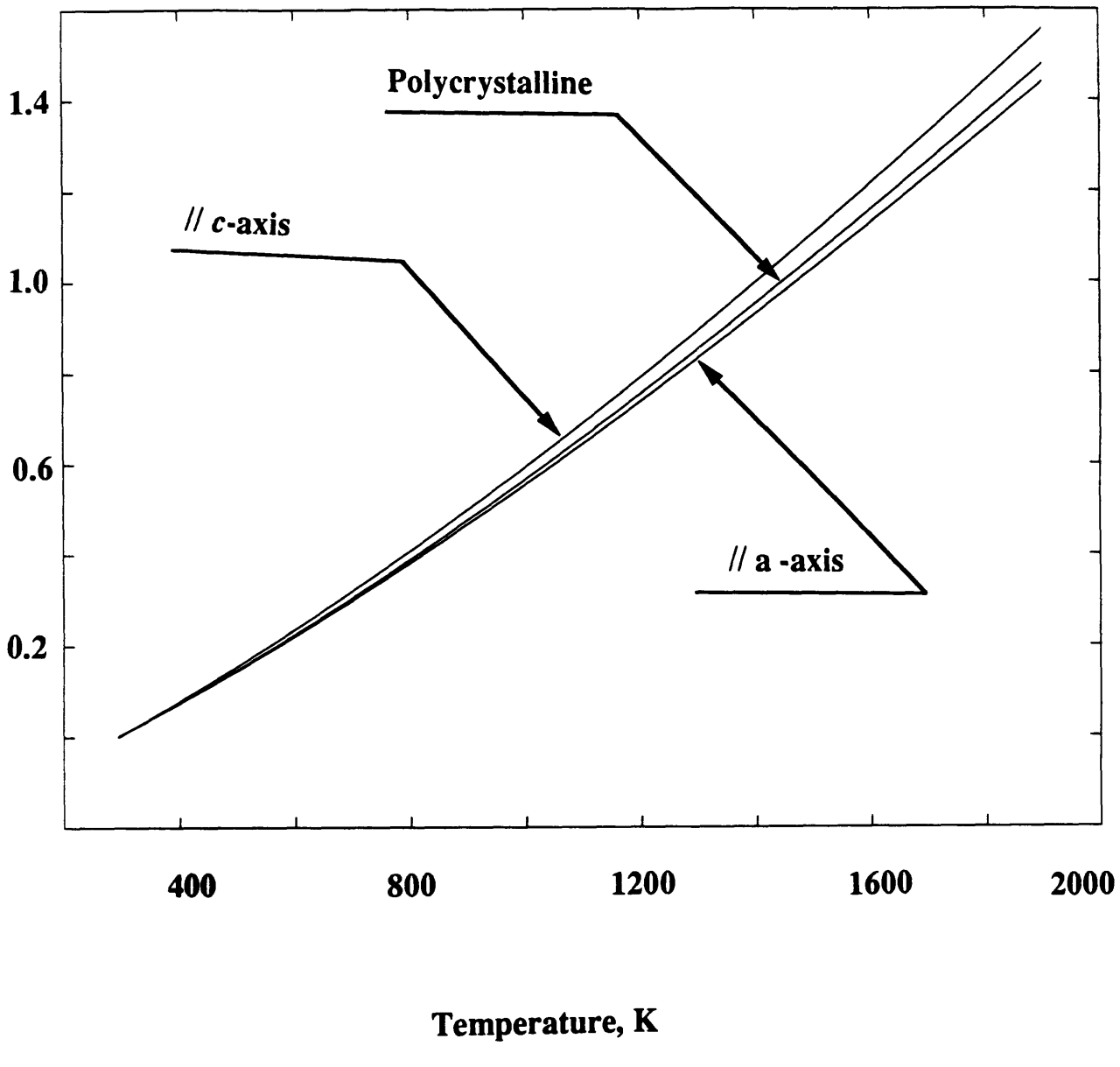

Figure 1.1 CTE's of Al_2O_3 in different crystallographic directions [1.6].

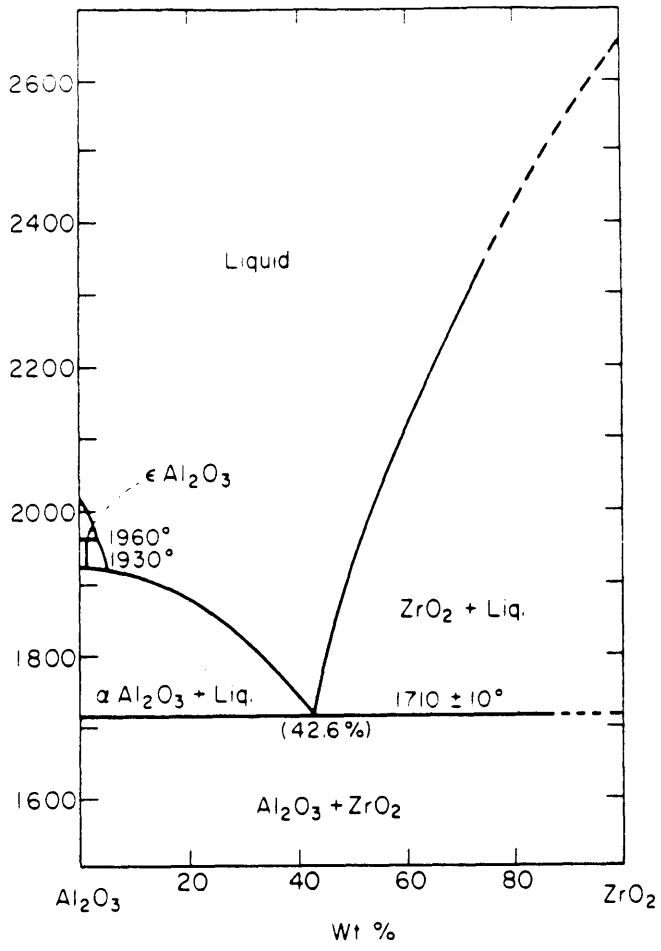

Figure 1.2a Phase diagram of the system Al_2O_3 - ZrO_2 [1.8]

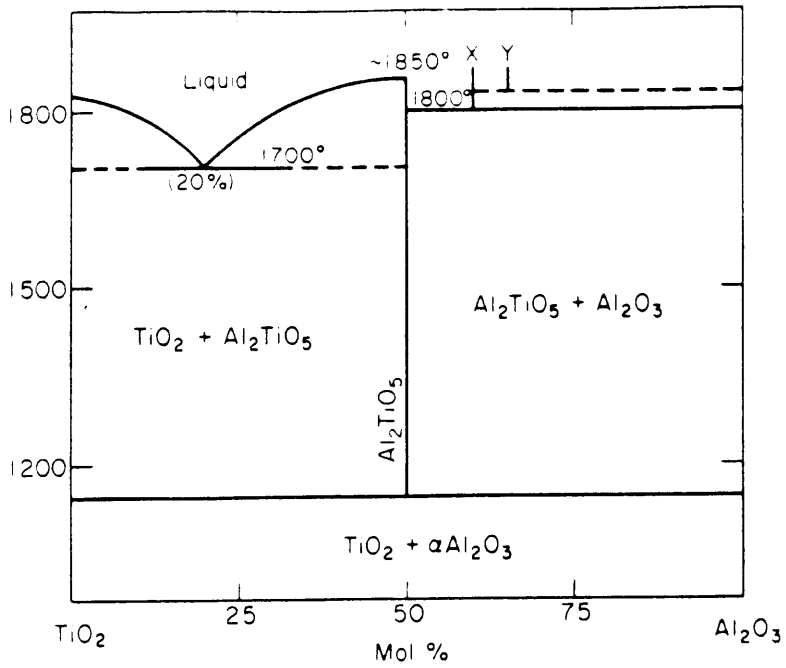

Figure 1.2b Phase diagram of the system Al_2O_3 - TiO_2[1.8]

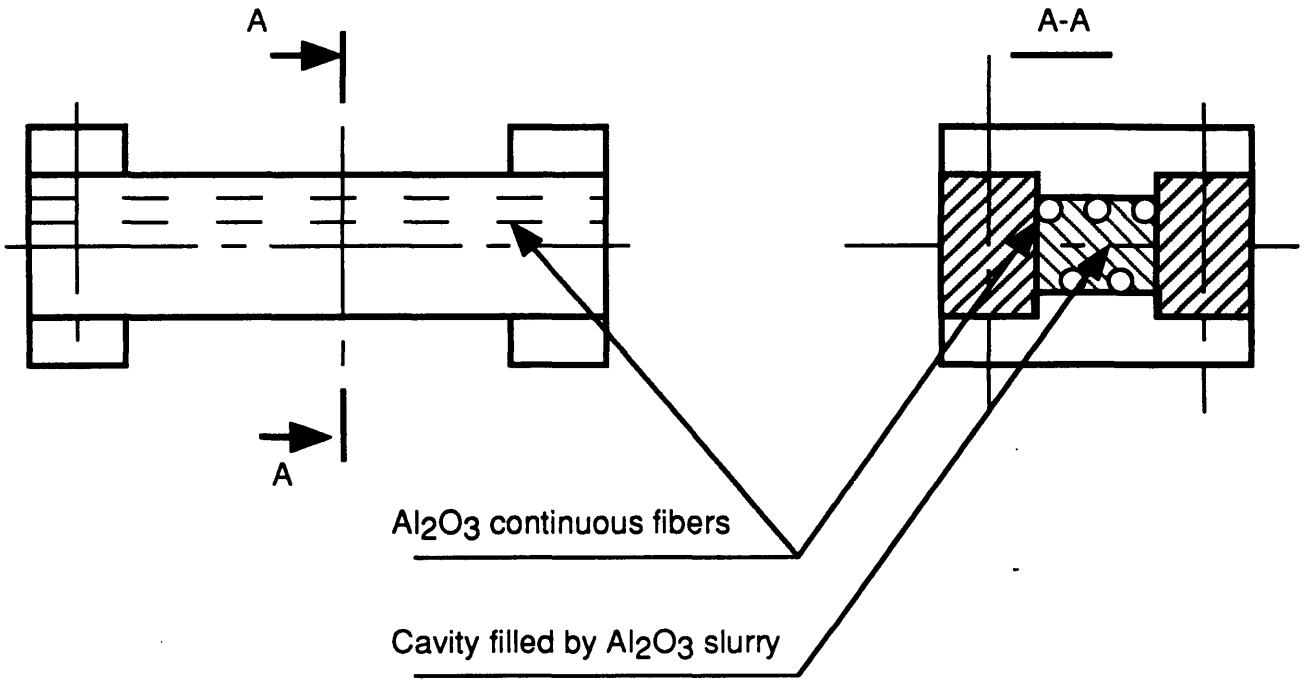

Figure 2.1 Mold used for processing of Al_2O_3/Al_2O_3 composite.

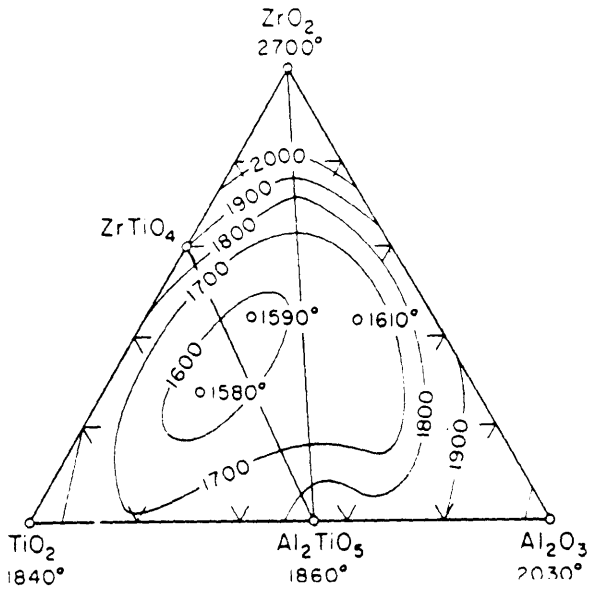

Figure 1.2c System Al_2O_3 - TiO_2 - ZrO_2; melting isotherms[1.8].

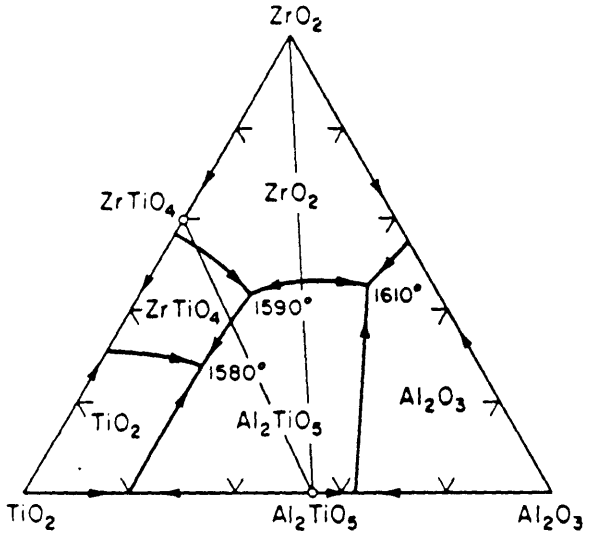

Figure 1.2d System Al_2O_3 - TiO_2 - ZrO_2; primary phases[1.8].

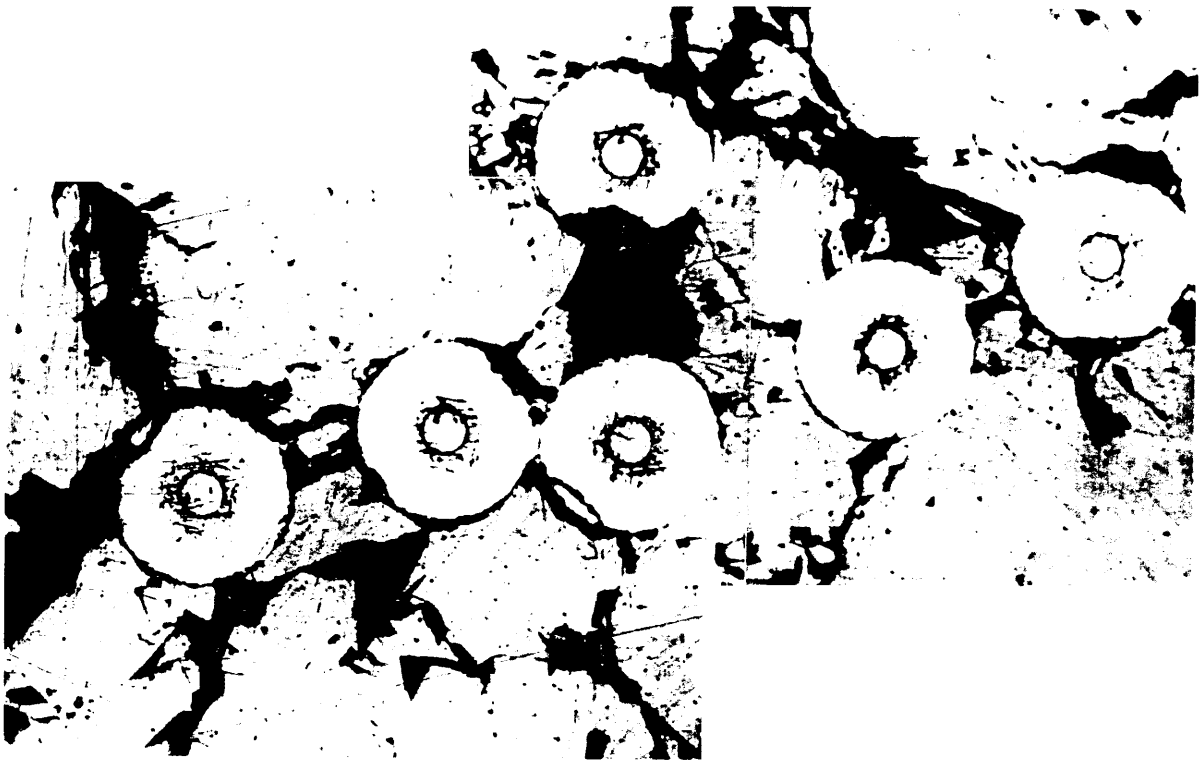

Figure 2.2a Model system consisting of Al_2O_3 matrix reinforced with SiC fibers pressureless sintered with the help of fugitive coating

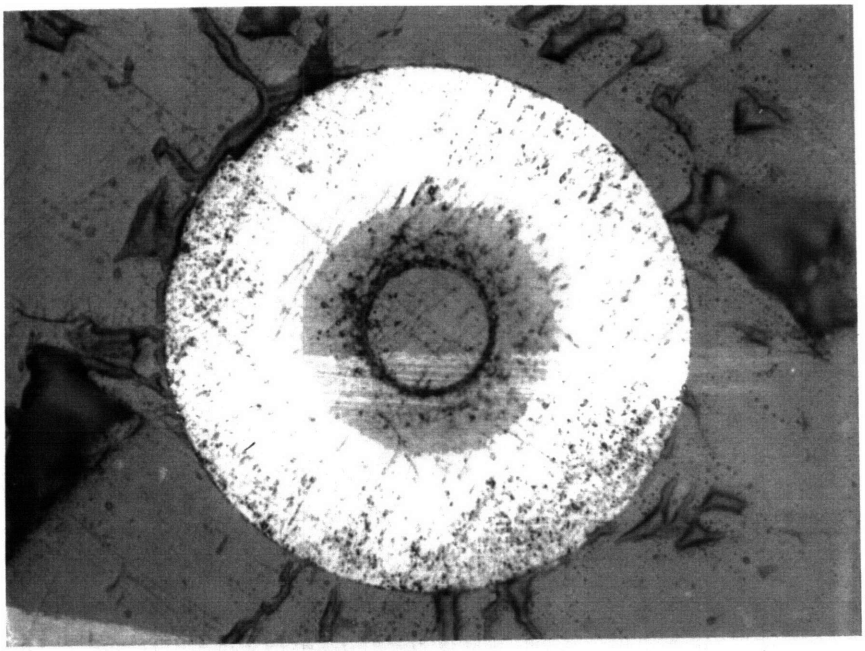

Figure 2.2b Fragment of the composite showing the SiC fiber imbedded into Al_2O_3 matrix. Fugitive coating deposited on the fiber prior to the sintering has been removed and Al_2O_3 matrix filled in the gaps.

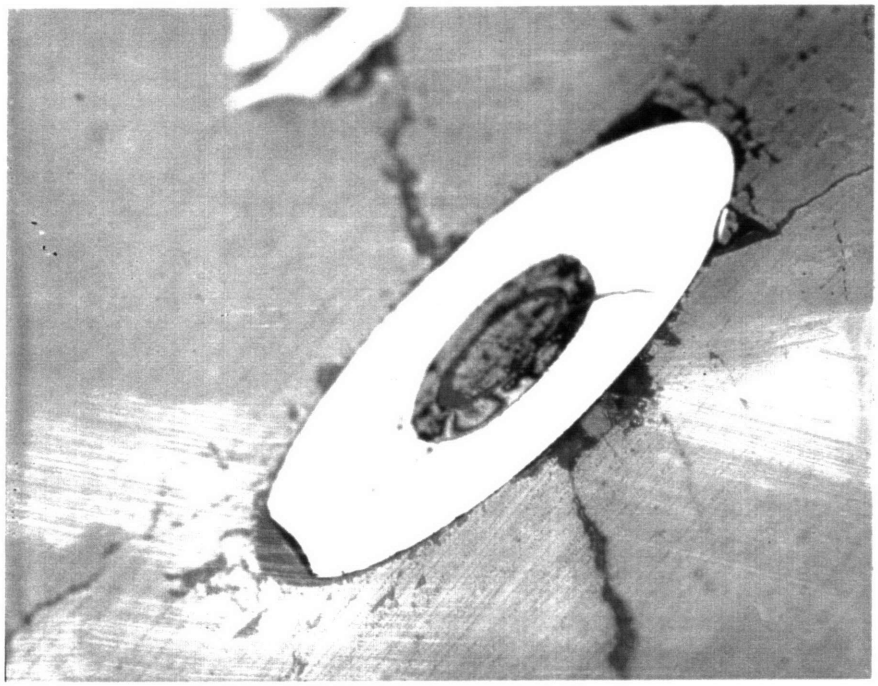

Figure 2.3a Skewed cross section of a SiC fiber in Al_2O_3 matrix

Figure 2.3b Skewed cross section of a SiC fiber in Al_2O_3 matrix under higher magnification.

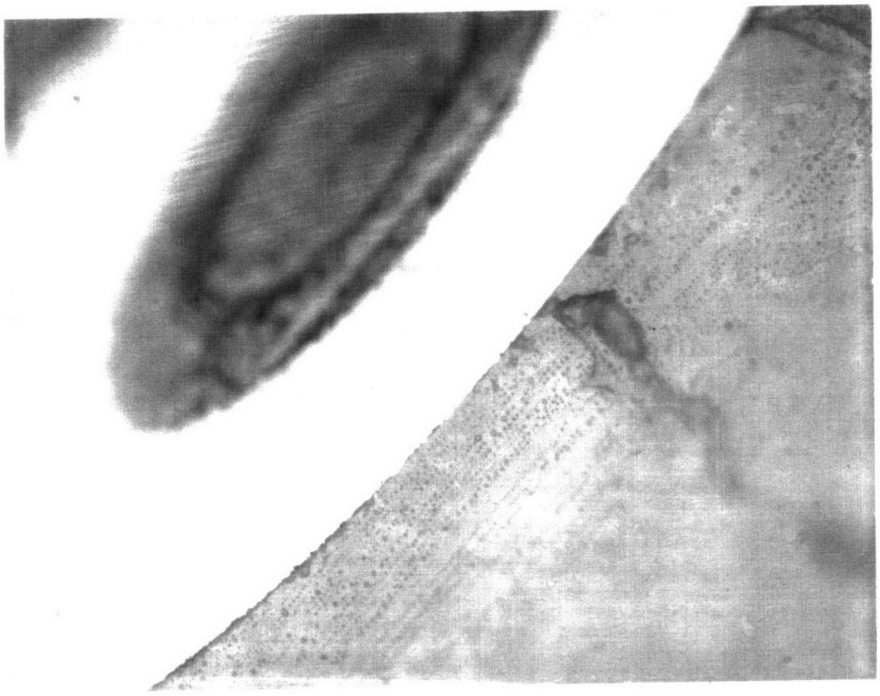

Figure 2.4 Skewed cross section of a SiC fiber in Al_2O_3 matrix. Interface between the fiber and the matrix

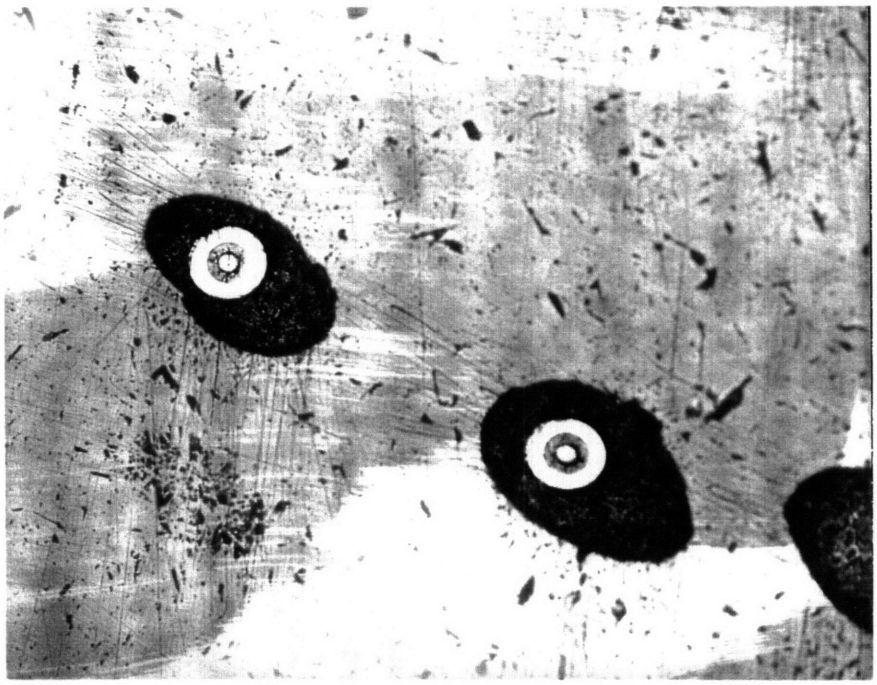

Figure 2.5 Cross section of a SiC fiber in Al_2O_3 matrix. The matrix did not fill in the gaps during the shrinkage.

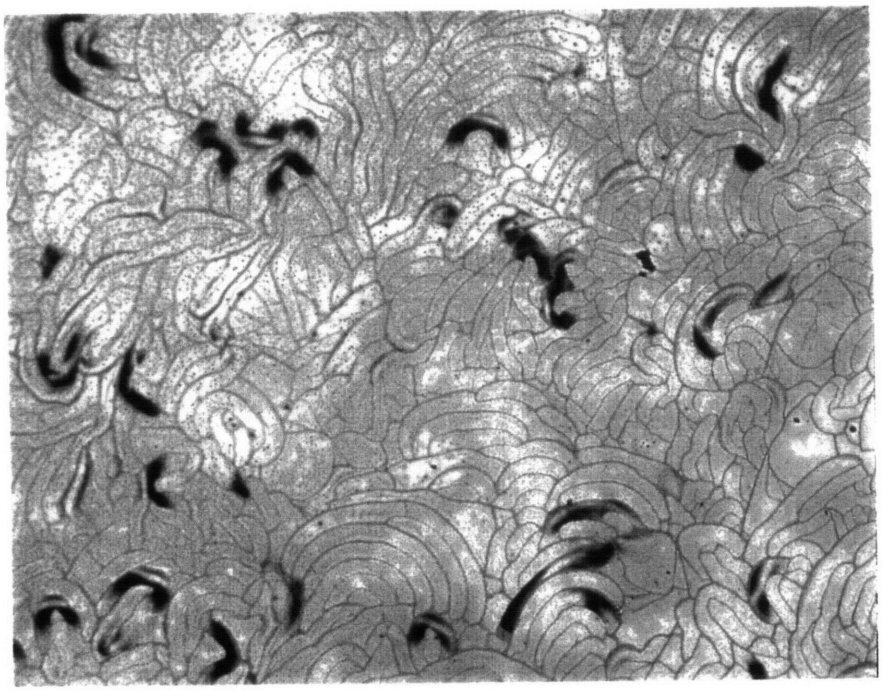

Figure 2.3.1 Crack pattern in SiC coating on Al_2O_3 substrate after exposure to 1200 ^{0}C.

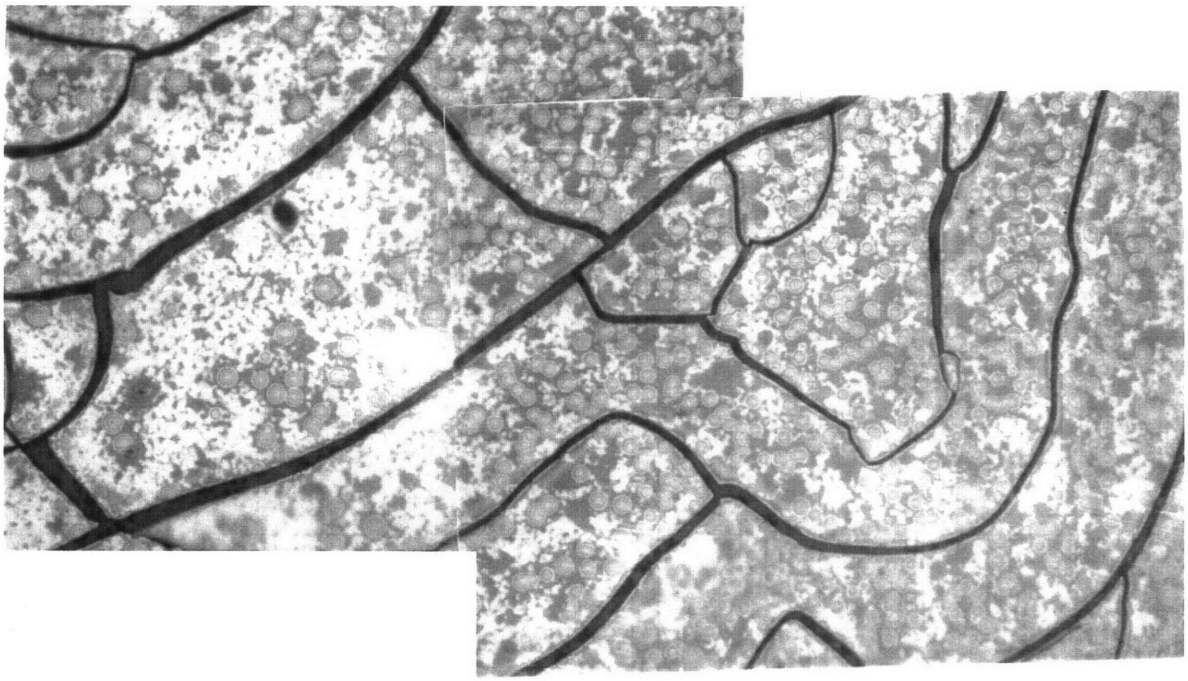

Figure 2.3.2 Fragment of SiC coating on Al_2O_3 substrate after exposure to 1200 °C.

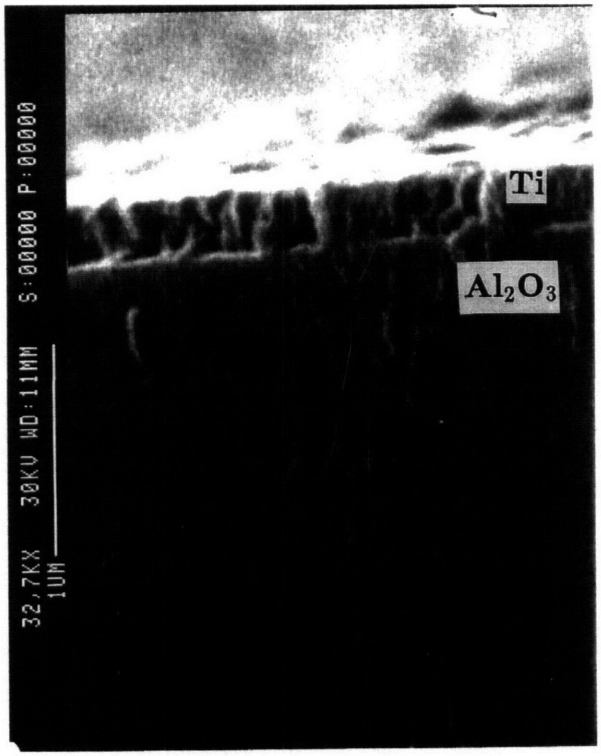

Figure 2.3.3 **E-BEAM EVAPORATED Ti COATING ON A FLAT SINGLE CRYSTAL Al_2O_3 SUBSTRATE**

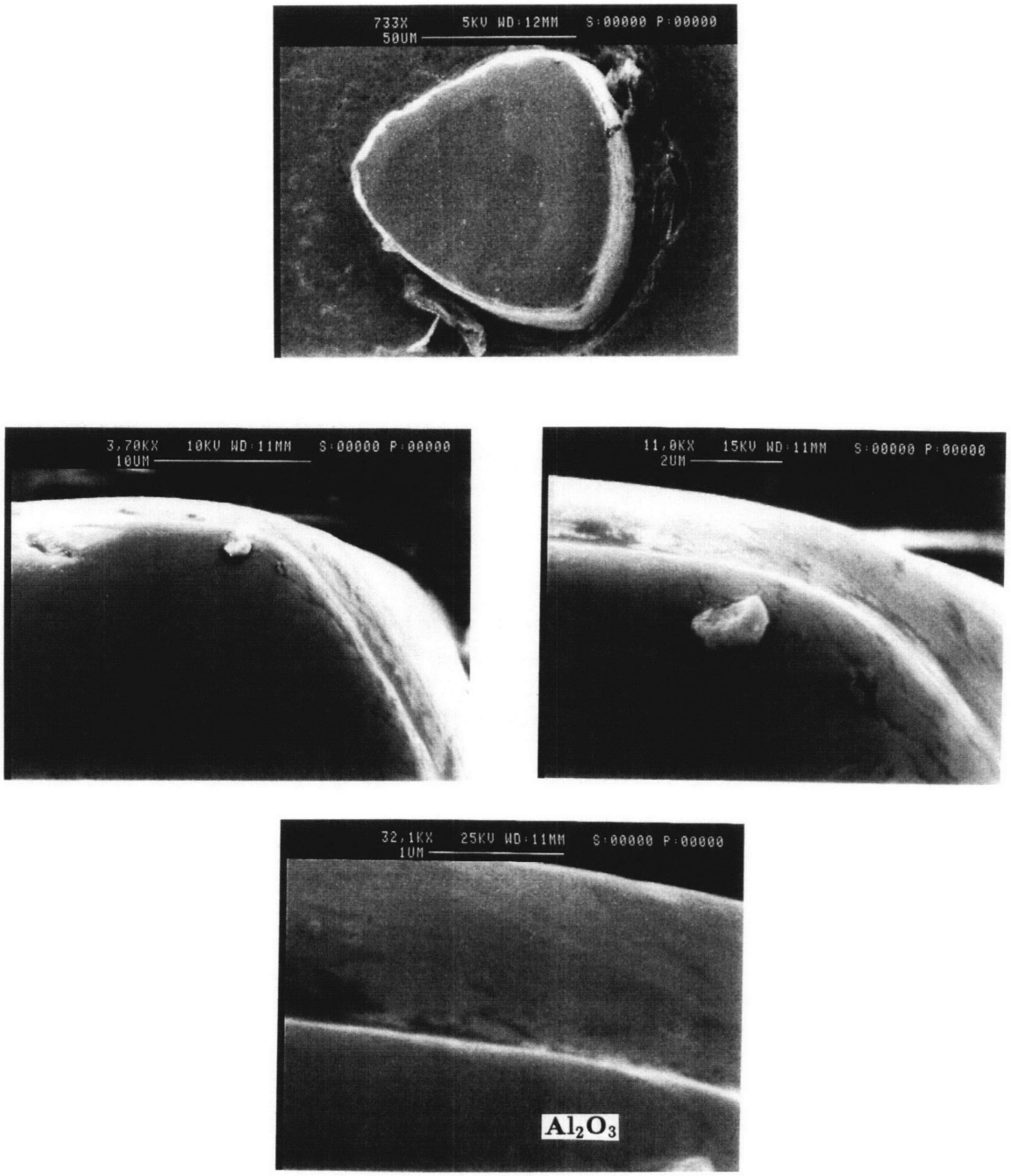

FIGURE 2.3.4a

SPATTERED Ti METALLIC COATING ON SAPHICON^R SAPPHIRE FIBER

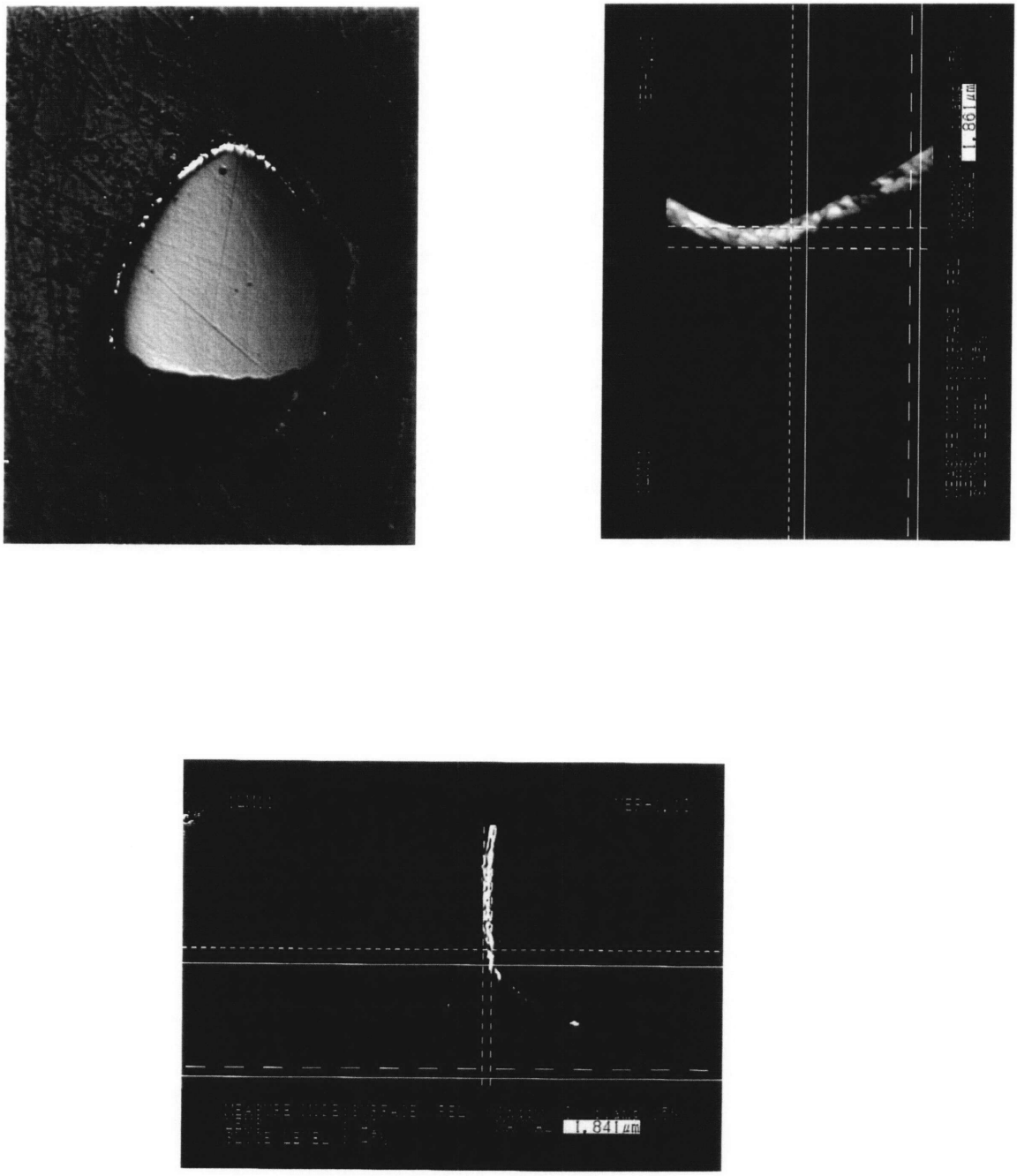

FIGURE 2.3.4b

SPATTERED Ti METALLIC COATING ON SAPHICON^R SAPPHIRE FIBER

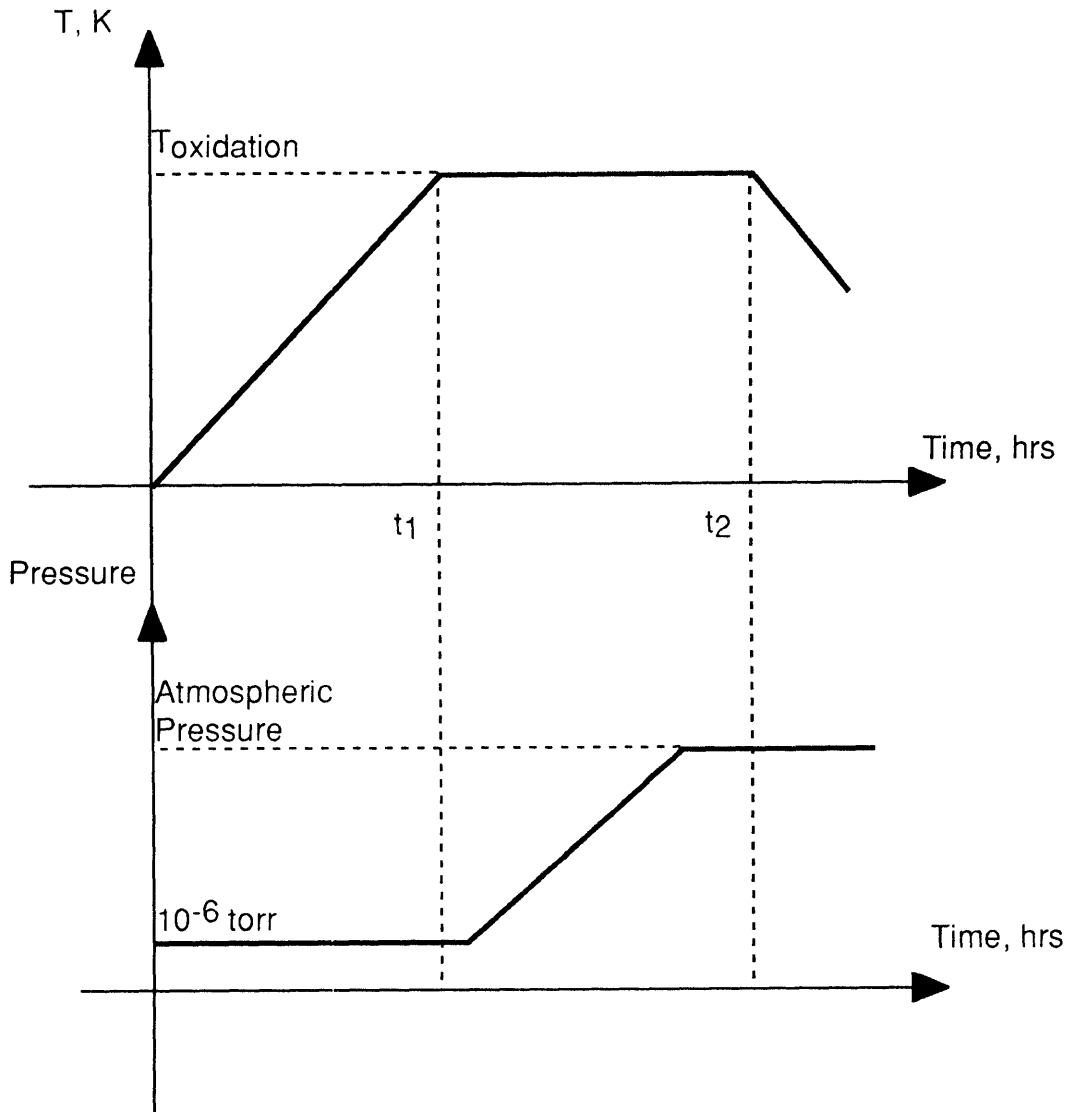

Figure 2.3.5 (Temperature and pressure vs time) diagram

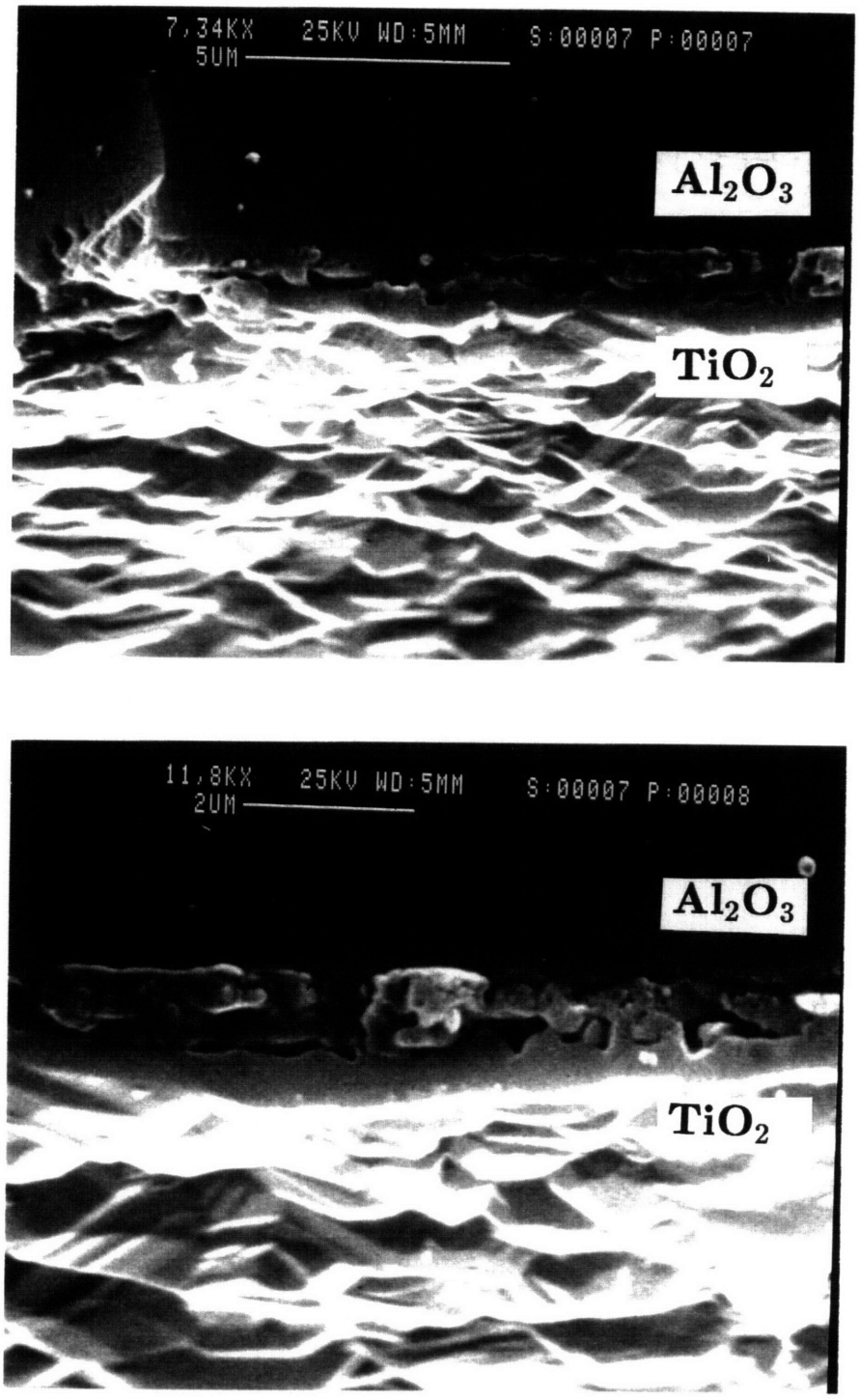

FIGURE 2.3.6

TiO_2 COATING ON SINGLE CRYSTAL Al_2O_3 SUBSTRATE OXIDIZED AT 1100°C

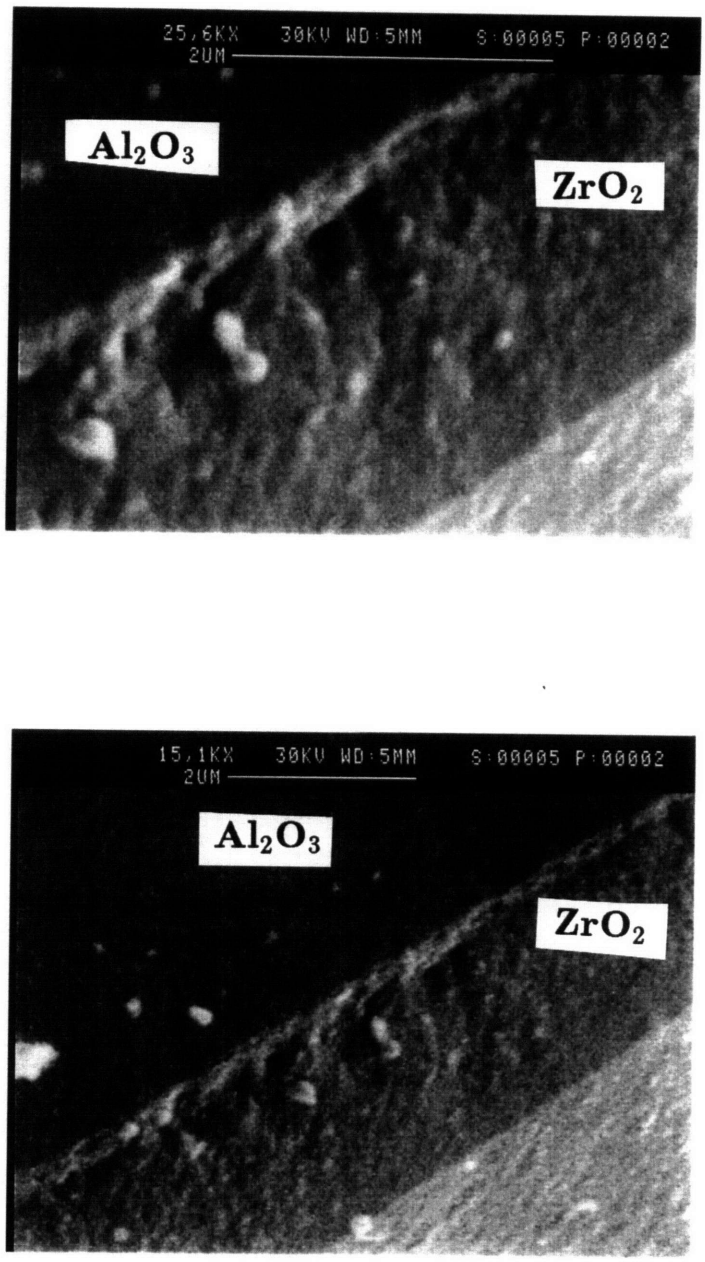

FIGURE 2.3.7

ZrO_2 COATING ON SINGLE CRYSTAL Al_2O_3 OXIDIZED AT 1100°C

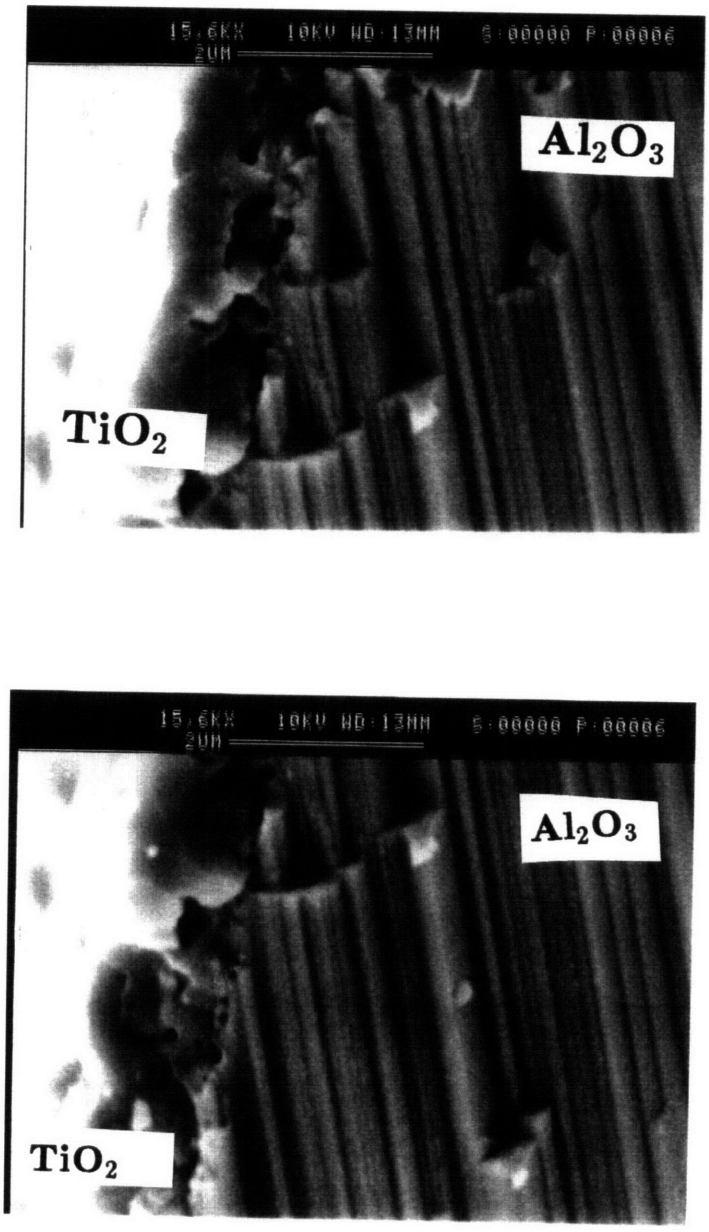

FIGURE 2.3.8a

TiO_2 COATING ON SAPHICON^R SAPPHIRE FIBER AFTER OXIDATION AT 1200°C

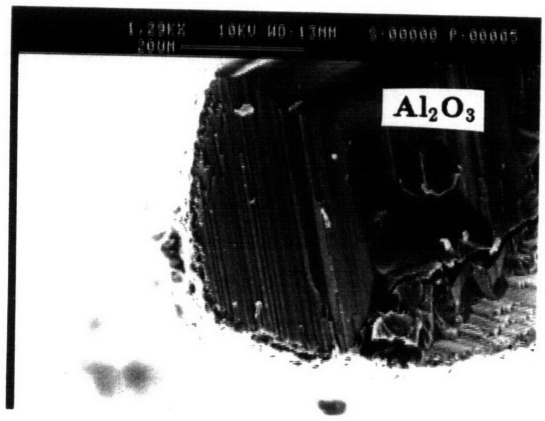

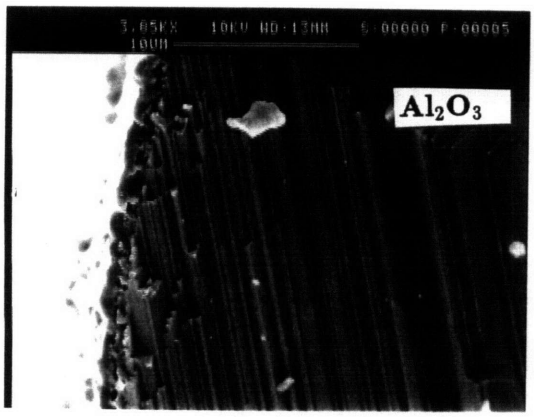

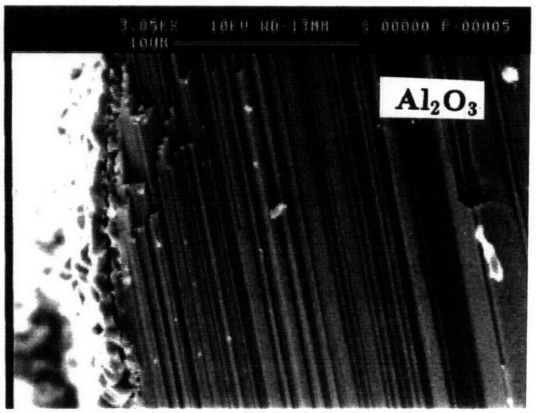

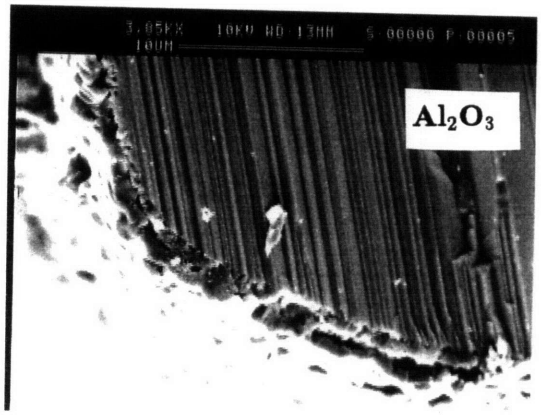

FIGURE 2.3.8b

TiO_2 COATING ON SAPHICON^R SAPPHIRE FIBER AFTER OXIDATION AT 1200°C

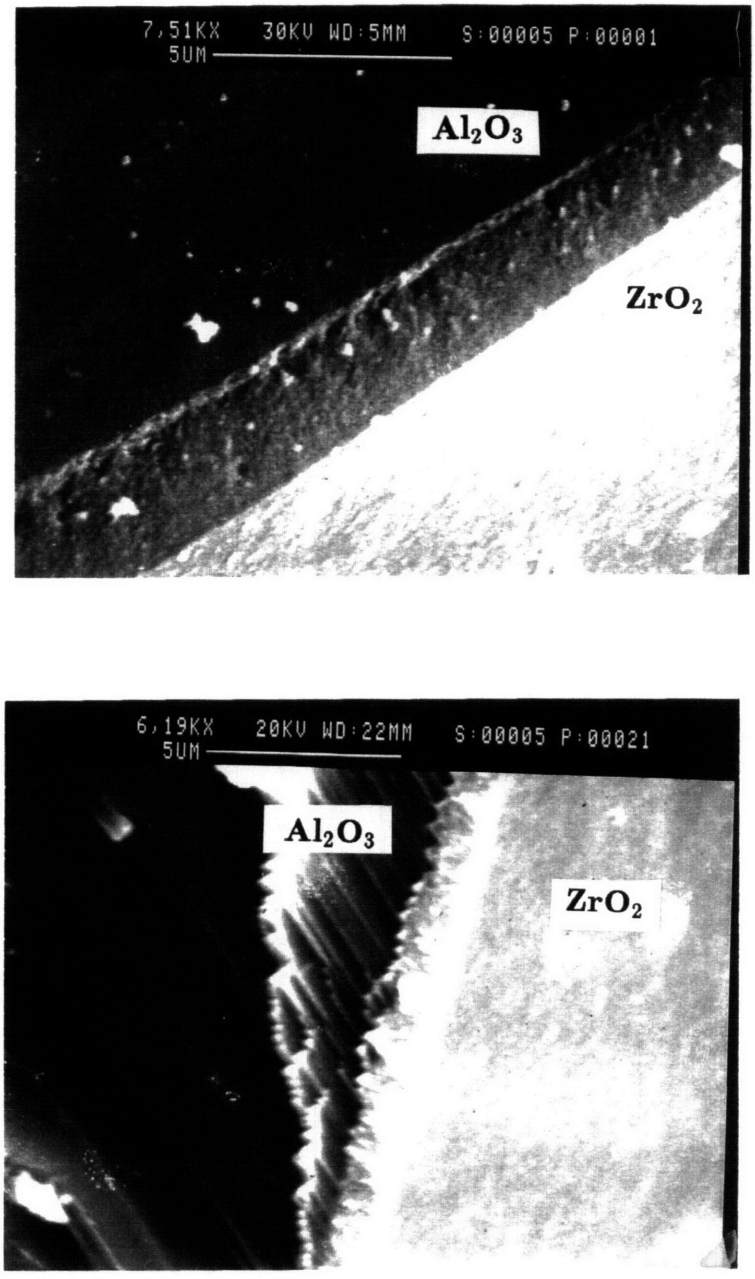

FIGURE 2.3.9

ZrO_2 COATING ON SINGLE CRYSTAL Al_2O_3 OXIDIZED AT 1100°C

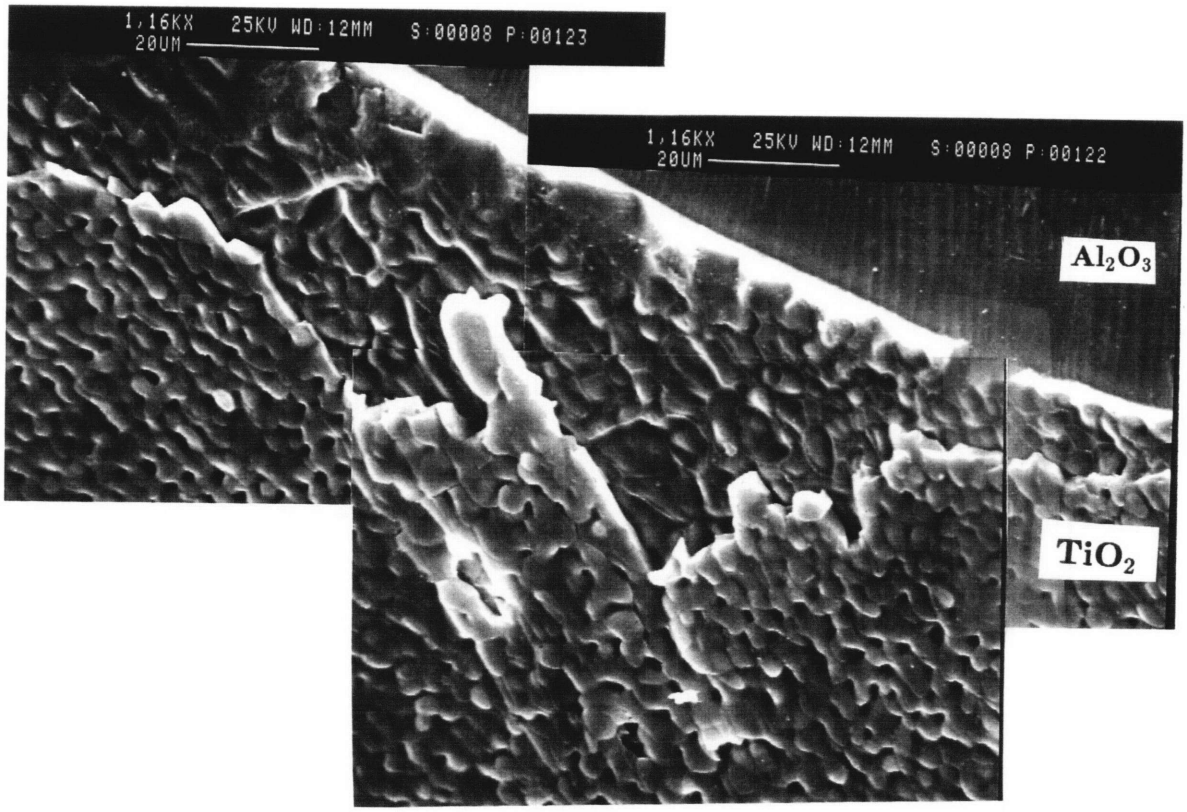

FIGURE 2.3.10a

TiO_2 COATING ON Al_2O_3 SINGLE CRYSTAL SUBSTRATE AFTER EXPOSURE TO 1600° FOR 4 HOURS

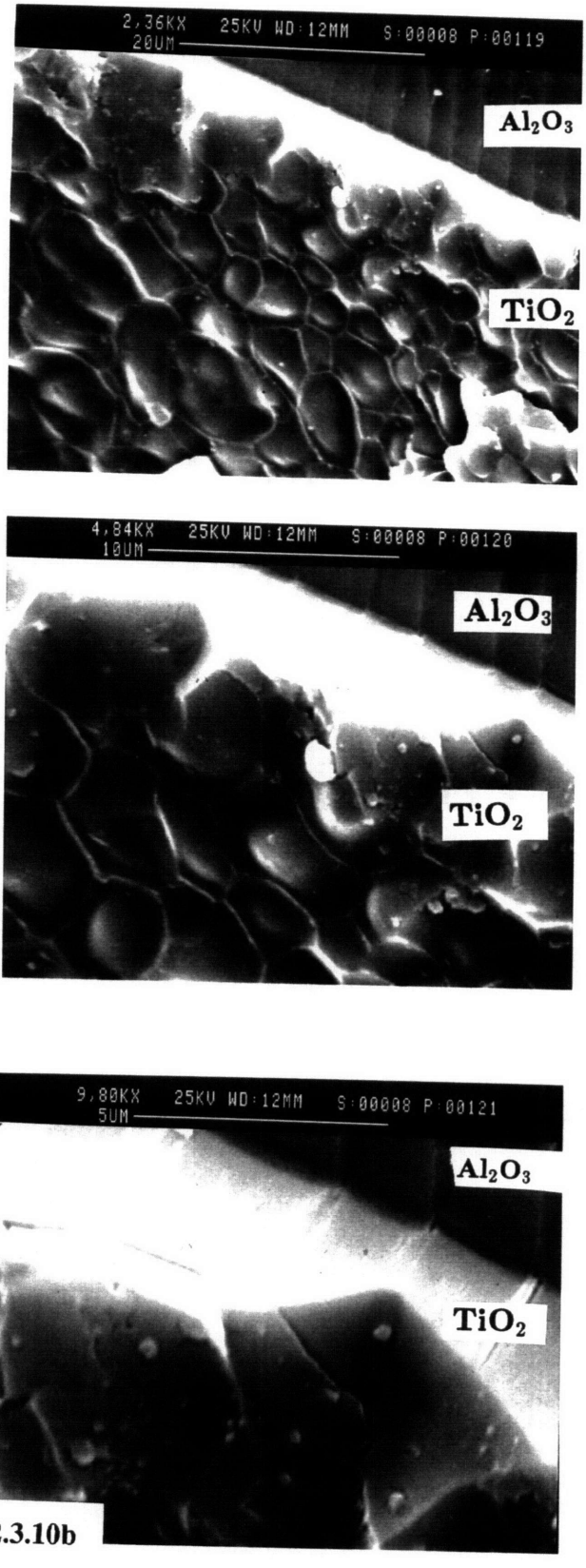

FIGURE 2.3.10b

TiO_2 COATING ON Al_2O_3 SINGLE CRYSTAL SUBSTRATE AFTER EXPOSURE TO 1600° FOR 4 HOURS

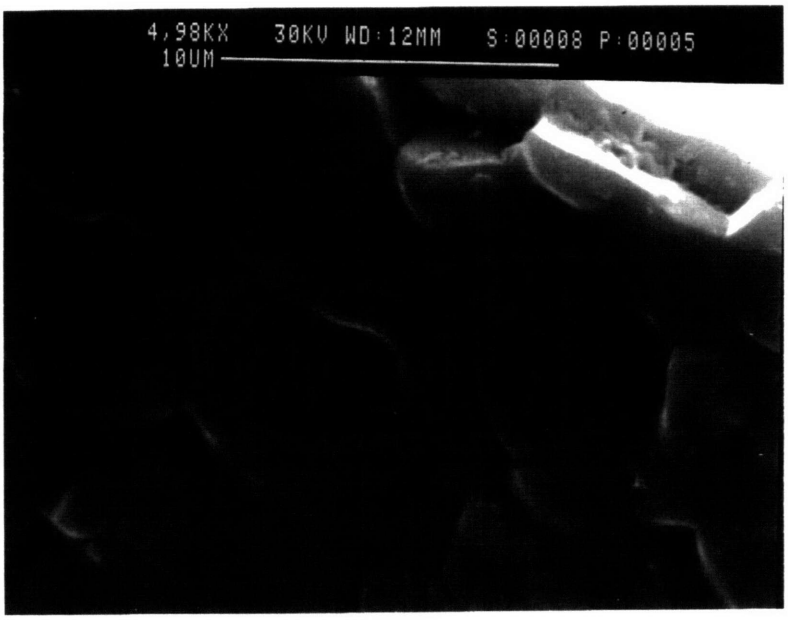

FIGURE 2.3.11

OUTER LAYER OF TiO2 COATING. 1600C, 4hrs.

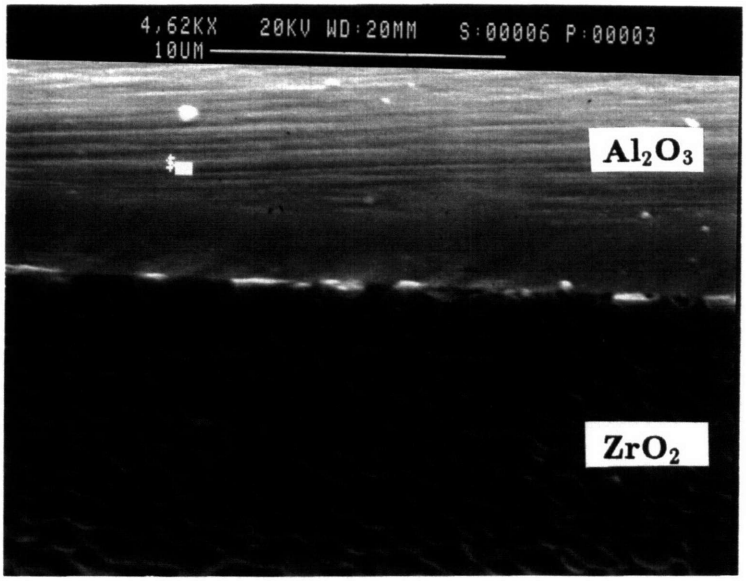

FIGURE 2.3.12
ZrO_2 COATING ON Al_2O_3 SINGLE CRYSTAL SUBSTRATE AFTER EXPOSURE TO 1600° FOR 4 HOURS

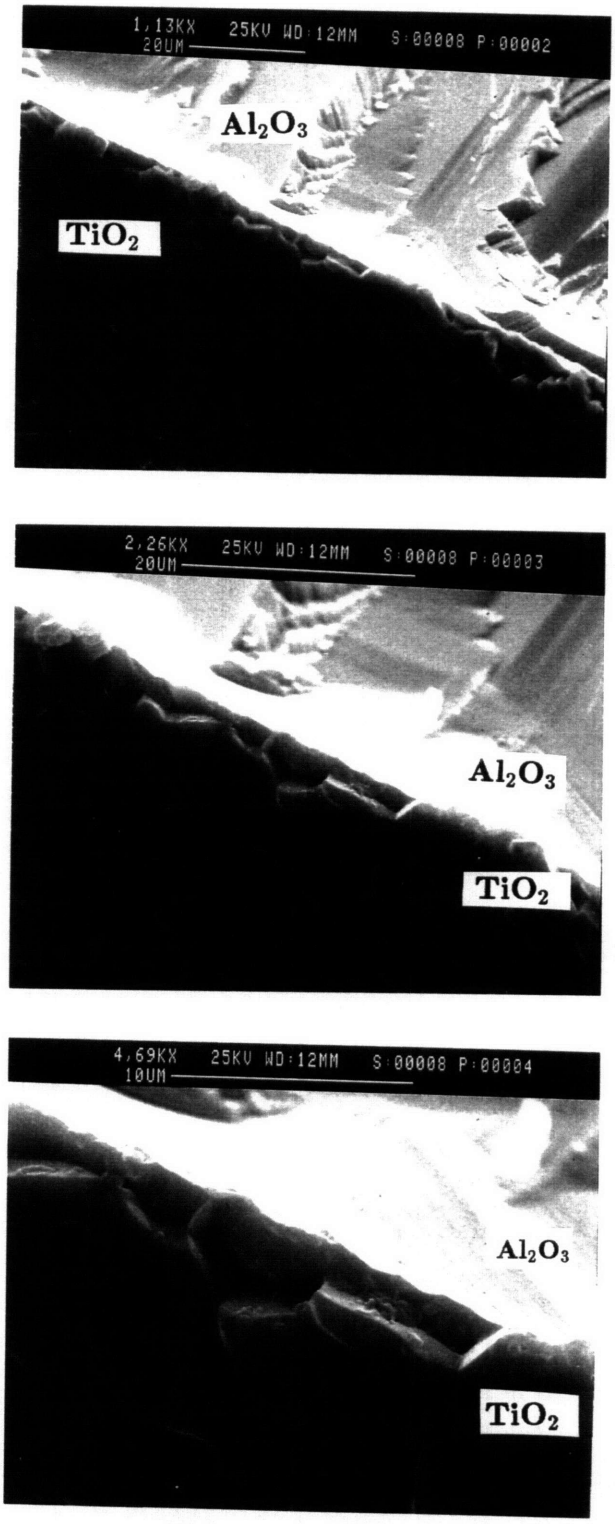

FIGURE 2.3.13

TiO_2 COATING ON Al_2O_3 SINGLE CRYSTAL SUBSTRATE AFTER EXPOSURE TO 1600° FOR 4 HOURS

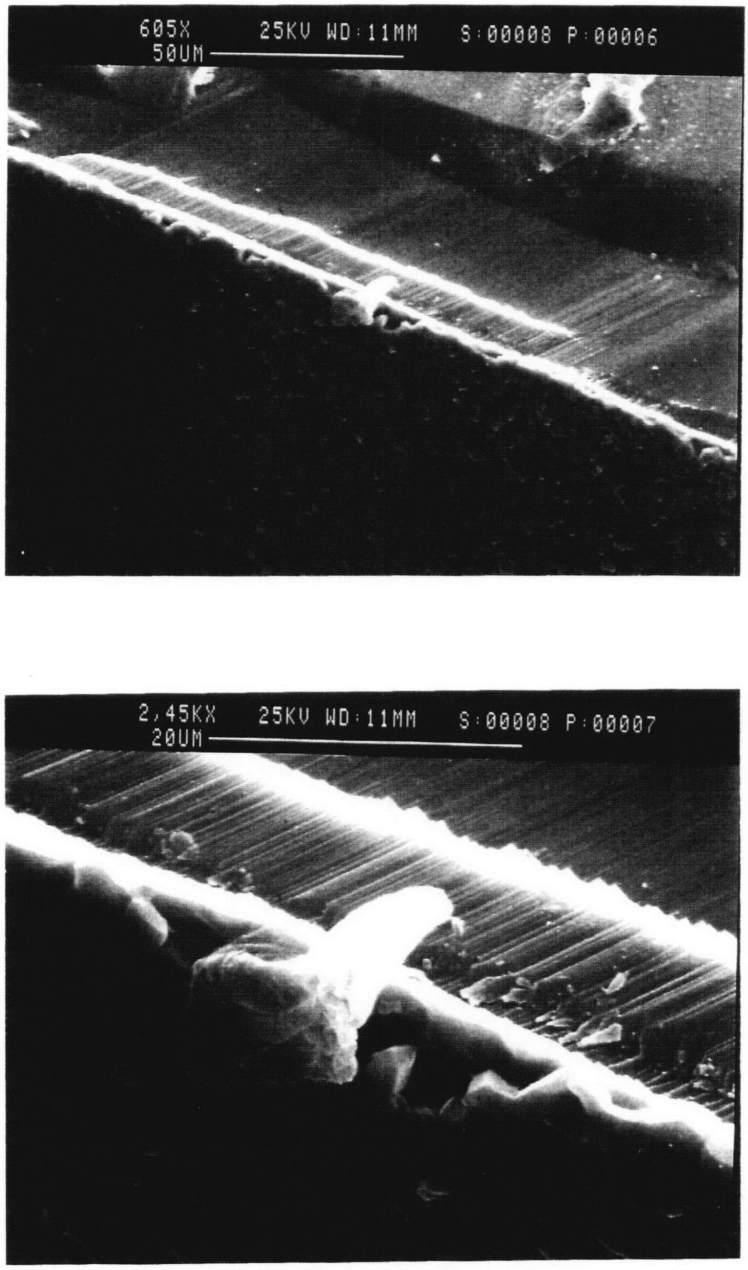

FIGURE 2.3.14a

LARGE SINGULAR GRAINS OF TiAl2O5. 1600C, 4 hrs.

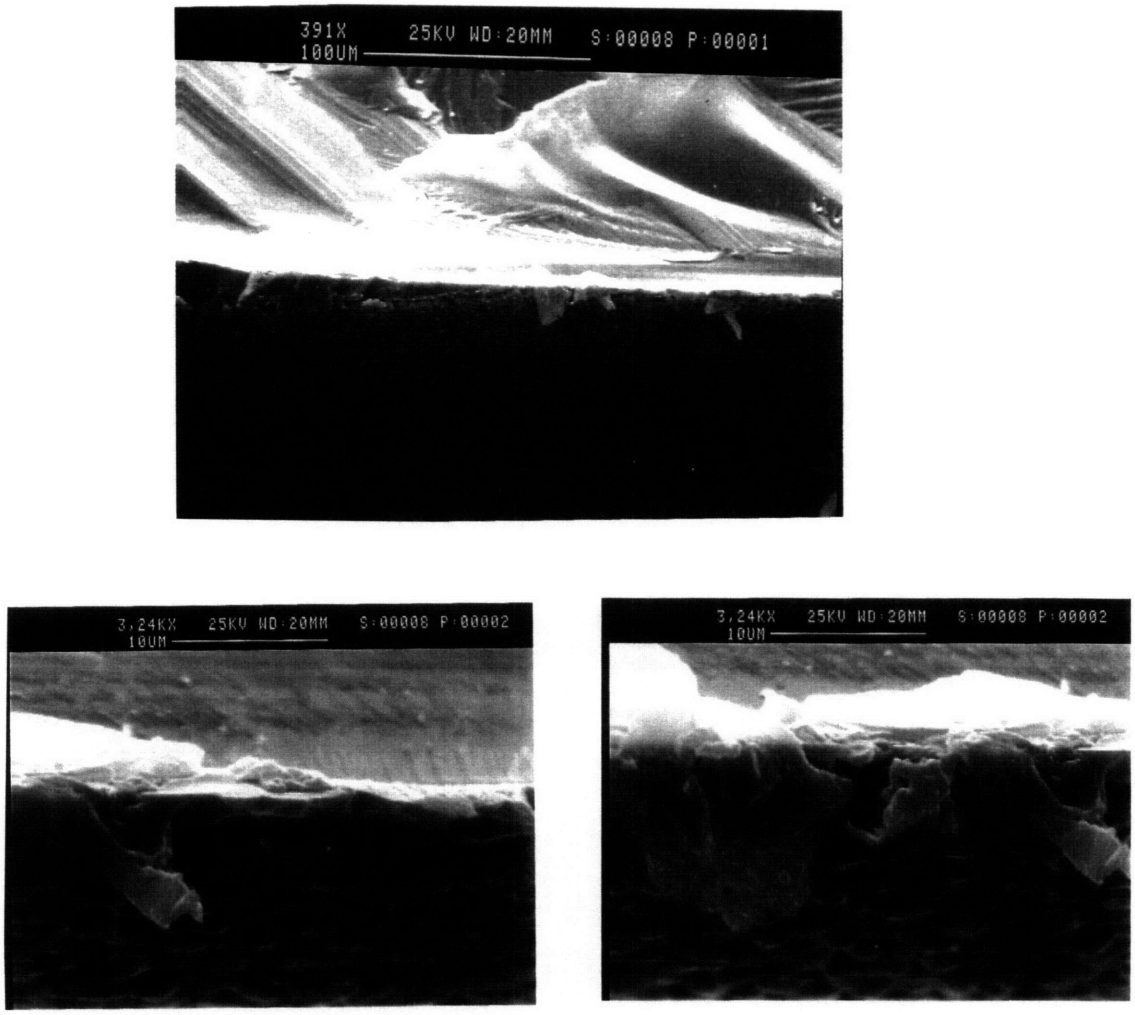

FIGURE 2.3.14b

LARGE SINGULAR GRAINS OF TiAl2O5. 1600C, 4 hrs.

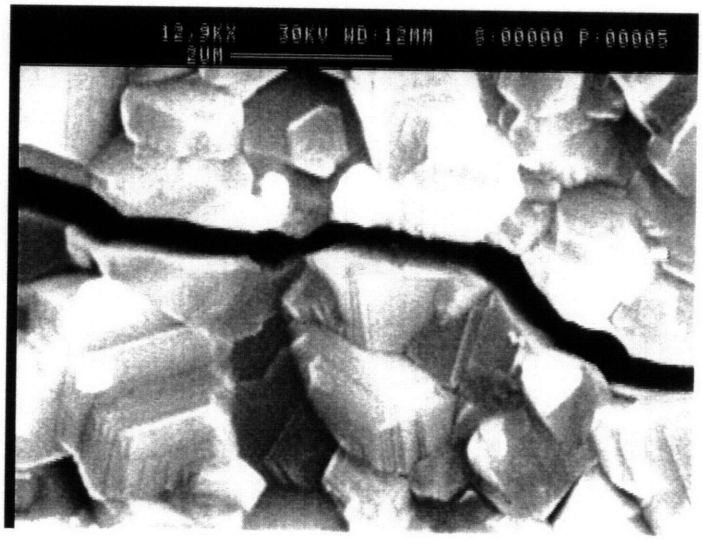

FIGURE 2.3.15

FRACTURE OF TiO_2 COATING

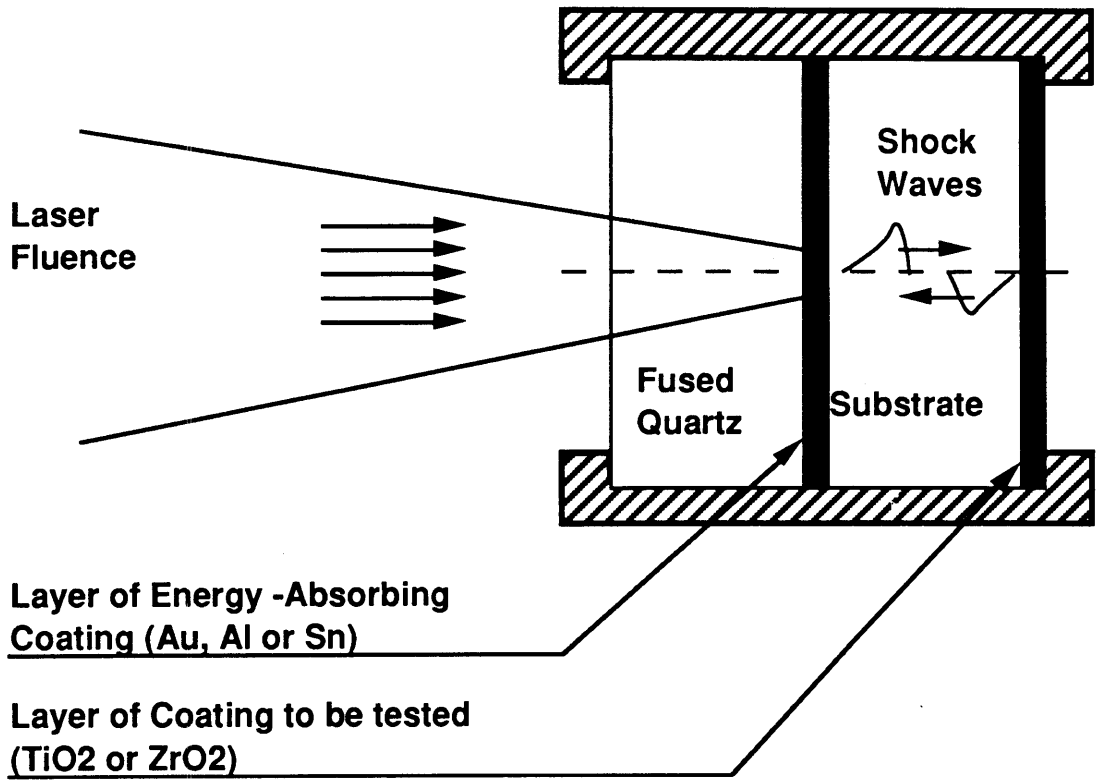

Figure 3.1 Schematic of a specimen in the special holder

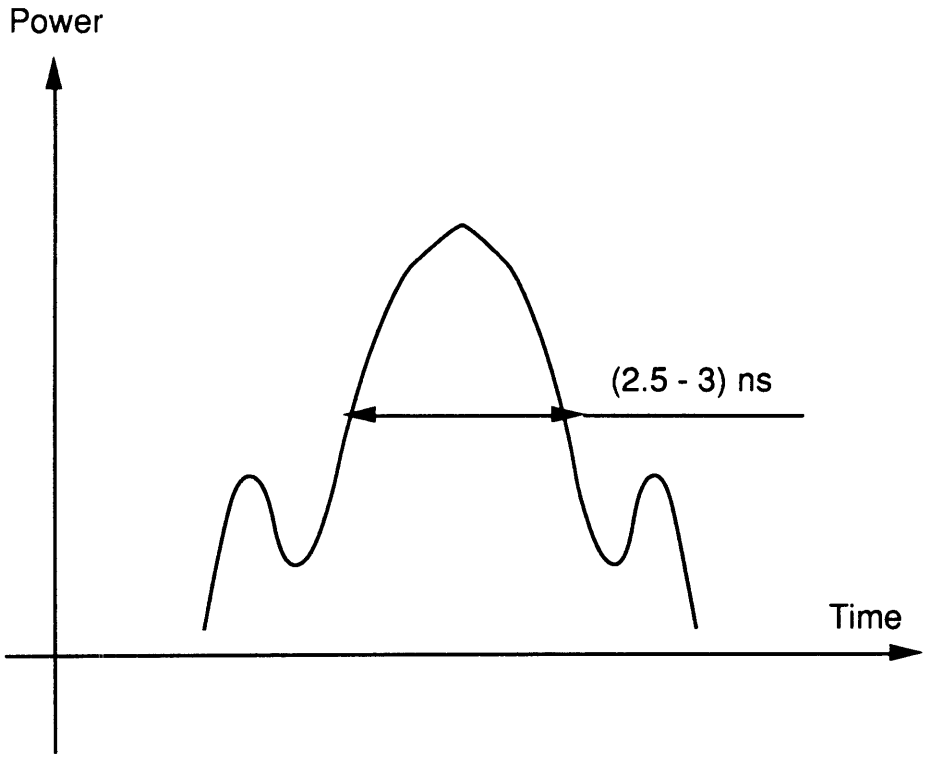

Figure 3.2 Temporal profile of a DSR-3 laser beam

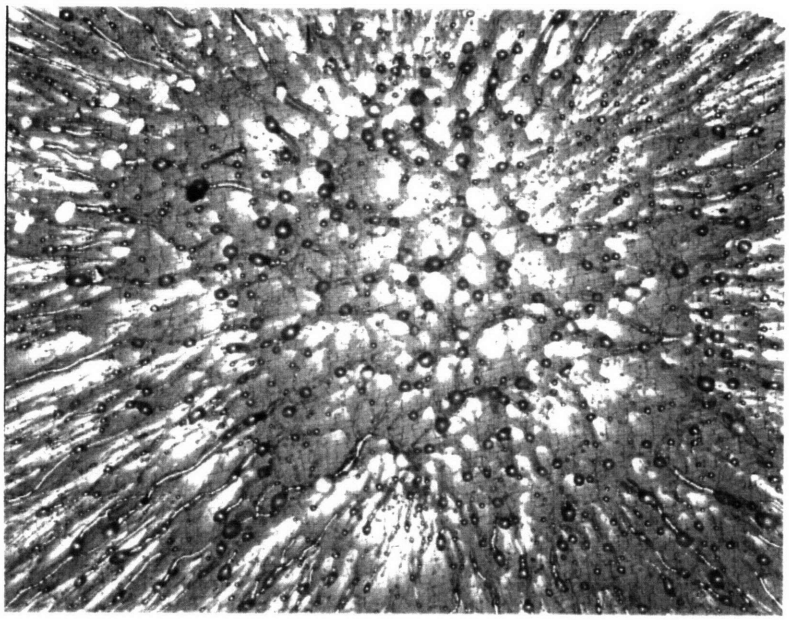

(a)

(b)

Figure 3.3 **(a) Crater in Au energy absorbing coating formed by a laser pulse; (b) Fragment showing a pattern of cracks in Al_2O_3 substrate.**

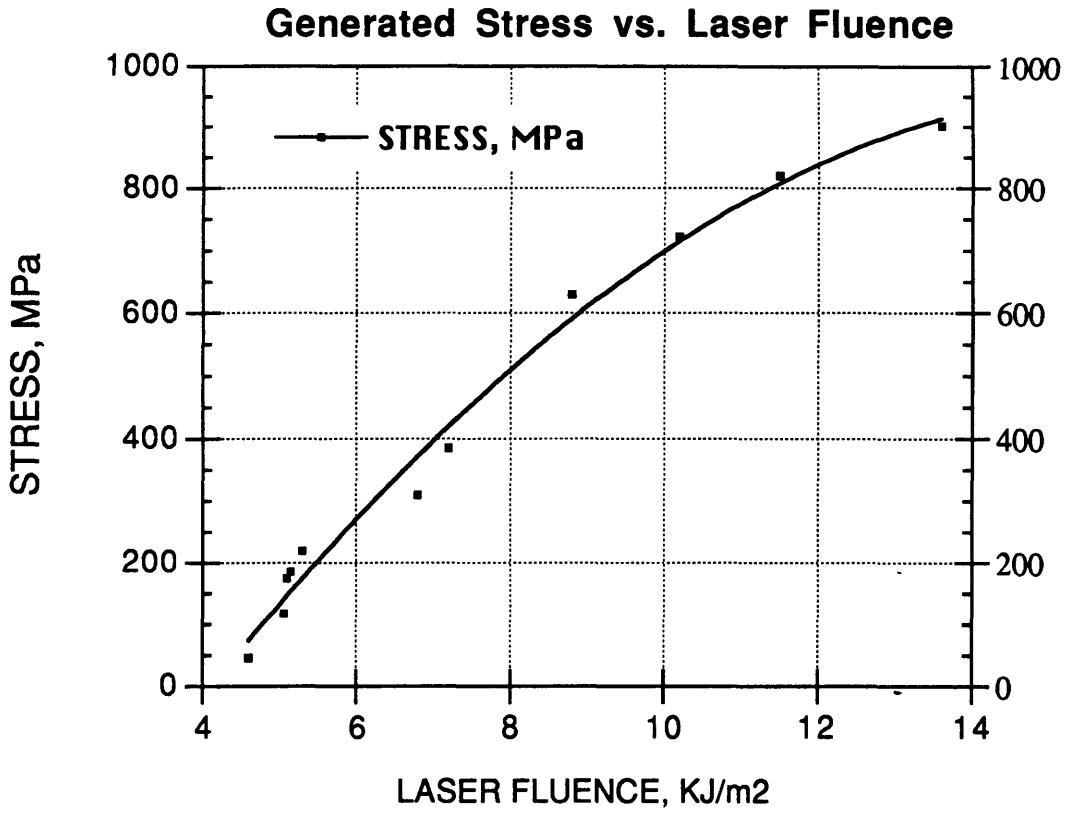

Figure 3.4 Stress generated in Sn energy absorbing coating vs. laser fluence

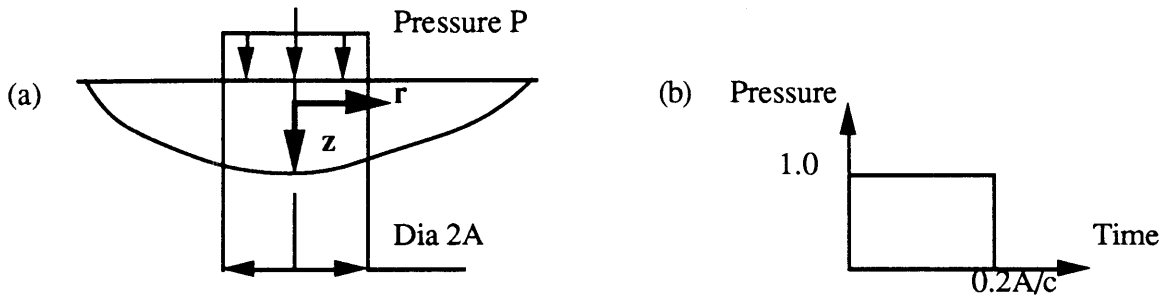

Figure 3.5 **(a) Spatial distribution and**

(b) temporal profile of the load used in the computer simulation.

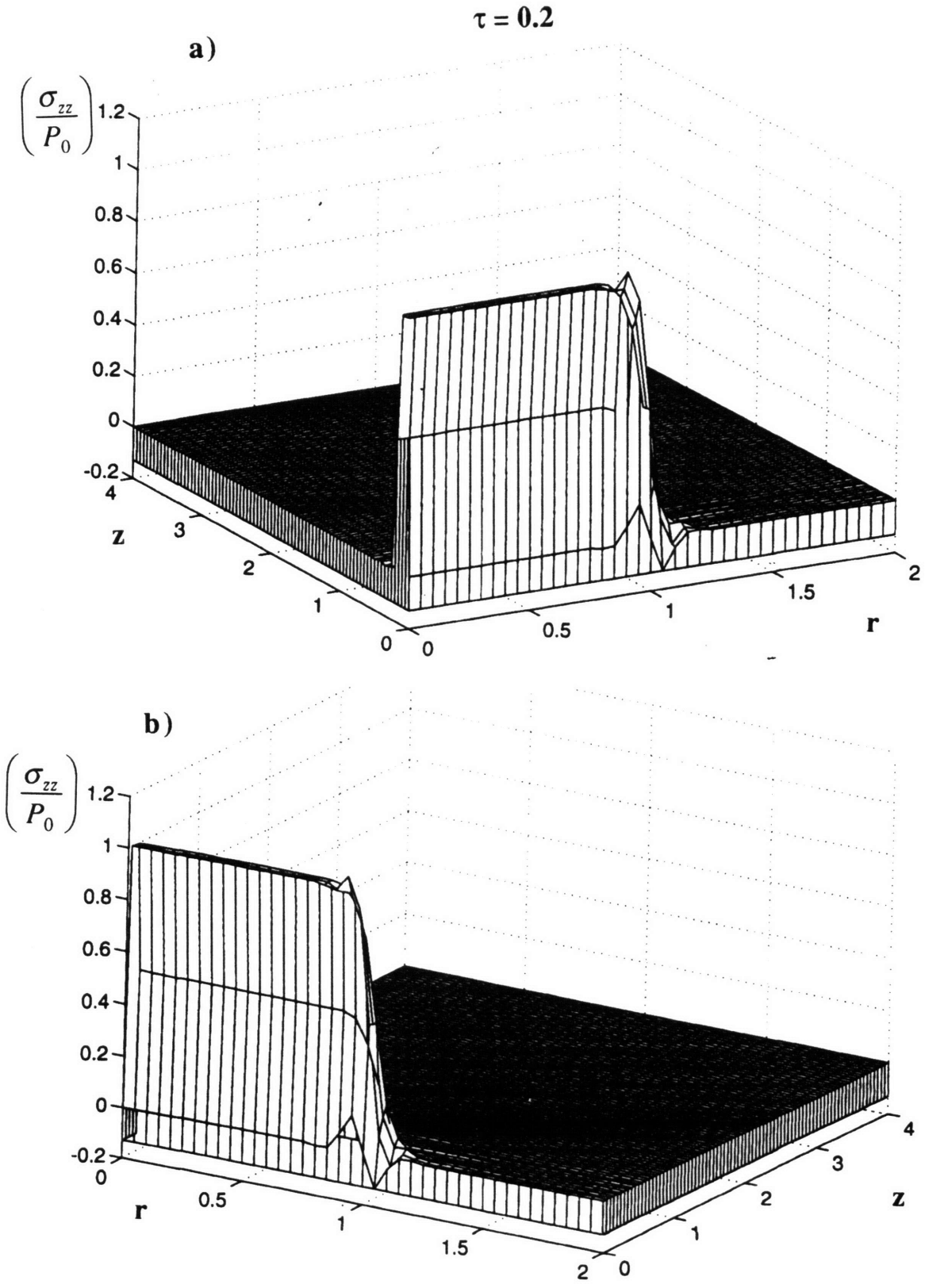

Figure 3.6. Stress distribution in the elastic wave at time $\tau = 0.2$

$\tau = 0.3$

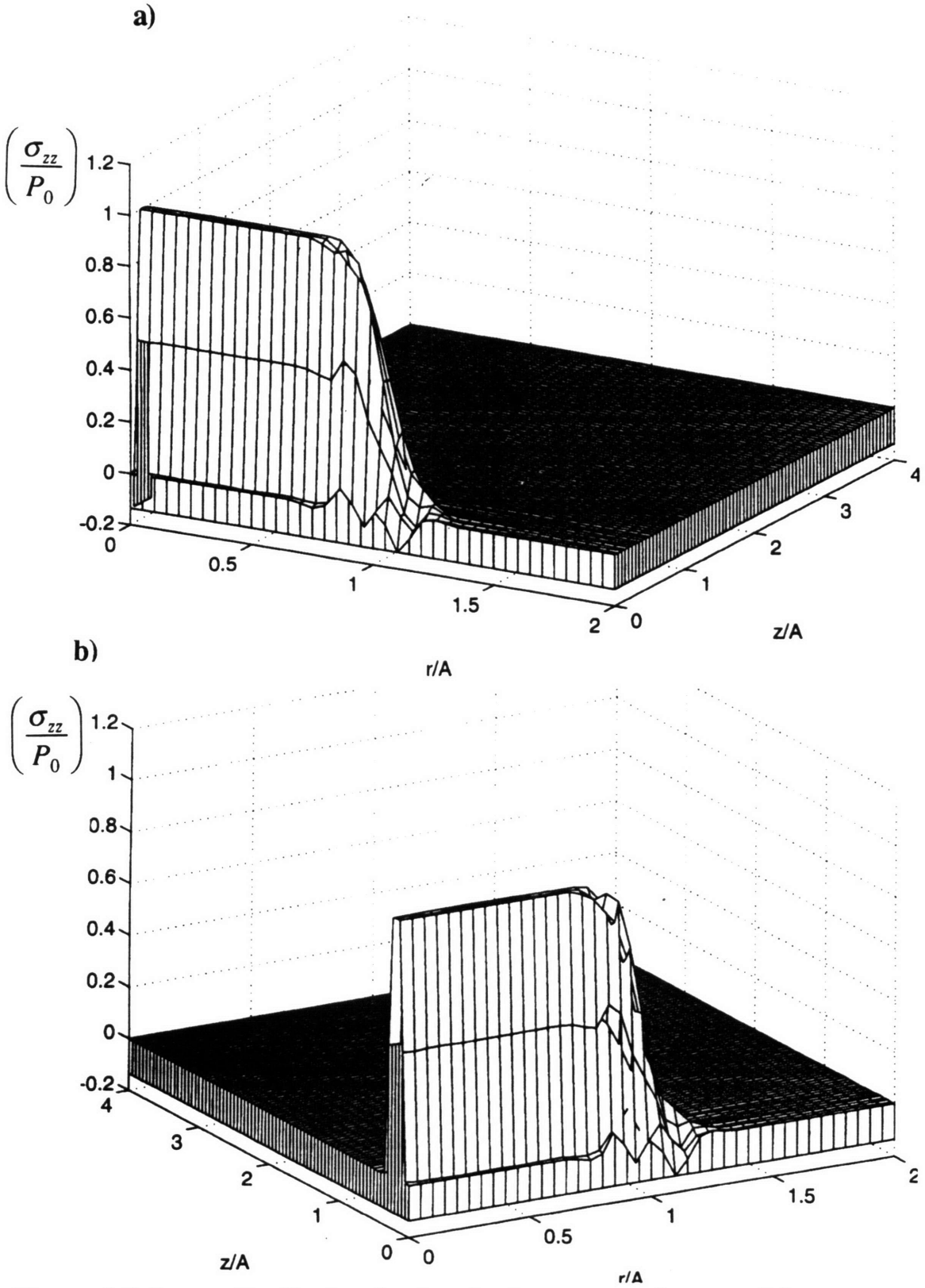

Figure 3.7 Stress distribution in the elastic wave at time $\tau = 0.3$

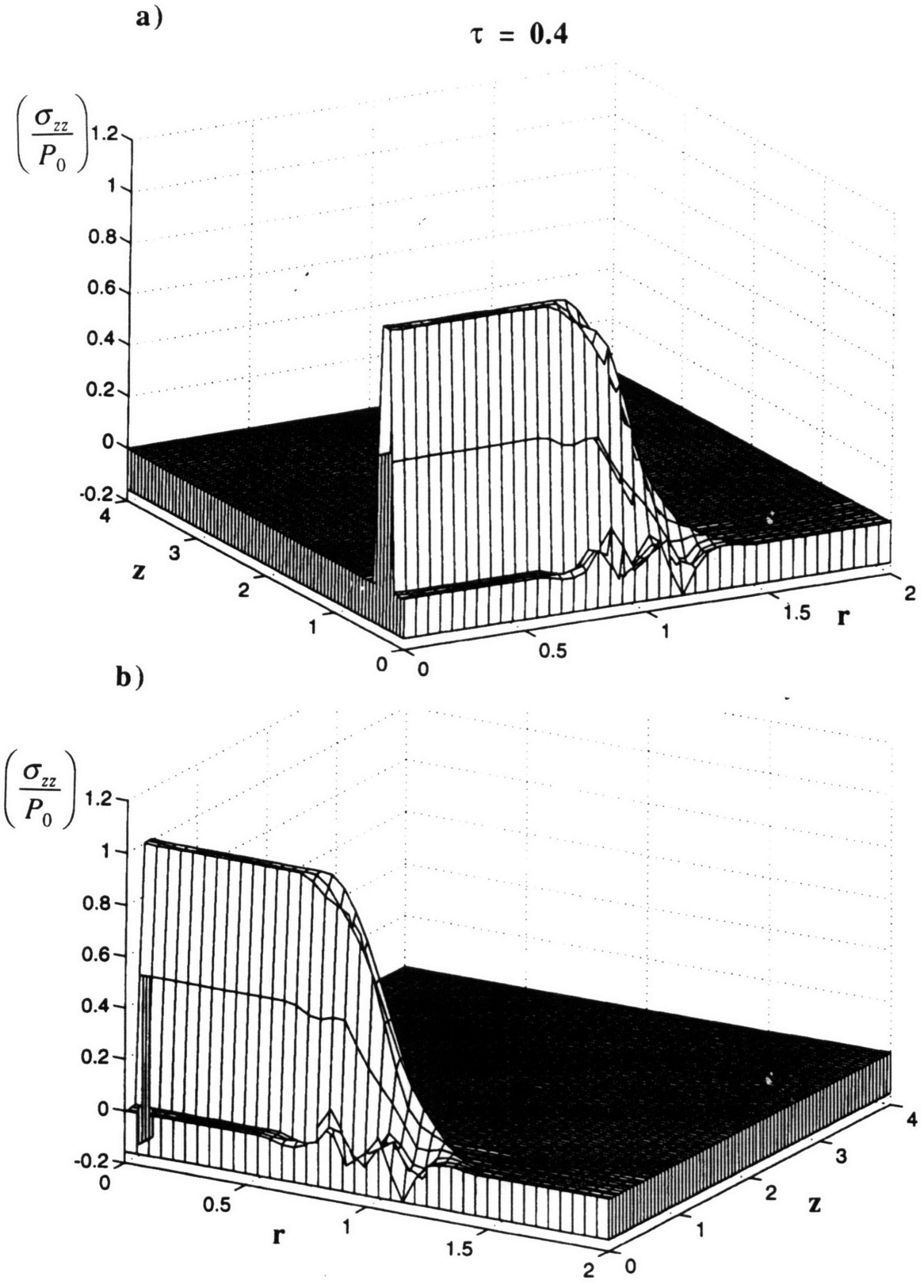

Figure 3.8 Stress distribution in the elastic wave at time τ = 0.4

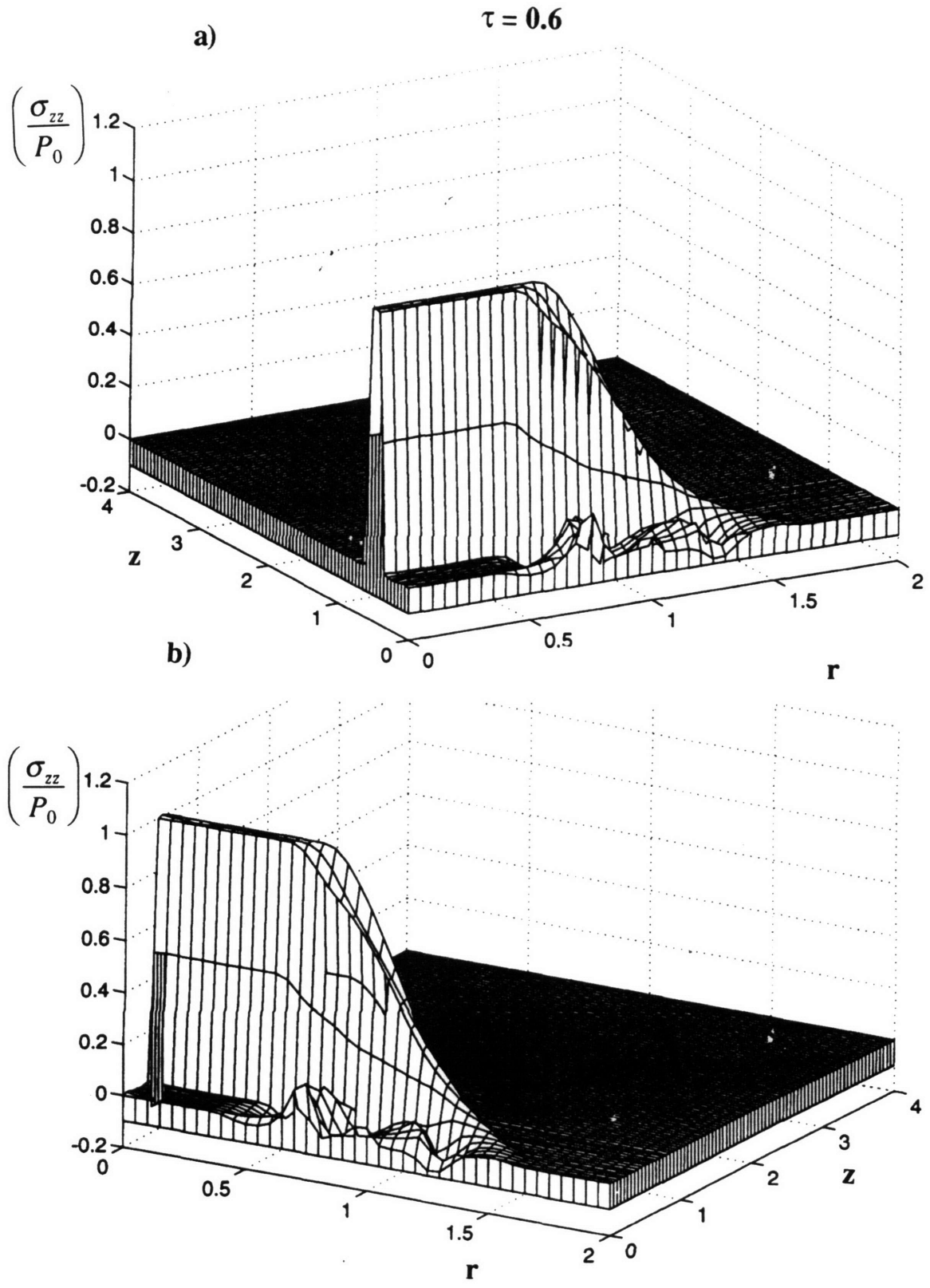

Figure 3.9 Stress distribution in the elastic wave at time t = 0.6

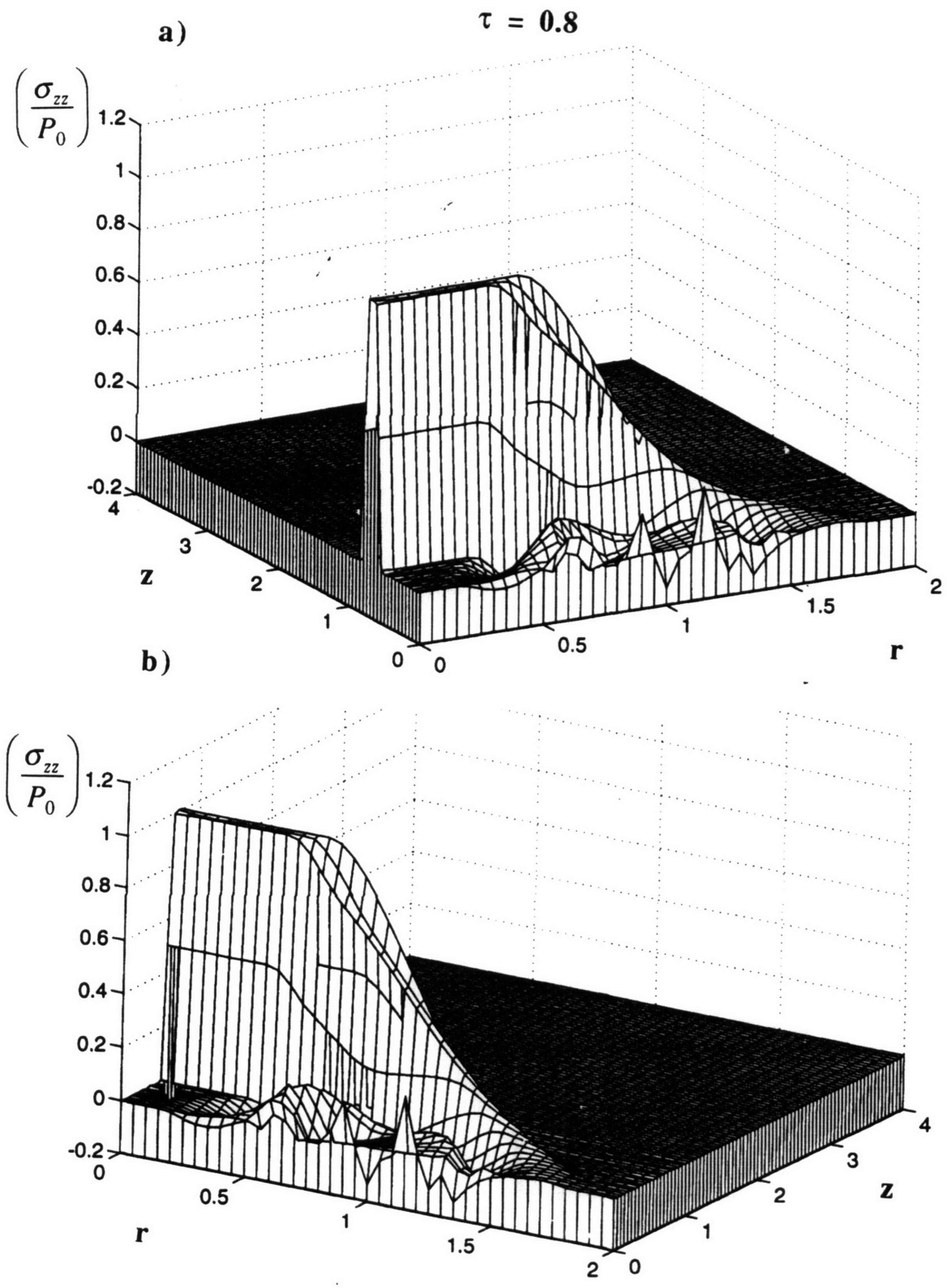

Figure 3.10 Stress distribution in the elastic wave at the time τ = 0.8

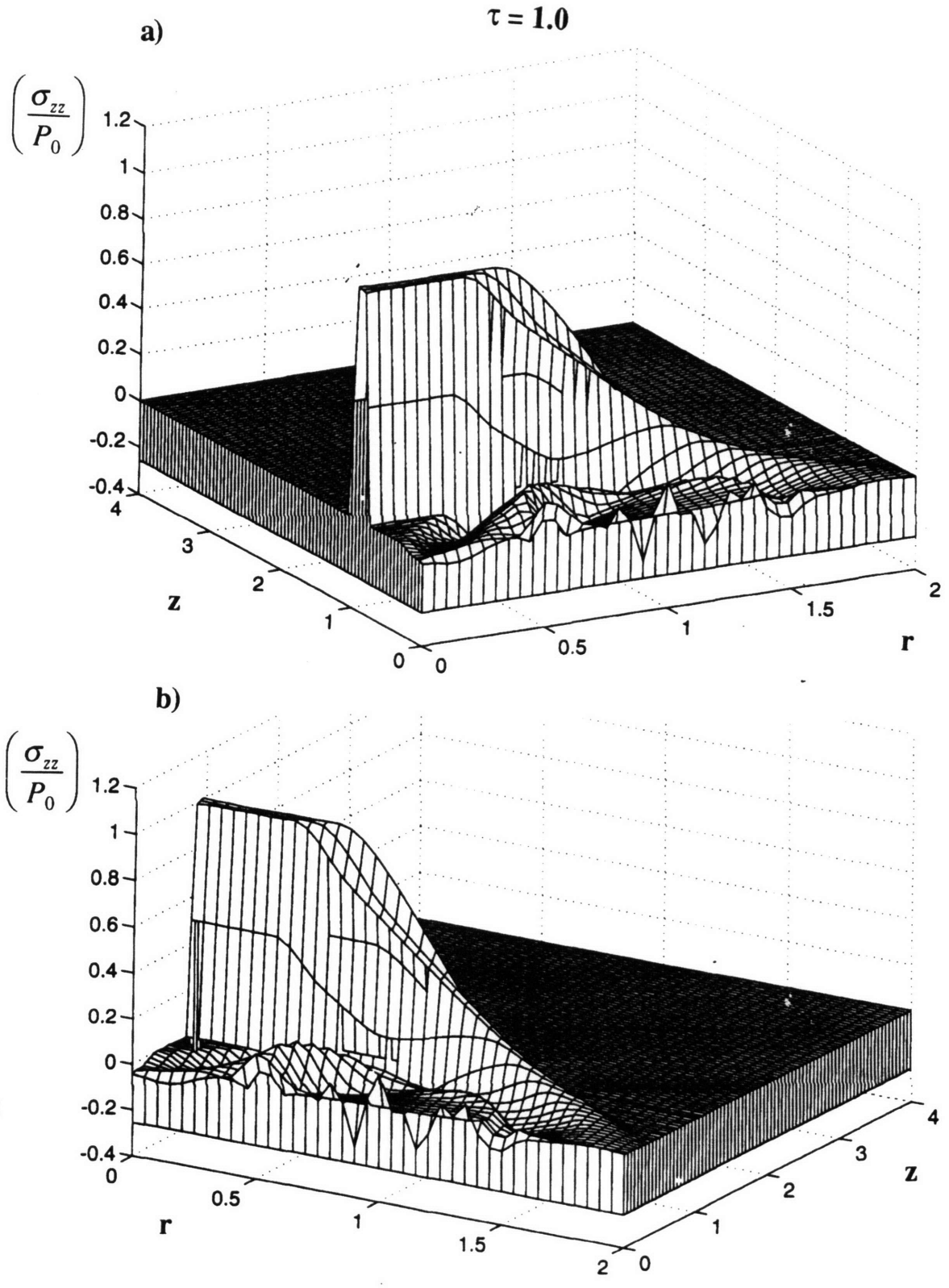

Figure 3.11. Stress distribution in the elastic wave at the time $\tau = 1.0$

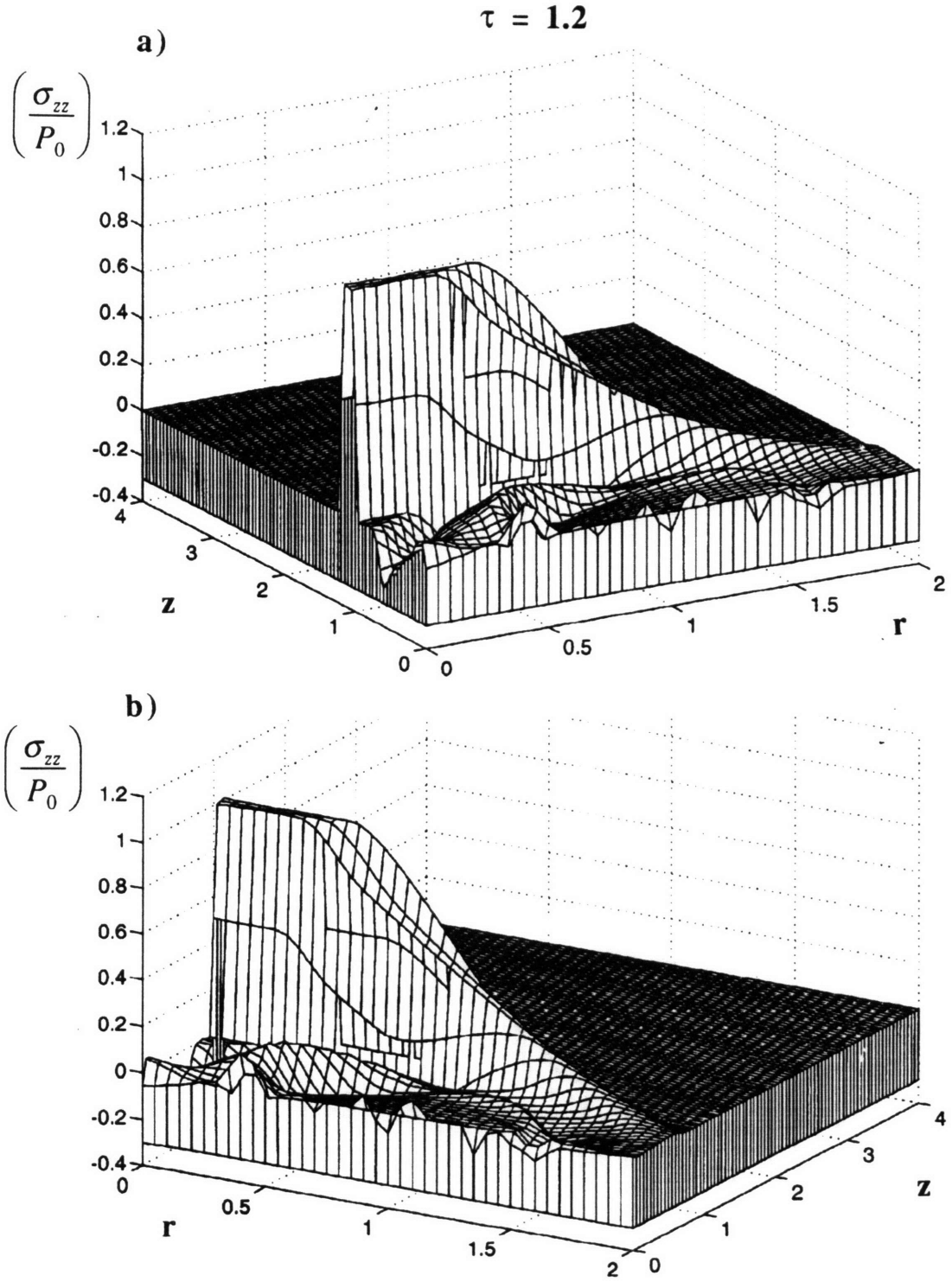

Figure 3.12 Stress distribution in the elastic wave at the time τ = 1.2

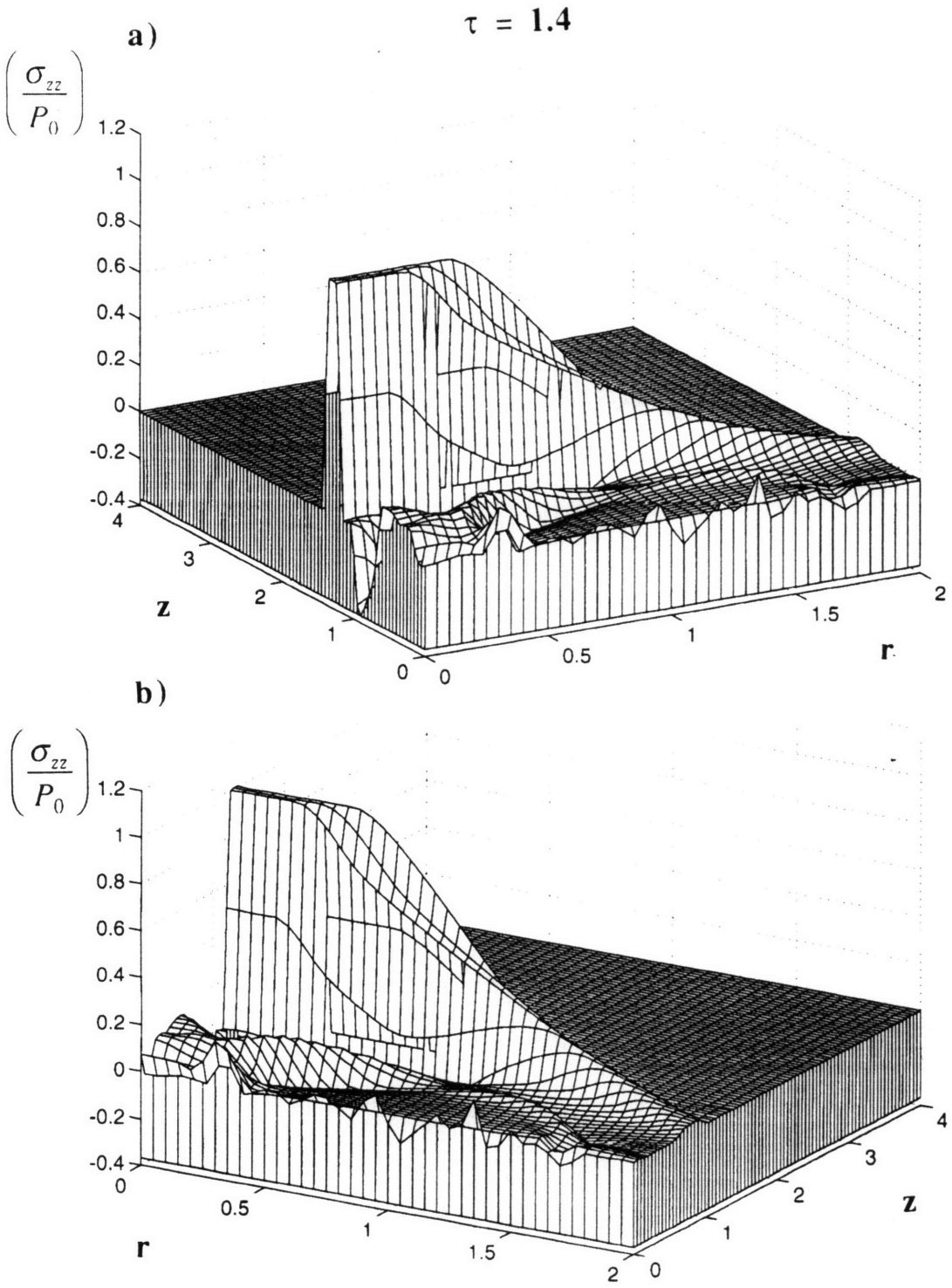

Figure 3.13 Stress distribution in the elastic wave at the time τ = 1.4

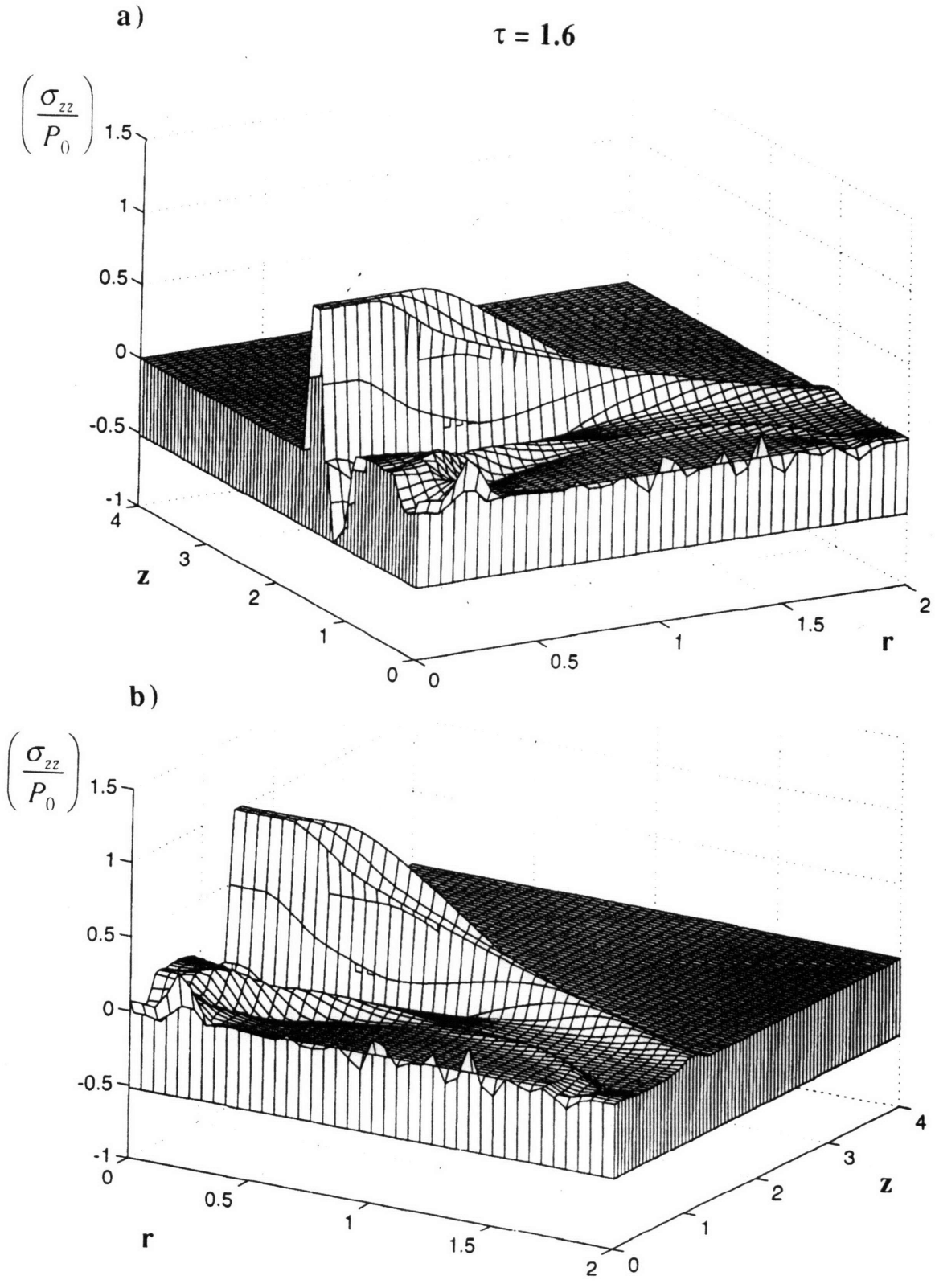

Figure 3.14 Stress distribution in the elastic wave at time τ = 1.6

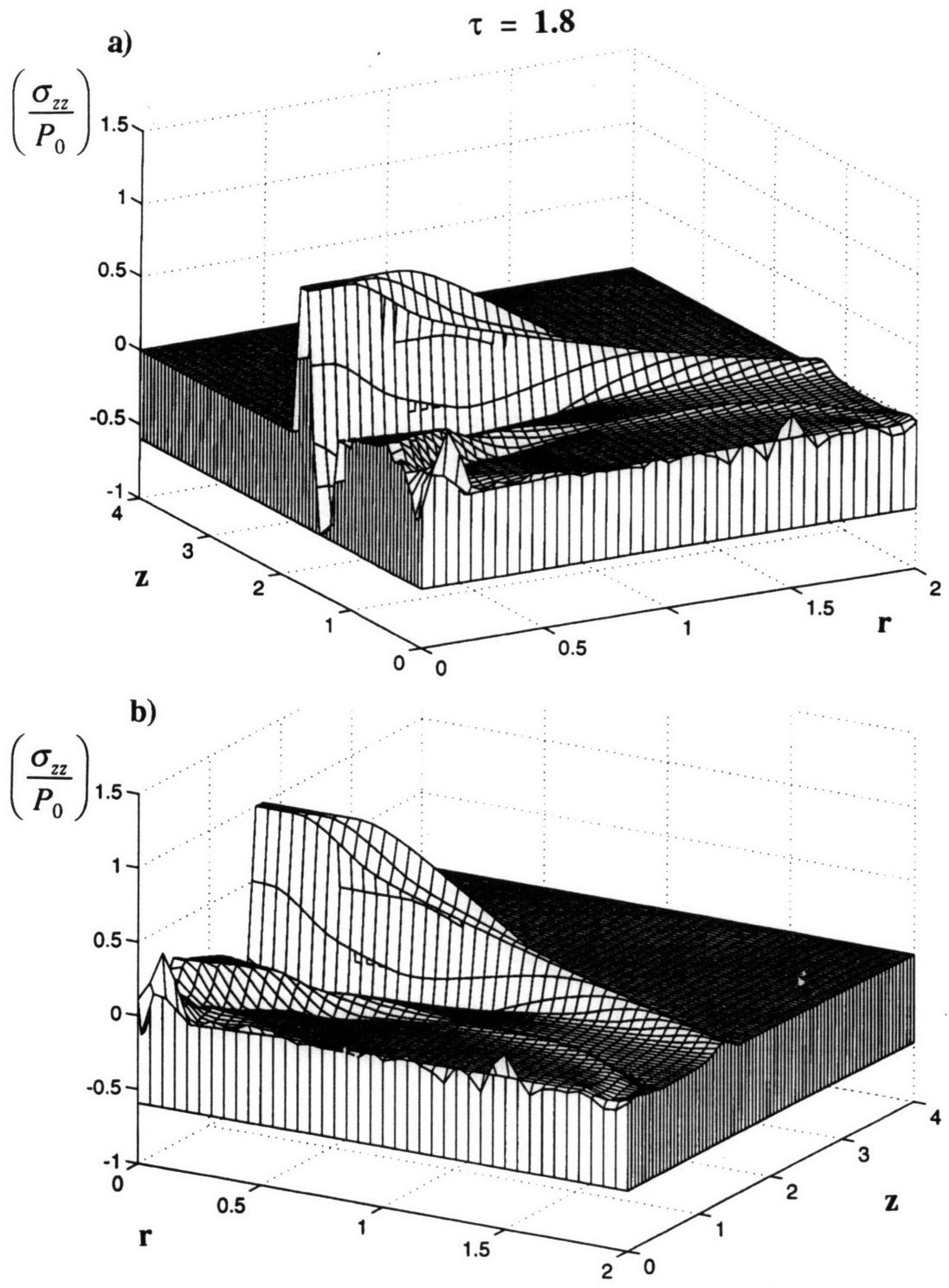

Figure 3.15 Stress distribution in the elastic wave at the time τ = 1.8

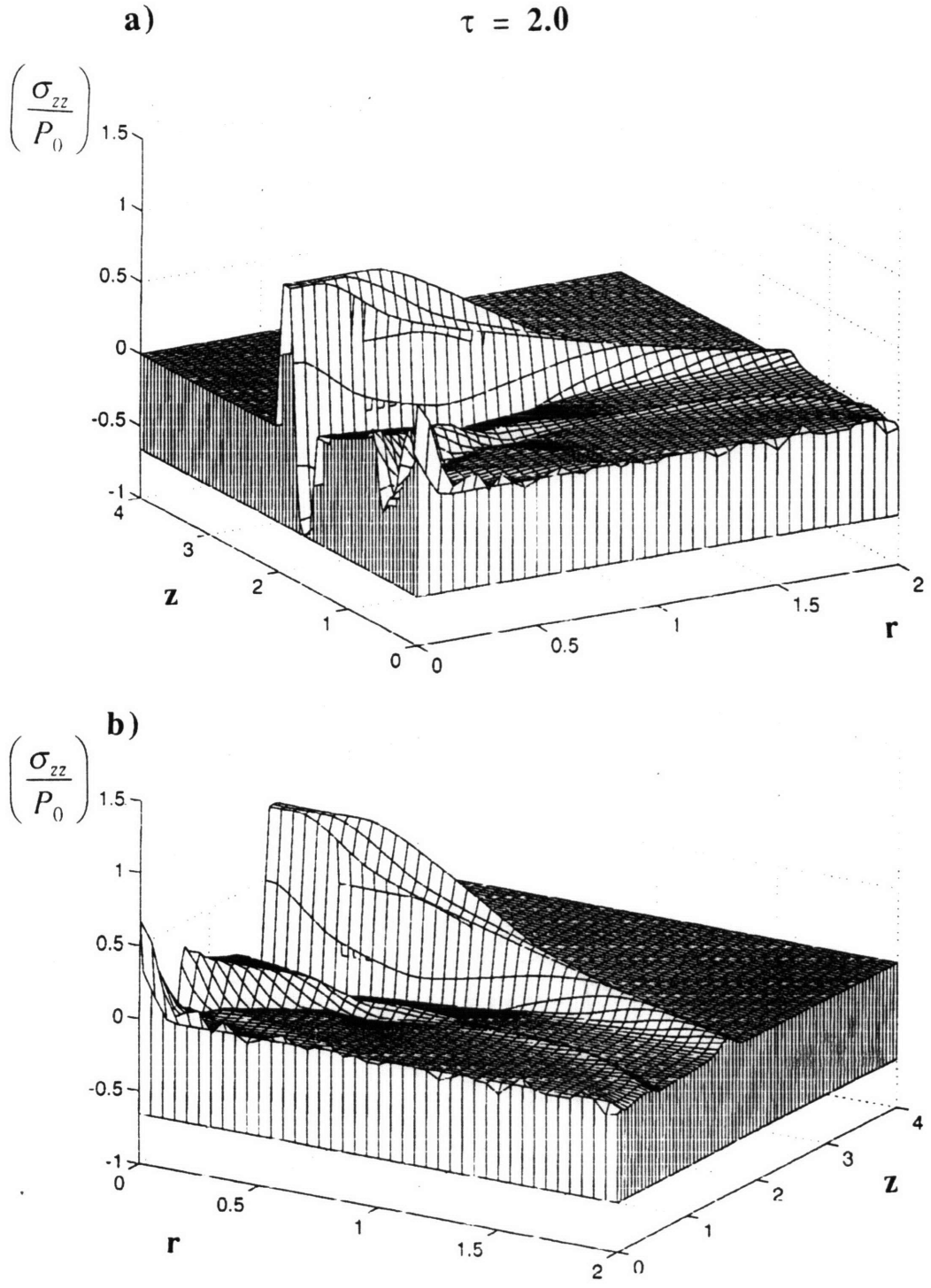

Figure 3.16 Stress distribution in the elastic wave at the time τ = 2.0

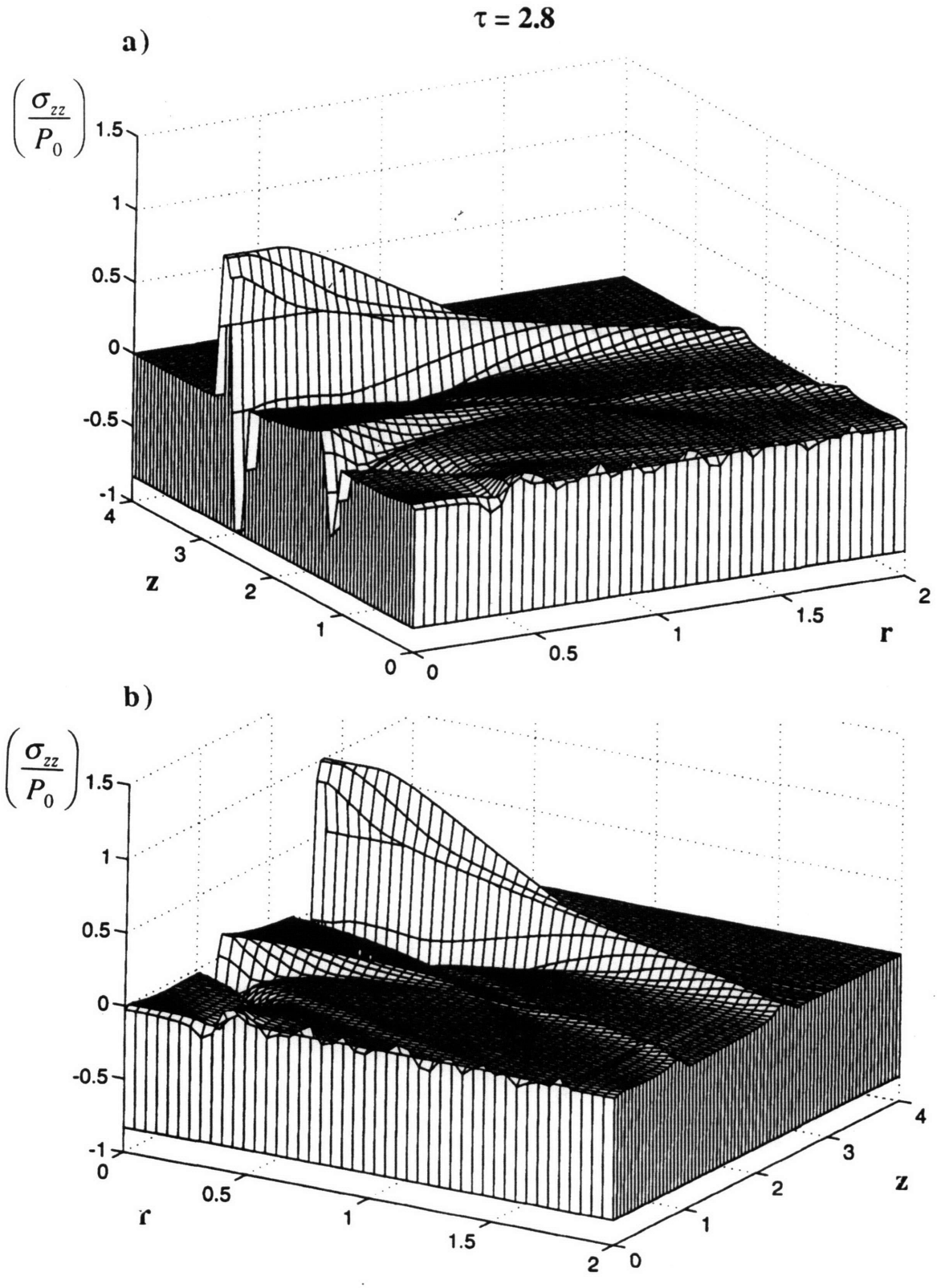

Figure 3.17 Stress distribution in the elastic wave at the time τ = 2.8

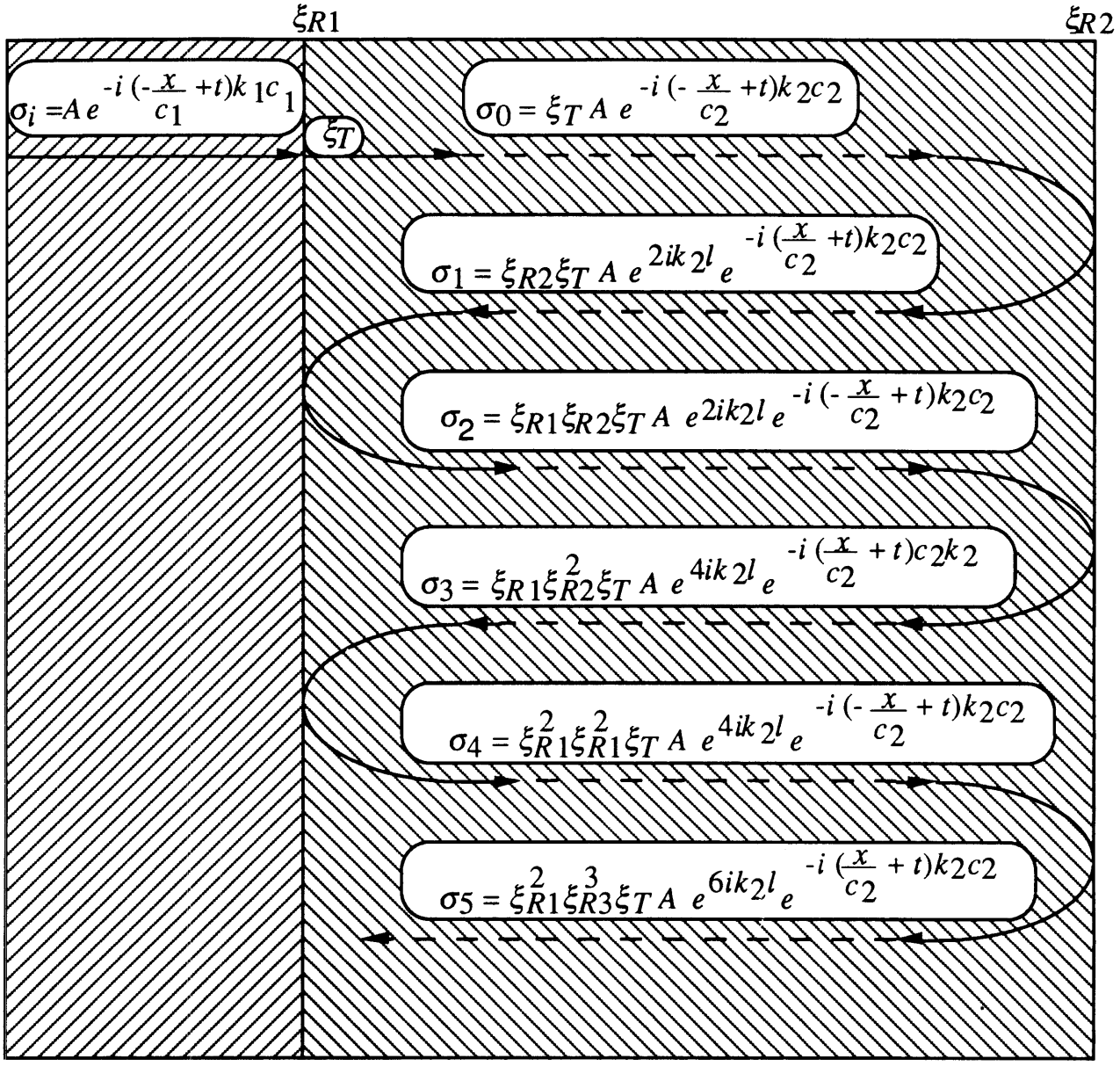

Figure 3.18 Elastic wave transmission and reflection at the bimaterial interface, formed by the substrate and the coating.

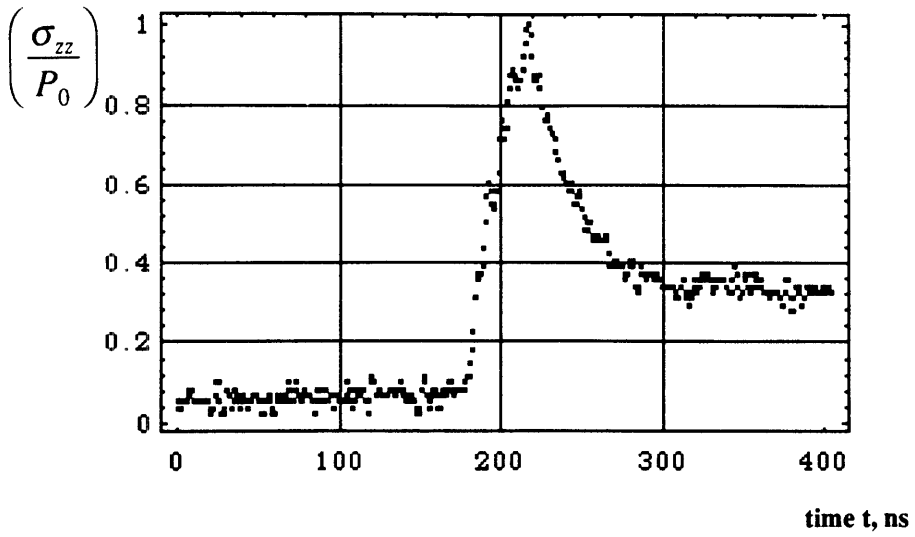

(a)

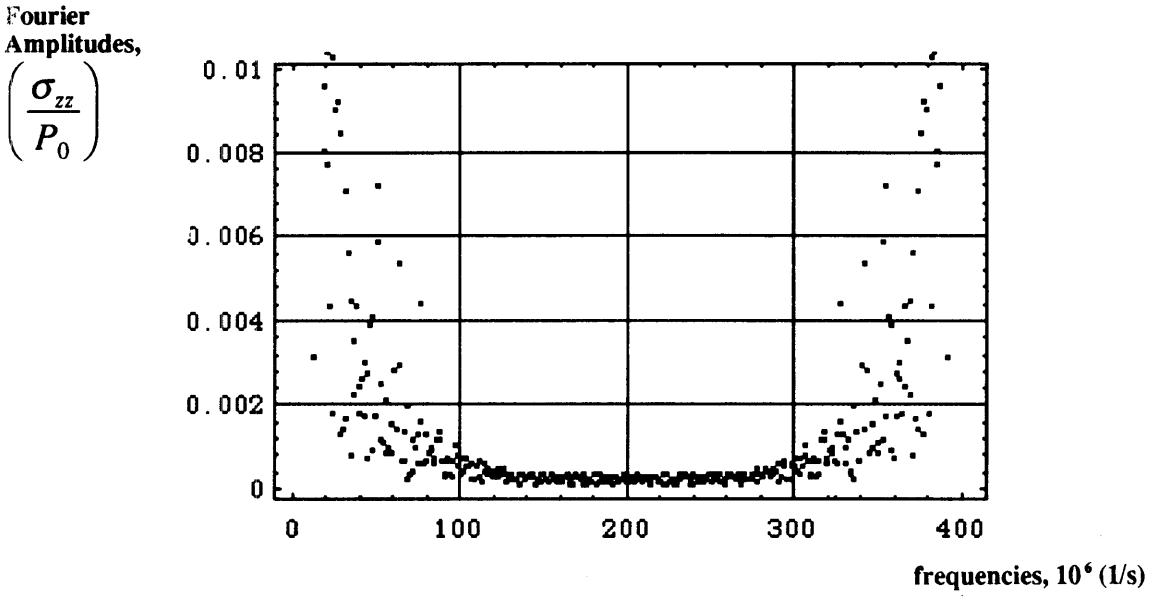

(b)

Figure 3.19 (a) Pressure pulse, acting on the energy absorbing interface, as recorded by piezoelectric transducer and

(b) its Spectrum.

Experiment was conducted under the conditions described in Section 3.6

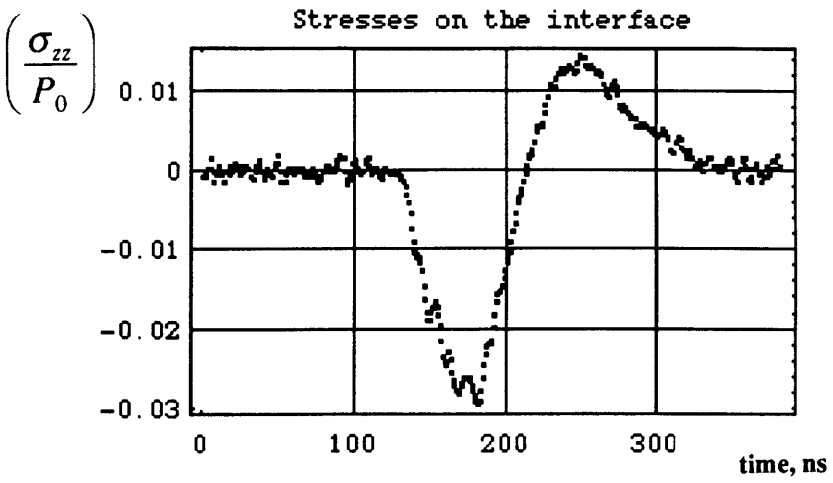

Figure 3.20,(a)

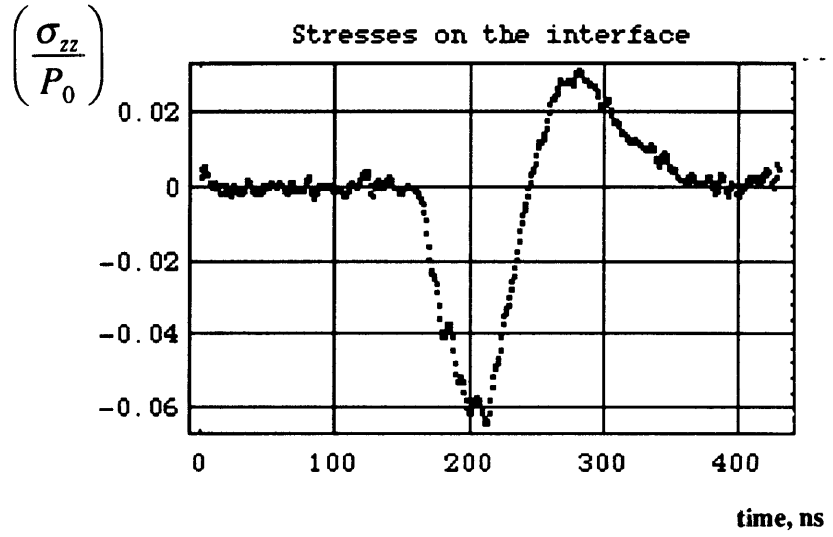

Figure 3.20,(b)

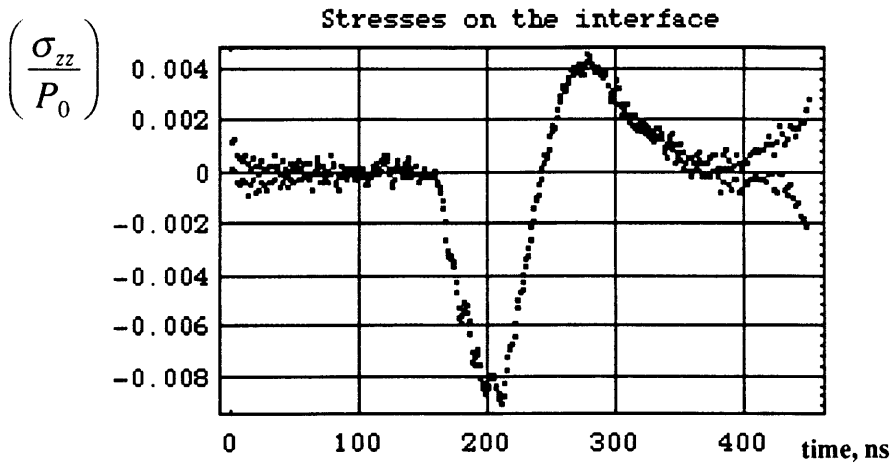

Figure 3.20, (c)

Figure 3.20 Stress histories on the bimaterial interface:

(a) identical elastic constants of the substrate and the coating;

(b) TiO_2 coating on Al_2O_3 substrate;

(c) ZrO_2 coating on Al_2O_3 substrate.

Properties of TiO_2, ZrO_2 and Al_2O_3, used in computation, are given in the Table 3.1, Chapter 3.

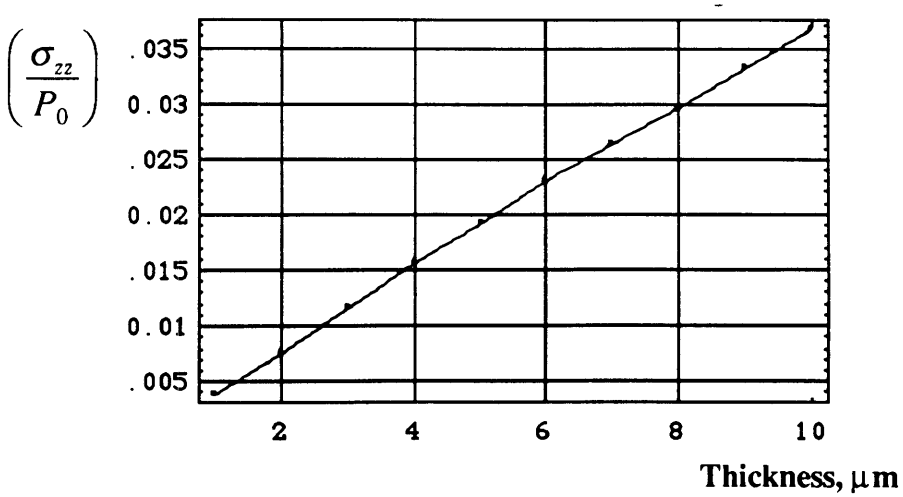

(a)

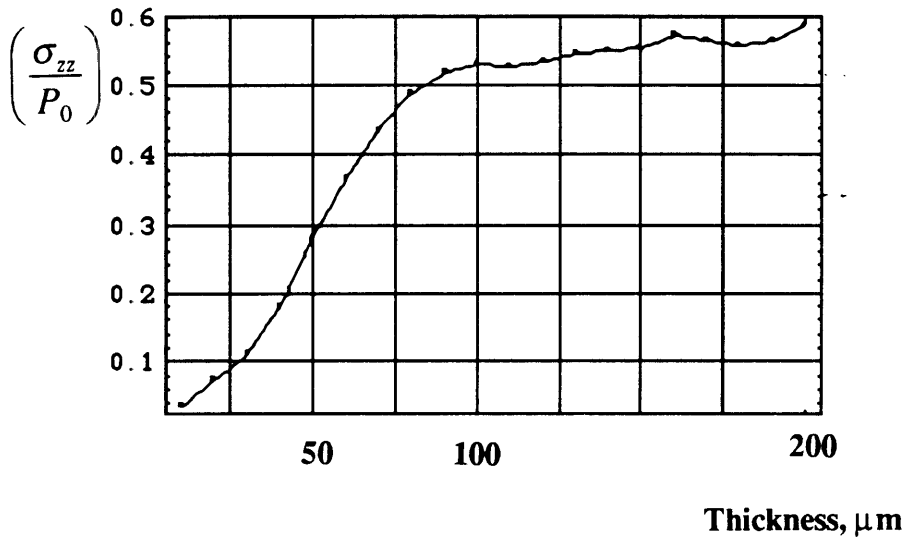

(b)

Figure 3.21 Dependence of maximum tensile stress amplitude across the bimaterial interface, normalized with respect to the pressure pulse P_0, on the coating thickness for C coating on Si substrate :

(a) for the coating thicknesses of up to 10μm and

(b) for the coating thicknesses of up to 200μm.

Properties of C and Si, used in this computation, are given in the Table 3.1, Chapter 3.

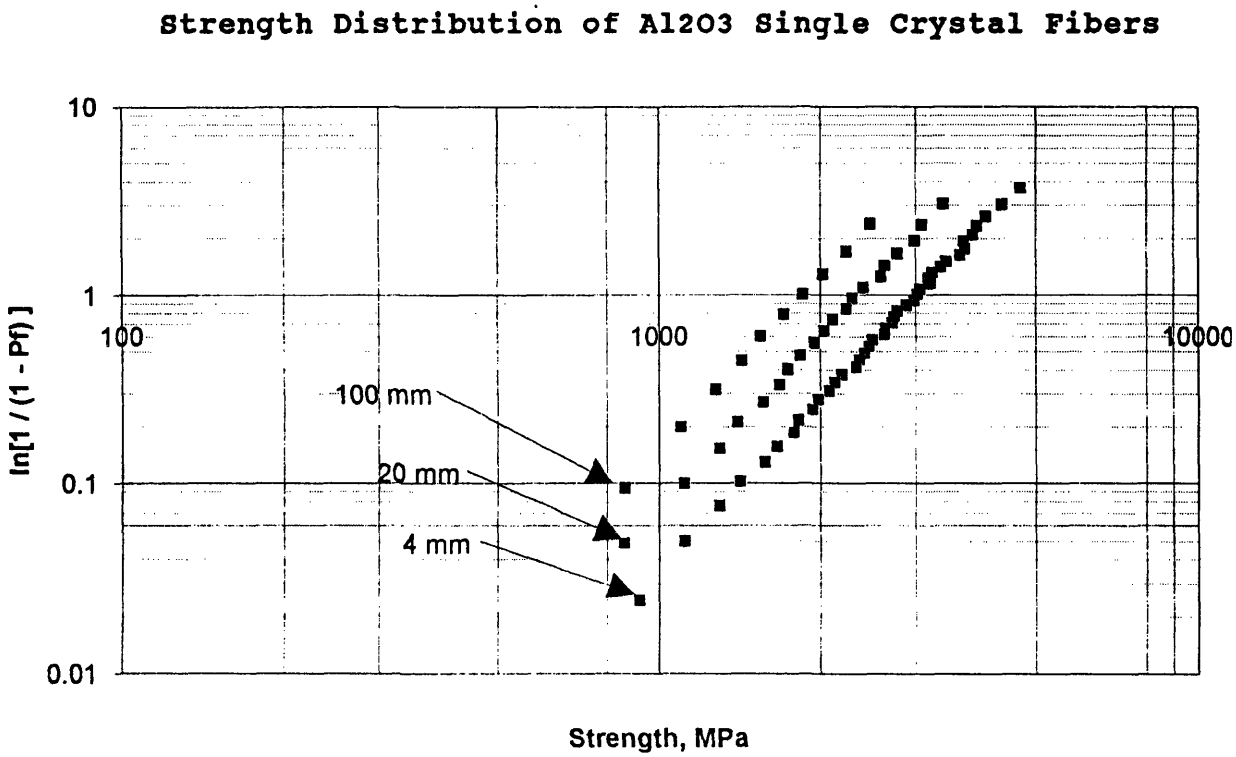

Figure 4.1. **Distribution of tensile strengths of Al_2O_3 single crystal fibers of 120 μm diameter, manufactured by Advanced Crystal Product Inc.**

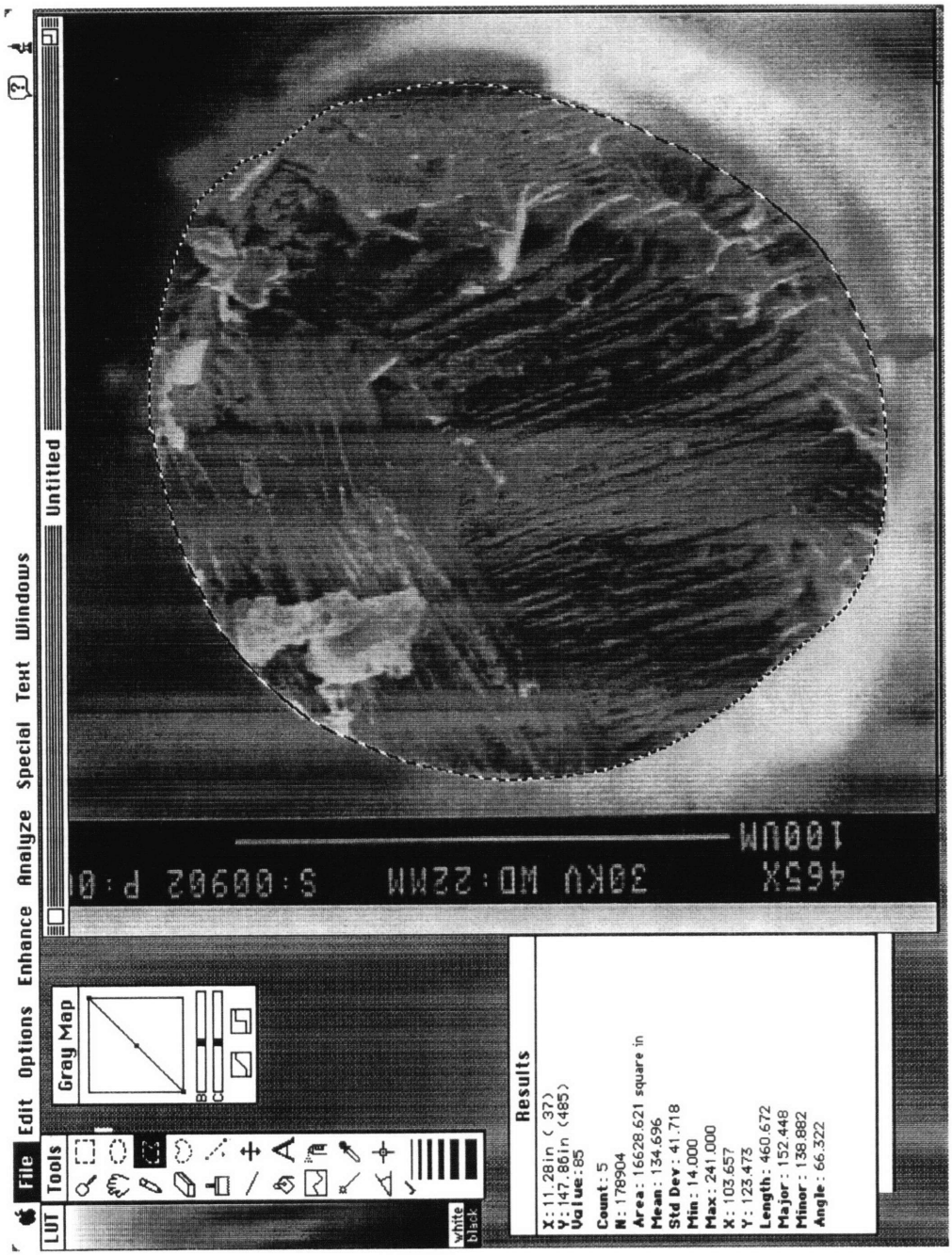

Figure 4.2 Fracture surface of Al_2O_3 single crystal fiber

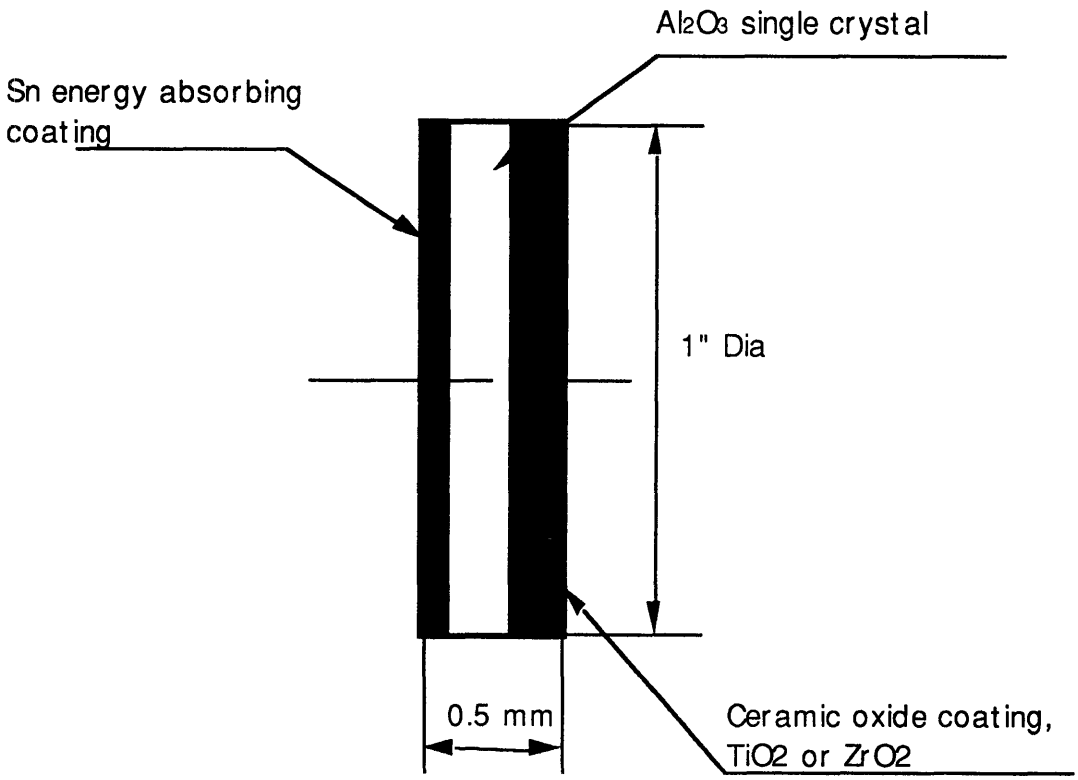

Figure 4. 3 Specimen used in laser spallation experiments

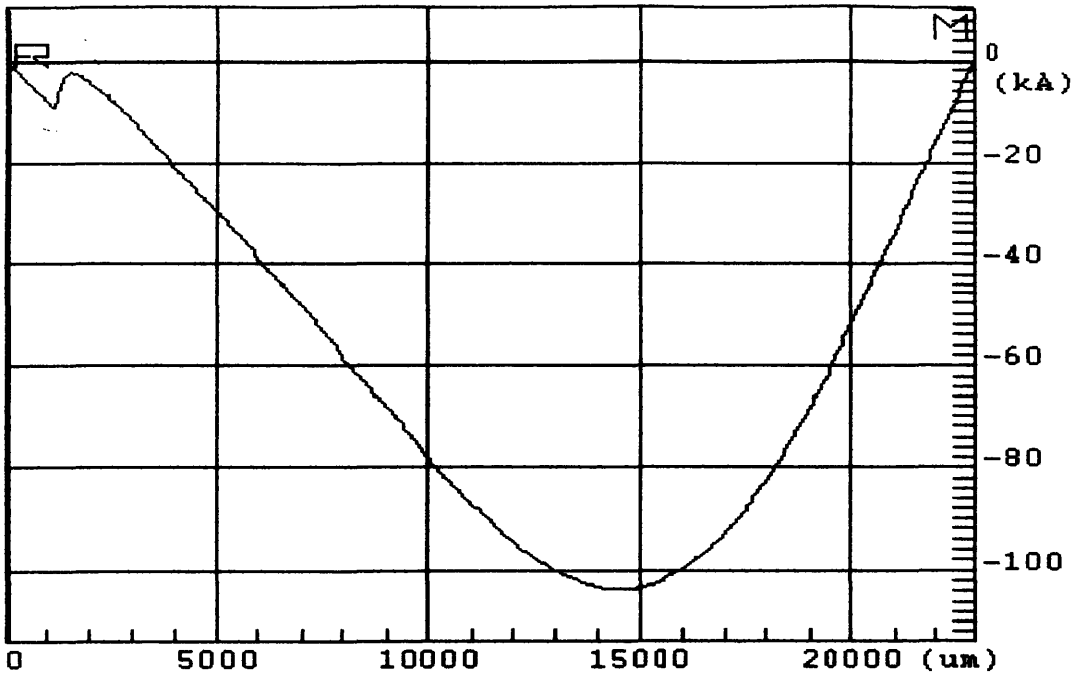


```
DEKTAK 8000  Version 2.03
PROG FILE NAME: LJHGA.mp
SCAN ROUTINE #: 1
TIME  OF  SCAN: 13:13:52 Sat Dec 12 1992
DATA FILE NAME: D:\DEKTAK\data\mapdata.001
Scan ID........ Zr
Location....... 82434um,171006um,110.814
Scan Length.... 22912um
Resolution..... 1.527 um/sample
Stylus Force... 80mg
R. Cursor...... -201A @ 50.00um
M. Cursor...... -103A @ 22900.00um
Vert. Delta.... 98A
Horiz. Delta... 22850.00um
Filters........ No
ANALYTIC FUNCTIONS:        R:um; M:um
```

Figure 4.4 Thickness profile of a Al_2O_3 wafer, coated with ZrO_2

ZrO_2, grid.

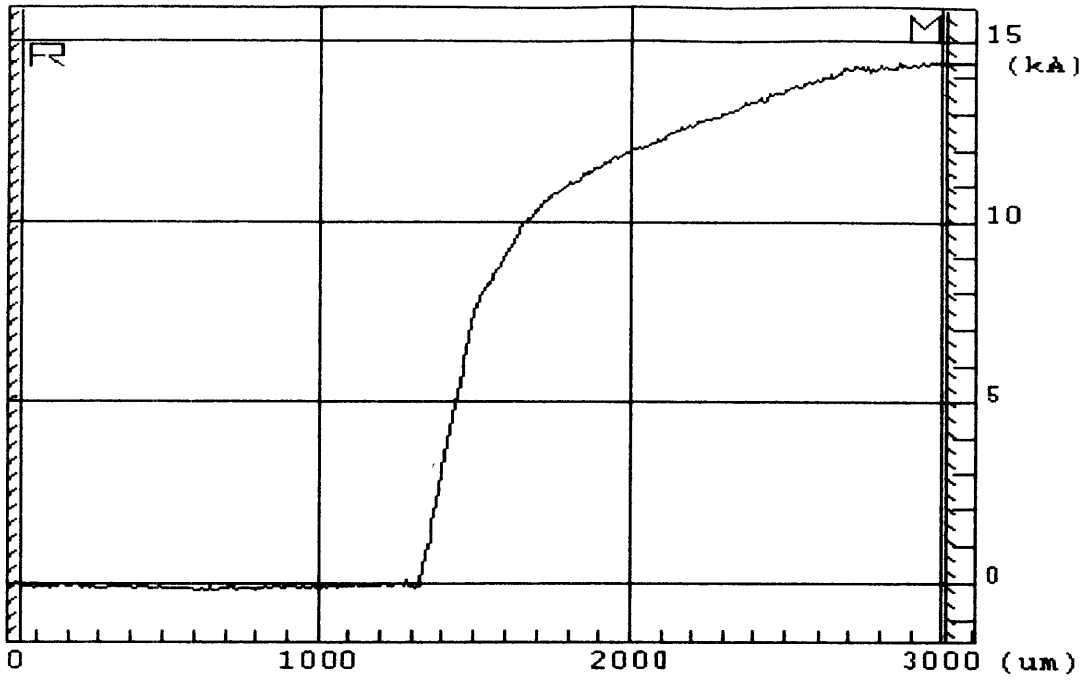

Al_2O_3 ZrO_2

```
DEKTAK 8000  Version 2.03
PROG FILE NAME:  LJHGA.mp
SCAN ROUTINE #:  1
TIME  OF  SCAN:  12:03:33 Sat Dec 12 1992
DATA FILE NAME:  d:\dektak\data\mapdata.001
Scan ID.........  4
Location........  81396um,169664um,  90.040
Scan Length.....  3108um
Resolution......  0.207 um/sample
Stylus Force....  100mg
R. Cursor.......  -15A @ 50.00um
M. Cursor.......  14422A @ 3021.14um
Vert. Delta.....  14437A
Horiz. Delta....  2971.14um
Filters.........  No
ANALYTIC FUNCTIONS:        R:um; M:um
```

Figure 4.5 Results of thickness measurements of a step, formed by ZrO_2 coating on Al_2O_3 substrate

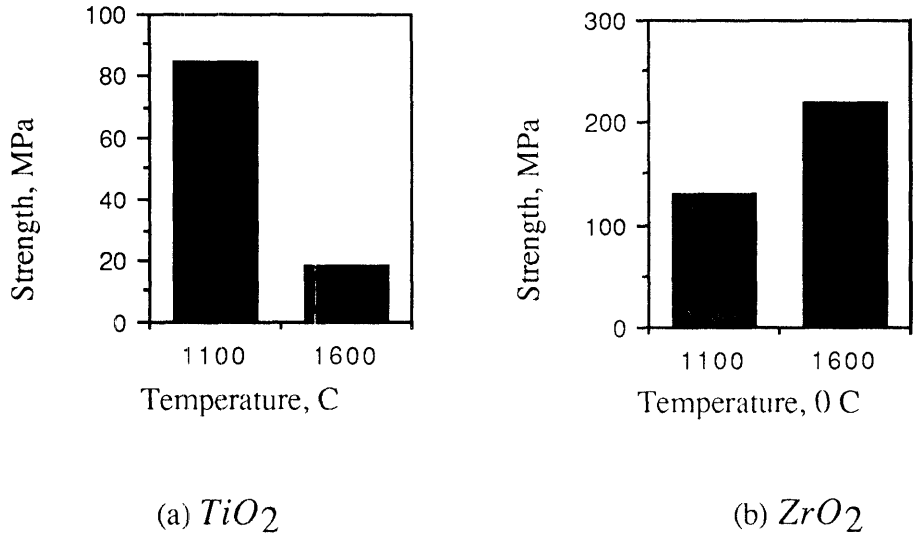

(a) TiO_2 (b) ZrO_2

Figure 4.6 Adhesive strengths of (a)TiO_2 and (b)ZrO_2 coatings on Al_2O_3 substrates vs. oxidation temperature.

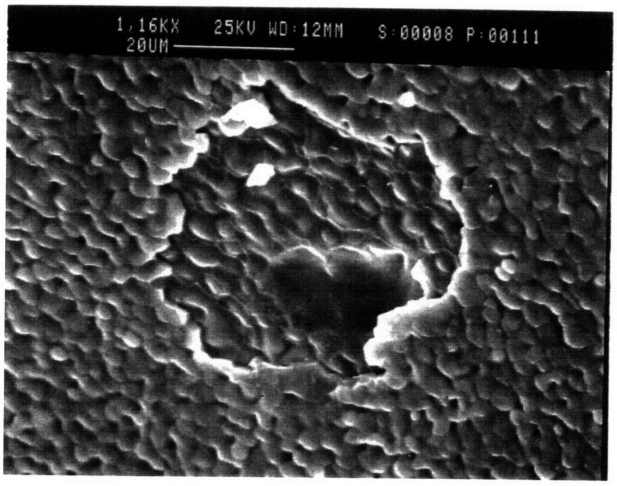

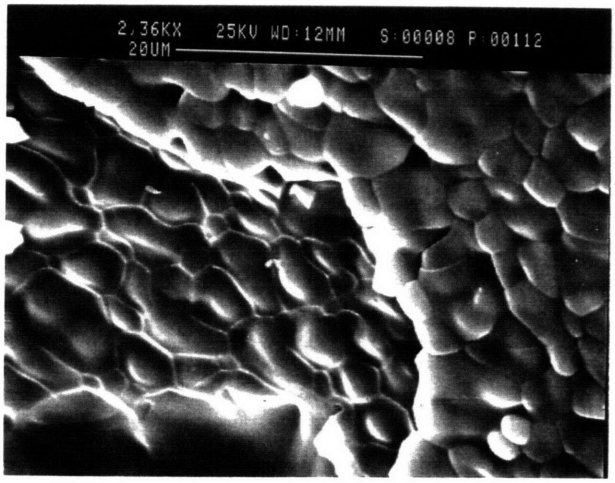

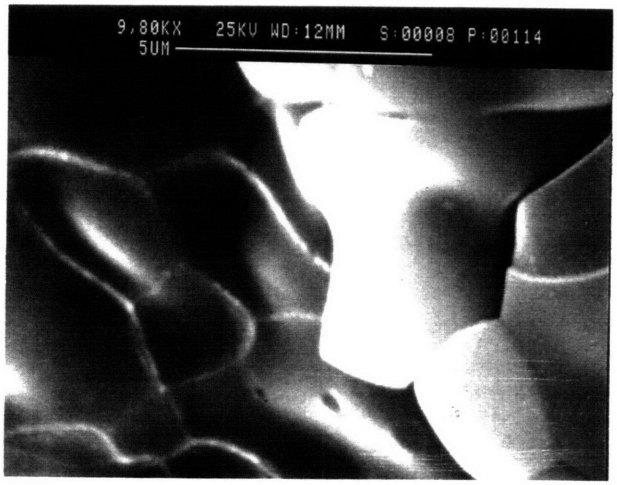

Figure 4.7a

SPALLED AREA OF TiO_2 COATING ON Al_2O_3 SUBSTRATE

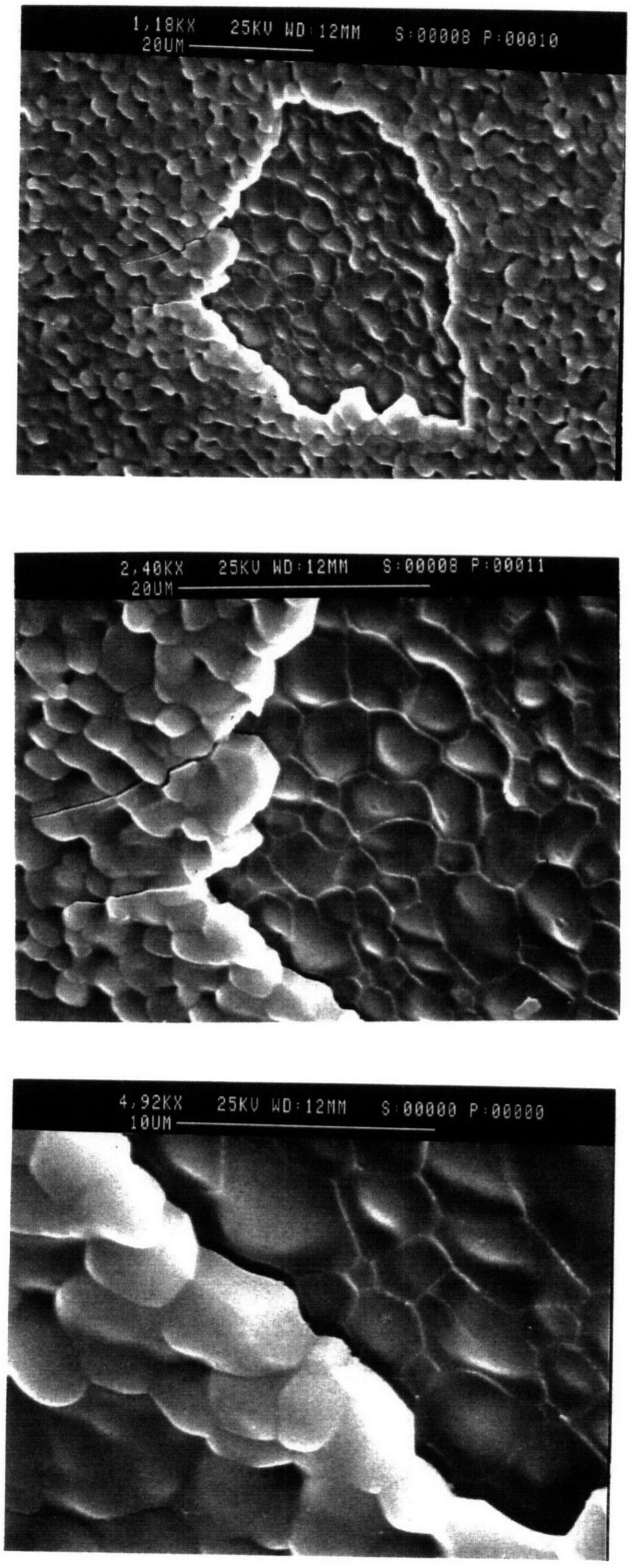

Figure 4.7b

SPALLED AREA OF TiO_2 COATING ON Al_2O_3 SUBSTRATE

(a)

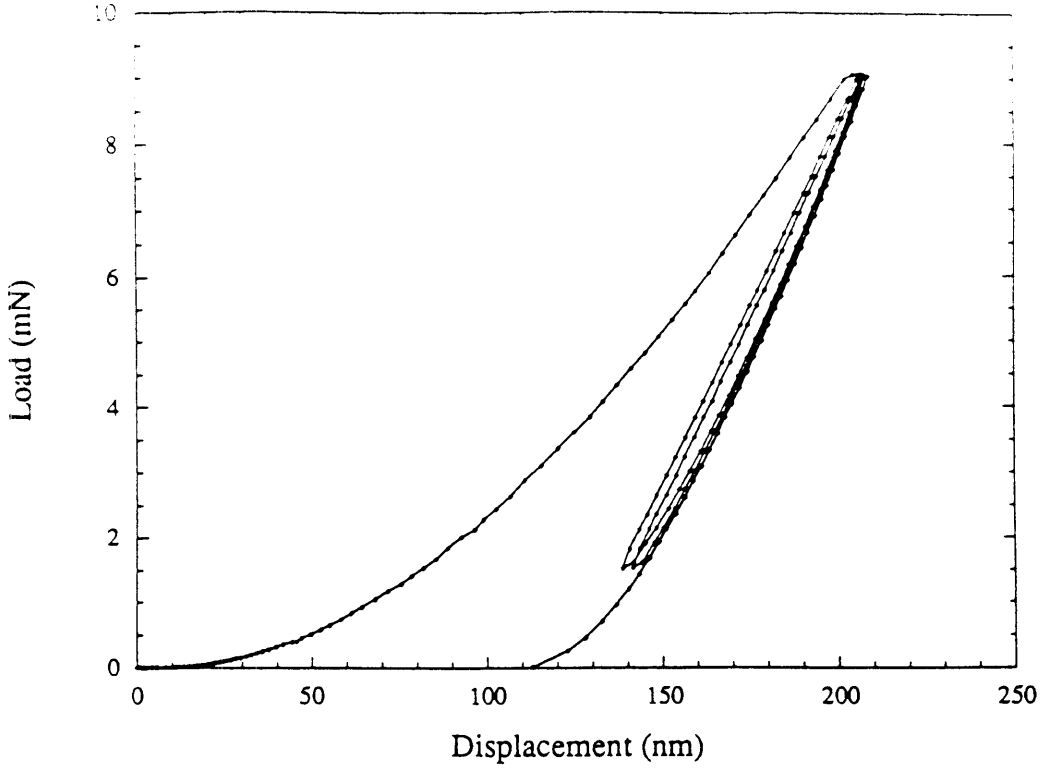

(b)

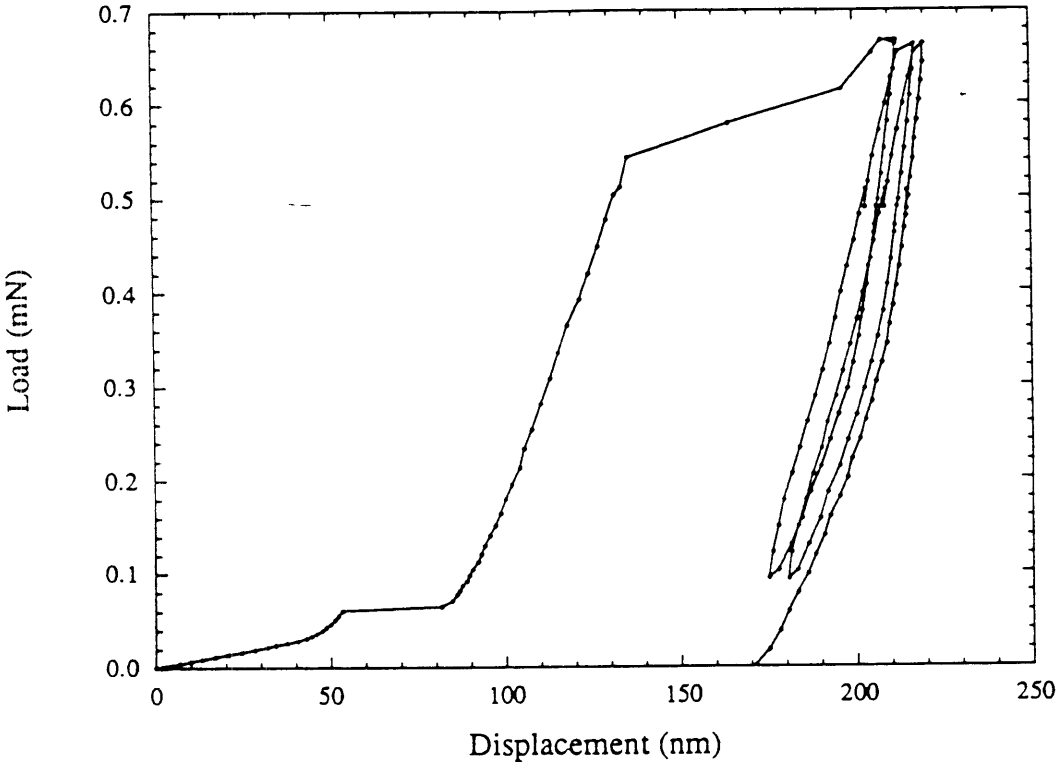

Figure 4.8. Typical indentation in (a)ZrO_2 and (b)TiO_2

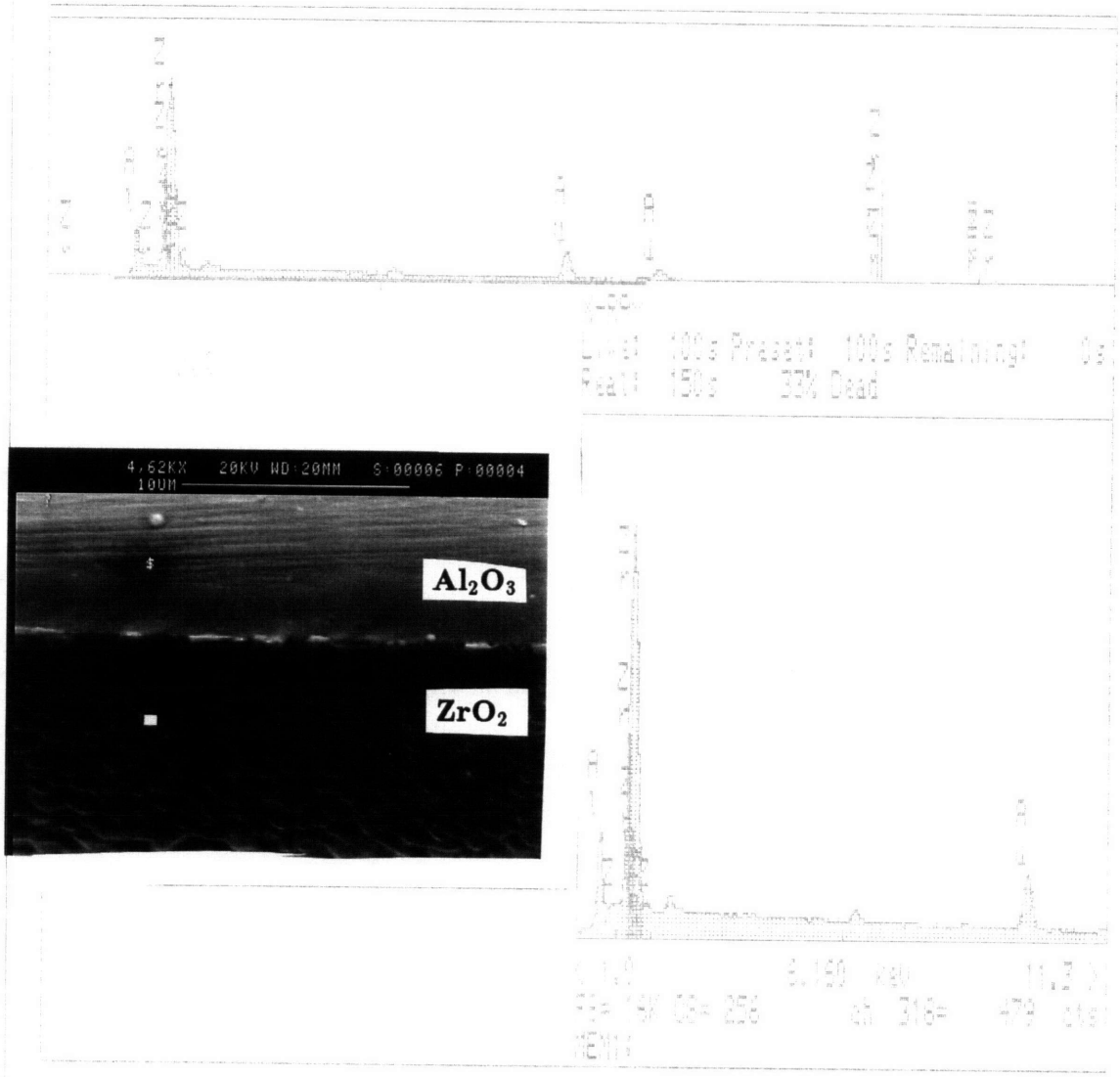

ZrO_2 COATING ON Al_2O_3 SINGLE CRYSTAL SUBSTRATE AFTER EXPOSURE TO 1600° FOR 4 HOURS

Figure 4.9a Results of the study of diffusion of Al through the ZrO_2 coating.

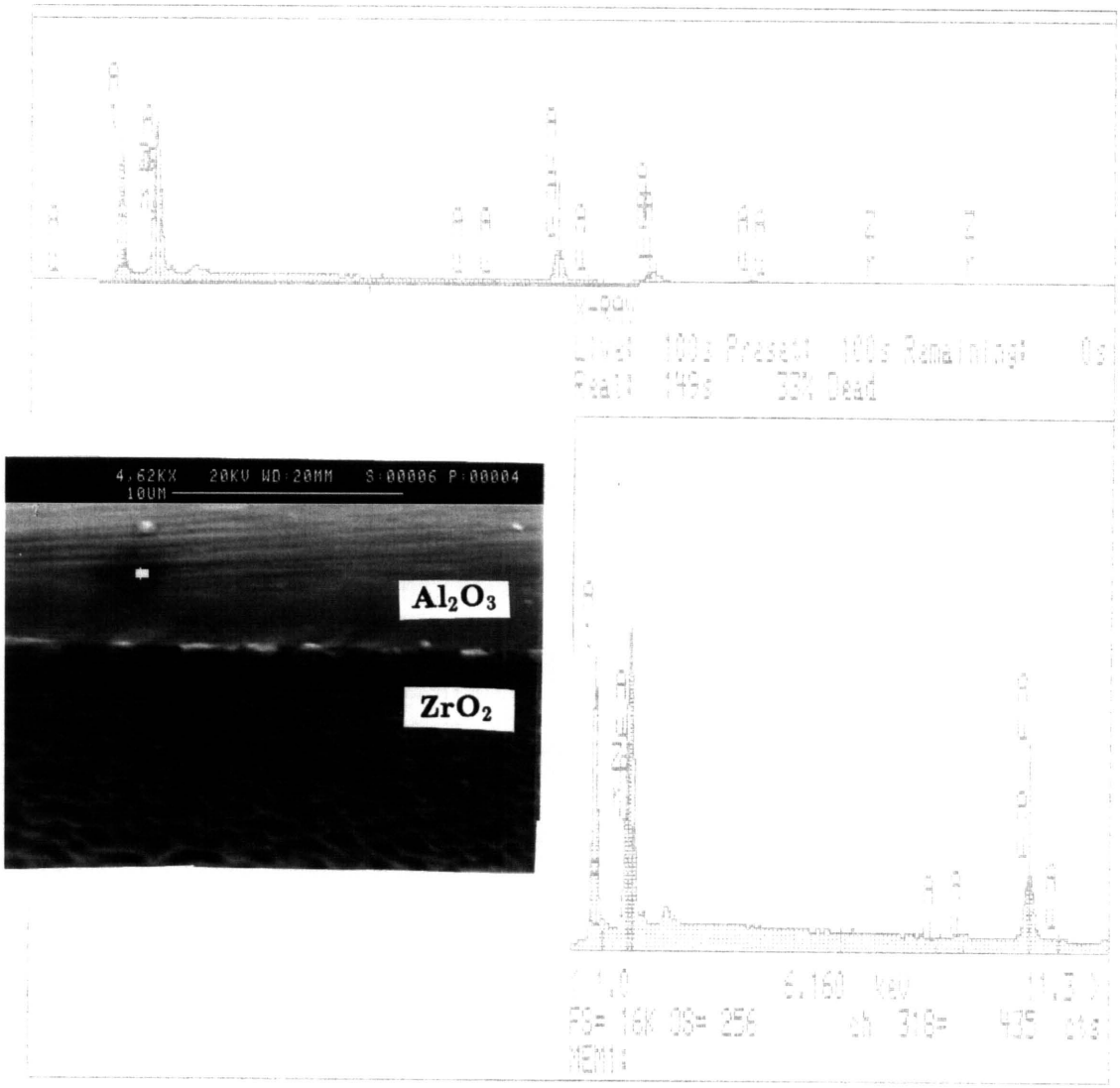

ZrO_2 COATING ON Al_2O_3 SINGLE CRYSTAL SUBSTRATE AFTER EXPOSURE TO 1600° FOR 4 HOURS

Figure 4.9b Results of the study of diffusion of Zr from the coating into Al_2O_3.

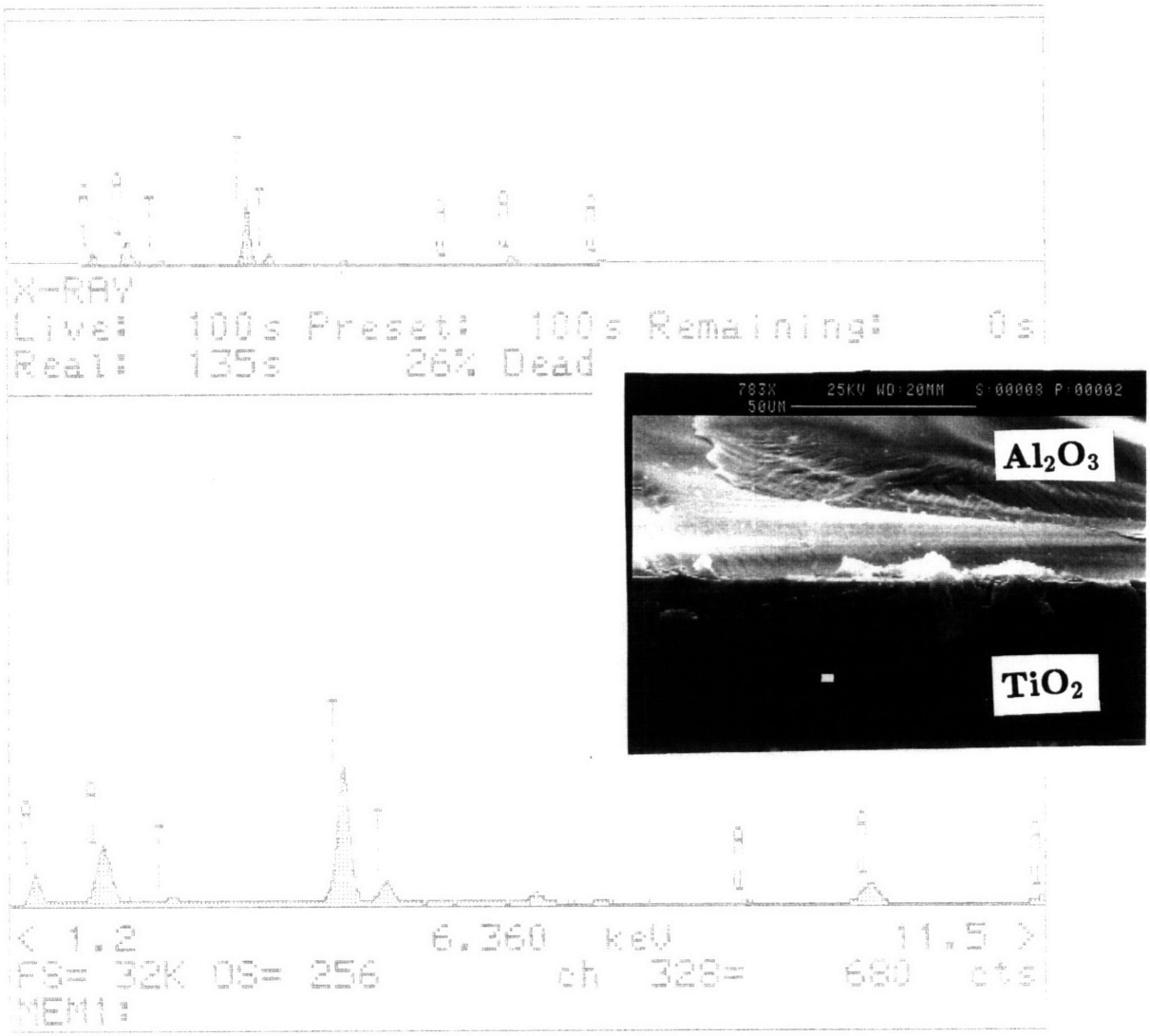

Figure 4.10a Results of the study of diffusion of Al through the TiO_2 coating.

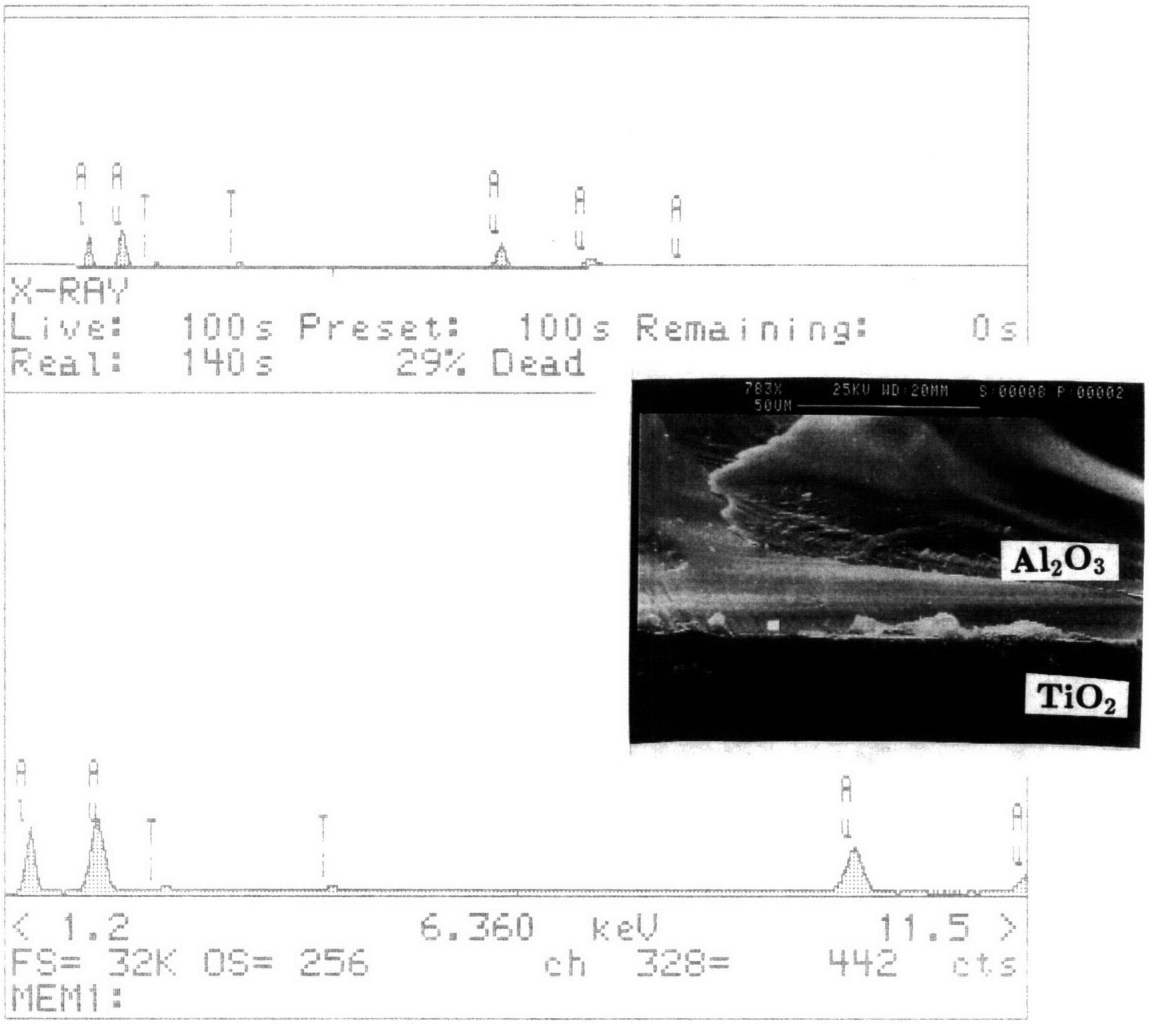

TiO_2 COATING ON Al_2O_3 SINGLE CRYSTAL SUBSTRATE AFTER EXPOSURE TO 1600° FOR 4 HOURS

Figure 4.10b Results of study of diffusion of Ti into Al_2O_3

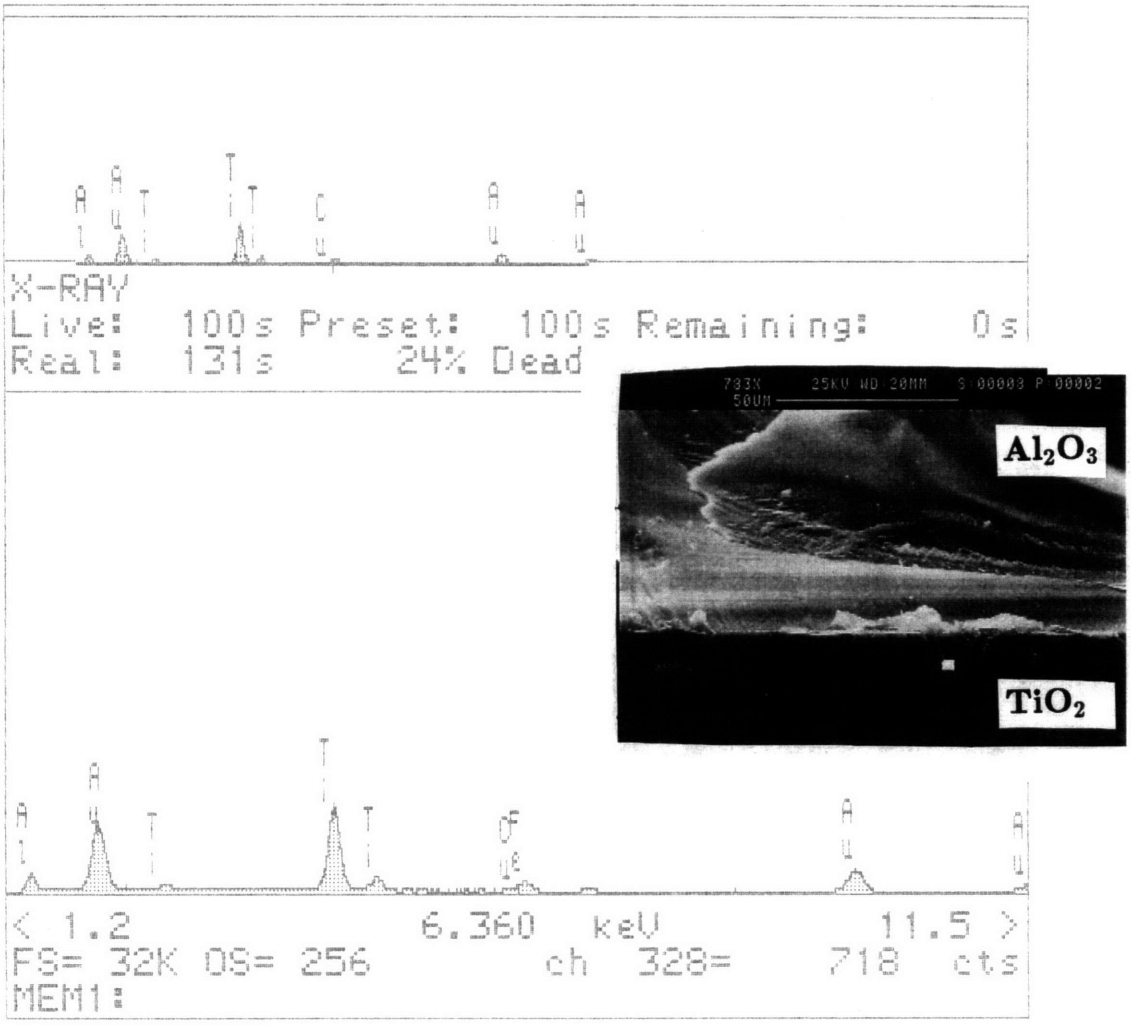

TiO_2 COATING ON Al_2O_3 SINGLE CRYSTAL SUBSTRATE AFTER EXPOSURE TO 1600° FOR 4 HOURS

Figure 4.10c Results of elemental study of formed $TiAl_2O_5$

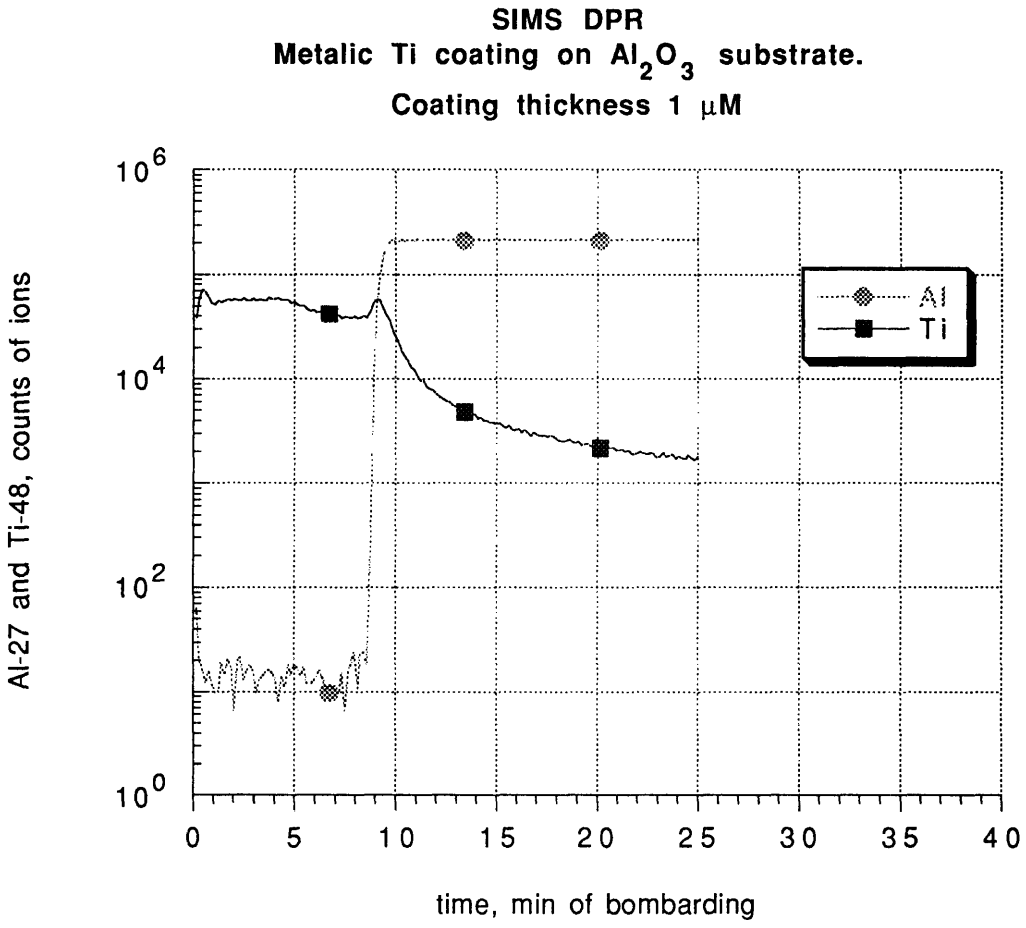

Figure 4.11 Results of SIMS generated depth profile of Ti coating on Al_2O_3 substrate as measured through the Al-27 and Ti-48 distribution in depth around the coating-substrate interface.

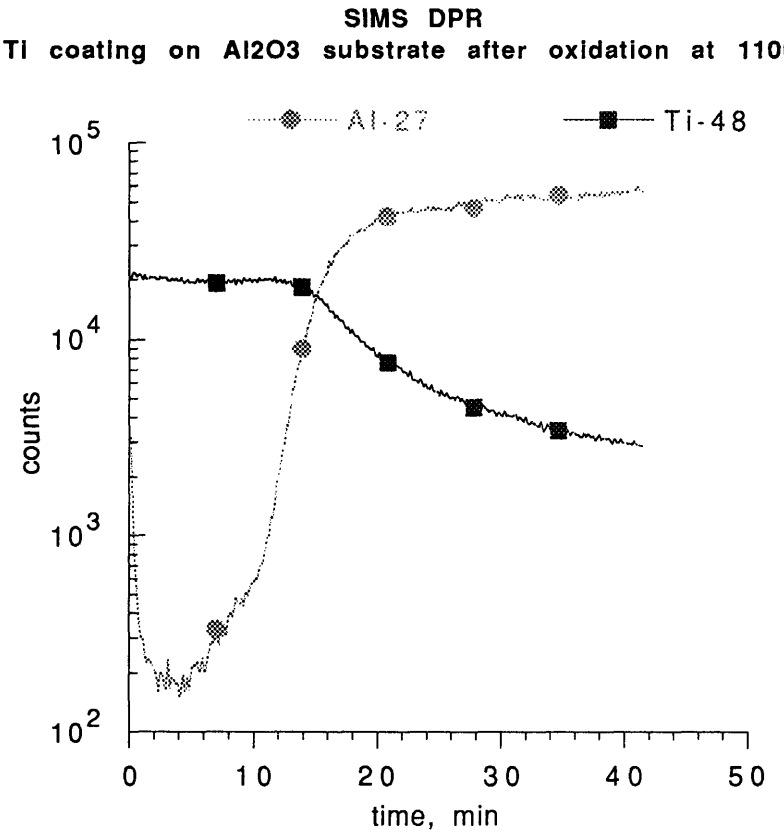

Figure 4.12 Results of SIMS generated depth profile for TiO_2 coating after oxidation at 1100 °C, showing some inter diffusion of Ti and Al

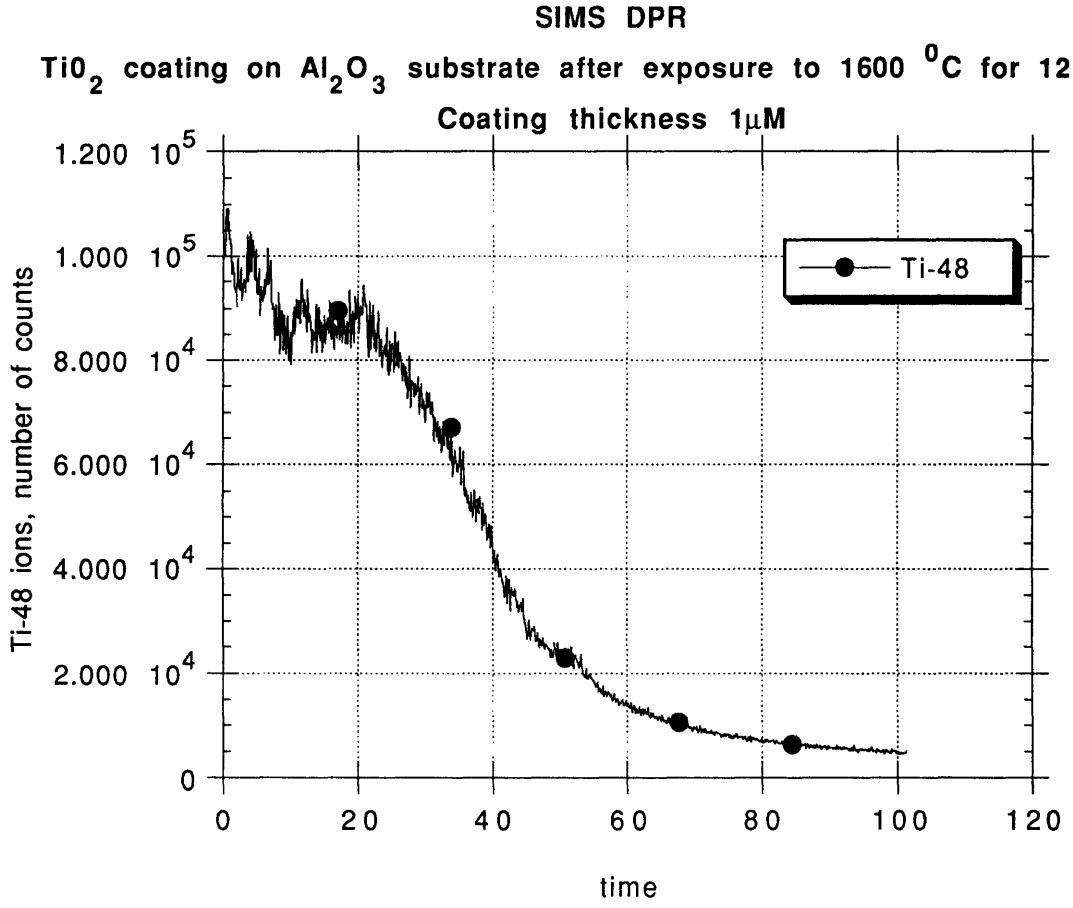

Figure 4.13 Ti ions traced in TiO_2 coating on Al_2O_3 substrate after exposure to 1600 °C for 12 hours

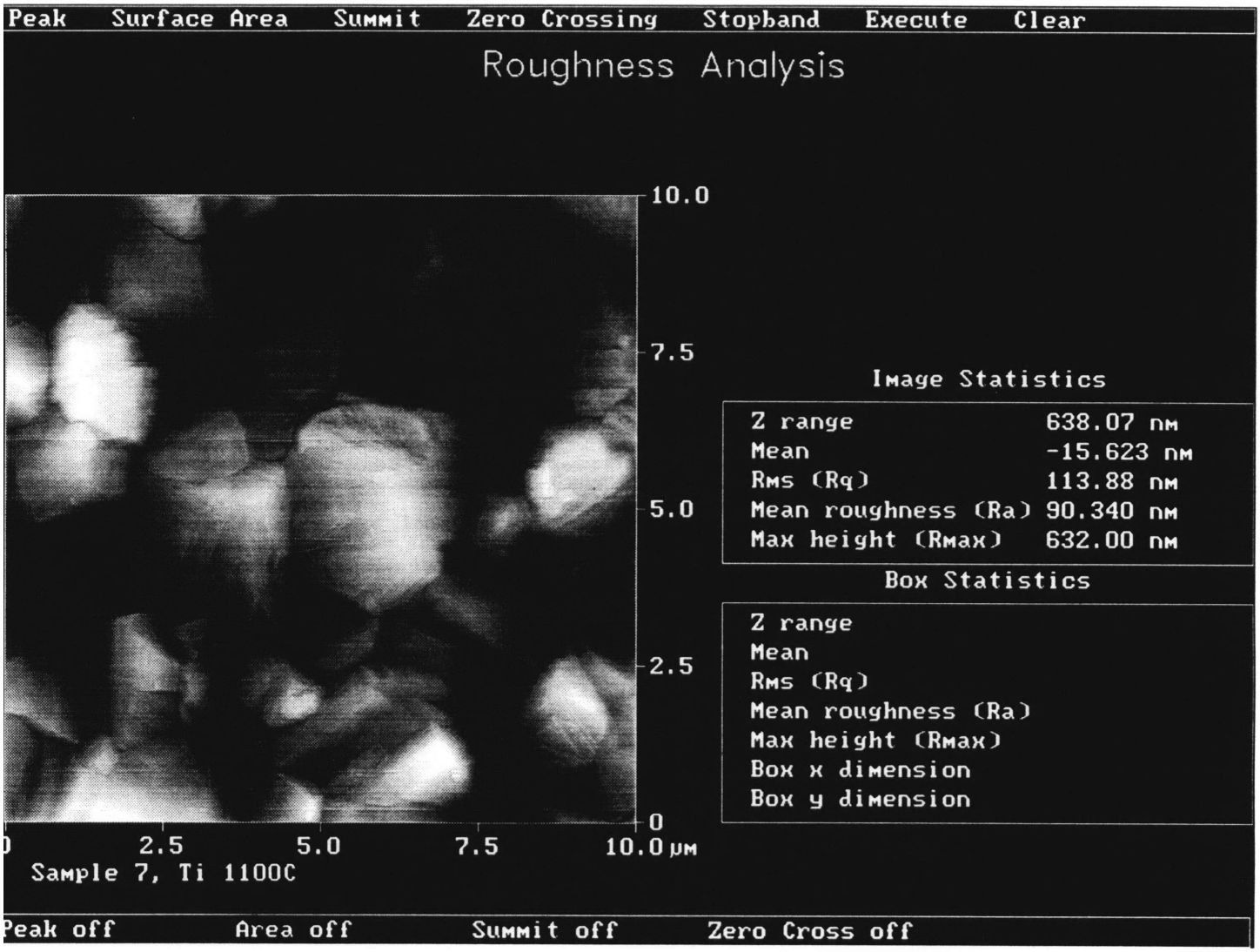

Figure 4.14 AFM study of TiO_2 coating

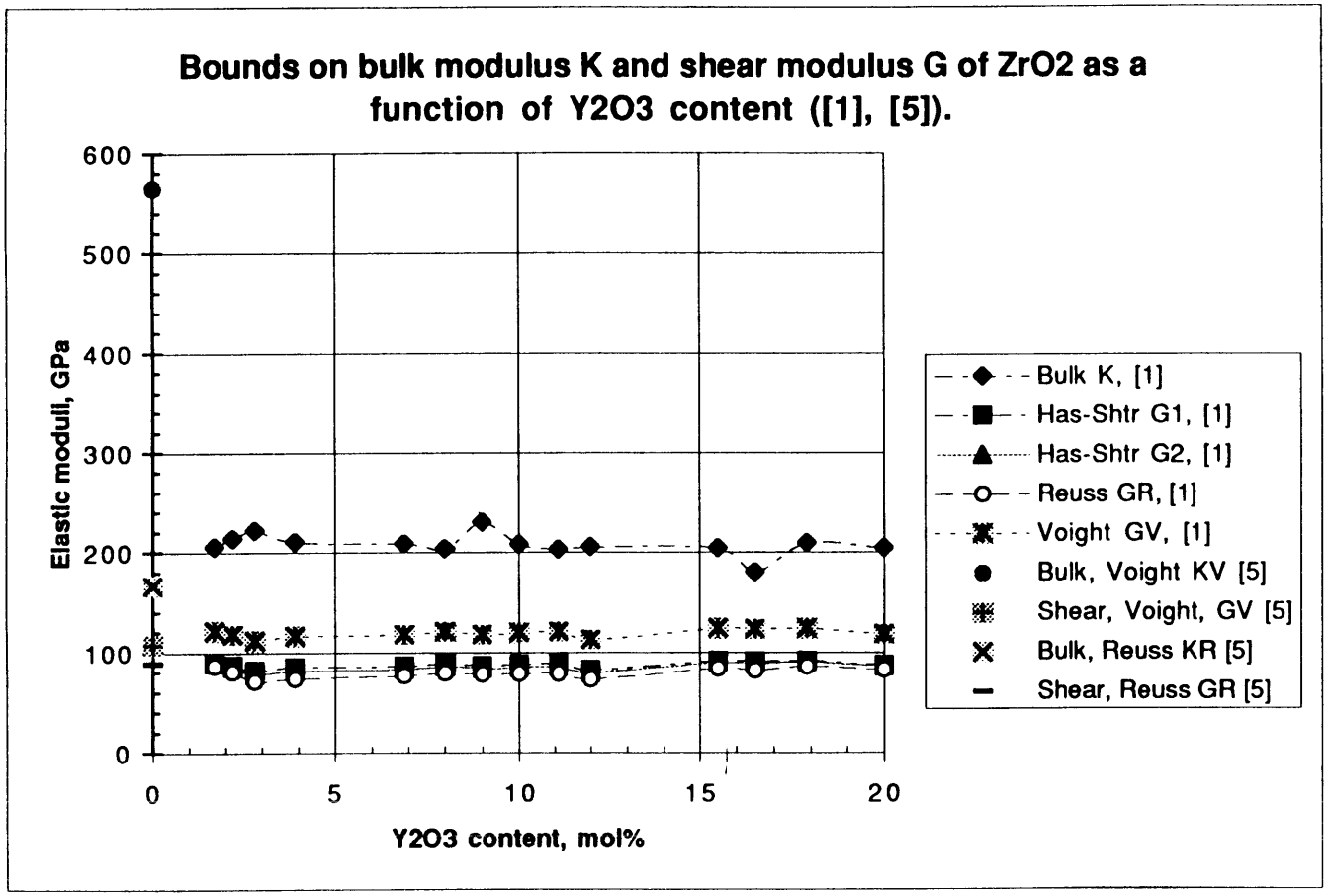

Figure 5.1a Elastic constants of ZrO2 as a function of Y2O3 content

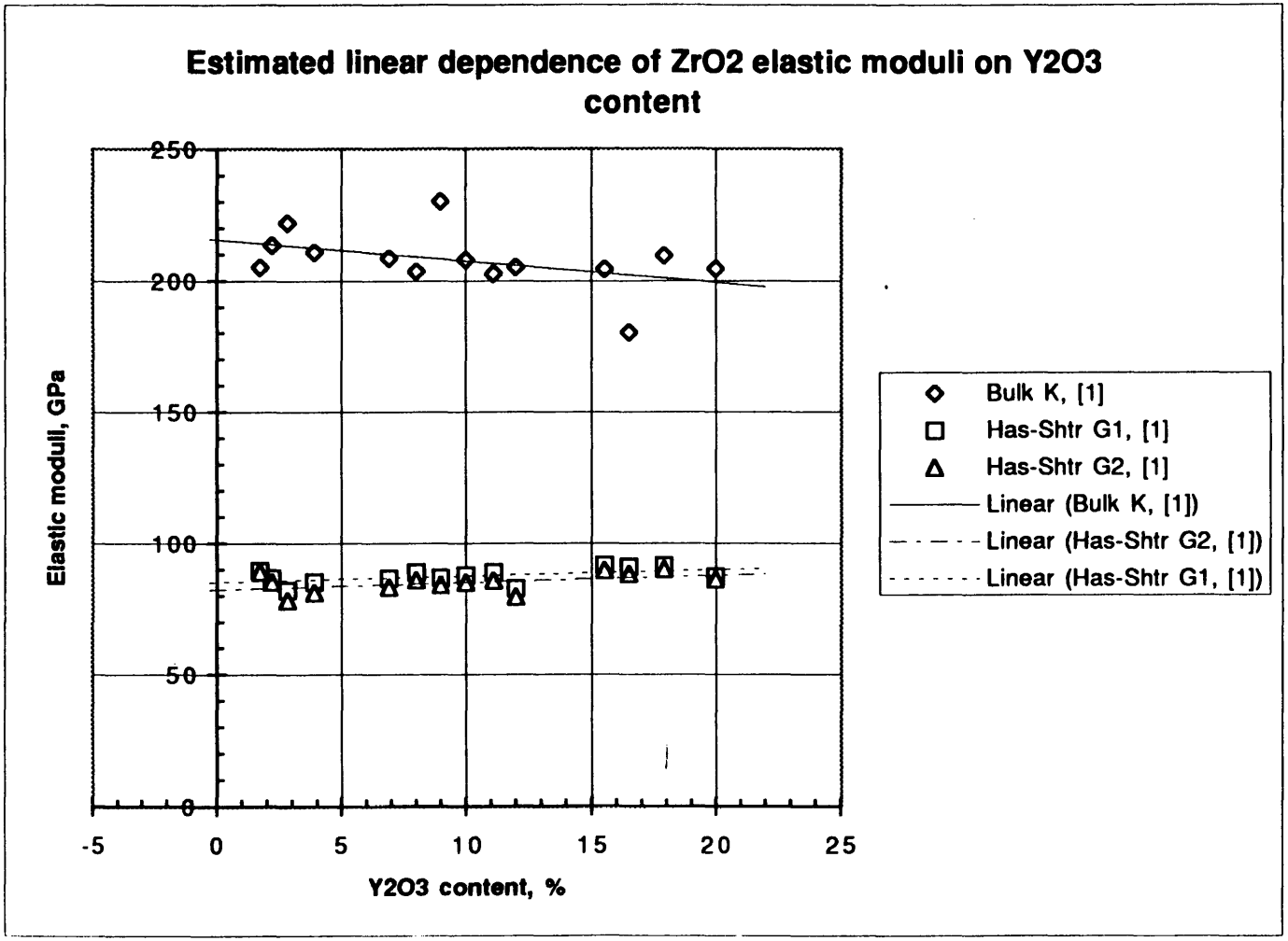

Figure 5.1b Elastic constants of ZrO2 as a function of Y2O3 content

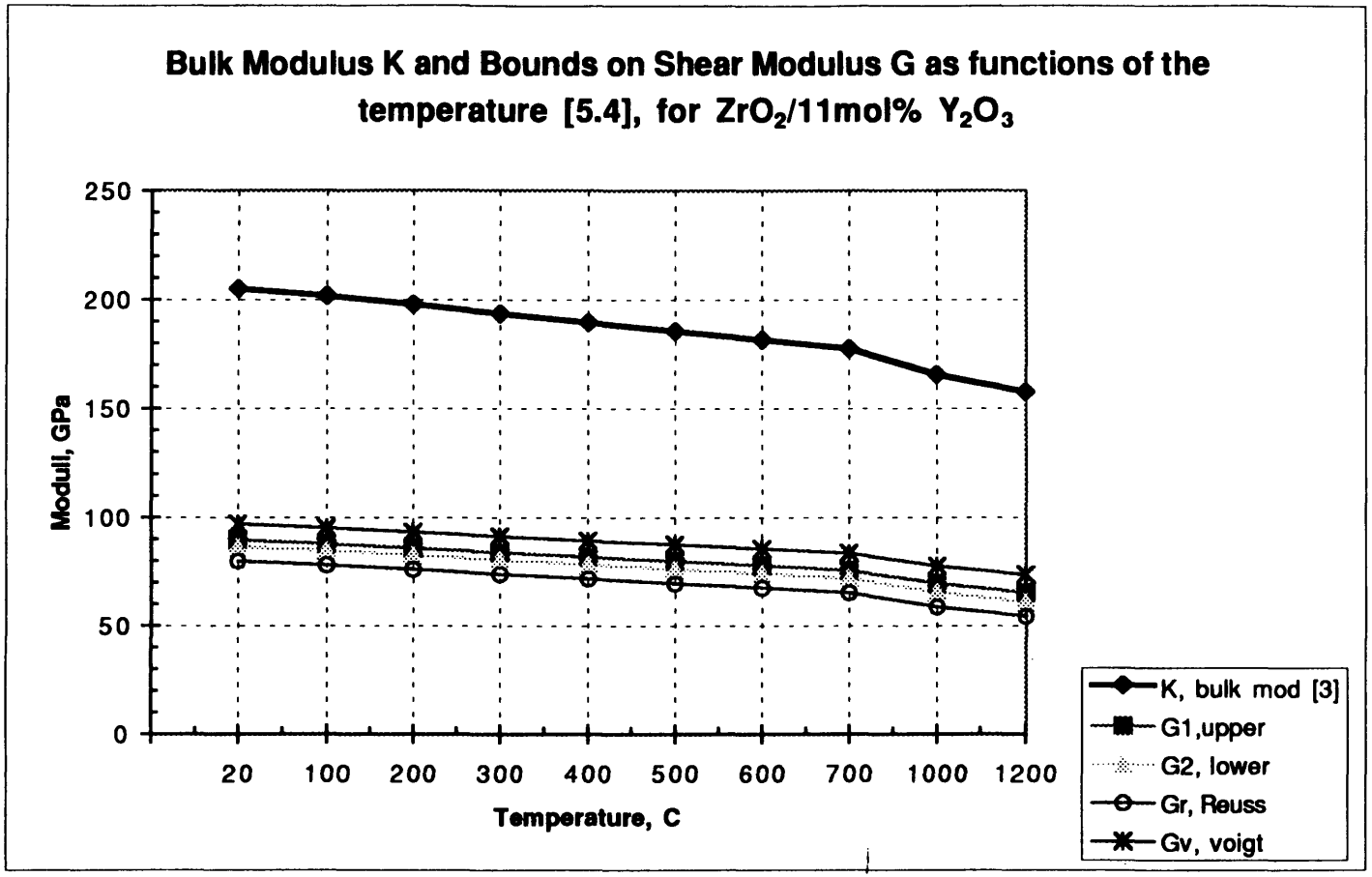

Figure 5.2 Extrapolated elastic constants for fully stabilized zirconia [5.4]
K - Bulk modulus
G1 and G2 - upper and lower Hashin-Shtrickman bounds on shear modulus
Gr and Gv - Reuss and Voigt averages on shear modulus

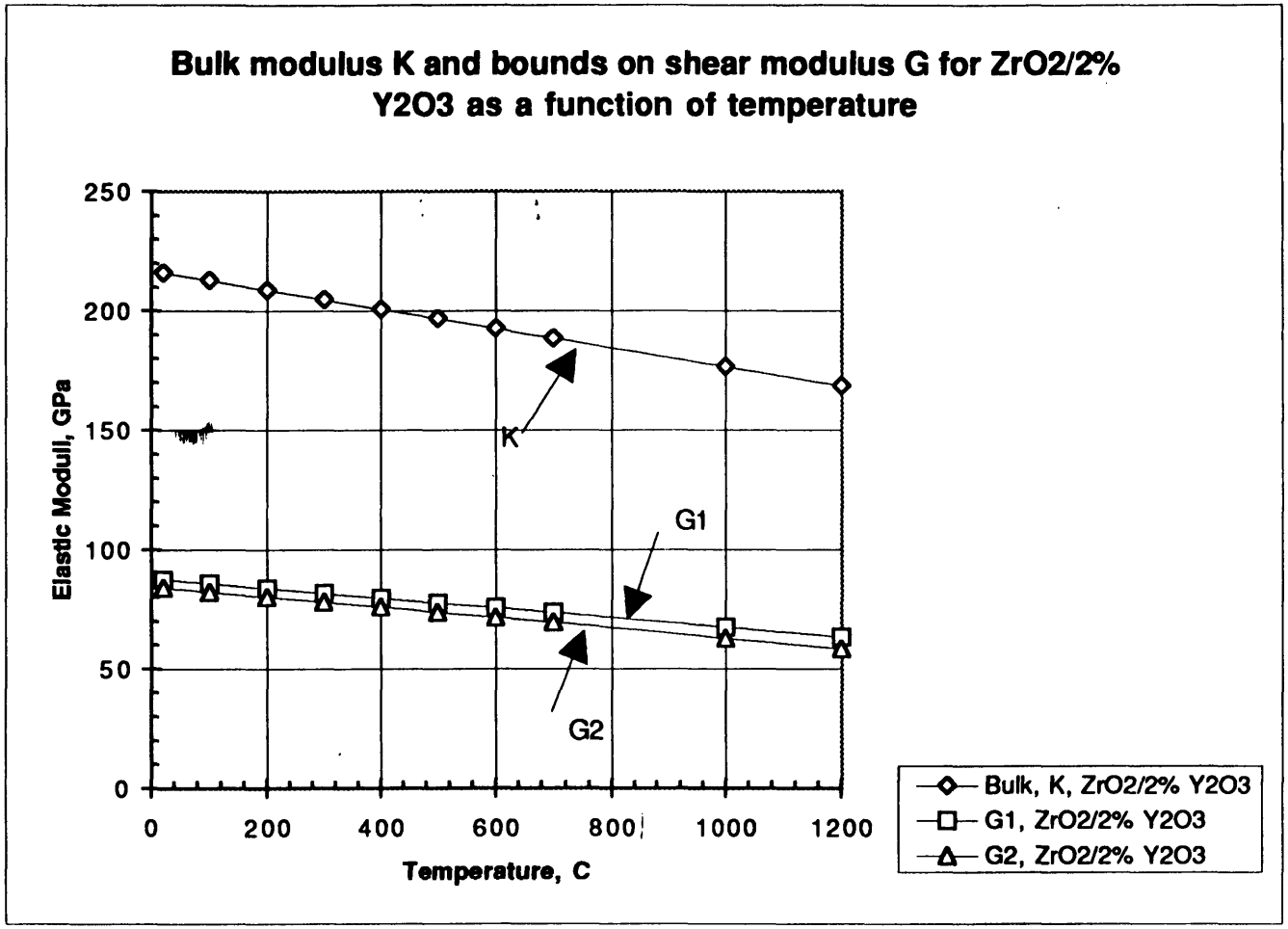

Figure 5.3. Elastic constants of PSZ in the temperature range 20 C 1200 C.
K - Bulk Modulus
G1 - upper Hashin-Shtrickman Bound on a shear modulus
G2 - lower Hashin-Shtrickman Bound on a shear modulus

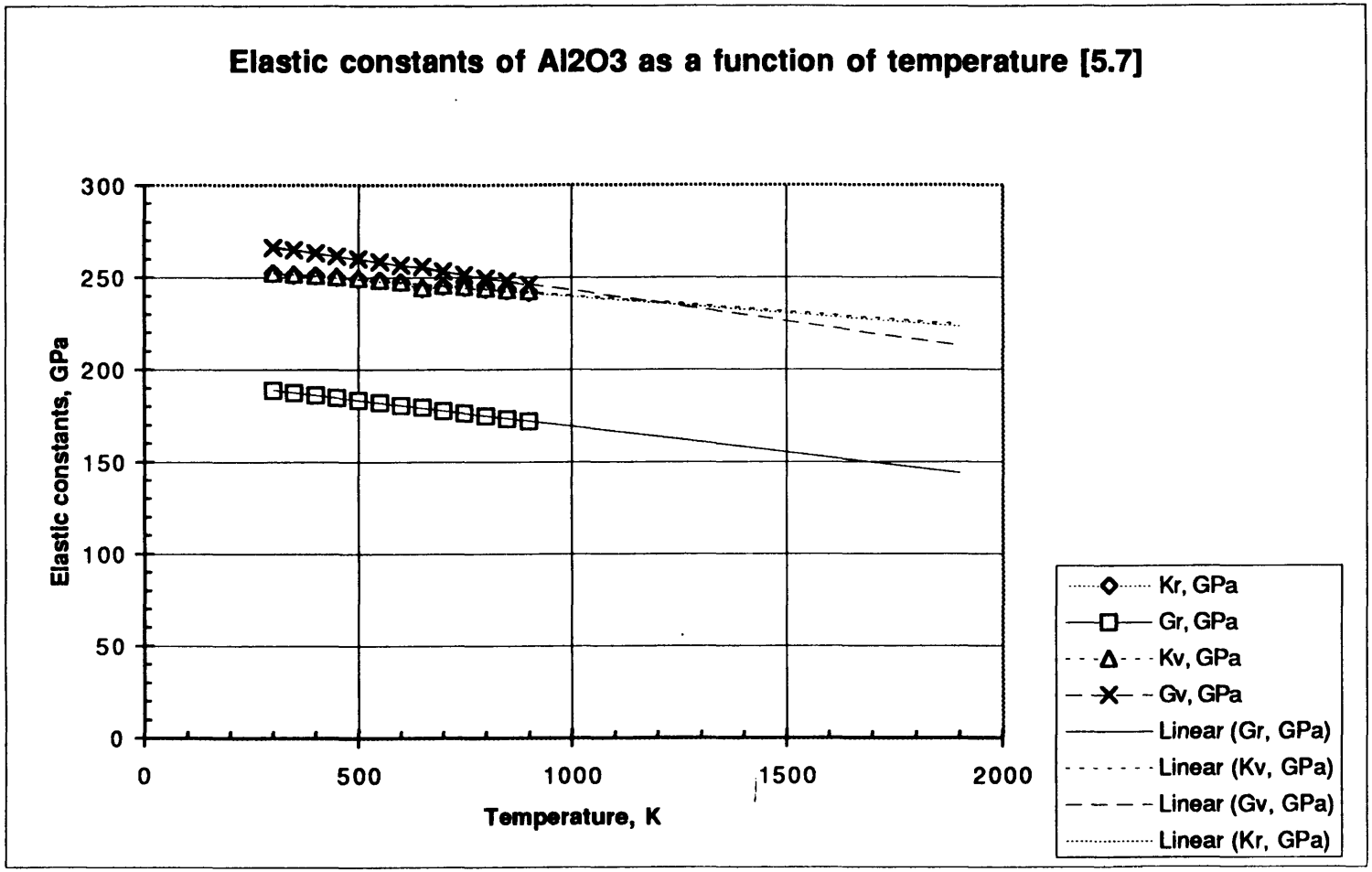

Figure 5.4 Extrapolated elastic constants of Al2O3
Kv and Kr - Voigt and Reuss averages on a bulk modulus
Gv and Gr - Voigt and Reuss averages on a shear modulus

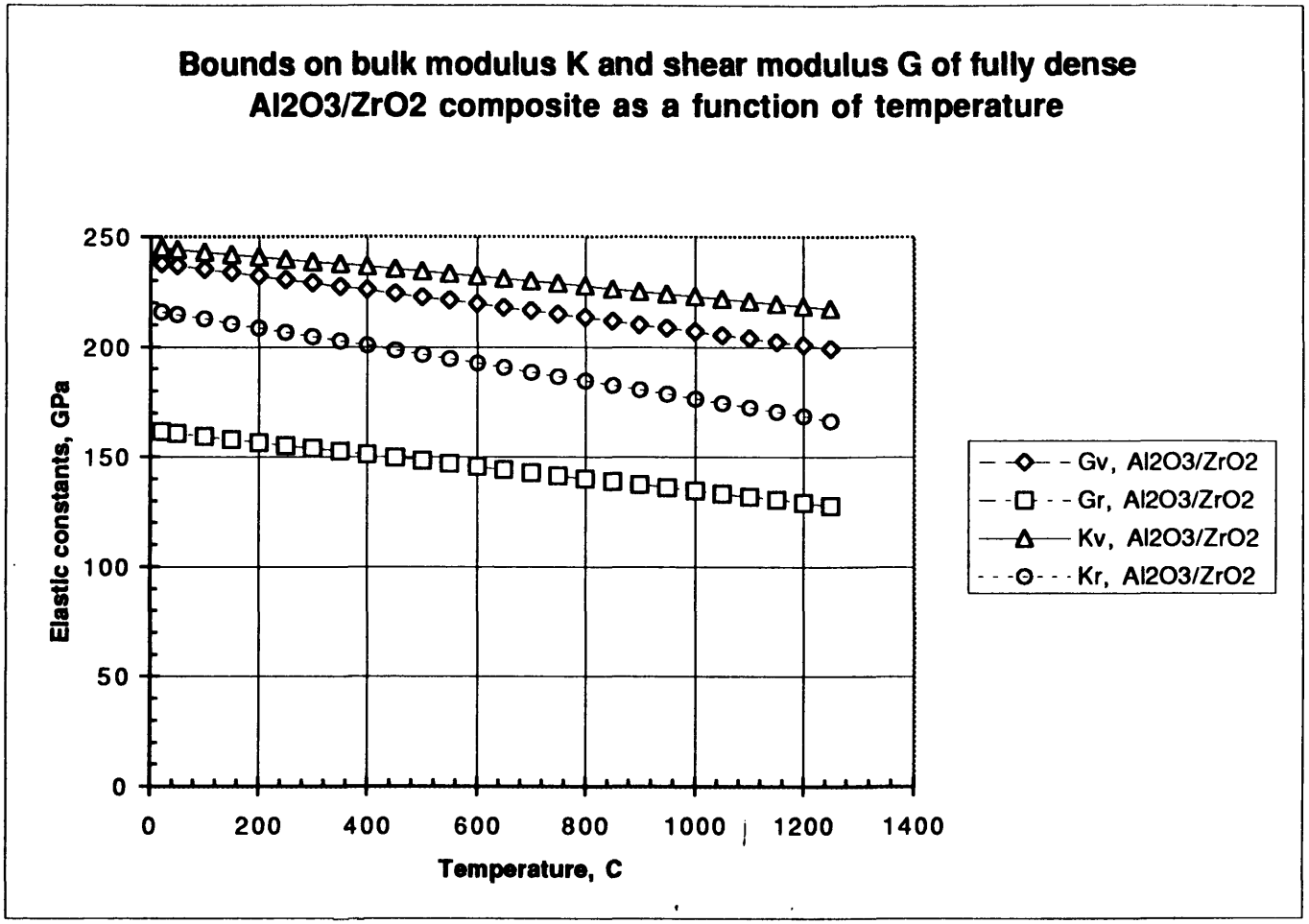

Figure 5.5 Elastic constants of Al2O3/ZrO2/Y2O3 composite as a function of temperature
Gv and Gr - Voigt and Reuss averages on shear modulus
Kv and Kr - Voigt and Reuss averages on bulk modulus

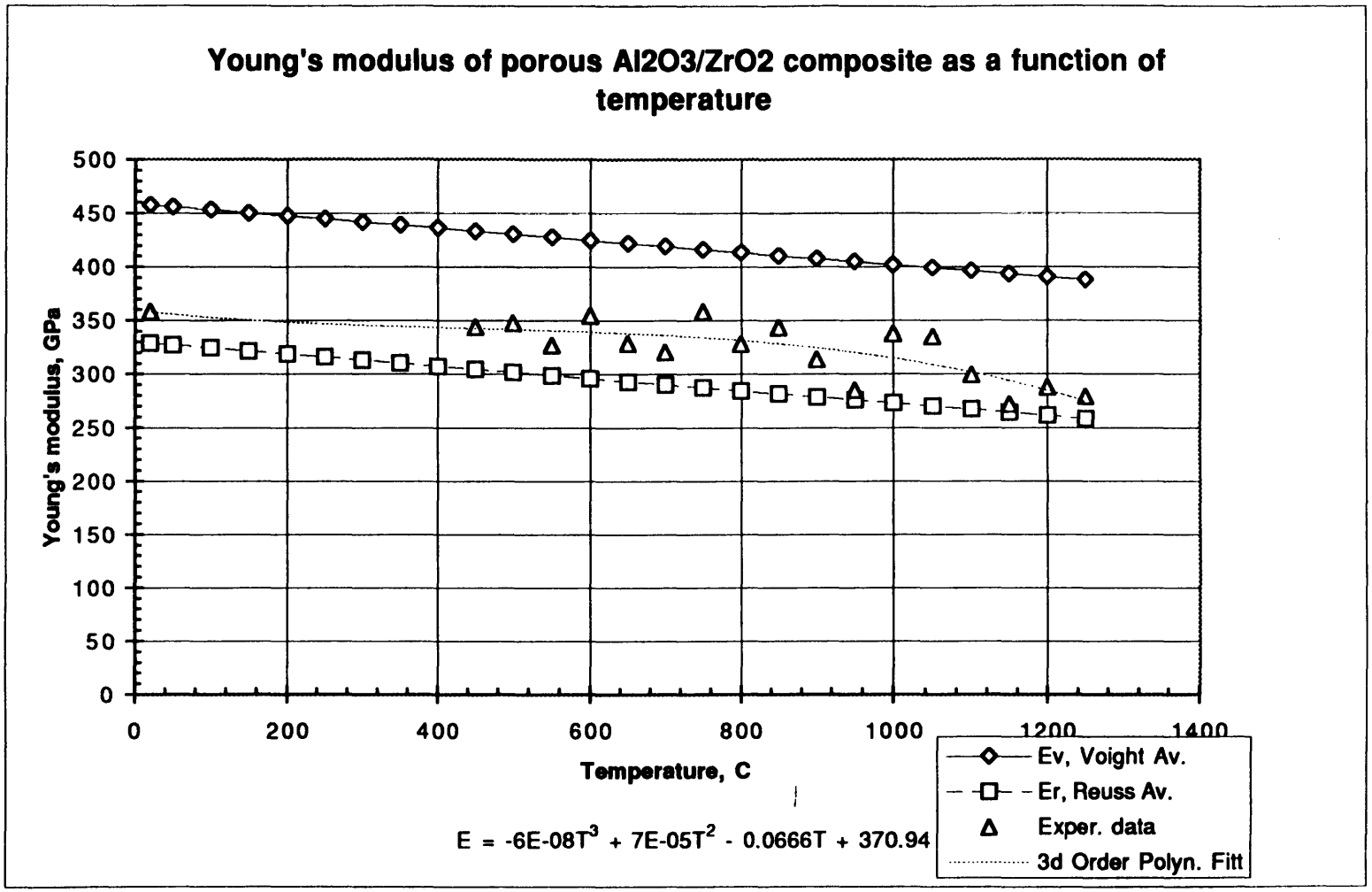

Figure 5.6 Elastic constants of RBAO as a function of the temperature

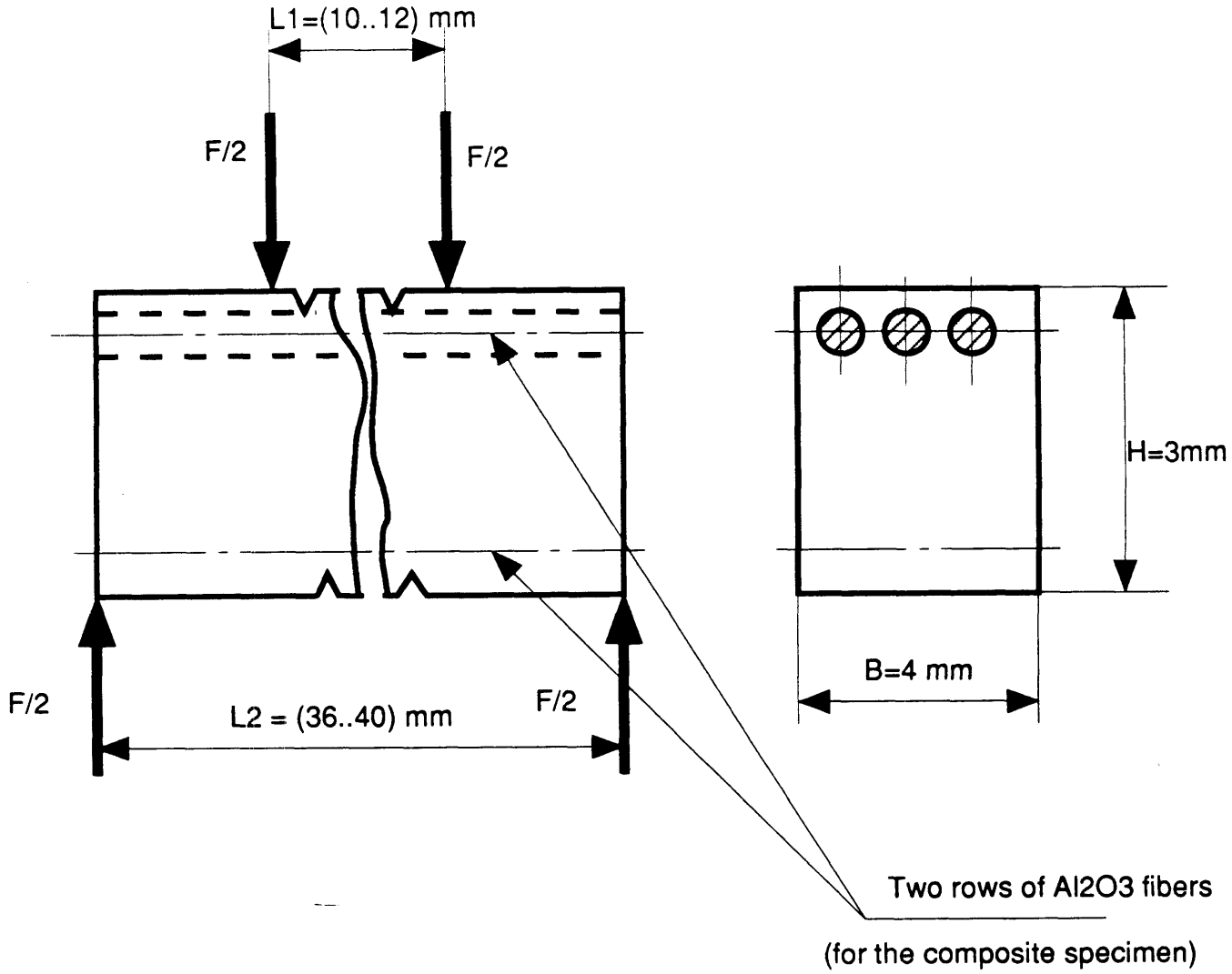

Figure 5.7 Bending Specimen

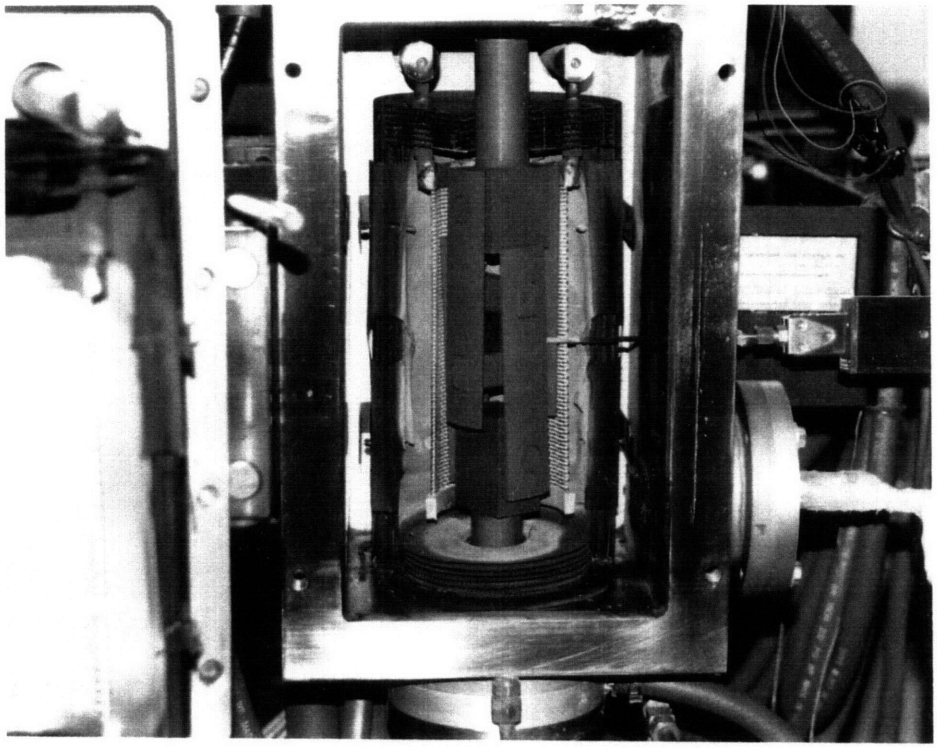

Figure 5.8 Vacuum chamber with the bending fixture

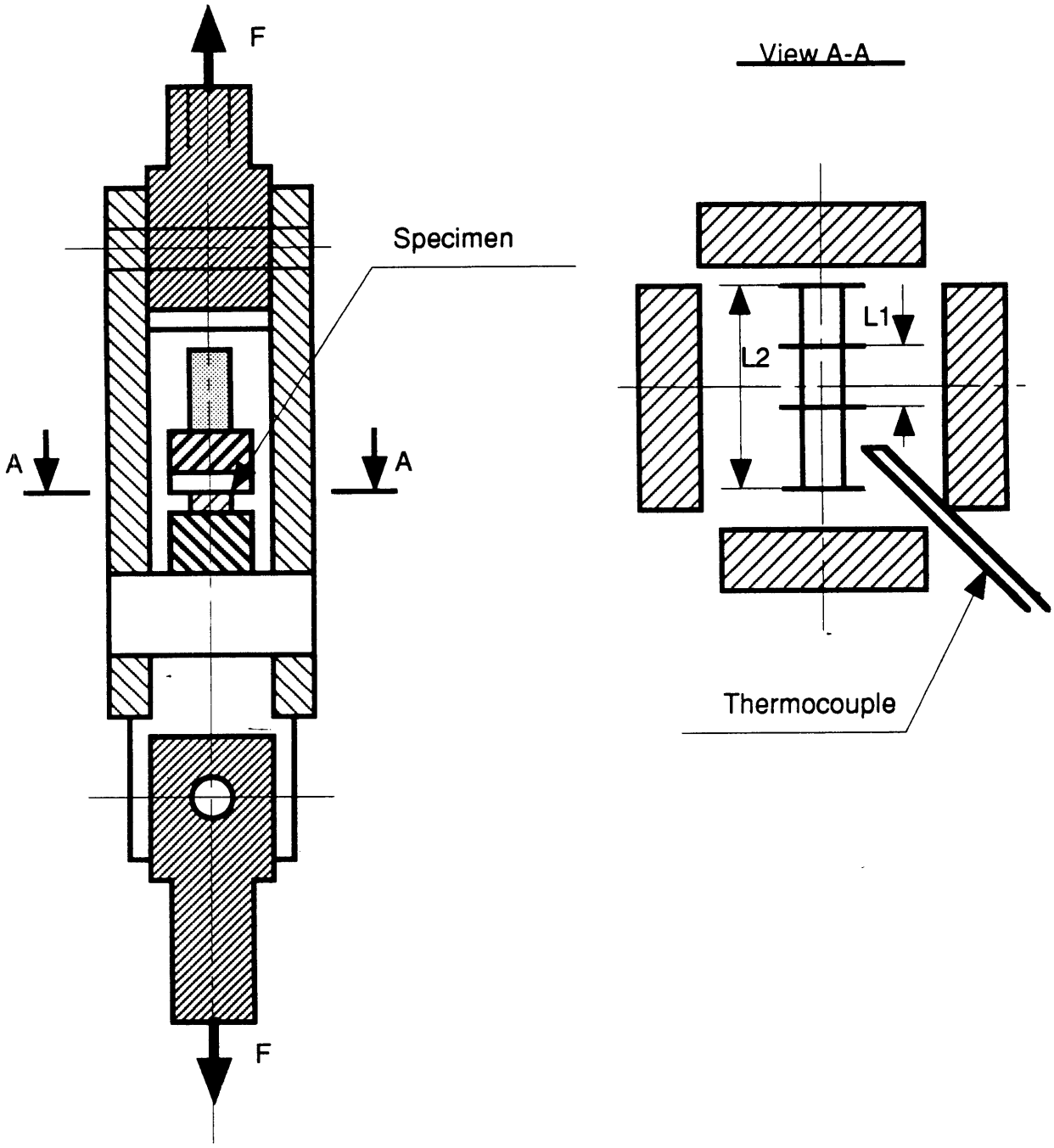

Figure 5.9 Bendind fixture

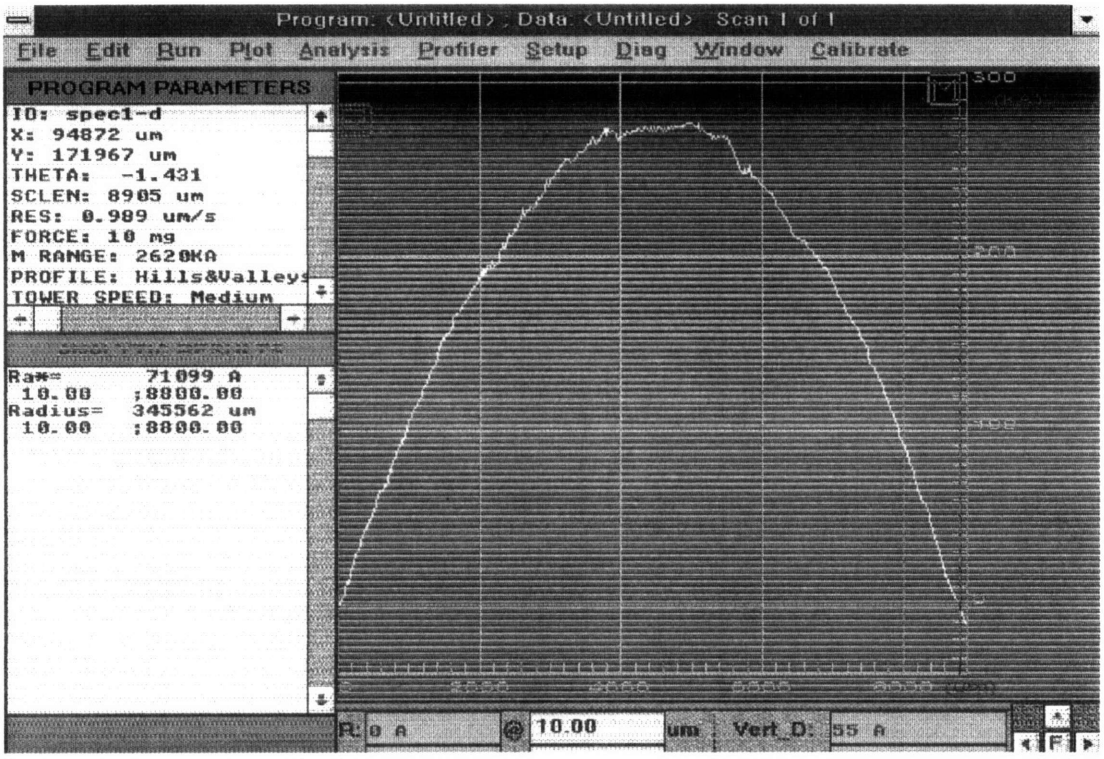

Figure 5.10a Final curvature of an inner span of a crept RBAO specimen as measured by a profilometer

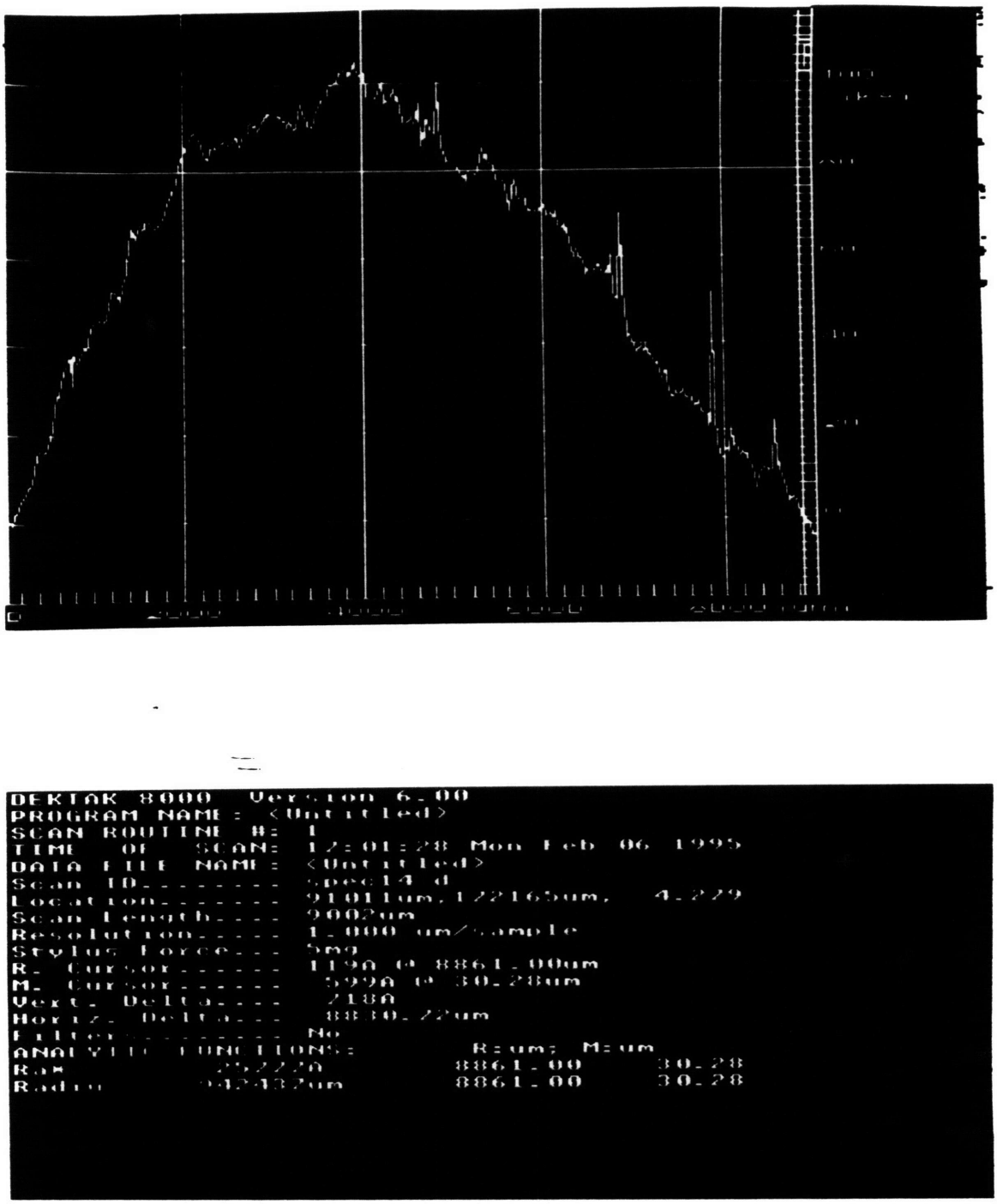

Figure 5.10b Final curvature of an inner span of a crept Al_2O_3 / Al_2O_3 specimen as measure by a profilometer

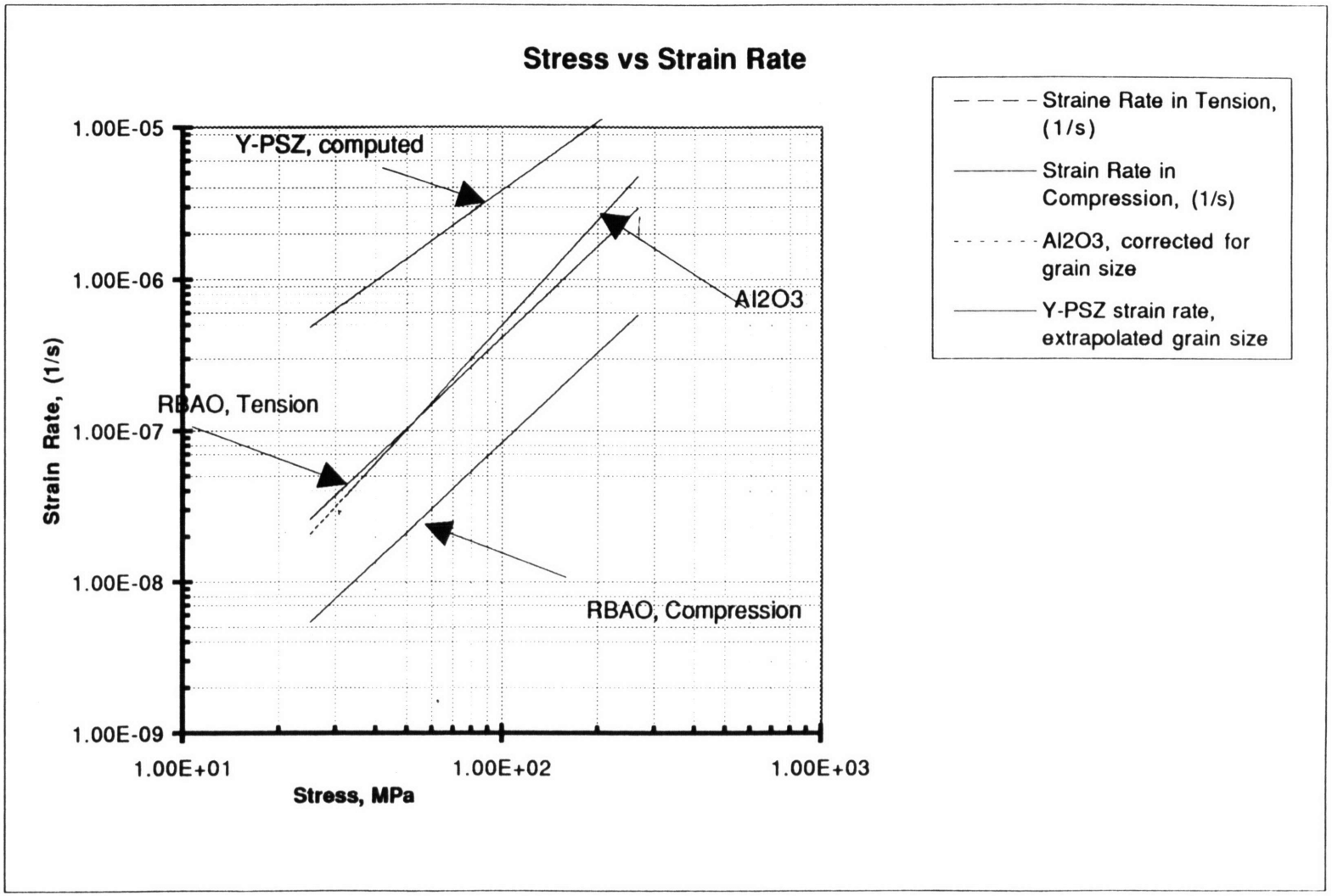

Figure 5.12 RBAO creep rate as a function of stress

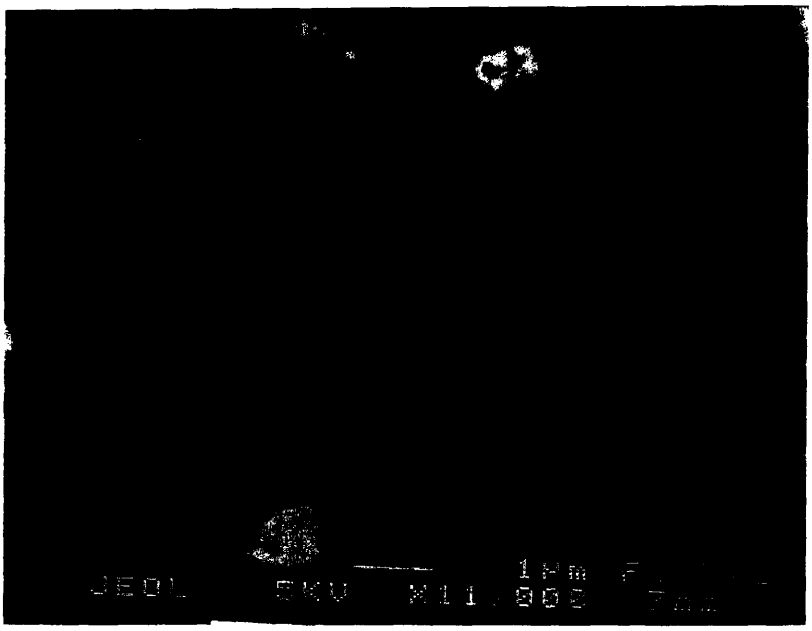

a)

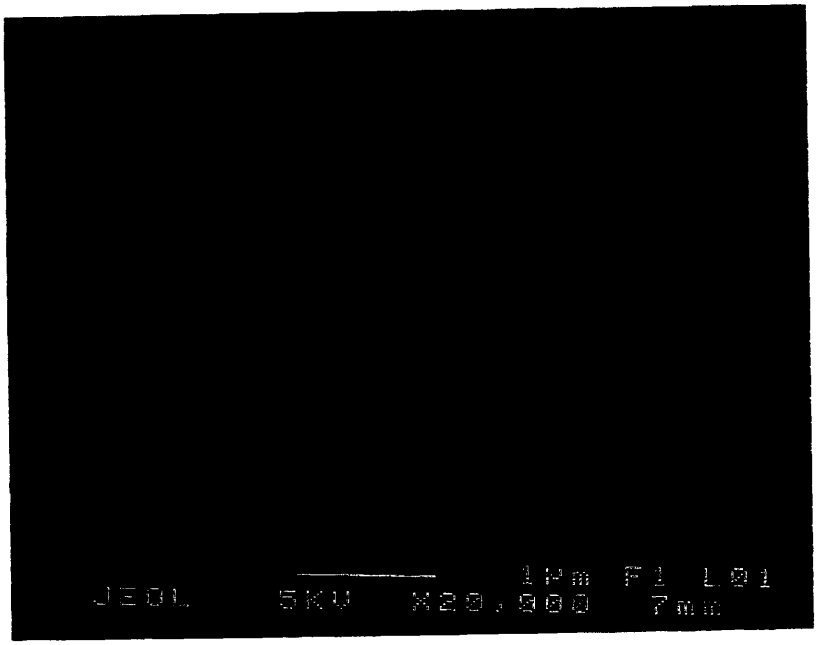

b)

Figure 5.13 Structure of RBAO. Lighter fields are ZrO_2, darker fields are Al_2O_3.

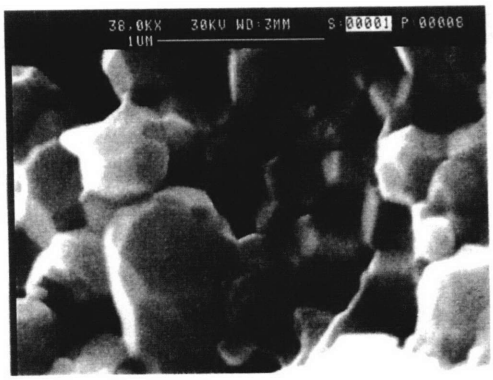

a)

b)

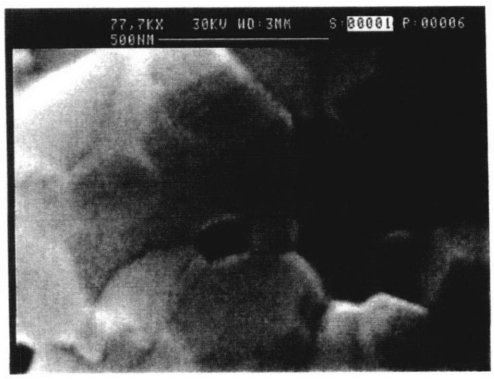

c)

d)

Figure 5.14 Intergranual voids generation and void opening as a result of grain boundary sliding during the creep in RBAO.

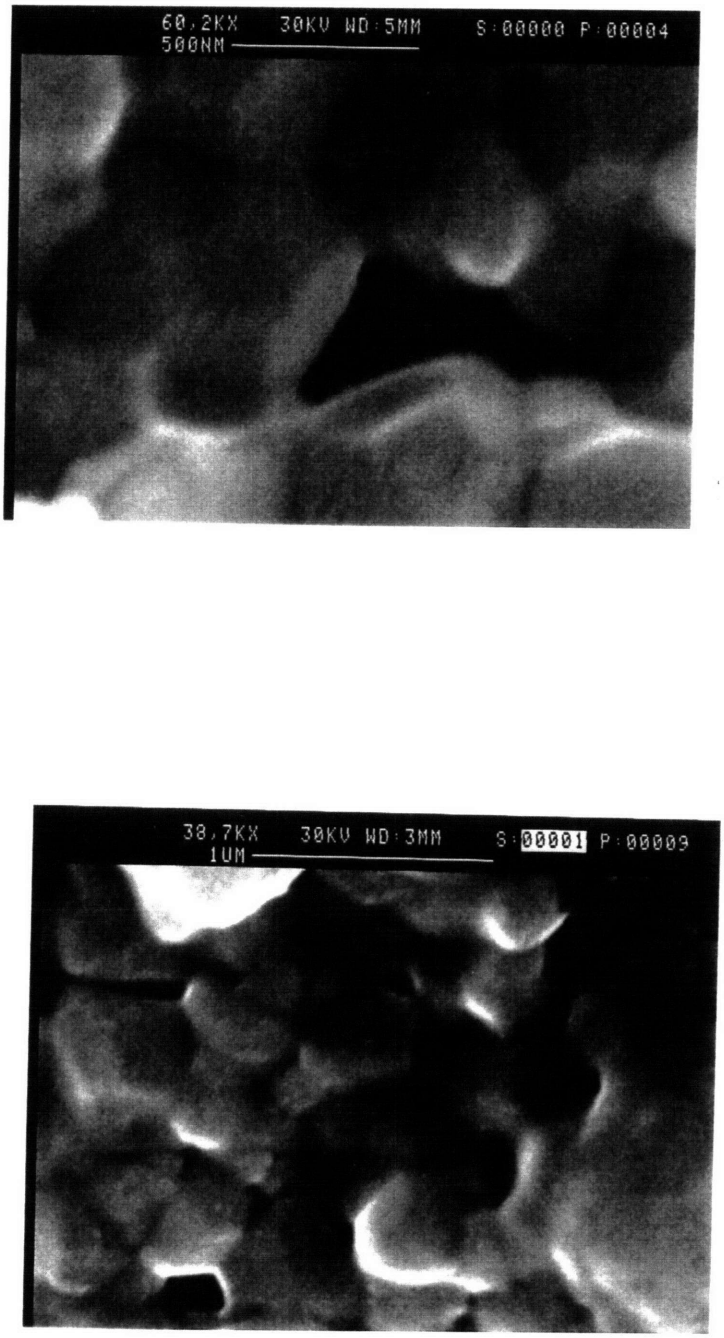

Figure 5.15 Intergranual facet openings in crept RBAO

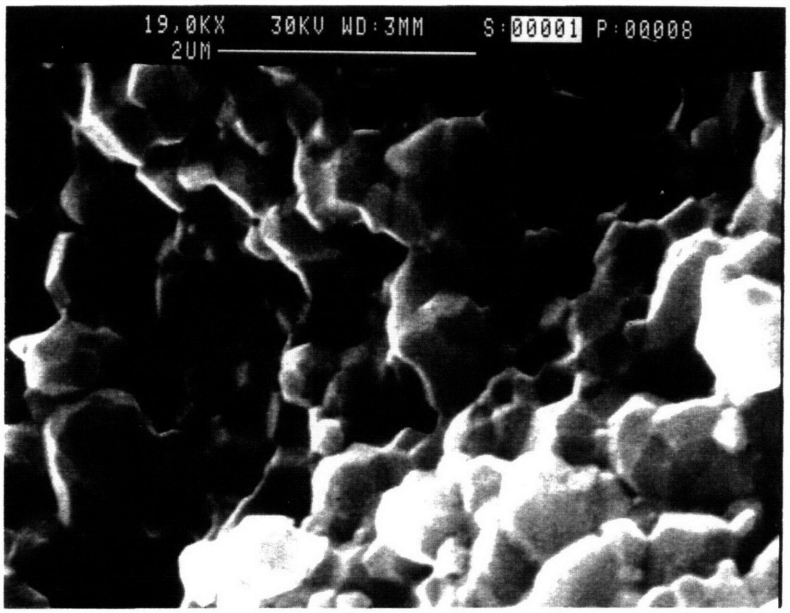

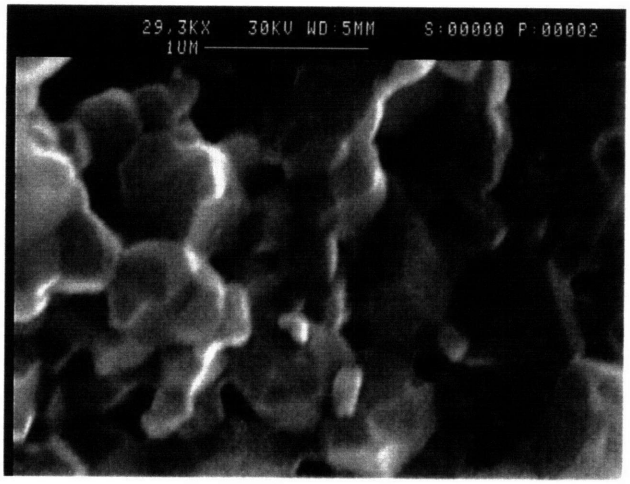

Figure 5.16 Fracture surface of RBAO crept RBAO.

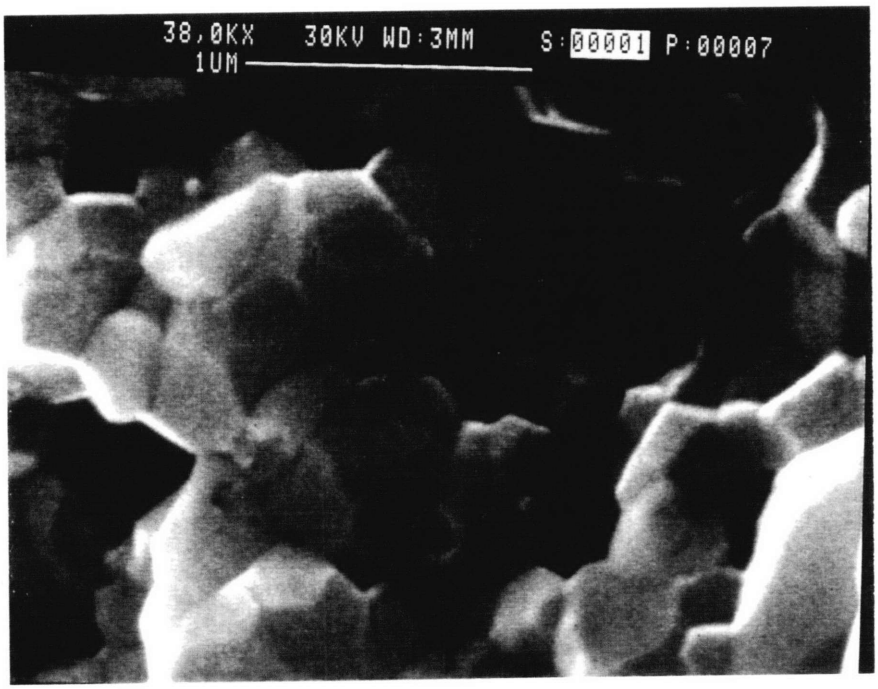

Figure 5.17a

Figure 5.17b

Figure 5.17 Four grain corner cavity in crept RBAO

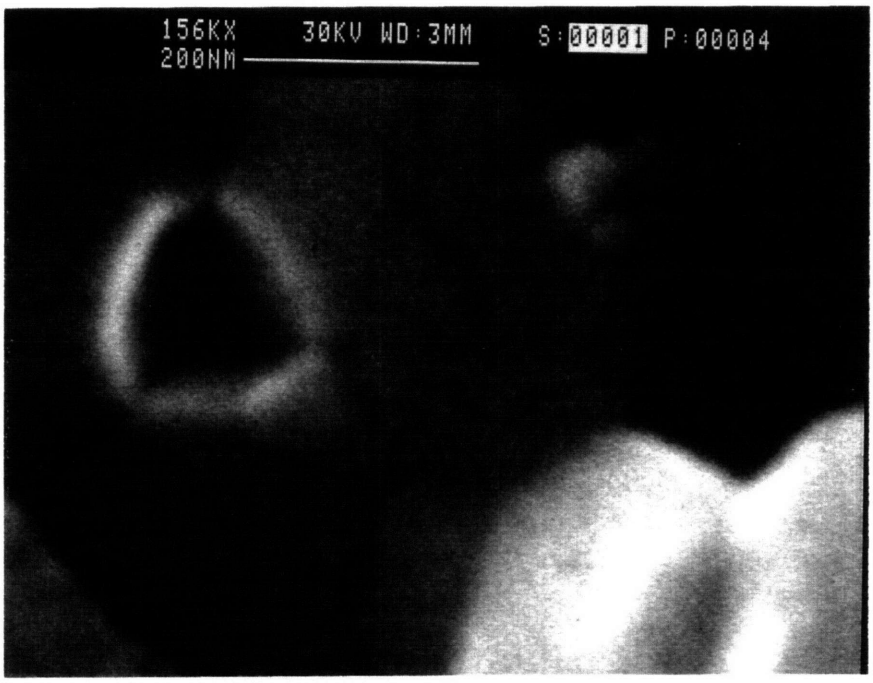

Figure 5.17c

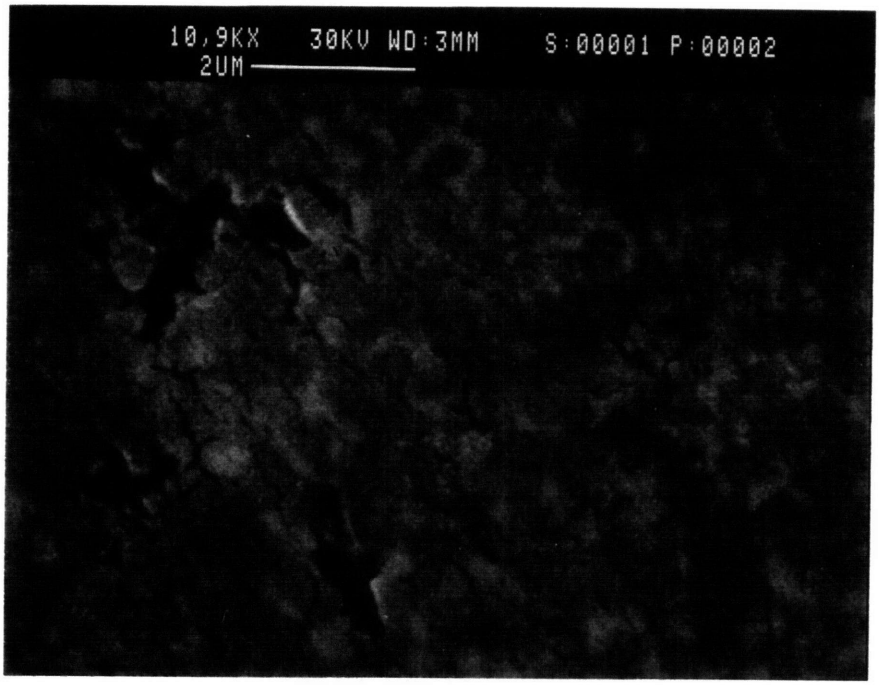

Figure 5.18a)

Figure 5.18 Cracks on the tensile surface of crept RBAO

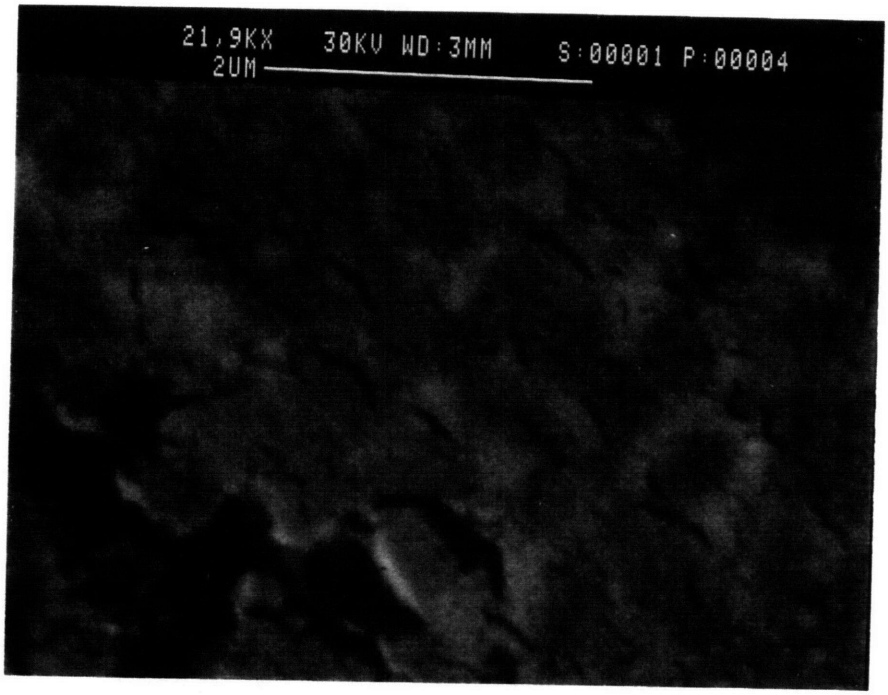

Figure 5.18b)

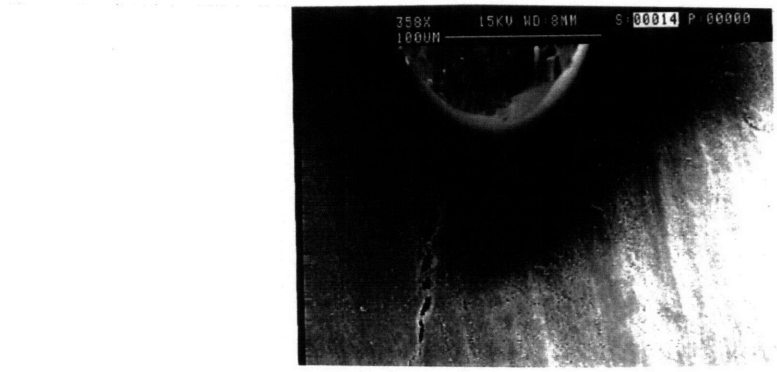

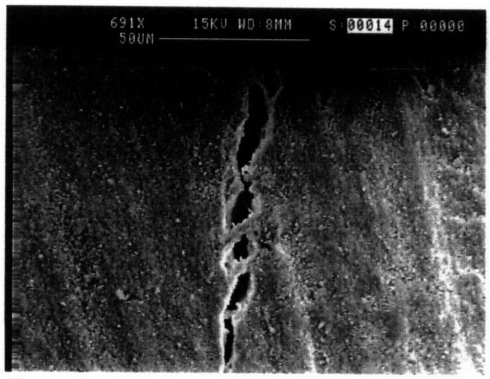

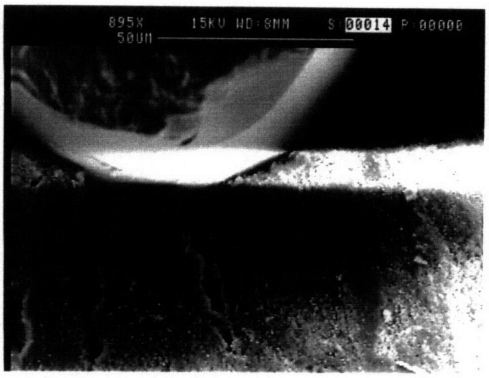

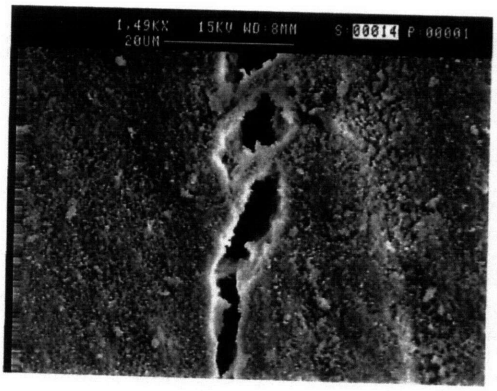

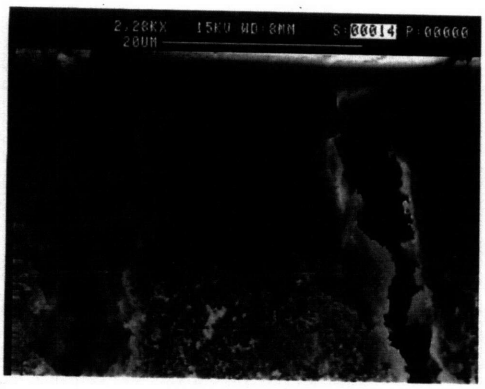

Figure 5.19 Structure of cracks in the matrix of Al_2O_3 / Al_2O_3 composite.

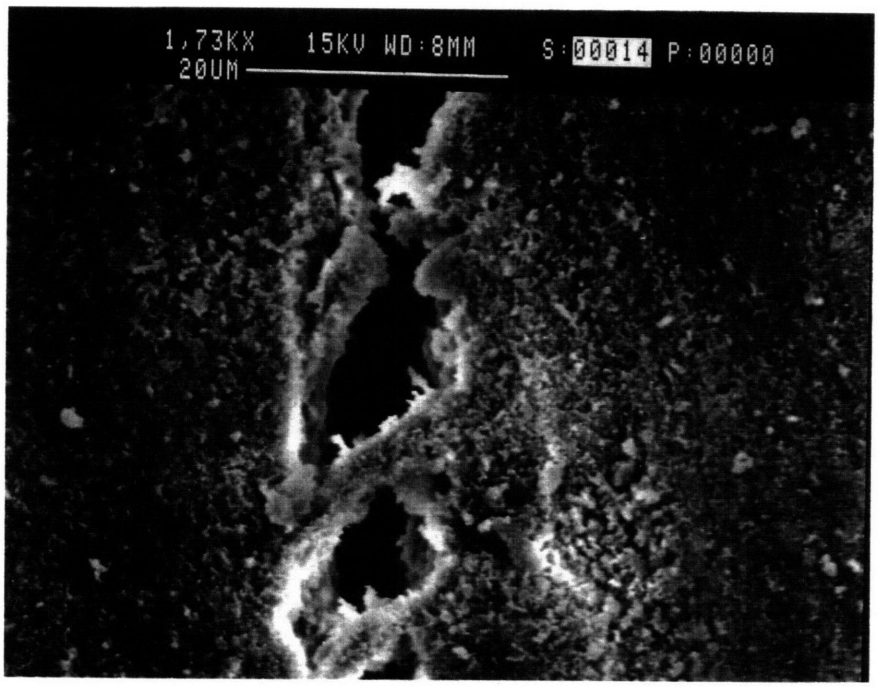

Figure 5.19f

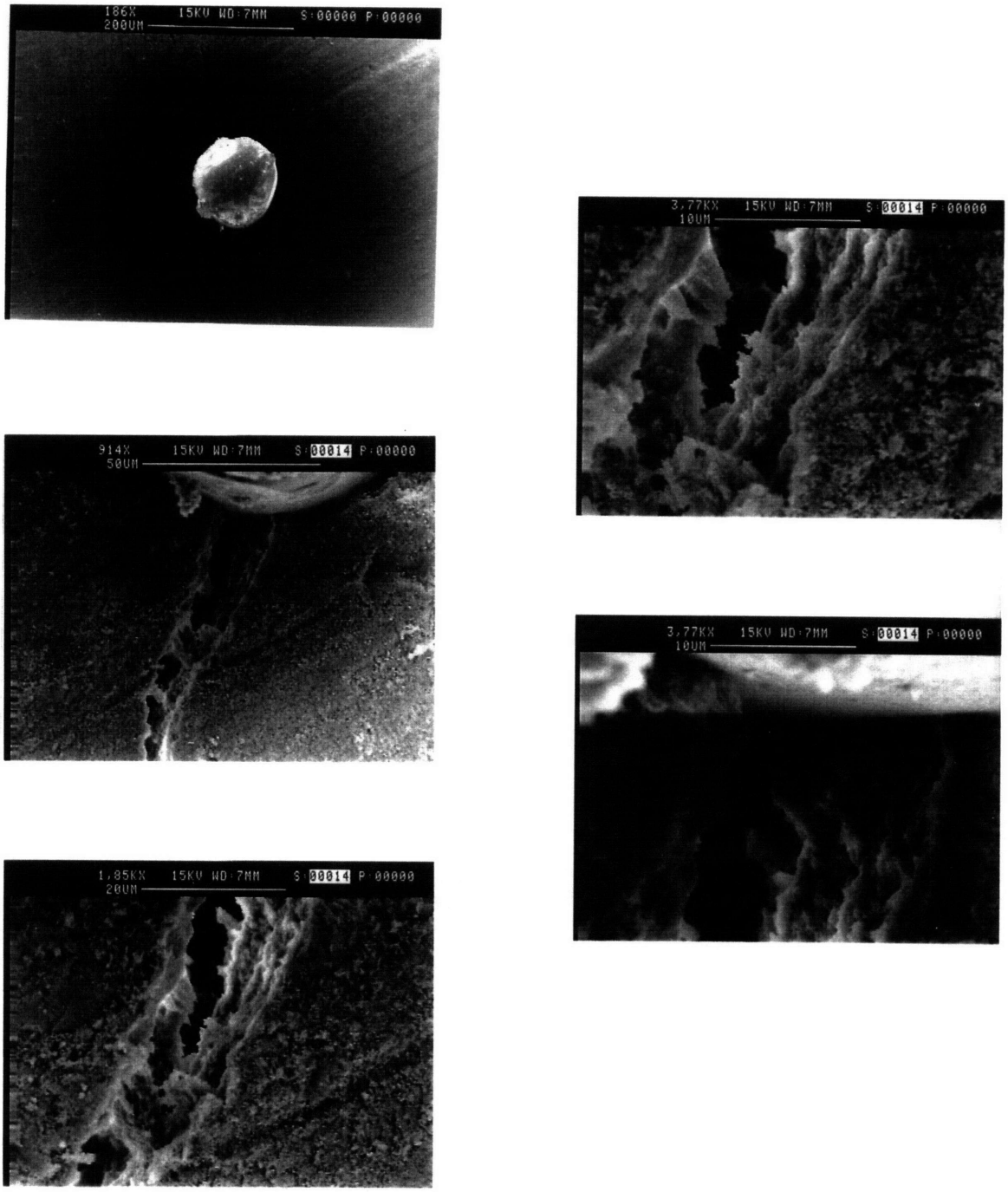

Figure 20 Structure of cracks in the matrix of Al_2O_3 / Al_2O_3 composite

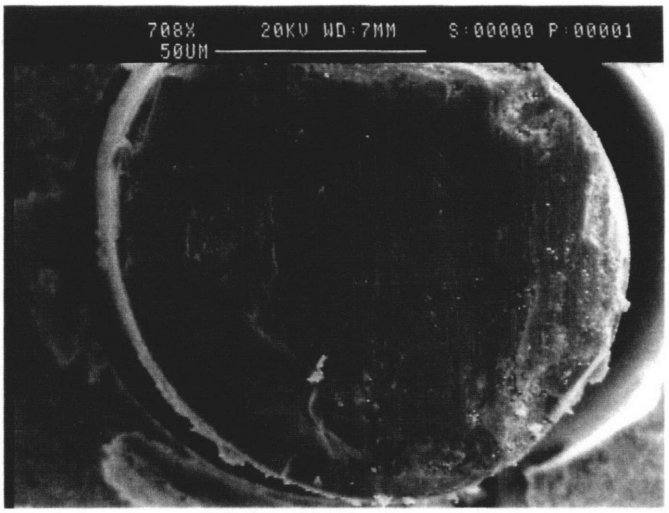

Figure 5.21a

Figure 5.21 Clearances between the fibers and the matrix in Al_2O_3 / Al_2O_3 composite

Figure 5.21b

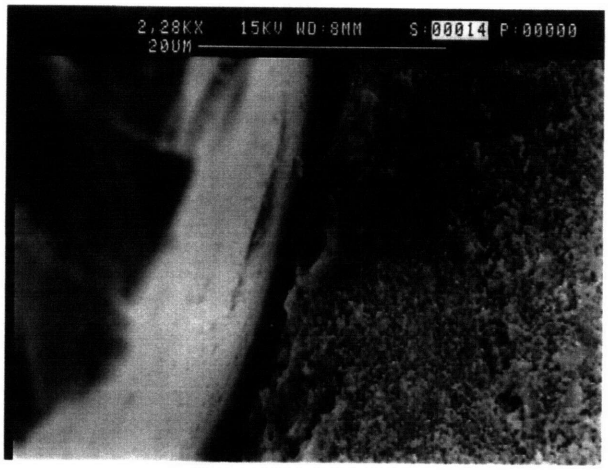

Figure 5.21c

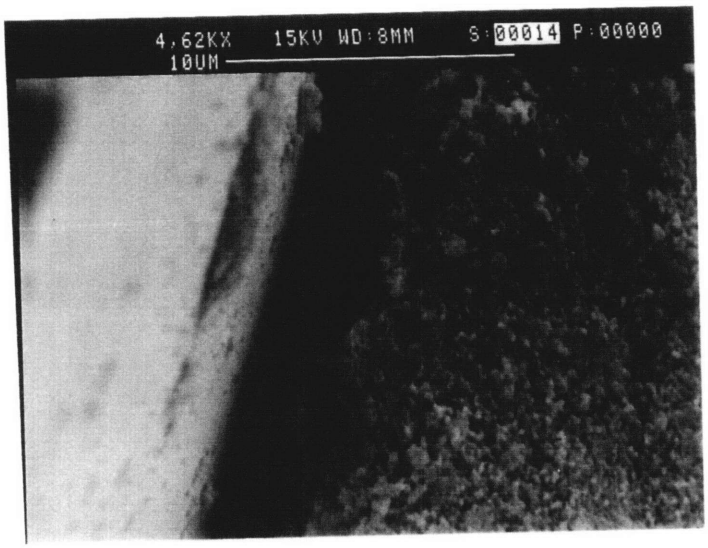

Figure 5.21d

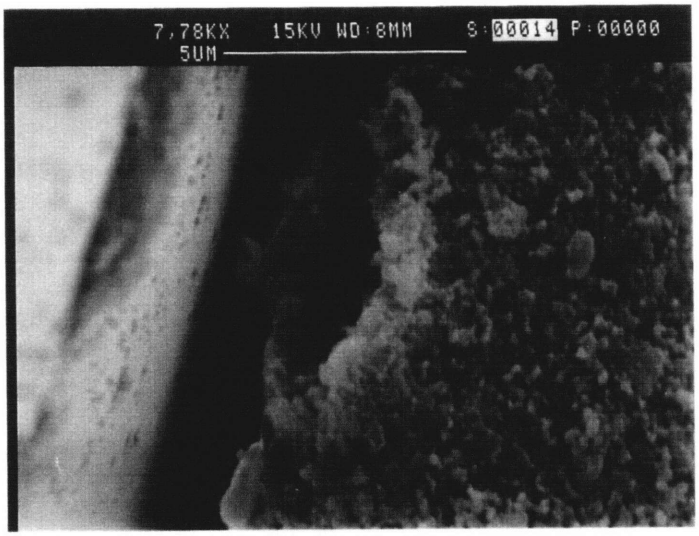

Figure 5.21e